

2022-12-01

Hydrothermal Alteration Targeting And Geophysical Mineral Exploration Of Eureka And Sylvanite Mining Districts, Southwest New Mexico

Kenneth Singh
University of Texas at El Paso

Follow this and additional works at: https://scholarworks.utep.edu/open_etd



Part of the [Geology Commons](#), and the [Geophysics and Seismology Commons](#)

Recommended Citation

Singh, Kenneth, "Hydrothermal Alteration Targeting And Geophysical Mineral Exploration Of Eureka And Sylvanite Mining Districts, Southwest New Mexico" (2022). *Open Access Theses & Dissertations*. 3728.
https://scholarworks.utep.edu/open_etd/3728

This is brought to you for free and open access by ScholarWorks@UTEP. It has been accepted for inclusion in Open Access Theses & Dissertations by an authorized administrator of ScholarWorks@UTEP. For more information, please contact lweber@utep.edu.

HYDROTHERMAL ALTERATION TARGETING AND GEOPHYSICAL MINERAL
EXPLORATION OF EUREKA AND SYLVANITE MINING DISTRICTS,
SOUTHWEST NEW MEXICO

KENNETH C. SINGH

Master's Program in Geological Science

APPROVED:

Philip C. Goodell, Ph.D., Chair

Antonio Arribas, Ph.D.

Marianne Karplus, PhD.

Hugo Gutierrez, Ph.D.

Raed AlDouri, Ph.D.

Stephen L. Crites, Jr., Ph.D.
Dean of the Graduate School

Copyright ©

by

Kenneth C. Singh

2022

HYDROTHERMAL ALTERATION TARGETING AND GEOPHYSICAL MINERAL
EXPLORATION OF EUREKA AND SYLVANITE MINING DISTRICTS,
SOUTHWEST NEW MEXICO

by

KENNETH C. SINGH

THESIS

Presented to the Faculty of the Graduate School of

The University of Texas at El Paso

in Partial Fulfillment

of the Requirements

for the Degree of

MASTER OF SCIENCE

Department of Earth, Environmental and Resource Sciences

THE UNIVERSITY OF TEXAS AT EL PASO

December 2022

Acknowledgements

Special thanks to Dr. Antonio Arribas, Dr. Jose Hurtado, and Dr. Hugo Gutierrez for their help and use of their labs and equipment. Without their help the x-ray diffraction, mineral spectroscopy, and electrical resistivity would not have been available options. To Dr. Munazzam Ali Mahar, Carmel Murillo, Joshua Lewis, Jerrika Stark, David West, Yeshey Seldon, Oskar Alvarez, Daphne Short, Fernando Vasquez and Alfredo Torres for all the hard work you put in on all the many long days spent out in the field it is greatly appreciated. I learned valuable lessons from all of you and I hope I was able to help you learn something too. For the x-ray diffraction lab work you helped me with, thank you to Hannah Buamono and David Mueller. Thank you to Annette Veilleux, without your help and support I never would have made it this far. And sorry for always showing up at your office without an appointment to bug you. A special thank you to Mike Jacobs for your help, equipment, and guidance along the way. You are one of the best men and mentors I have ever known and hope to spend many more adventures with you on other journeys as well. A big thank you to Sergio Macias for taking time away from your family to work with me utilizing the Spectral Geologist software and being a sounding board for ideas and hypotheses. Your work was invaluable, and I truly thank you from the bottom of my heart. To my good friend Dr. Jose ‘Tony’ Garcia. From Cuba to Argentina we have had many great adventures together and hope to have more as we spread our wings in the industry, thank you my friend. To all my Marine brothers who have shed blood, sweat, and tears with me. I love all of you and thank you for laying your lives on the line every day for me. A special thank you to the best man I have ever known, Lance Corporal Jeremy Wade Burris. I know you are watching me while guarding the gates of heaven brother, thank you for inspiring me to be the kind of man you were. I hope I have made you proud and know I will see you again someday. An enormous thank you to all my advisors and professors. Without you I would not be here today; your guidance and dedication to science is an inspiration. I would like to thank the entirety of staff, facility, and student body at the University of Texas at El Paso for all the help I

received from everyone over the 7 years I have spent at UTEP. Everyone that I interacted with gave me hope, help, advice, and/or guidance in some way, so thank you. To my Morenci Freeport family for the help, support, and guidance during my 2021 summer internship. The valuable lessons learned have and will help me throughout the rest of my career, thank you. To my mom, brother, and aunts for always being there when I felt lost and alone, and for still loving me although I put you all through so much. You have all made me a better man. I would like to give a thank you to the rest of my family and friends for being there for me through the good and bad times, I realize that sometimes I can be a bit much to handle but you all stuck with me, thank you. And last but certainly not least, I would like to thank Dr. Philip Goodell. You have been the best mentor and guiding hand anyone could have asked for. I am proud to call you my friend, but more than that you have acted sometimes as an older brother, father, grandfather, and little brother. You have given me more opportunities than I probably deserved and never gave up on me, thank you and this is for you!

Abstract

As part of the southwestern North American porphyry copper province, mining of natural resources in New Mexico has historically played a crucial role in economic development for over 150 years including this project area in the Little Hatchet Mountains. The northern half of the Little Hatchet Mountains lies in Grant County and includes the Eureka Mining District (EMD) whereas the southern half is in Hidalgo County and includes the Sylvanite Mining District (SMD), 38 miles southeast of Lordsburg. The EMD, a copper and silver-lead mining district from 1880-1961, had a total estimated production from the Laramide veins of 2.9 million lbs. Pb, 1.7 million lbs. Zn, 500,000 lbs. Cu, 5,000 ounces Au, and 450,000 ounces Ag (McLemore et. al, 1996). The SMD, a silver-gold mining district from Laramide skarn, vein, and placer deposits occur in the district and production including 2,500 ounces Au, 130,000 lbs. Cu, and 8,000 lbs. Pb from 1902-1957. This study focuses on remote sensing hydrothermal mineral alteration zones detected using Mars 2014 USGS shapefiles in the Basin and Range province, which assisted in the targeting of subsequent electromagnetic and electrical resistivity surveys that were conducted of potential mineral deposits. Electromagnetics survey readings, using the Geonics EM34-3XL that reach a depth of 180 ft, have resulted in interesting anomalies. These surveys have also allowed us to determine where the electrical resistivity surveys, using the SuperSting R8 112 electrode 5 m interval spacing for a max depth profile of 111 m, were performed. Spectral microscopy on 18 samples was conducted to test remote sensing ground truth certainty. X-ray diffraction was performed on 7 of the samples to test the accuracy of the mineral spectroscopy results. The present study is enhancing the knowledge base of these mining districts and southwest New Mexico as well as providing new geophysical results for future exploration.

Table of Contents

Acknowledgements	ivv
Abstract	vi
Table of Contents	vii
List of Tables	viii
List of Figures	ix
Chapter 1: Introduction.....	1
Chapter 2: Geologic Background.....	6
2.1 Stratigraphy.....	6
2.2 Structure and Regional Tectonics.....	11
2.3 Mineralogy.....	17
Chapter 3: Methodology.....	21
3.1 Remote Sensing.....	21
3.2 Electromagnetics.....	22
3.3 Electrical Resistivity.....	27
3.4 Mineral Spectroscopy.....	29
3.5 X-ray Diffraction.....	31
Chapter 4: Data and Results.....	33
4.1 Remote Sensing.....	33
4.2 Electromagnetics.....	36
4.3 Electrical Resistivity.....	40
4.4 Mineral Spectroscopy.....	42
4.5 X-ray Diffraction.....	48

Chapter 5: Interpretations.....	49
5.1 Remote Sensing.....	49
5.2 Electromagnetics.....	51
5.3 Electrical Resistivity.....	54
5.4 Mineral Spectroscopy.....	56
5.5 X-ray Diffraction.....	58
5.6 Discussion and Speculation.....	60
Chapter 6: Conclusions and Future Work.....	63
References	65
Appendix	77
A1 Remote Sensing.....	77
A1.1 Flow Chart.....	77
A2 Electromagnetics.....	78
A2.1 Figures.....	78
A2.2 Tables.....	86
A2.3 Flow Charts.....	89
A3 Electrical Resistivity.....	92
A3.1 Figures.....	92
A3.2 Flow Charts.....	96
A4 Mineral Spectroscopy.....	97
A4.1 Figures.....	97
A4.2 Flow Charts.....	150
A5 X-ray Diffraction.....	151

A5.1 Figures.....	151
A5.2 Flow Charts.....	158
A6 Additional Figures and Tables.....	159
Vita.....	162

List of Tables

Table 1. Spectroscopy Mineral Identification.....	42
Table 2. Spectroscopy vs XRD	59

List of Figures

Figure 1. Topographic map of the Little Hatchet Mountain with prospects.....	3
Figure 2. Little Hatchet Mountains Stratigraphic Column.....	6
Figure 3. Geologic map of the Little Hatchet Mountains.....	7
Figure 4. Geologic map cross-section.....	8
Figure 5. Eureka area of Zeller 1970 map.....	9
Figure 6. Sylvanite area of Zeller 1970 map.....	10
Figure 7. Map shows the multiple stages of compression and extension.....	11
Figure 8. Sample of limonite gossan	18
Figure 9a-d. Rock samples from SMD.....	19
Figure 10. Basic physics of passive remote sensing satellites	21
Figure 11. Magnetic field of an electric current.....	22
Figure 12. Electromagnetics Surfer to ArcGIS Flow Chart.....	23
Figure 13. An intermittent d.c. current that models.....	25
Figure 14. Electric field in a half-space extension.....	27
Figure 15. Electrical resistivity dipole-dipole electrode array.....	28
Figure 16. GER 3700.....	29
Figure 17. Bruker D2 Phaser.....	32
Figure 18. ArcGIS base topographic map EMD with alteration; 1:10,000.....	33
Figure 19. ArcGIS base topographic map SMD with alteration; 1:13,000.....	34
Figure 20. Eureka electromagnetics 40V map.....	36
Figure 21. Sylvanite electromagnetics 40V map.....	37
Figure 22. Electrical resistivity survey lines.....	40

Figure 23. Electrical resistivity inverted conductivity model, south to north.....	41
Figure 24. Electrical resistivity inverted conductivity model, southeast to northwest.....	41
Figure 25. Sample 001_A_1; results of mineral spectroscopy.....	43
Figure 26. Sylvinite: Sample 001_A_1; with modifications.....	44
Figure 27. Standard wavelength (CSV import data) with no slight modifications.....	44
Figure 28. Results in the visible and near-infrared (VNIR) Primary TSA result	45
Figure 29. Results in the visible and near-infrared (VNIR) Multiple results overlay.....	45
Figure 30. VNIR Goethite: The Spectral Analyst (TSA) possible results.....	45
Figure 31. Sample 001_A_1: 61% Chlorite-Fe + 22% Jarosite+16% Gypsum.....	46
Figure 32. Sample 001_A_1: 61% Chlorite-Fe + 22% Jarosite+16% Gypsum.....	46
Figure 33. The Spectral Analyst (TSA) possible results.....	47
Figure 34. XRD results for sample A1 with top mineral matches.....	48
Figure 35. Illustrated deposit model of a porphyry copper deposit.....	50
Figure 36. Table of typical ranges in conductivity/resistivity.....	51
Figure 37. Electrical resistivity inverted conductivity model, south to north	54
Figure 38. Electrical resistivity inverted conductivity model, southeast to northwest.....	55
Figure 39. Idealized cross-section of high-sulphidation epithermal and porphyry environment..	56
Figure 40. Theoretical model showing possible inferred porphyry	61
Figure 41. Theoretical model showing possible inferred porphyry with alteration	62

Chapter 1: Introduction

West of New Mexico lies one of the world's great metal-bearing provinces, Arizona. With rapid technological advancement in today's world, copper is particularly important and may be found in small to large deposits throughout New Mexico, Arizona, Utah, Nevada, and in a world-class open-pit deposit such as Morenci in Arizona. Gold and silver deposits are abundant in Nevada, and to a lesser extent, throughout the Southwest. Numerous geologists have examined the geology and mineral resource potential of these porphyry copper deposits (PCD) over the last 50 years or more. Porphyry copper (molybdenum, gold) deposits are large deposits that contain disseminated, breccias and stockwork veinlets of copper and molybdenum sulfides associated with porphyritic intrusions (Schmitt, 1966; Lowell and Guilbert, 1970; Kesler, 1973; Lowell, 1974; Titley and Beane, 1981; Cox and Singer, 1986; Seedorff et al., 2005; McLemore, 2008). These copper deposits typically are found in and around relatively small porphyritic diorite, granodiorite, monzonite, and quartz monzonite plutons that were intruded at relatively high crustal levels, commonly within 1-6 km of the surface, and are surrounded by crudely concentric zones of hydrothermal alteration (Lowell and Guilbert, 1970; Seedorff et al., 2005; McLemore, 2008). Volatiles, primarily steam and other gases, build up within the magma and ultimately there is enough pressure to fracture the solidified intrusive porphyry and adjacent host rocks above the magma chamber. Hydrothermal solutions are released through these fractures and react with the host rocks, altering them in a characteristic, concentric zonation. The two types of mineral enrichment are hypogene and supergene. Hypogene copper and molybdenum minerals account for 1–2 volume percent of hypogene ore and occur in several forms: (1) disseminated in host rocks as discrete, less than or equal to 1-mm anhedral to subhedral crystals that replace feldspars and other minerals internally and along grain boundaries or in millimeter-to-centimeter

clotlike aggregates with hydrothermal biotite and other silicate, sulfate, and oxide minerals; (2) in veins, less than 1 millimeter to several centimeters wide, with micrometer to millimeter quartz, pyrite and other hypogene minerals; vein aspect varies from sharply planar veins that are continuous for meters to curvilinear, diffusely margined and discontinuous veins that pinchout within centimeters; and (3) in breccia matrices with quartz and other hypogene minerals, sometimes in millimeter-to-centimeter subhedrons and euhedrons; breccia clasts and matrices vary greatly in aspect, dimension and composition (John et. al, 2010). Hypogene minerals that commonly occur with copper and molybdenum minerals are quartz, pyrite, sericite (muscovite; potassium mica), chlorite, epidote, biotite, potassium feldspar, magnetite, and anhydrite. In some PCDs, hypogene ore includes the copper minerals, tennantite/tetrahedrite, enargite, and covellite, which occur with quartz, pyrite, sericite, kaolinite, alunite, and pyrophyllite in sericitic and advanced argillic alteration zones. Supergene ore contains minable copper minerals and a large number of other minerals precipitated from descending, low-pH groundwater that dissolved hypogene copper minerals and redeposited copper in minerals stable in low-temperature, oxidizing environments. Numerous dissolution-precipitation cycles lead to reconcentration of copper in subjacent, laterally extensive deposits known as supergene oxide deposits and chalcocite enrichment blankets or enriched copper sulfide zones, and less commonly in distal concentrations known as exotic oxide deposits. Common copper minerals in oxide ores include malachite, azurite, cuprite, tenorite, chrysocolla, native copper, copper wad, and atacamite; numerous other copper carbonate, oxide, silicate, and sulfate minerals are present in small amounts. These minerals occur as crystalline aggregates and crystals that fill fractures and line

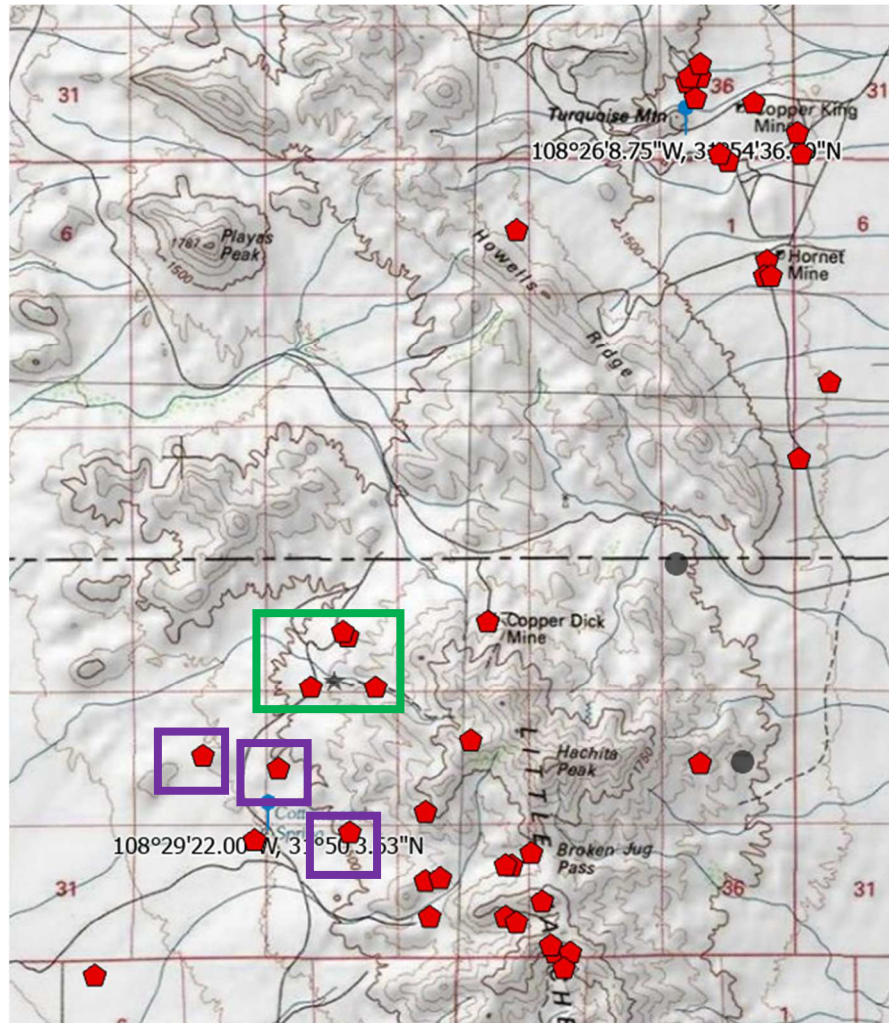


Figure 1. Topographic map of the Little Hatchet Mountains with Eureka (north) and Sylvanite (south) targets denoted with blue lollipops. Red pentagons mark previous prospects (Appendix Tables A6.2.2 and A6.2.3; McLemore et.al, 1996). Approximate location of Figure 8, limonite gossan outcrop, outlined with the green square and purple squares highlighting the prospects.

voids in leached capping, and in micrometer-to-millimeter aggregates that impregnate alteration and primary minerals in enriched copper sulfide ore, and less often, in hypogene ore (John et. al, 2010). The outer hydrothermal zone (referred to as propylitic alteration) is typically characterized by epidote-chlorite-pyrite mineral assemblages. A quartz-sericite-pyrite (QSP) mineral assemblage alteration zone typically is found closer to the center and can overprint other

zones. A central potassic zone of biotite-orthoclase-chalcopyrite mineral assemblage is commonly associated with most of the ore. This hydrothermal alteration can include numerous additional types of mineral assemblages that commonly overlap (Seedorff et al., 2005; McLemore, 2008). Copper minerals, to varying degrees, are deposited as a part of this interaction between hydrothermal solutions along fractures in solid rock. The copper minerals are found as disseminations along thin fractures, zones of brecciation, and within larger veins, called stockwork veins. Typically, these deposits are very large, some in excess of a billion tons of mineralized rock. Copper grade varies from less than 0.10% copper to over 1% copper, with 2-5% pyrite and varying amounts of gold, silver, molybdenum, uranium, and other metals and nonmetals (McLemore, 2008). Eureka and Sylvanite are two possible PCD mineral districts in southwest New Mexico (Figure 3) that have been poorly characterized and described. Selection of this region was partially due to prospecting of the area that has been ongoing for over a century and may be seen on Figure 1 (Appendix Tables 5.2.2 and 5.2.3; McLemore, 1996).

Genesis relationships of the area have been proposed but not tested. between the 1880s to the 1950s. From these mines and prospects extraction ore consisted of Au, Ag, Cu, Mo, Zn, Pb, Te, Bi, As, W, V, and Ba. Their degree of development differs between mainly adits, pits, and shafts. Using remote sensing according to Mars 2014, economic deposits such as gold and copper are typically associated with hydrothermally altered rocks (John et. al, 2010), which typically consist of one or more hydrous zones of alteration minerals containing at least one mineral that exhibits diagnostic spectral absorption features in the VNIR through the SWIR and (or) the thermal-infrared TIR regions (Hunt and Ashley, 1979; Abrams et. al, 1983; Spatz and Wilson, 1995). These areas were targeted for exploration geophysics.

The hydrothermally altered rocks on the surface at Eureka and Sylvanite were separated into groups containing chalcedony, opal, and amorphous silica; calcite-dolomite and epidote-chlorite; alunite-pyrophyllite-kaolinite; and sericite-muscovite; and were identified using the Advanced Spaceborne Thermal Emission and Reflection Radiometer (ASTER) on the Terra satellite (terra.nasa.gov/). Exploration geophysics conducted included electromagnetics, electrical resistivity, mineral spectroscopy, and x-ray diffraction. The remote sensing and geophysical exploration survey targeting and performance for the potential identification and confirmation of mineralization of these mineral deposits has helped in their determination and suggest that these methods may be utilized in other regions. The results of this study give a better understanding of alteration mineralization and conductivity and resistivity anomalies of the targeted areas in southwestern New Mexico. Implications of this study may be used to further explain the potential mineralization of areas considered to be zones where emplacement of porphyry copper deposits may have taken place within New Mexico and others in the southwest. Digital models and maps resulting from this study may help to develop the next stage of exploration and determine potential drill targets to confirm the conclusions provided by this thesis and develop an understanding of the porphyry deposits in the Little Hatchet Mountains.

Chapter 2: Geologic Background

Stratigraphy

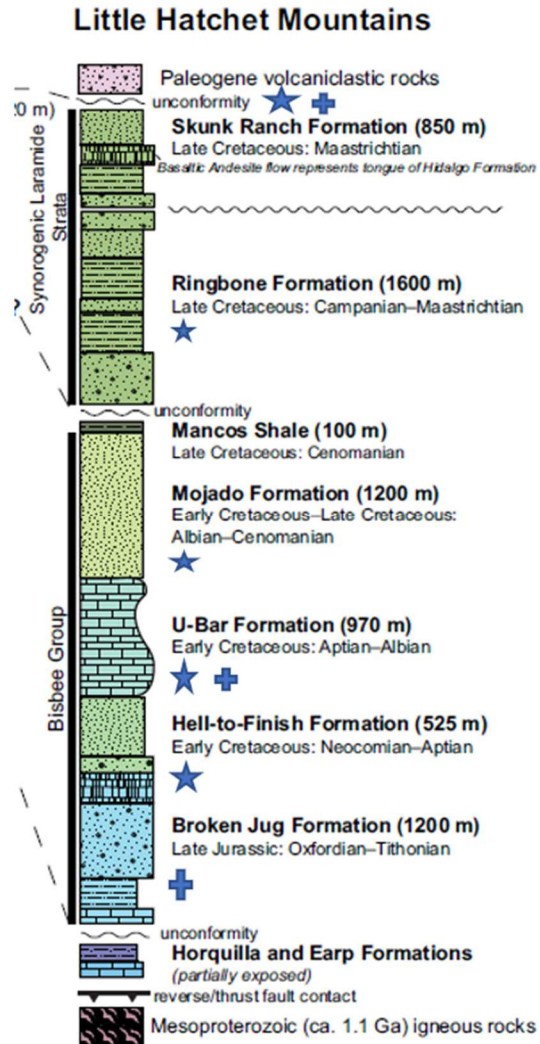


Figure 2. Generalized stratigraphic section of the Little Hatchet Mountains with stars representing formations in the EMD and plus signs representing the SMD (Clinkscales and Lawton 2017)

The Broken Jug limestone formation consists of pure, shaly, and sandy limestone, interbedded with shale, sandstone, and conglomerate. In places pure limestone predominates, elsewhere shaly or sandy limestone are associated with considerable sandstone (Lasky 1947).

The Hell-to-Finish Formation consists mostly of red shale, gray shale, red siltstone, limestone-

cobble conglomerate, arkose, and sandy (arkosic) limestone. The U-Bar Formation, which is characterized by marine limestone, is conformable with the Hell-to-Finish Formation below and

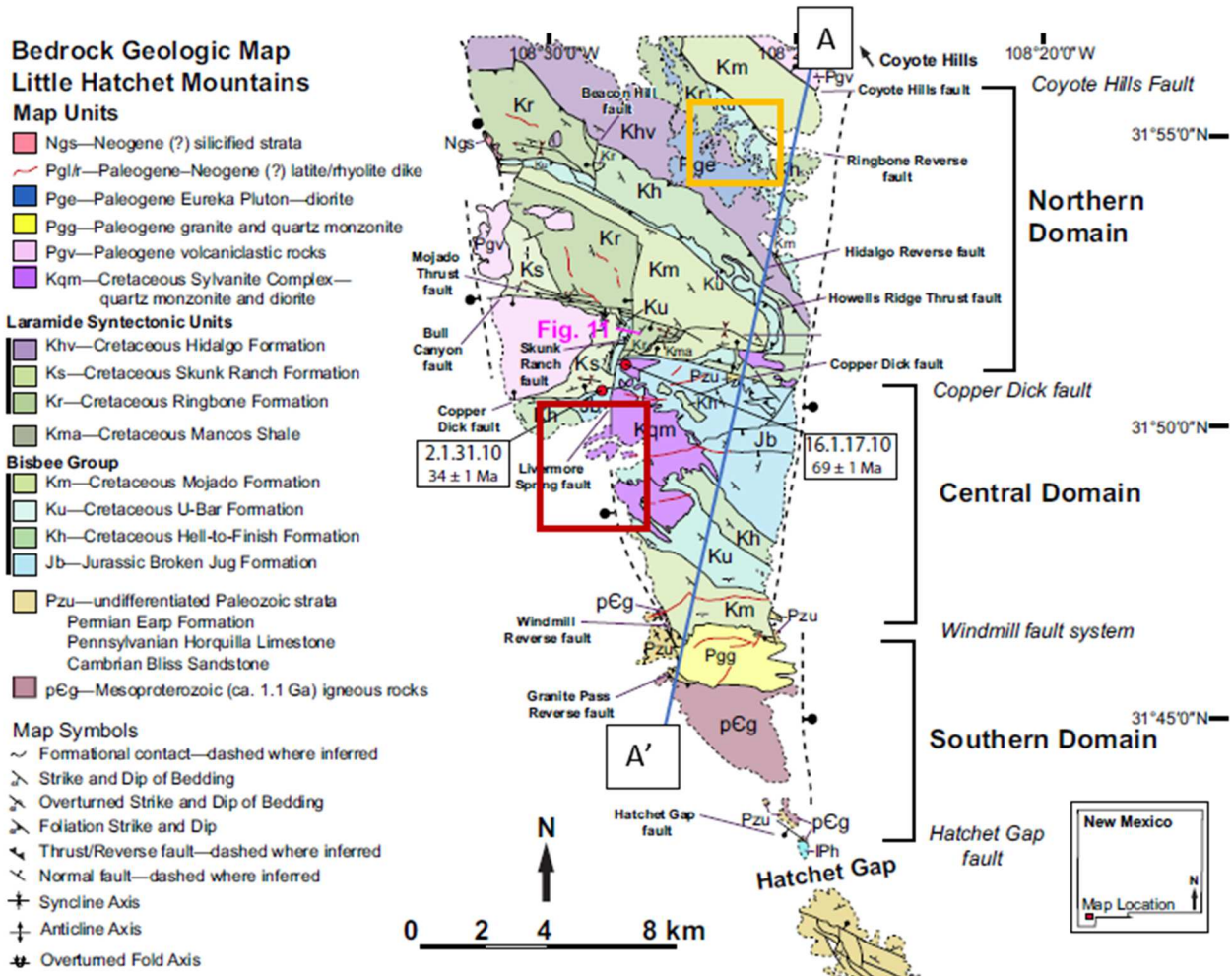


Figure 3. Geologic map of the Little Hatchet Mountains with Eureka Mining District area in the orange box and Sylvanite Mining District area in the red box. The blue line A-A' represents cross-section in Figure 3 (Clinkscales and Lawton 2017).

the Mojado Formation above.

The Mojado Formation consists mainly of gray and tan quartz sandstone beds with shale interbeds that are concealed in most areas. The Mojado Formation is overlain with angular unconformity by younger formations. The Ringbone Formation consists of beds and lenses of

limestone-cobble conglomerate are found at and near the base of the formation in most places. The Sylvanite Intrusive Complex occurred in the south-central part of the Little Hatchet Mountains from Stone Cabin Gulch to the Copper Dick mine. A large diorite stock lies south of the old townsite of Sylvanite. It joins a large monzonite stock that extends from Sylvanite northward and northwestward for several miles. Several smaller outcrops of quartz monzonite lie within and near the monzonite. The Old Hachita Stock/Paleogene Eureka Pluton, a monzonite stock that crops out over an area of nearly 2 square miles west of Old Hachita. As in the Sylvanite intrusive complex, the stock exhibits variations in texture and composition. A wide dike of diorite crosses the stock in an east-west direction. The diorite intrudes the stock, but some monzonite dikes seem to be younger (Zeller 1970). This section belongs to Lasky 1947 and Zeller 1970. Zeller's geologic maps of the Eureka and Sylvanite areas are shown in Figures 5 and 6.

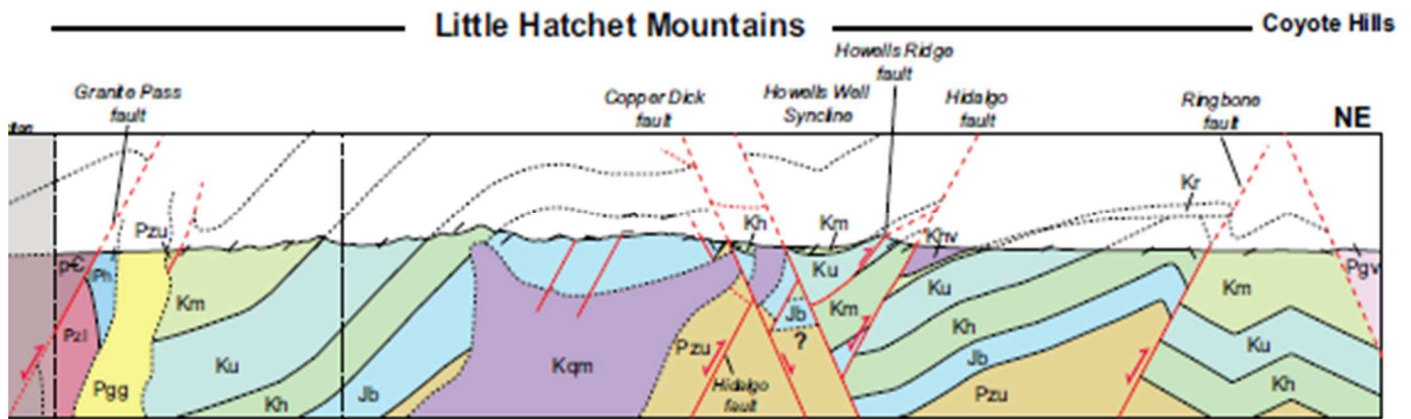


Figure 4. Geologic map cross-section from A to A' on Figure 2 (Clinkscales and Lawton 2017).

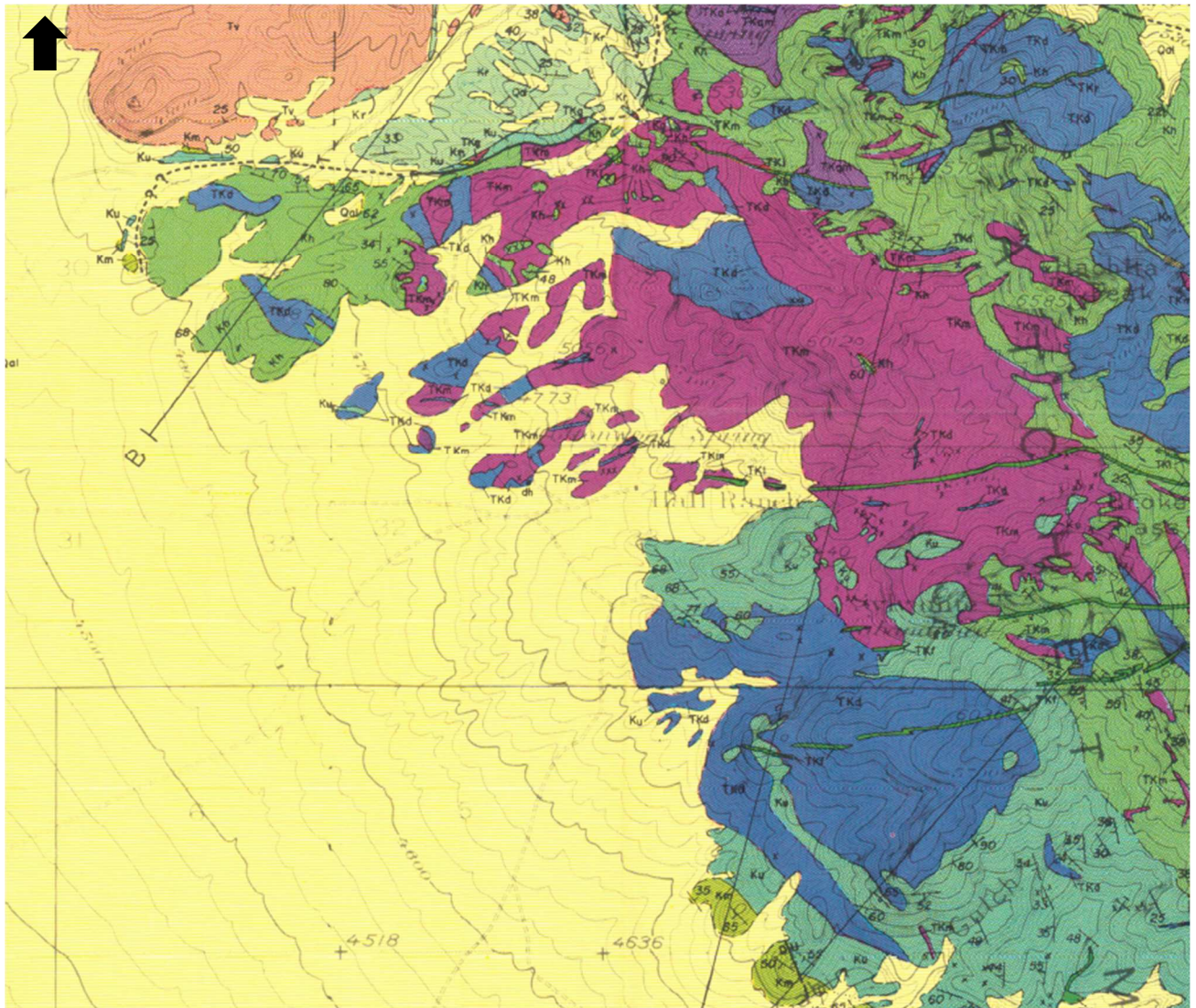


Figure 6. Zoomed-in Sylvanite area of Zeller 1970 map, see Figure 4 for explanations.

Structure and Regional Tectonics

The Little Hatchet Mountains lie to the south of the intersection between the Texas and Santa Rita lineaments, which when concerning ore deposits in New Mexico is important due to

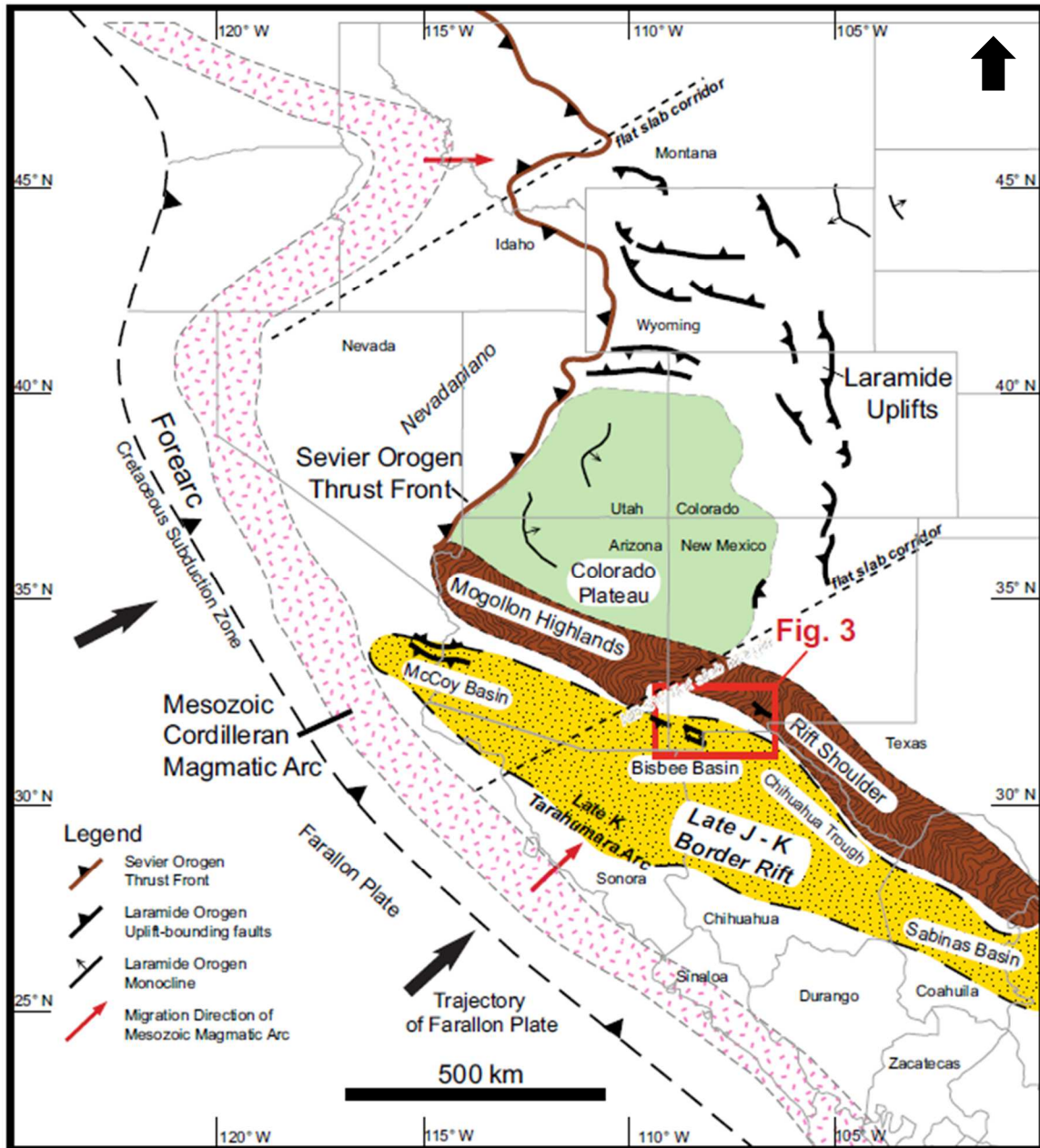


Figure 7. Shows the multiple stages of compression and extension, and the Late Jurassic-Cretaceous Border Rift with basins highlighted in yellow as mobile belt. Fig.3 outlines the project area in a red rectangle (Clinkscales and Lawton 2017)

the high yield deposits between the Morenci and Santa Rita lineaments further north. In the northern Little Hatchet Mountains Laramide deformation is a thick-skinned deformation event that occurred in two discrete pulses, a Late Cretaceous shortening event accompanied by basement up lift and later Eocene transcurrent deformation that reactivated the former basement-involved faults (Hodgson, 2000).

The two pulses were defined in the Little Hatchet Mountains on the basis of inferred discrete Campanian– Maastrichtian and Eocene ages for the Laramide syntectonic Ringbone and Skunk Ranch Formations, respectively (e.g., Lawton et al., 1993; Basabilvazo, 2000). Recent studies integrating structural-stratigraphic relations with U-Pb dating of syn-Laramide clastics and interbedded tuffs demonstrate that no significant hiatus occurs between the Ringbone and Skunk Ranch Formations. Instead, the unconformity represents a progressive unconformity along intrabasinal thrust faults with no evidence of Paleogene deposition and major shift in Laramide kinematics. Igneous rocks bracketed for the oldest episode, between ca. 76 and 70 Ma, crop out within and near the Little and Big Hatchet Mountains, including exposures in the central and northern Little Hatchet Mountains. Northeastward migration of Cretaceous magmatism and volcanism is inferred as a result of progressive shallowing of the Farallon plate (e.g., Coney and Reynolds, 1977).

The Hatchet Mountains are underlain mainly by Paleozoic and Mesozoic rocks; Precambrian granite is exposed in the gap between them. Late Cretaceous or Paleocene stocks intrude the Little Hatchet rocks (Lasky, 1947; Zeller, 1965 and 1970; Thompson and Jacka, 1981; Drewes, 1988). Rocks of both mountain ranges have been deformed by northeast-southwest-oriented compressional deformation, of about Paleocene age, with some noteworthy changes in deformational style from north to south. Rocks of the southern half of the Little

Hatchet Mountains, the northern part of the Big Hatchet Mountains, and the gap between them are cut by a series of northwest-trending strike-slip faults, possibly having left slip. Such movement is indicated on the northeastern faults of the northwest-trending set by left-lateral offset of the Bliss Sandstone. The essential features are a major structural break to the northeast, separating a thinner plate system of the fold-and-thrust zone from a thicker plate system of the eastern intermediate zone. This change in thickness is marked by a shift of a main decollement position from the incompetent Permian rocks in the east to a position at the base of the Paleozoic sequence in the west.

The Bisbee Group was deposited in a still larger basin shown by Hayes (1970) to have had a northwest-trending axis that plunged gently southeast. The northwestern part of the basin was subaerial estuarine and fluvial, and the southeastern part was marine, as indicated by the distribution of reefal limestones. The bulk of the Bisbee Group was derived from the west: sediment was likely transported east into the broad fluvial basin along the orogenic front and then southeast along the axis of the basin to the Bisbee marine embayment. The evidence of Cordilleran direction of transport can generally be distinguished from that of the Miocene extensional event of the hinterland zone. In many places there, the overprinted compressional fabric has the same orientation as the younger extensional fabric, a situation once again hinting at some genetic tie between the Cordilleran orogeny and the basin-and-range detachment faulting event (Clinkscapes and Lawton 2017).

The Paleozoic Pedregosa basin was autogeosynclinal, receiving thick deposits of Middle Mississippian crinoidal limestones, Late Mississippian arenaceous calcarenites, Pennsylvanian limestones, and Wolfcampian interbeds of limestone, black shale, and redbeds (Kottlowski 1964). The Chihuahua trough and Bisbee basin presently make up what was the Pedregosa basin

that then transitions into the McCoy basin further west concluding the mobile belt (Figure 7). The change from rift basin to foreland basin is recorded by the deposition of more than 1400 m of fluvial and marginal marine strata of the Mojado Formation and Mancos Shale (e.g., Lucas and Lawton, 2005). Siliciclastic strata of the Mojado Formation and correlative Beartooth Quartzite in the Burro Mountains and Cookes Range record a volcanic and recycled orogen source terrane with east-directed paleocurrents sourced from a retroarc fold-thrust belt to the west (Mack, 1987; Machin, 2013).

By mid-Cenomanian time, the foreland basin in southern New Mexico was contiguous northward with the Cordilleran foreland basin of northern New Mexico, Colorado, and Utah. Late Cretaceous to Eocene Laramide orogenesis involved the breakup of the Cordilleran foreland by uplift of basement-involved blocks along reverse and thrust faults (Dickinson and Snyder, 1978; Cross, 1986; Seager and Mack, 1986; Dickinson et al., 1988; Mack and Clemons, 1988). Laramide uplifts consist of thick-skinned, basement-involved features that generally flank intermontane basins dominated by alluvial, fluvial, and lacustrine deposits. Laramide uplifts and basins in southern New Mexico are oriented northwest-southeast and bounded by reverse faults that generally verge northeast (Seager, 2004) and contain upper Cretaceous to Paleogene continental and volcanic deposits (Basabivazo, 2000; Seager et al., 1997; Lawton, 2008; Jennings et al., 2013; Amato et al., 2017). The distribution of these uplifts and basins is rendered uncertain by Cenozoic basin fill that extensively buries the Laramide syntectonic rocks and structures; moreover, structural overprinting by multiple deformation episodes also confounds interpretation of the kinematic history.

Diorite indicated on the geologic map of Zeller (1970) is Jurassic basalt intruded by the Sylvanite plutonic complex (Figure 6; Lawton and Harrigan, 1998; Clinkscales and Lawton,

2014). The topography of the range and mapped fault relationships indicate that the bounding faults are discontinuous along strike with fault terminations giving way to relay or transfer zones similar to those described by Faulds and Varga (1998). North of Granite Pass, upper Jurassic to Cretaceous strata of the Bisbee Group (Lawton and Olmstead, 1995; Lucas and Lawton, 2005) comprise an extensive south-southwest–dipping panel that dominates the central domain. The central domain contains the only recognized exposures of Jurassic Broken Jug Formation in southwestern New Mexico (Lawton and Harrigan, 1998; Lucas and Lawton, 2000), but correlative upper Jurassic strata are present in the Chiricahua Mountains of southeast Arizona (Lawton and Olmstead, 1995; Olmstead and Young, 2000).

The Bisbee Group is intruded by the Late Cretaceous Sylvanite Complex, near which the strata are extensively thermally metamorphosed. Bisbee strata are locally displaced by minor east-west, west-northwest–east-southeast–trending normal faults with <10 m of offset, rhyolite dikes, and thrust faults. Conjugate west-northwest–east-southeast and east-northeast–west-southwest rhyolite dikes that intrude Bisbee Group strata yielded $^{40}\text{Ar}/^{39}\text{Ar}$ ages between 32 and 27 Ma (Cleary, 2004). The Livermore Spring fault displaces the western segment of the Copper Dick fault southward relative to its eastern segment in the footwall of the Livermore Spring fault. The strike separation between the western and eastern traces of the Copper Dick fault is likely augmented by oblique slip along the Livermore Spring fault, as recorded by fault slickenlines (53° , 223° , rake = 37° , Clinkscales and Lawton 2017). No Paleogene rocks are exposed east of the Livermore Spring fault or south of the Copper Dick fault. The Hidalgo Formation crops out extensively north of the Hidalgo fault. North of the Hidalgo fault, the Bisbee Group and Ringbone Formation are limited to the northeastern part of the range, where they are folded into an anticline- syncline pair adjacent to the Ringbone thrust fault (Zeller, 1970;

Hodgson, 2000). The Hidalgo Formation unconformably overlies the Hell-to-Finish, U-Bar, and Ringbone formations and is intruded by Oligocene diorite dikes of the Eureka intrusive complex (Figure 5; Zeller, 1970; Channell et al., 2000). The Ringbone Formation unconformably overlies the U-Bar Formation in the hanging wall of the Ringbone fault, which emplaces Ringbone, Hell-to-Finish, and U-Bar strata over the Mojado Formation. The absence of the Mojado Formation from the hanging wall near the Mojado thrust trace (Zeller, 1970) indicates thrust displacement and resulting erosion of the Mojado Formation prior to Ringbone deposition. The thinning of upper Jurassic to upper Cretaceous strata north of the Little Hatchet Mountains can be attributed to the fault block geometry of the Bisbee basin and proximity to the rift shoulder of the Mogollon Highlands. In addition, a similar north-northeast thinning trend for lower-upper Cretaceous rocks can be attributed to the geometry of a post-rift early Late Cretaceous foreland basin (Mack, 1987; Clinkscales and Lawton, 2014 and 2017). The majority of this section belongs to Clinkscales and Lawton 2017. Clinkscales and Lawton's geologic map and cross-section of the Little Hatchet Mountains may be seen in Figures 3 and 4.

Mineralogy

The SMD's target area at Cottonwood Springs lies on an alluvial fan with prospects skirting the north, northeast, and east (Figure 2 purple squares). Samples taken from Cottonwood Springs, Figures 9a-9d, show mineral evidence of possible mineral deposition. Three of the samples contain jarosite, goethite, gypsum, and quartz (Figures 9a, 9b, and 9d) with two of those also containing malachite (Figure 9b and 9d). The last sample (Figure 9c) is of epidote.

Approximately 1.5 km north of Cottonwood Springs following the road, an outcrop of limonite gossan can be found (Figure 8). Nickel and Daniels (1986) classified gossan as fertile and barren based on bulk metallic content. Conversely, this weathering product of sulfide-bearing rocks is generally defined disregarding its probable economic value (Thornber and Taylor, 1992; Mahmoudi et al., 2018). They also classified with regard to the abundance of a limonitic set of minerals (e.g., hematite, goethite or jarosite) (Anderson, 1982; Nickel and Daniels, 1986; Sillitoe and Perelló, 2005; Mahmoudi et al., 2018). Because of the insoluble nature of iron oxide, -oxyhydroxides (e.g., lepidocrocite, goethite, and hematite) gossans mostly develop close to exposed sulfidic rocks (Blanchard, 1968; Andrew, 1980, 1984, 2000; Mahmoudi et al., 2018). Thus, they are valuable guides in the preliminary exploration of sulfide deposits (Wilhelm and Kosakevitch, 1979; Andrew, 2000; Mahmoudi et al., 2018). These samples provided evidence enough to prompt further study of the area which includes the project making up this paper; i.e. remote sensing, electromagnetics and electrical resistivity surveys, mineral spectroscopy, and x-ray diffraction.



Figure 8. Sample of limonite gossan taken from outcrop 1 km /north of Cottonwood Springs as seen on Figure 1 green square.



Figure 9a. Rock sample (a) is altered diorite that contains pyrite, quartz, gypsum, goethite, and jarosite. Collected from the SMD at Cottonwood Springs.

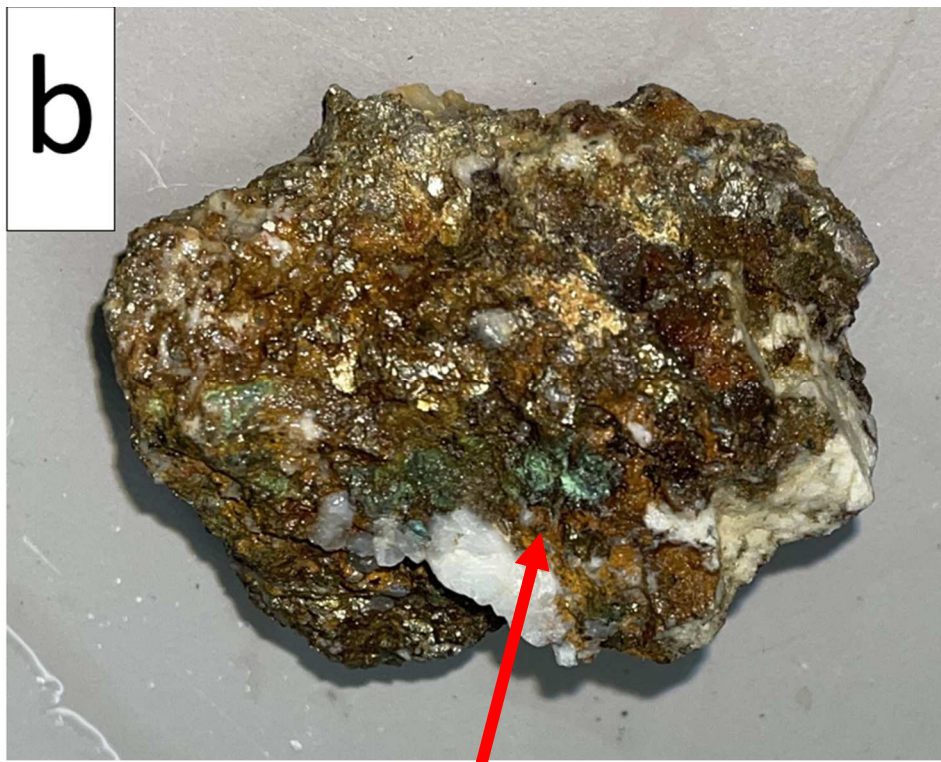


Figure 9b. Rock sample (b) is altered diorite that contains pyrite, quartz, gypsum, goethite, malachite (red arrow), and jarosite. Collected from the SMD at



Figure 9c. Rock sample (c) is epidote. Collected from the SMD at Cottonwood Springs.



Figure 9d. Rock sample (b) is altered diorite that contains pyrite, quartz, gypsum, goethite, malachite (red arrow) and jarosite. Collected from the SMD at

Chapter 3: Methodology

Remote Sensing

Remote sensing of hydrothermal mineral alteration zones in the Eureka and Sylvanite mining districts was used to target electromagnetics and electrical resistivity geophysical surveys. Due to the areas being suspected porphyry deposits, the alteration zones were discriminated by the minerals hydrous quartz, chalcedony, opal, and amorphous silica; calcite-dolomite and epidote-chlorite; alunite-pyrophyllite-kaolinite; and sericite-muscovite types using the USGS alteration mineralization shapefiles in ArcGIS (Mars 2014). This data was ascertained through the Advanced Spaceborne Thermal Emission and Reflection Radiometer (ASTER).

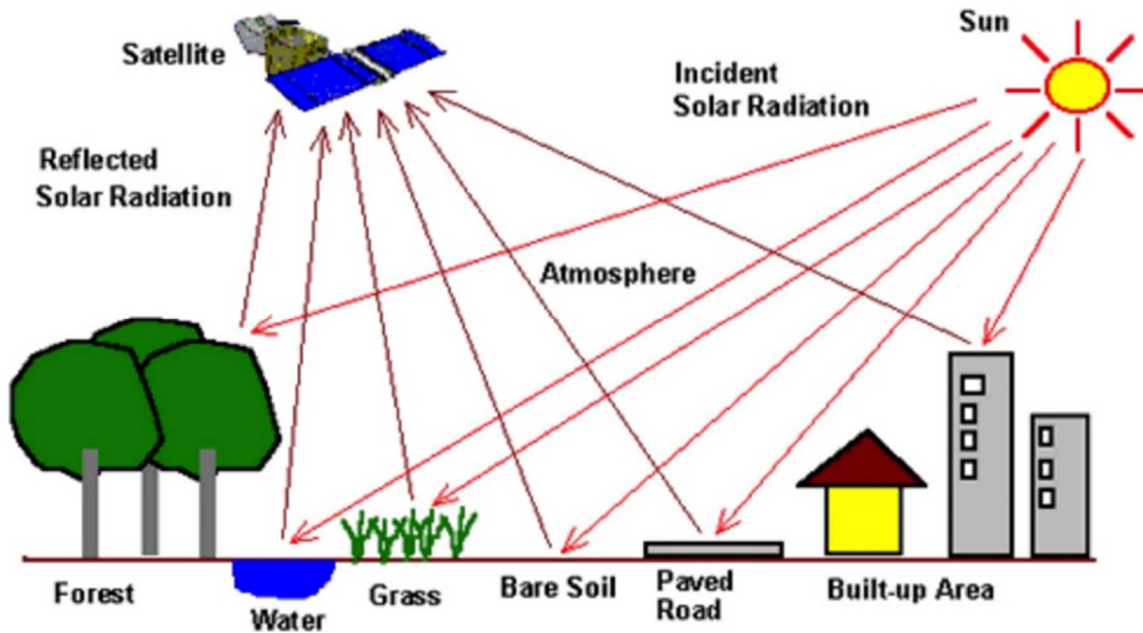


Figure 10. Basic physics of passive remote sensing satellites (Soimart and Ketcham, 2016)

ASTER is the only high spatial resolution instrument on the Terra platform (Figure 8 and terra.nasa.gov/).

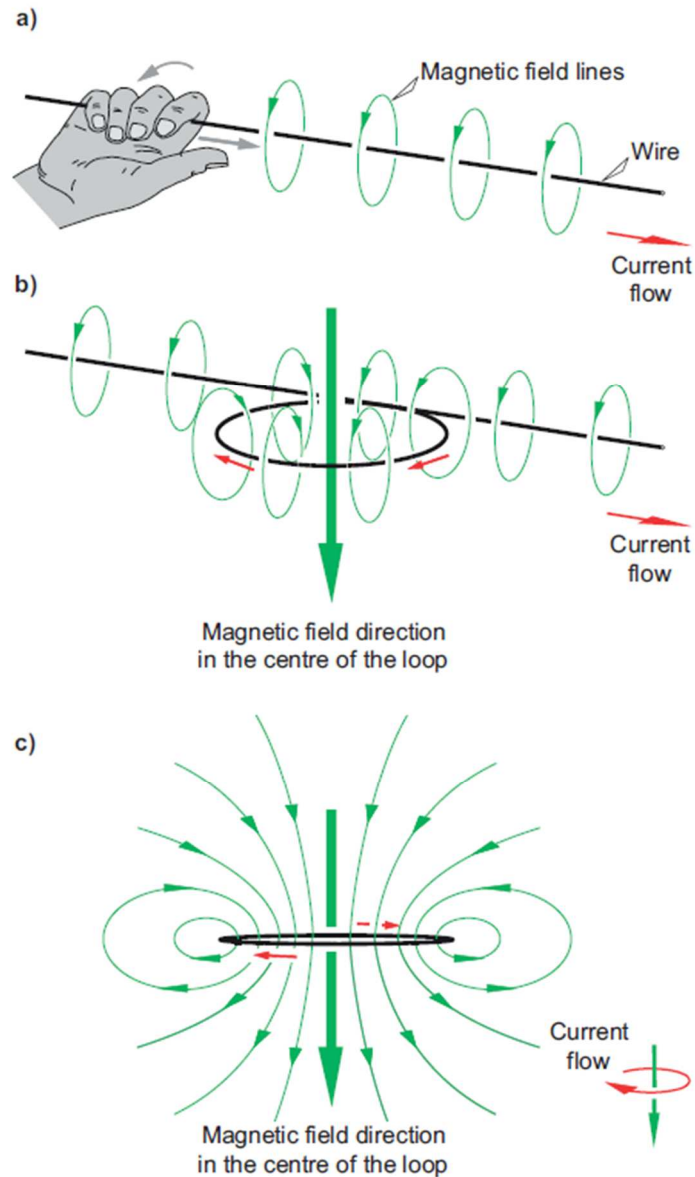
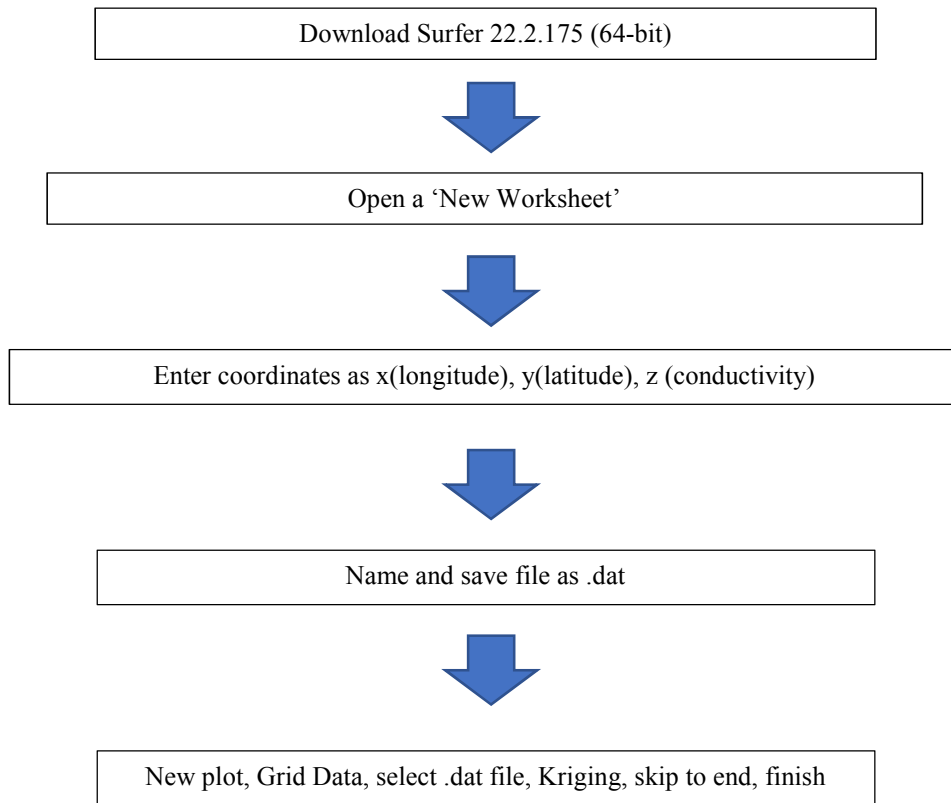


Figure 11. Magnetic field of an electric current (Dentith and Mudge 2014).

Electromagnetics

The Eureka and Sylvanite target areas were set into grids using the Terrain Navigator Pro software (Appendix Figures A2.1.1 and A2.1.5; terrainnavigator.com) and then transferred to a Garmin GPSMAP 60CSx (garmin.com/en-US/p/310). The Geonics EM34-3XL electromagnetic survey system was used for data collection (Appendix Flow Chart A2.3.1;

geonics.com/html/em34-3.html) and the electromagnetic theory model behind its function can be viewed in Figure 7. The Sylvanite grid is ~5600x4400 ft with 256 total Grid Data Acquisition Points (GDAP) and 79 total collected GDAPs (Appendix Figure A2.1.5). The Eureka grid is ~2000x1600 ft with 48 total GDAPs and 29 total collected GDAPs (Appendix Figure A2.1.1). The survey readings at each grid GDAP consisted of 40 ft and 20 ft vertical (V), and 40ft and 20 ft horizontal (H) datasets. Surfer software was utilized to create grid plots and conductivity ‘hotmaps’ for 40V, 40H, 20V, and 20H at the GDAP coordinates (goldensoftware.com/products/surfer). The maps were then imported and used as overlays in Google Earth Pro (www.google.com/earth/versions/) and ArcGIS Pro (Figure 9; www.esri.com/en-us/arcgis/products/arcgis-pro/overview). A total of ~220 people hours contributed to these surveys.



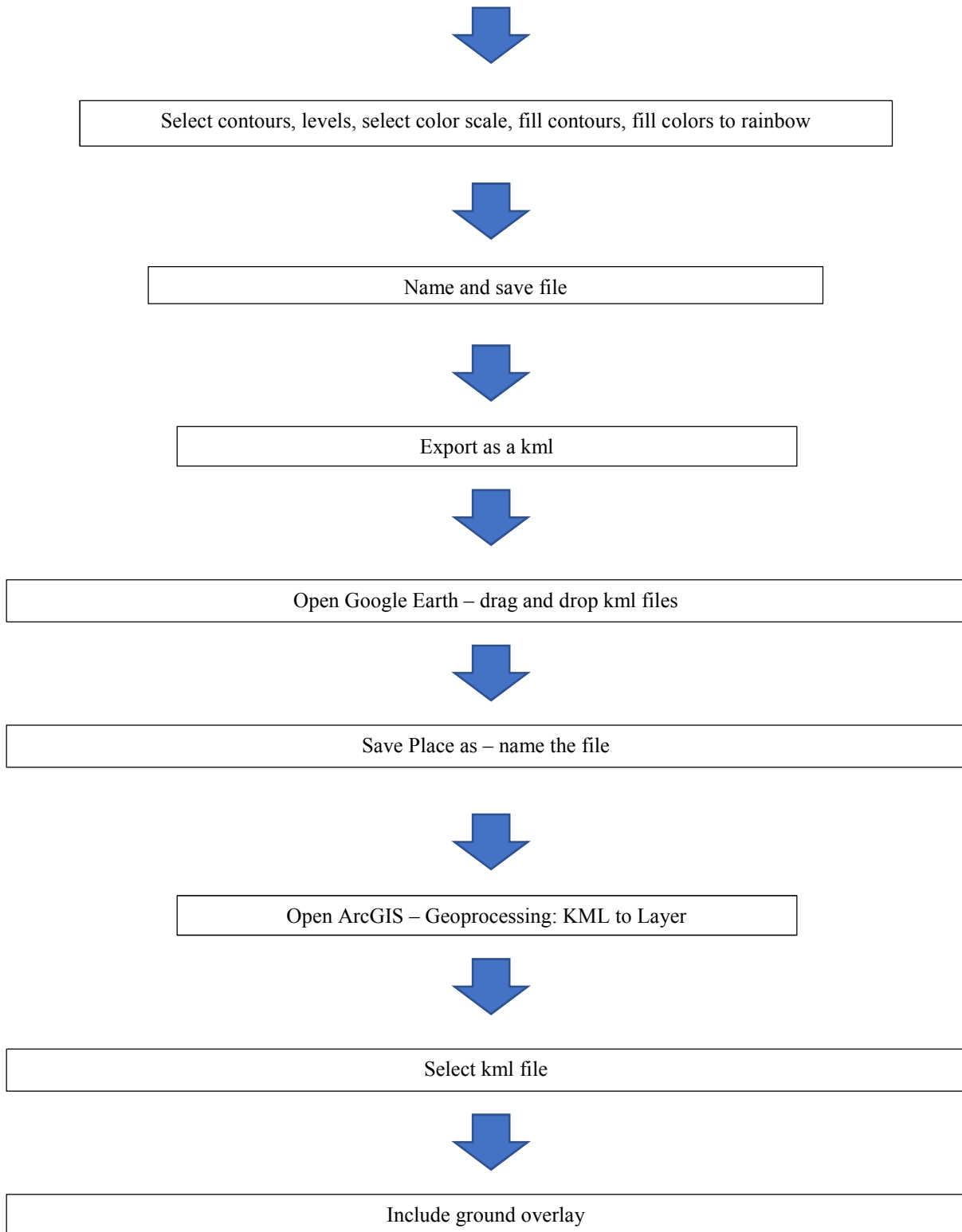


Figure 12. Surfer to ArcGIS Flow Chart

When electrical charges move, i.e. when an electric current is flowing, a magnetic field is formed around them and the intensity (strength) of the field is proportional to the magnitude of the current. For current flowing through a straight length of wire, the magnetic field is described by circular field lines concentric to the current (Figure 8a). The direction of the magnetic field is dependent on the direction of current flow and described by the 'right-hand' rule (Figure 8a). The strength of the field decreases with increasing distance from the current flow (the wire).

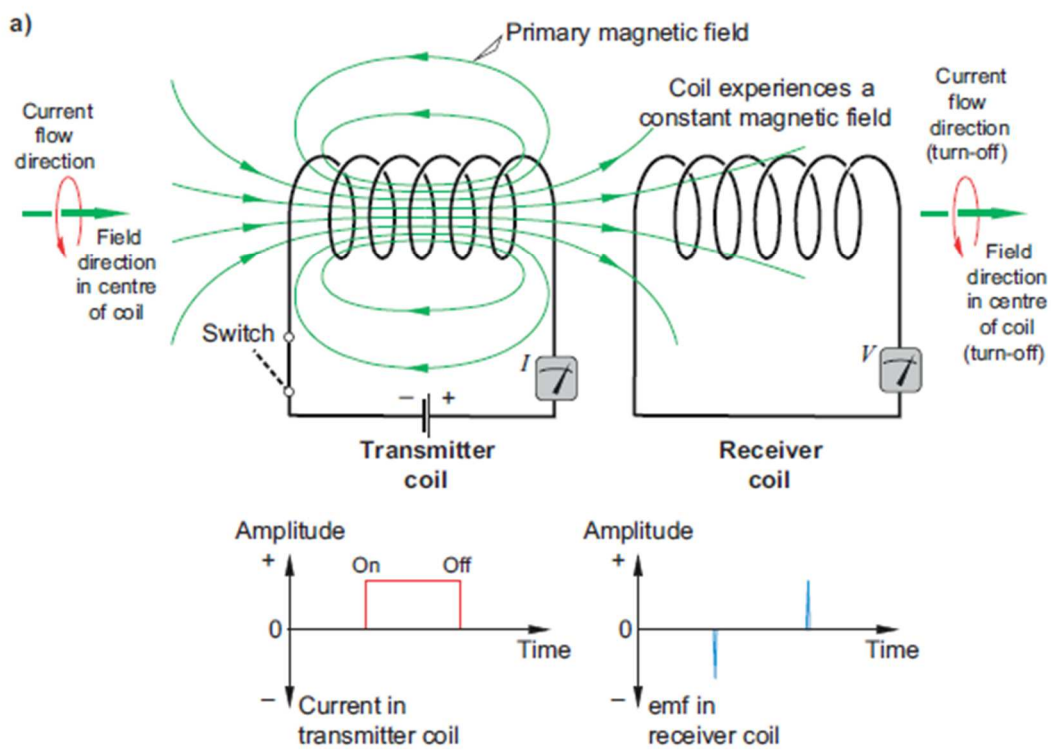


Figure 13. An intermittent d.c. current that models the Geonics EM34-3XL electromagnetics induction (Dentith and Mudge 2014).

When a current-carrying wire is formed into a single circular loop (Figure 8b and 8c) the field is strongest inside and in the plane of the loop, where the field lines point in the same direction and are parallel to the axis of the loop. The direction of the current flow determines the direction of the magnetic field. When a current-carrying wire is formed into a series of electrically connected

loops it forms a coil (Dentith and Mudge 2014). As seen in Figure 10 before the current is turned on there is no changing primary magnetic field so there is no induction in the detector coil. When the current is turned on a steady-state magnetic field is rapidly established. Only at the instances of turn-on and, later, at turn-off does the receiver coil experience a change in the magnetic field. Simultaneously and instantaneously, an emf pulse is induced into the receiver coil causing current to flow. At other times when a steady-state current is established, the magnetic field experienced by the receiver coil is once again constant so there is no emf induced in it. A crucial characteristic of the induced emf is that it causes a current to flow in the receiver coil whose magnetic field attempts to prevent the field around the coil from changing (Dentith and Mudge 2014).

Electrical Resistivity

The purpose of electrical resistivity surveys is to determine the subsurface resistivity distribution by making measurements on the ground surface. From these measurements, the true resistivity of the subsurface can be estimated. The ground resistivity is related to various geological parameters such as the mineral and fluid content, porosity, and degree of water

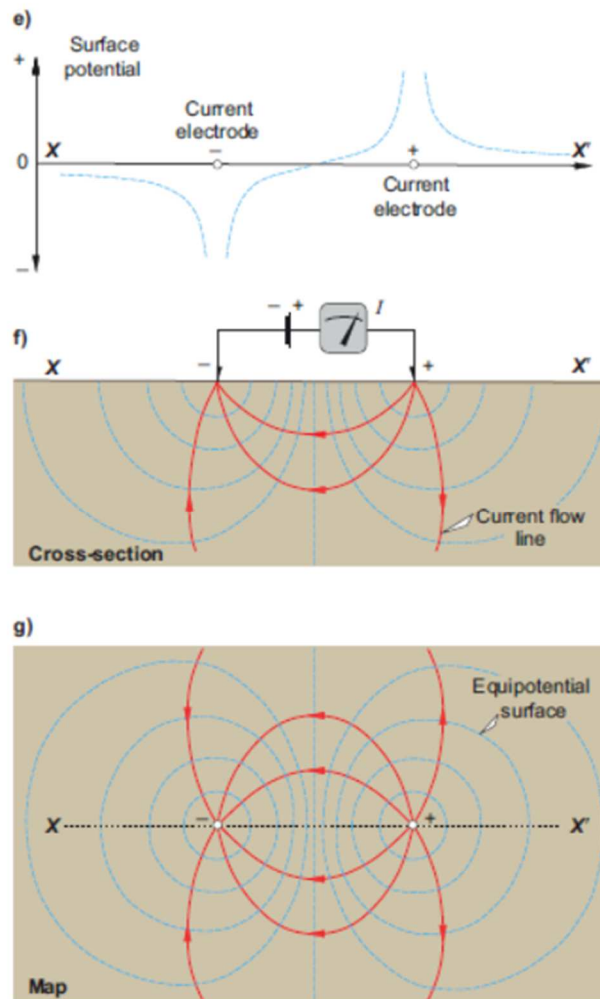


Figure 14. Electric field in a half-space and the associated surface potential formed by a dipole (Dentith and Mudge 2014).

saturation in the rock. Resistivity surveys were conducted using an 8-channel SuperSting R8 IP earth resistivity meter with two surveys perpendicular to one another using 112 electrodes, with

an inter-electrode space of 5 m (Figure 18, agiusa.com/). The center point for the transect survey was determined from the electromagnetics survey analysis. Total survey length will be 555 m each. The dipole–dipole (DDP) array (Figure 11 and 12) was utilized enabling the gathering of a dense mesh of data points to establish a high horizontal resolution (Dahlin and Zhou, 2004; Loke, 2013), which facilitates solving of vertical structures considered to be probable in the area. It should be known that the DDP array has a lower signal-to-noise ratio than do other arrays making it more reliable for interpretation.

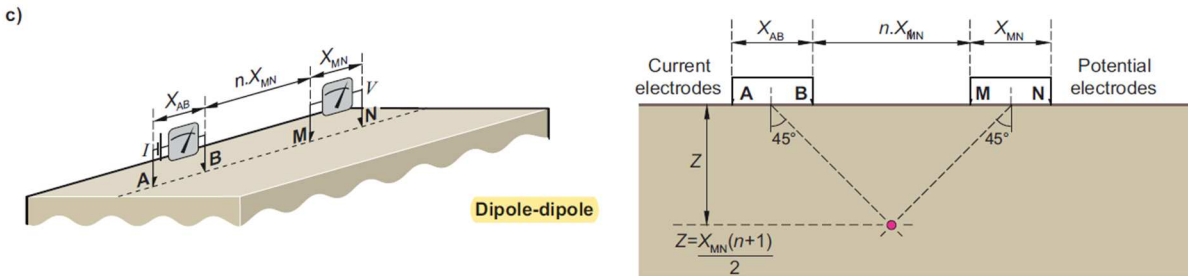


Figure 15. Electrical resistivity dipole-dipole electrode array and plotting convention model (Dentith and Mudge 2014).

Utilization for building models were performed with AGI EarthImager™ 2D which is a two-dimensional resistivity and induced polarization (IP) inversion modeling software (Appendix Flow Charts A3.3.2 and A3.3.3; agiusa.com/). Flow charts for the SuperSting R8 and AGI EarthImager™ 2D can be found in Appendix under Flow Charts Electrical Resistivity. The software converts electrically gathered data into a 3D rendering presented using an advanced volume display. A total of ~110 people hours contributed to these surveys.

Mineral Spectroscopy

While conducting electromagnetics surveys, 18 SMD samples of outcrops with coordinates and areas of interest were collected. The GER 3700 Spectrometer from Geophysical Environmental Research Corp. (Figure 19 and Schaepman et al. 1994) with a spectral range of 300 – 2500 nm, runs with a Compaq Contura 410C laptop, and TDK FDD-100A 3.5' floppy disk drive to USB that enables data transfer was utilized for data extrapolation. Microsoft Excel CSV files were created from data files. The Spectral Geologist 8.0.7.4. (For flow chart see Appendix Flow Charts A4.2.1) software was used for the analysis of the samples (research.csiro.au/thespectralgeologist/). This software compares the sample to ASCII Reference

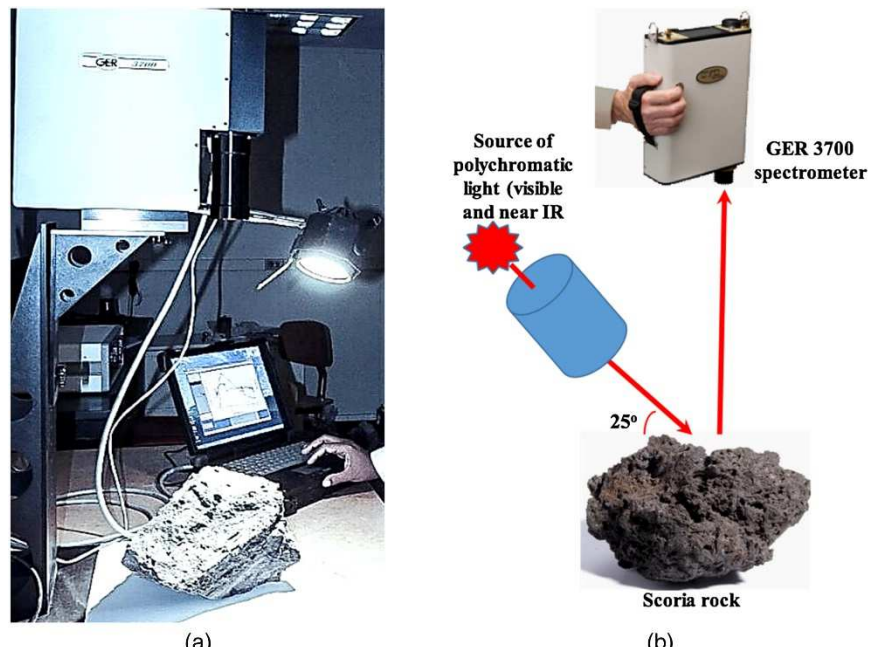


Figure 16. GER 3700 a) lab setup, b) field setup and function (Saleem Aldossari et. al 2019).

Library and provides ‘best fit’ graph analyzation in the short-wave Infrared (SWIR) and visible and near-infrared (VNIR) spectrums. The result is an identification of alteration minerals.

‘Unreliable Result’ can be seen in the background of many of the 18 samples graphs (Figures 21-28 and Appendix Figures A4.1-A4.102), this is due to the mineral wavelength graphed being far

outside the normal parameters when in comparison to the ASCII Reference Library, but this still represents the best fit trend per graph.

X-Ray Diffraction

X-ray powder diffraction is a fast method for determining the phase content of polycrystalline material. Every material exhibits a typical 'X-ray fingerprint', which is stored in databases such as the ICDD PDF2 or PDF4. This fingerprint is utilized in the DIFFRAC.EVA software for phase identification. Furthermore, automatic scaling of the patterns from the database relative to the measured intensities gives the semi-quantitative phase composition. Pulverized geological material was measured with the D2 PHASER. The data, collected within 45 minutes, show a very good counting statistics. Minor phases of less than 1 wght-% are clearly identified. From this initial idea has come the more modern versions such as this Bruker D2 Phaser. Of the 18 samples studied using mineral spectroscopy 6 were analyzed with x-ray diffraction (XRD) for an accuracy comparison. The Bruker D2 Phaser is a novel desktop XRD diffraction tool enabling the analysis of poly-crystalline material. It is equipped with an integrated PC and a flat screen monitor. The new and very easy-to-use workflow software Diffrac.Suite allows measurement and analysis right out of the box. The D2 Phaser is the most compact and fastest, all-in-one crystalline phase analysis tool available on the market. It is mobile and easy to install with only the need for standard electrical power. The D2 Phaser is therefore ideal for laboratory or on-location operation, in other words, it is a true Plug'n Analyze System.



Figure 17. Shows a zoomed region (intensities are cut at about 10% of the maximum intensity) of the diffraction data together with the result of the phase identification and a picture of the desktop Bruker D2 Phaser

Chapter 3: Data and Results

Remote Sensing

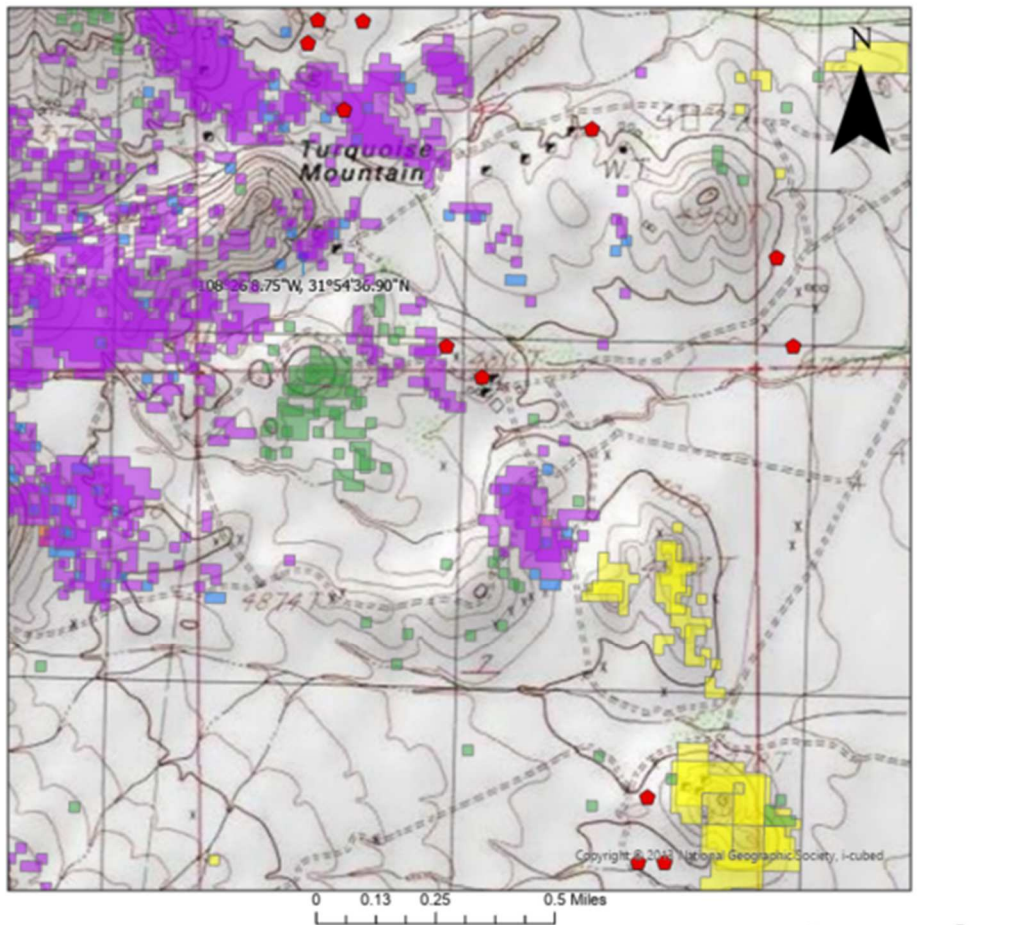


Figure 18. ArcGIS base topographic map of Eureka target area alteration mineralization, 1:10,000 (Mars 2014).

The USGS hydrothermal alteration shapefiles from Mars 2014 were imported into ArcGIS Pro and mapped to layout for the EMD and SMD (Figure 14 and 15). For the Eureka target that can be seen in Figure 14, high concentrations of sericite-muscovite alteration around Turquoise Mountain can be seen along

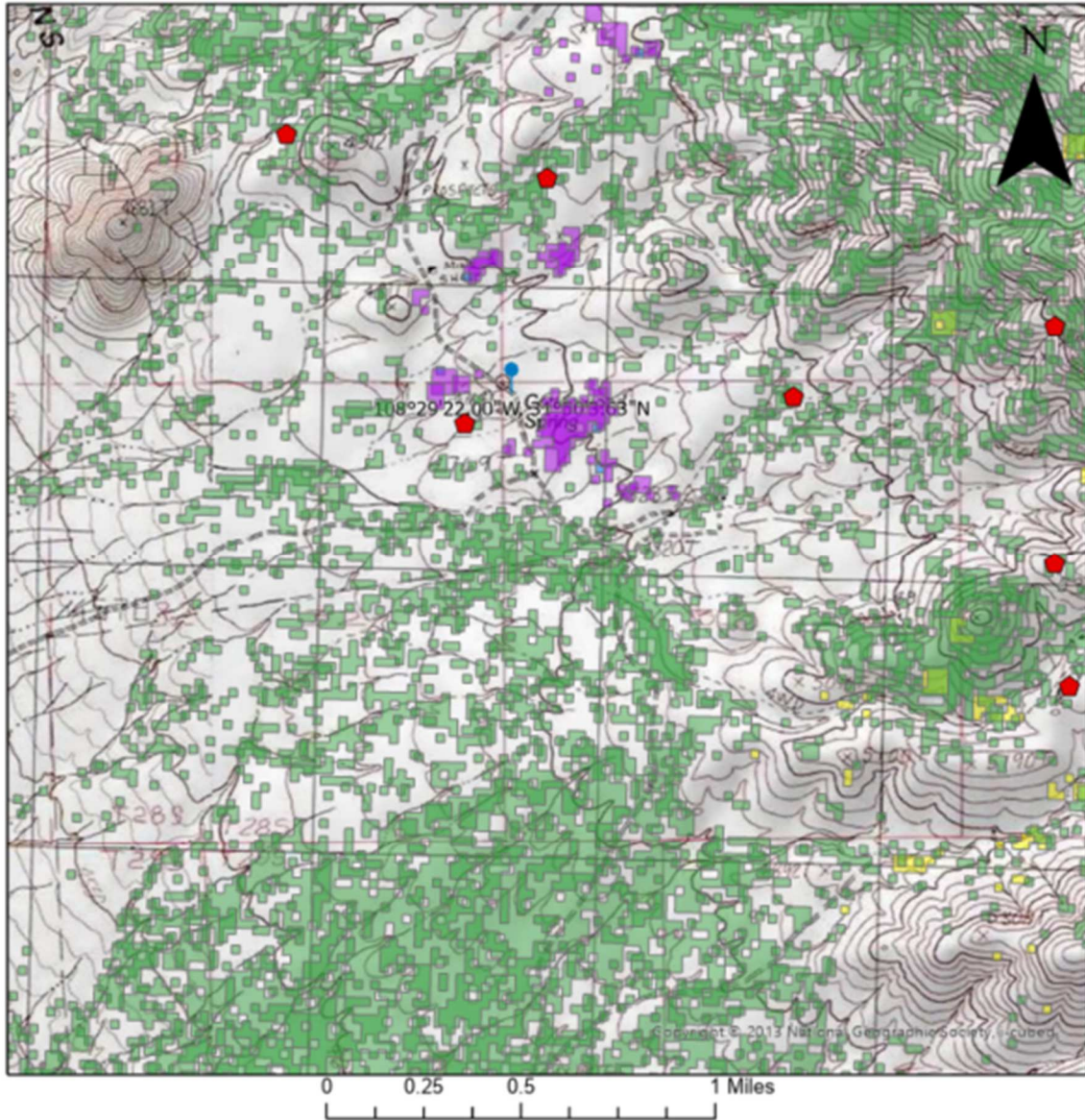


Figure 19. ArcGIS base topographic map of Sylvania target area alteration mineralization, 1:13,000 (Mars 2014). See Legend in Figure 18.

with the sporadic low concentrations of alunite-pyrophyllite-kaolinite alteration. The center of the EMD map is highlighted by a high concentration of epidote-chlorite alteration with spread out low concentrations along the map edges. calcite-dolomite alteration is constrained to a highly concentrated section in the southeast corner of the map. The SMD map (Figure 15) shows

multiple high concentrations of sericite-muscovite alteration around Cottonwood Springs. The rest of the map shows high concentrations of epidote-chlorite alteration spread throughout.

Electromagnetics

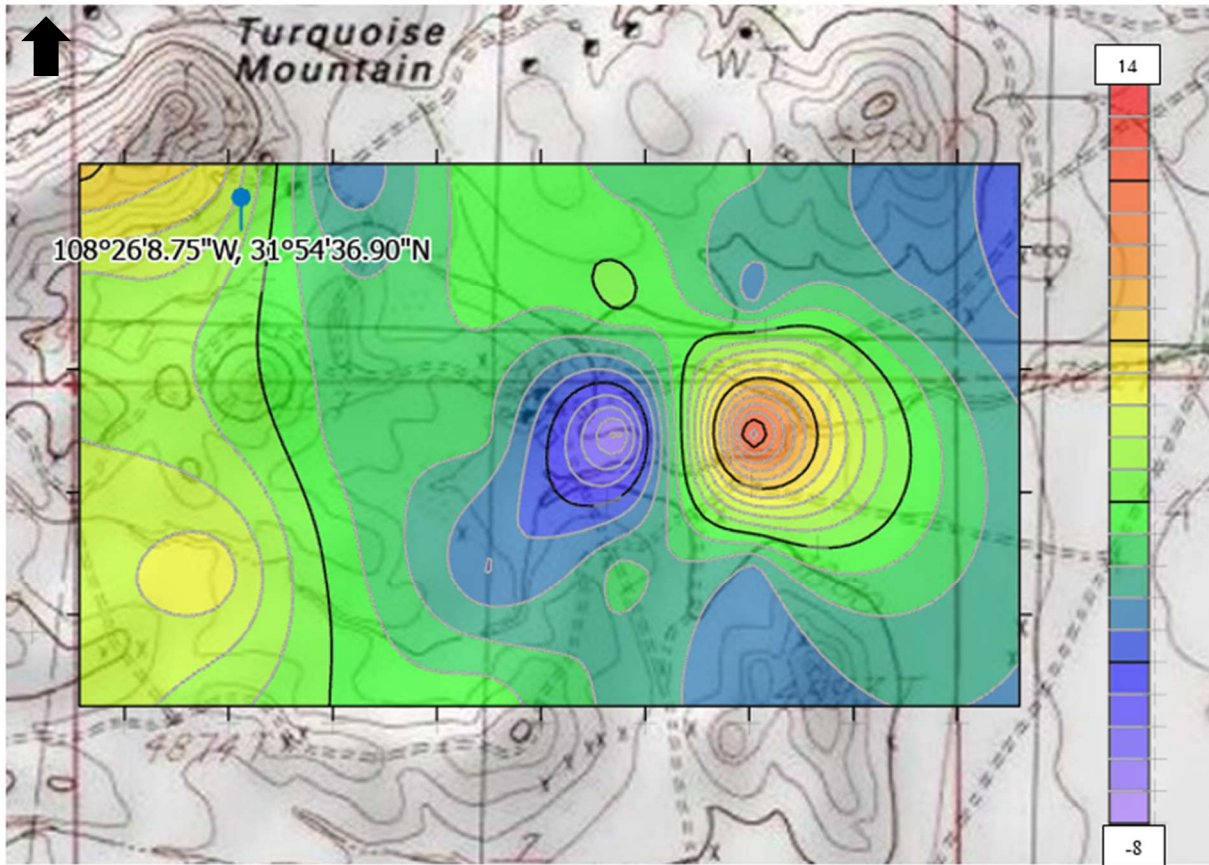


Figure 20. Eureka electromagnetics 40V map with conductivity high anomaly on the east side of the map.

The EMD 40V ‘hotmap’ (Figure 16), with a max depth profile of 180 ft, reveals a -7.6 milliSiemens per meter (mS/m), GDAP E7-4 (Appendix Electromagnetics Table A2.2.1) low anomaly bounded to the east by a 13.8 mS/m, GDAP E8-3 (Appendix Electromagnetics Table A2.2.1) map anomaly high. The 40H map shown in the Appendix Figure A2.1.2, has high values of 6.2 mS/m at GDAP E4-2 mS/m and 7.4 mS/m at GDAP E5-6 (Appendix Electromagnetics Table A2.2.1) in the northwest and a high value anomaly of 10.7 mS/m at GDAP E7-4. The area between these highs consists of conductivity lows for GDAPs E5-4, E5-5, E6-2, and E6-3 (Appendix EM Table A2.2.1). Another high/low bounded anomaly is shown for the 20V map

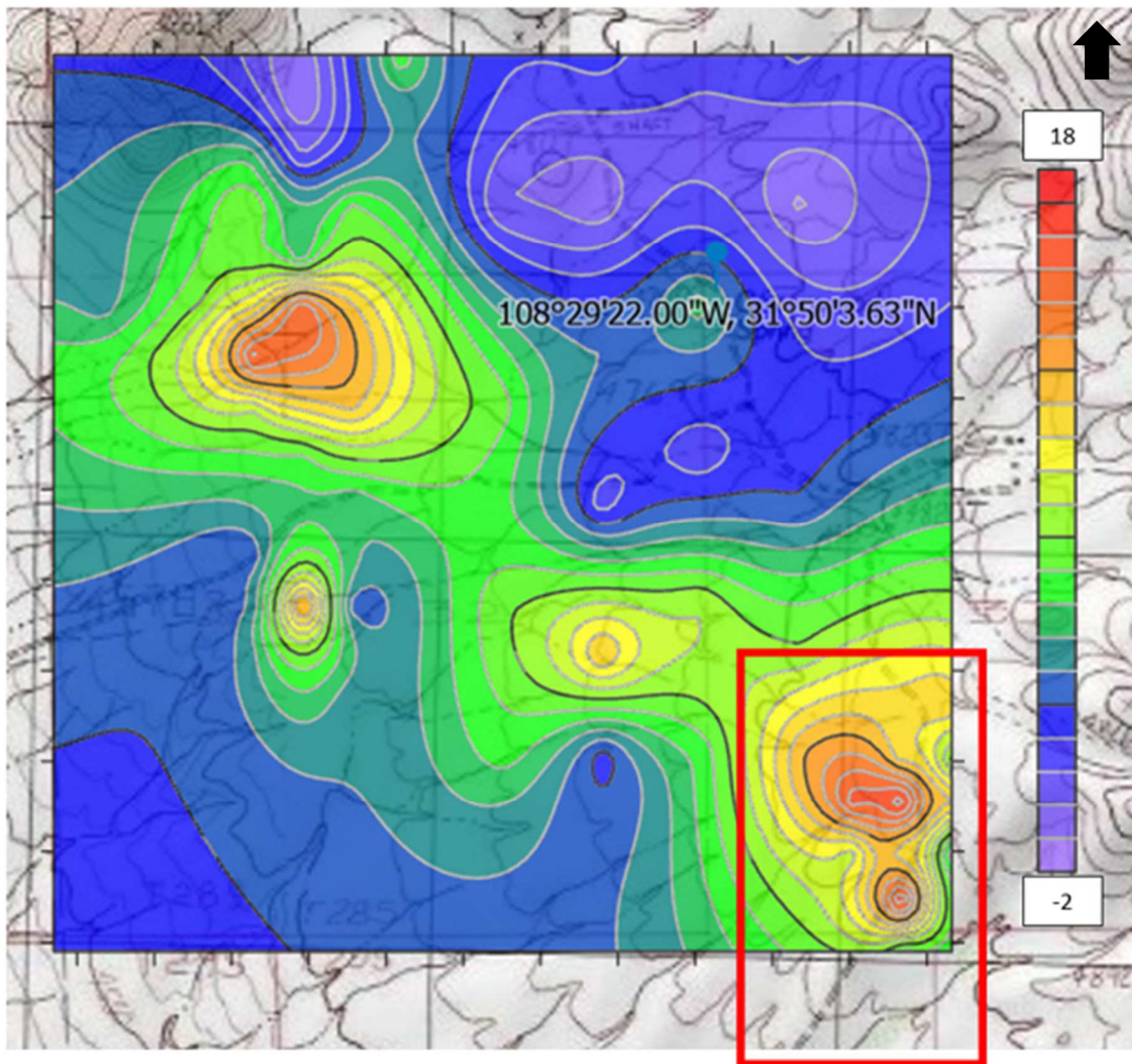


Figure 21. Sylvanite 40V, southeast to northwest trend of high anomalies. Figure 18 in southeast corner outlined with red rectangle.

(Appendix Figure A2.1.3) in the northwest section. The GDAP high is E3-6 with a conductivity reading of 5.8 mS/m and the bounded GDAP E5-6 has a reading of -0.2 mS/m. The high value for this map is at GDAP E8-3 with a reading of 16 mS/m. The anomaly high for the 20H map (Appendix Figure A2.1.4) had a reading of 29 mS/m at E7-4 adjacent to E8-3 (Appendix Electromagnetics Table A2.2.1) with a conductivity of 10.2 mS/m. The northwest high anomaly

for this map at E5-6 was 15.5 mS/m (Appendix Electromagnetics Table A2.2.1). This is like the 40H and 20V maps but the conductivity near surface is much higher since the depth profile for the 20H is only 60 ft.

The SMD 40V ‘hotmap’ (Figure 17) revealed numerous anomalies. The two highest anomalies occurred in the southeast region of the grid at SE-6 with a conductivity reading of 17.8 mS/m and SE-23 with a reading of 17.5 mS/m (Appendix Electromagnetics Table A2.2.2), as seen in Figure 16. The next two highest readings occurred in the northwest sector of the map. The GDAPs of L1-9, conductivity of 16.4 mS/m, and L2-6, reading of 16.1 mS/m (Appendix Electromagnetics Table A2.2.2). GDAP L2-12 (14.1 mS/m) lies between the two sets of highs and creates southeast to northwest trend anomalies. The last and lowest high is just south of the two northwest anomalies and rides the trend, L8-13 with 12.2 mS/m. Of particular note, the Cottonwood Springs section of the map (Figure 17, shown with the blue lollipop marker and coordinates) in the northeast contains conductivity lows at GDAPs L2-1 (-0.8 mS/m), L2-2 (-0.8 mS/m), L6-4 (0 mS/m), L8-4 (-0.7 mS/m), and L12-4 (-1.2 mS/m) with an area high at the spring (L10-6) of 5.5 mS/m. The 40H conductivity readings of the SMD reveal a southeast to north trend with the highest anomalies in the southeast (Appendix Figure A2.1.6). These highs include the GDAPs of SE-7 (18.6 mS/m), SE-15 (25.5 mS/m), and SE-16 (32 mS/m) (Appendix Electromagnetics Table A2.2.2). The Cottonwood Springs GDAP L10-6 had a reading of 26.5 mS/m with two low anomalies to the west and southwest at GDAPs L6-4 (0 mS/m), L8-4 (-0.7 mS/m), and L8-10 (1.5 mS/m) (Appendix Electromagnetics Table A2.2.2). The northwest section of the map contained three GDAP anomaly highs at L2-4 (12.3 mS/m), L2-6 (17 mS/m), and L3-10 (15.9 mS/m). The 20V GDAP anomaly highs (Appendix Figure A2.1.7) of the southeast are SE-16 (29 mS/m), SE-15 (27.1 mS/m), SE-7 (25.5 mS/m), and SE-1 (20 mS/m)

(Appendix Electromagnetics Table A2.2.2). The Cottonwood Springs reflected a conductivity high at L10-6 of 19.5 mS/m, while the northwest section GDAP highs were L2-4 (19.1 mS/m), L2-6 (15.9 mS/m), and L3-10 (18.1 mS/m). The 20H GDAP anomaly highs (Appendix Figure A2.1.8) of the southeast are SE-16 (28.8 mS/m), SE-15 (20.4 mS/m), and SE-7 (19.5 mS/m) (Appendix Electromagnetics Table A2.2.2). The Cottonwood Springs reflected a conductivity high at L10-6 of 32 mS/m, while the northwest section GDAP highs were L2-4 (17.7 mS/m), L2-6 (16.6 mS/m), and L3-10 (18.8 mS/m).

Electrical Resistivity

Based on the Electromagnetics surveys conducted, 2 electrical resistivity lines were deployed (Figure 18), a south-north line and a southeast-northwest line. The south to north line conductivity model can be seen in Figure 19 (Pseudosections and resistivity models can be seen in the Appendix Electromagnetics Figures A3.1.1 and A3.1.2). The conductivity readings for this line ranged from 1.2 to 39.4 mS/m. The southeast to northwest line conductivity model can be

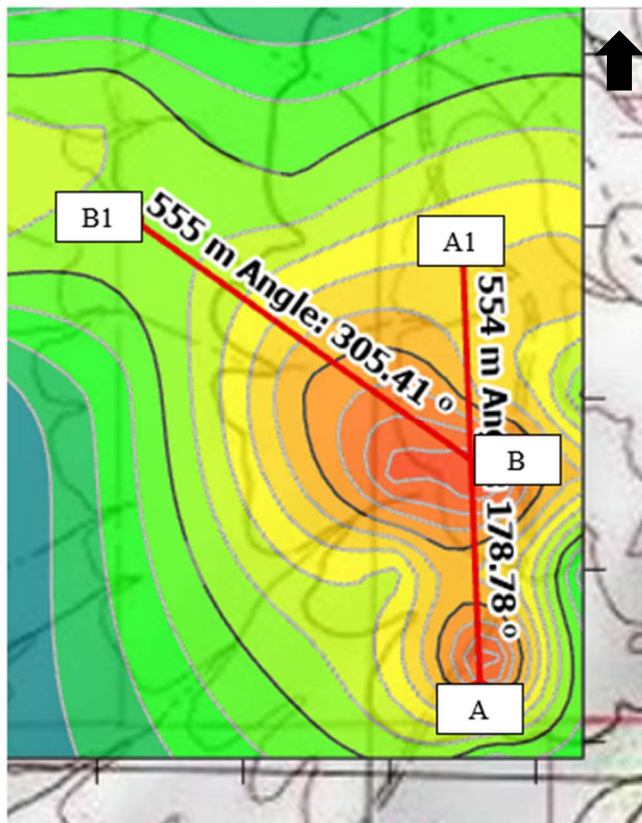


Figure 22. Electrical resistivity survey lines south (A)-north (A1) line, and southeast (B)-northwest (B1) line. Reference Figure 17 for location at the southeast corner outlined with red rectangle.

viewed in Figure 20. The conductivities for this model ranged from 0.73 to 472 mS/m.

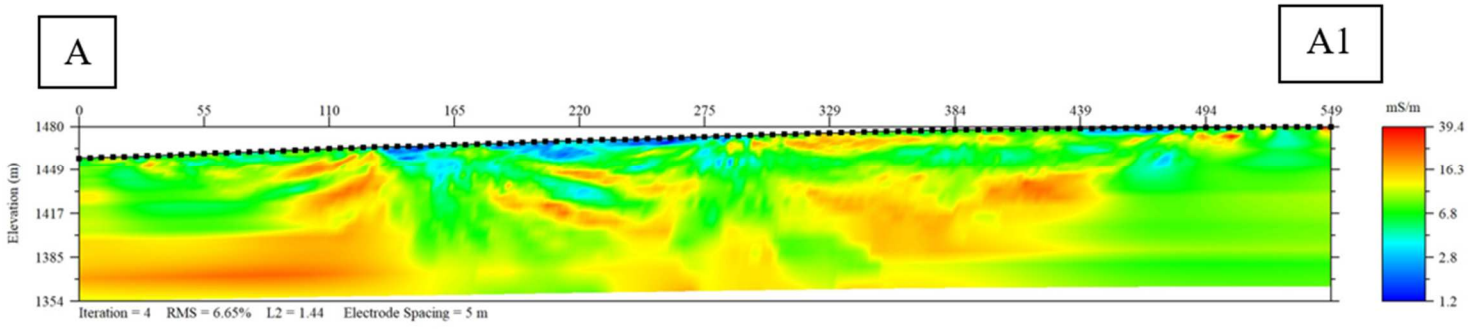


Figure 23. Electrical resistivity inverted conductivity model of the south (A) to north (A1) line, for reference check Figures 17 and 18.

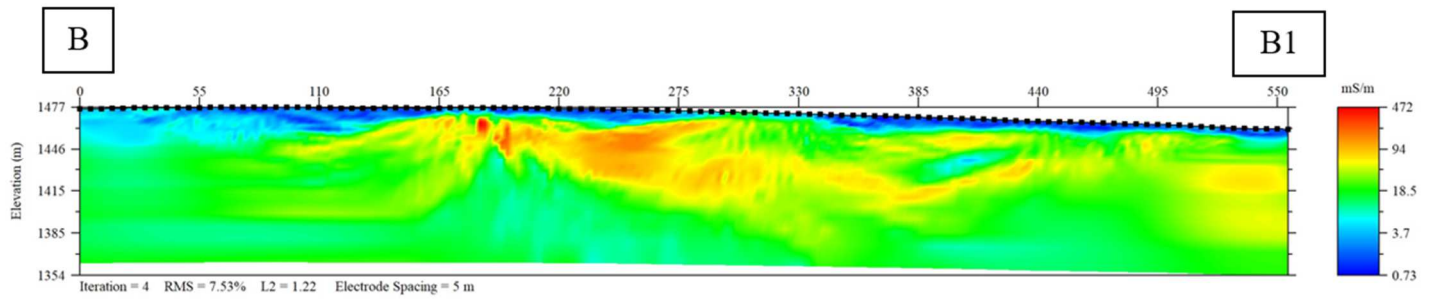


Figure 24. Electrical resistivity inverted conductivity model of the southeast (B) to northwest (B1) trend from midpoint of north to south line, for reference check Figures 17 and 18.

Mineral Spectroscopy

The Spectral Geologist software was used to interpolate 18 samples taken from the SMD. Figures 21-28 show the analyses utilized in VNIR and SWIR wavelengths to get a ‘best fit’ trend for Sample 001_A_1. In the visible and near-infrared spectrum as seen in Figures 25-26, according to the ASCI Reference Library that the software uses, Goethite is the most likely majority mineral graphed. In Figure 26 the other options for mineral combinations are shown. The short-wave infrared spectrum wavelengths for the same sample show (Figures 26-27) that the sample is comprised of a combination of 61% chlorite-Fe, 22% jarosite, and 16% gypsum. Figure 28 reveals the alternative options according to the ASCI Library. For the results of the remaining samples see Table 1 and Appendix Figures A4.1- A4.102.

Table 1. Spectroscopy Mineral Identification

Sample ID	Visible and Near Infrared	Short-Wave Infrared
Sample 001_A_1	Goethite	61% Chlorite-Fe + 22% Jarosite+16% Gypsum
Sample 002_A_2	Goethite	Gypsum
Sample 003_A_3	Goethite	56% Gypsum + 44% Epidote
Sample 004_B_5	Goethite	84% Chlorite-Fe + 16% Gypsum
Sample 005_C_1	Goethite	Dickite
Sample 006_C_2	Goethite	Gypsum
Sample 007_C_3	Goethite	Gypsum
Sample 008_C_4	Goethite	79 % Chlorite-Fe+ 21 % Alunite-Na
Sample 009_C_5	Goethite	Gypsum
Sample 010_C_6	64 % Hematite +36 % Goethite	39% Epidote + 35 % Jarosite +26 % Gypsum
Sample 011_C_7	Goethite	Chlorite-Fe
Sample 012_C_8	Goethite	Gypsum
Sample 013_D_1	Goethite	72 % Kaolinite-WX + 28% Epidote
Sample 014_D_2	Goethite	51 % Siderite + 49% Phengite
Sample 015_E_3	Goethite	Gypsum
Sample 016_I_1	Goethite	63 % Jarosite + 37 % Calcite
Sample 017_I_2	Goethite	Chlorite-FeMg
Sample 018_I_4	Goethite	68 % Rubellite + 32 % Gibbsite



Figure 25. Sample 001_A_1; results of mineral spectroscopy VNIR: goethite, and SWIR: 61% chlorite-Fe + 22% jarosite+16% gypsum

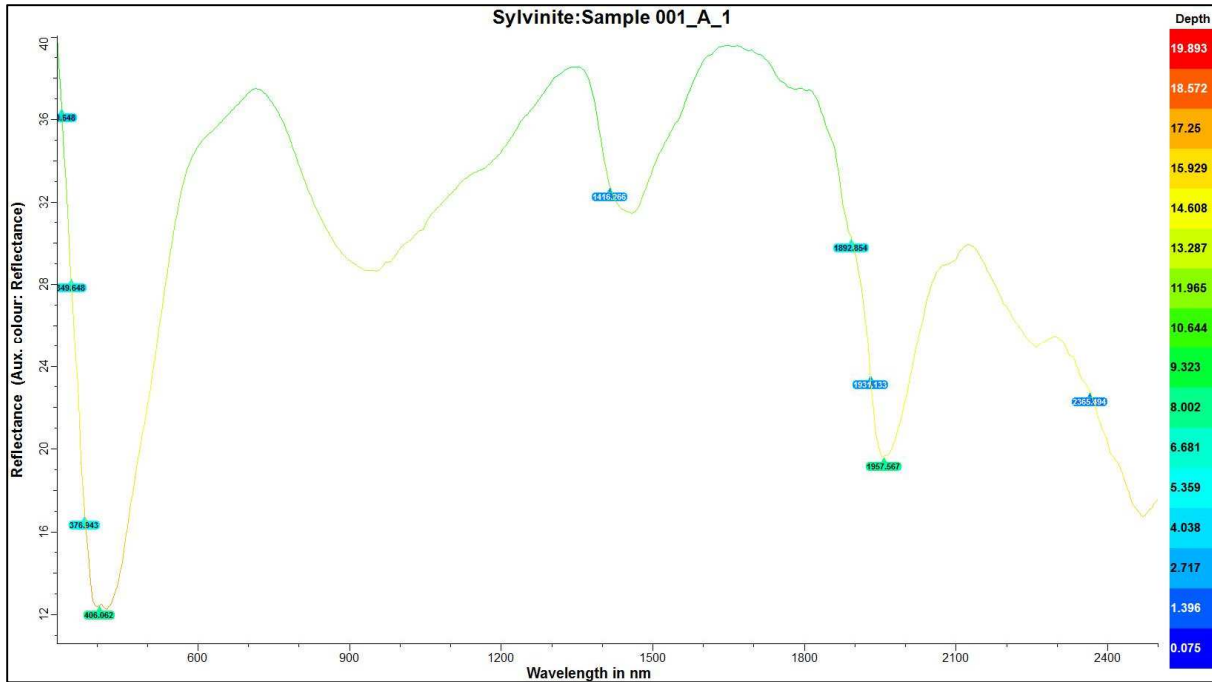


Figure 26- Sylvanite: Sample 001_A_1; with modifications such as features-wavelength (number tags) and smooth (Hi). Graph created by using The Spectral Geologist 8.0.7.4. software.

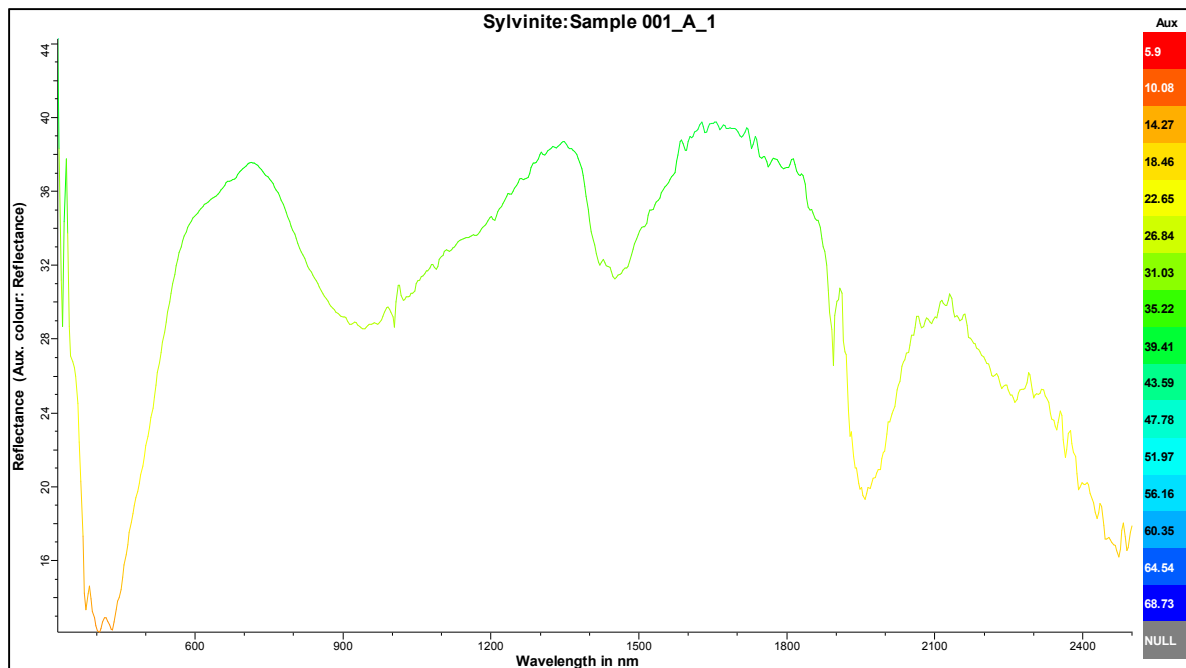


Figure 27-Sylvanite: Sample 001_A_1; Standard wavelength (CSV import data) with no slight modifications. Graph created by using The Spectral Geologist 8.0.7.4. software.

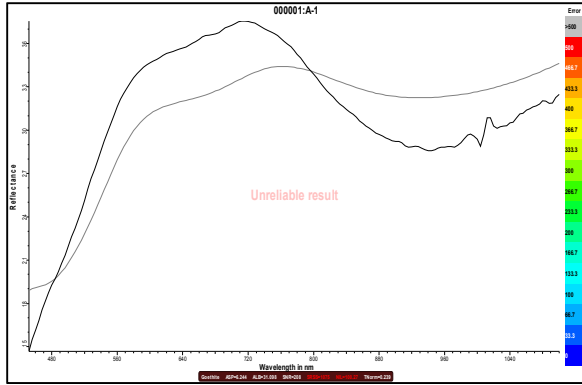


Figure 28- Sylvanite: Sample 001_A_1_Goethite- [1075]. Results in the visible and near-infrared (VNIR) Primary (Astrid) TSA result. Graph created by using The Spectral Geologist 8.0.7.4. software.

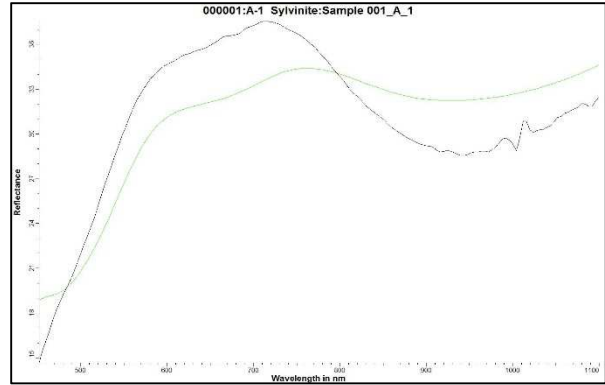


Figure 29-Sylvanite: Sample 001_A_1_Goethite [1075]. Results in the visible and near-infrared (VNIR) Multiple results overlay. Graph created by using The Spectral Geologist 8.0.7.4. software.

Candidate TSA results
*Goethite [1075]
Goethite [1257]
Hematite [1815]
Vegetation-Green [3592]
65%GalvanisedIron + 35%Goethite [694]
77%ODZincalume + 23%Goethite [797]
92%Goethite + 8%Hematite [1071]
70%Goethite + 30%Hematite [1135]
58%Goethite + 42%GalvanisedIron [1182]
59%ODZincalume + 41%Goethite [1184]
64%GalvanisedIron + 36%Hematite [1349]
97%Hematite + 3%Vegetation-Green [1808]
77%ODZincalume + 23%Vegetation-Green [3544]
65%Vegetation-Green + 35%GalvanisedIron [3587]

Figure 30- VNIR Goethite: The Spectral Analyst (TSA) possible results. The best fitting results is defined by an Astrid. Results are in the visible and near-infrared (VNIR).

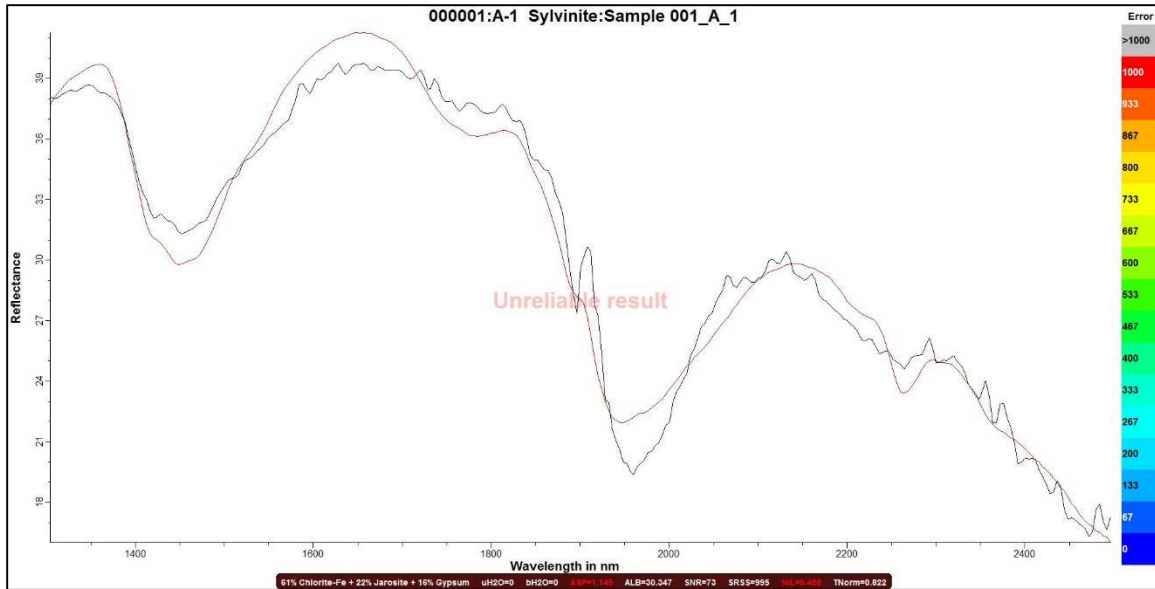


Figure 31- Sylvanite: Sample 001_A_1: 61% Chlorite-Fe + 22% Jarosite+16% Gypsum [995]. Results are in the Short-Wave Infrared (SWIR). Graph created by using The Spectral Geologist 8.0.7.4. software.

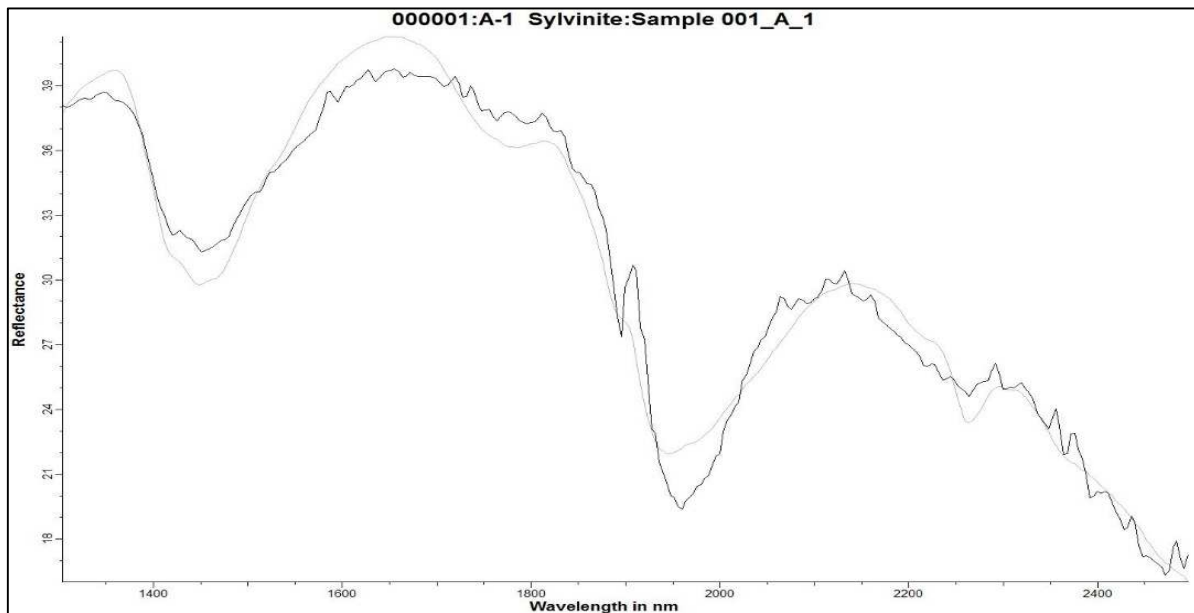


Figure 32- Sample 001_A_1: 61% Chlorite-Fe + 22% Jarosite+16% Gypsum [995]. Results are in the Short-Wave Infrared (SWIR). The General ASCII Reference Library (solid smooth) is overlaid with the CSV import data (rough jagged). Graph created by using The Spectral Geologist 8.0.7.4. software.

Candidate TSA results
56%Jarosite + 28%Gypsum + 16%Topaz [969]
*61%Chlorite-Fe + 22%Jarosite + 16%Gypsum [995]
40%Jarosite + 40%Kaolinite-WX + 21%Gypsum [995]
57%Jarosite + 27%Alunite-K + 17%YellowMarker [996]

Figure 33-The Spectral Analyst (TSA) possible results.

The best fitting results is defined by an Astrid. Results in Short-Wave Infrared (SWIR): 61% Chlorite-Fe + 22% Jarosite+16%Gypsum.

X-ray Diffraction

The XRD provided an accuracy check on the mineral spectroscopy results. According to the results of the XRD seen in Figure 28, the top match for the sample A1 is Gypsum. The next best matches (in order) are Montmorillonite, Phengite, Goethite, Quartz, Albite, and Calcite. This version of mineral identification like mineral spectroscopy is not exact. To see the graph results of the other 6 samples tested refer to Table 2 and the Appendix Figures A5.1.1 -A5.1.6.

Commander Sample ID (Coupled TwoTheta/Theta)

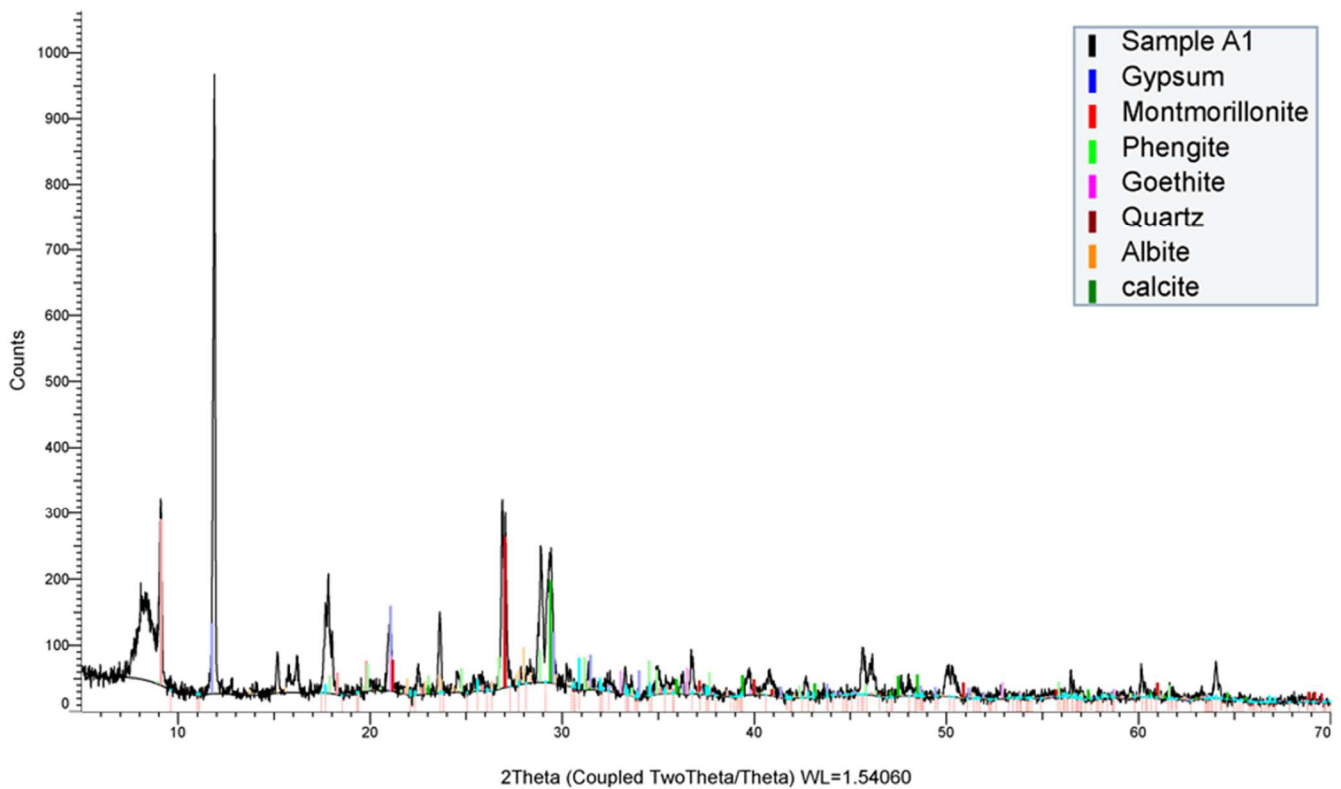


Figure 34. XRD results for sample A1 with top 7 mineral matches.

Chapter 5: Interpretations

Remote Sensing

In the idealized porphyry copper deposit model, a core of quartz and potassium-bearing minerals, mostly K-feldspar and biotite, is surrounded by multiple zones of alteration minerals (Fig. 20; Lowell and Guilbert, 1970). The hydrous zones are characterized by mineral assemblages, which contain at least one mineral that exhibits diagnostic spectral absorption features. The broad phyllic zone, which is commonly limonitic due to oxidation of pyrite, is characterized by muscovite-sericite, and the narrower advanced argillized rocks can be indexed by kaolinite, alunite, and pyrophyllite (Abrams and Brown, 1984; Spatz and Wilson, 1995; Hedenquist et. al, 2000; Mars and Rowan 2006; Mars 2014). The mineral assemblage of the outer propylitic zone is more variable due to country rock compositional differences, but epidote, chlorite, and carbonate minerals are common constituents. Titley (1972) noted that both country rock and intrusive rock can host copper mineralization, and both can be hydrothermally altered (Mars and Rowan 2006). When viewing the remote sensing map seen in Figure 13 for the EMD, we observe that sericite-muscovite is the predominant alteration type and that the advanced argillic minerals of kaolinite- alunite-pyrophyllite are seen sporadically throughout the area. Considering sericite-muscovite and advanced argillics are prevalent alteration minerals of PCDs (Figure 20), the hydrothermal alteration of Eureka coincides with what to look for according to the model and previous exploration efforts (John et. al, 2010). Through the interpolation of the remote sensing data, the area to the south of Turquoise Mountain allowed the ideal setting for the performance of the electromagnetics survey in the EMD. The remote sensing map for the SMD (Figure 14) showed a high concentration of epidote-chlorite alteration surrounding the Cottonwood Springs area that contained centralized high concentrations of sericite-muscovite

alteration. After interpolating the data, the decision was made to conduct the electromagnetic survey along the alluvial fan because of the high phyllic concentrations and due to the known presence of monzonitic and dioritic intrusions in the area (Figure 5; Lowell and Guilbert, 1970; Zeller, 1970; Seedorff et al., 2005).

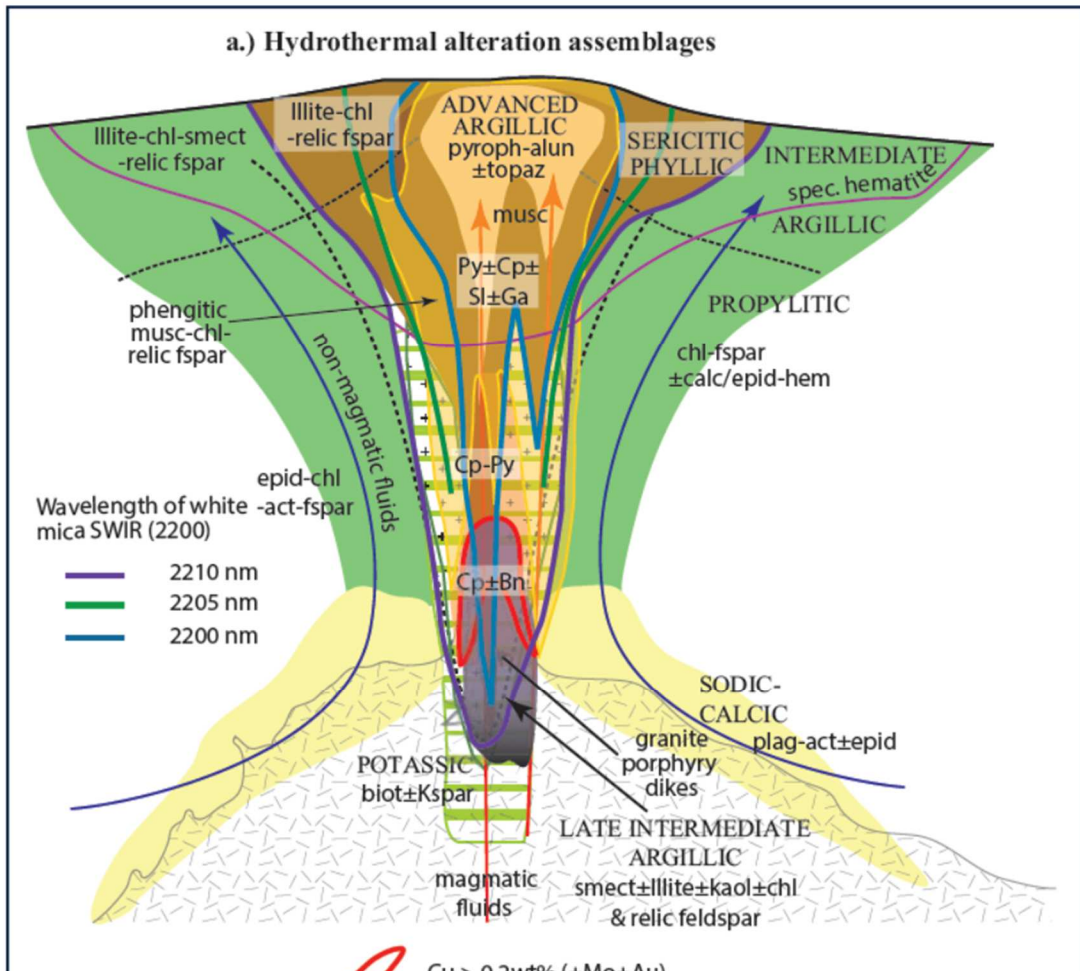


Figure 35. Vertical cross section of a typical porphyry Cu deposit showing distribution of hydrothermal alteration and sulfide minerals. Also shown are generalized contours of the 2,200-nm peak measured in SWIR instruments (Halley et. al, 2015).

Electromagnetics

Electromagnetics is proficient in direct detection of conductive sulfide deposits, in which large conductivity contrasts exist between the orebodies and country/host rocks or thin overburden cover (Haldar, 2017). According to Figure 20 (Dentith and Mudge, 2014) sulfides ('Sulphides') range from $\sim 10^{-3}$ to $\sim 10^7$ S/m (Seimens per meter) or $\sim 10^3$ to $\sim 10^{13}$ mS/m (milliSeimens per meter). Oxides range from $\sim 10^{-8}$ to $\sim 10^5$ S/m or $\sim 10^{-2}$ to $\sim 10^{11}$ mS/m. The EMD 'hotmaps' identify the presence of one significantly high anomaly in all variations,

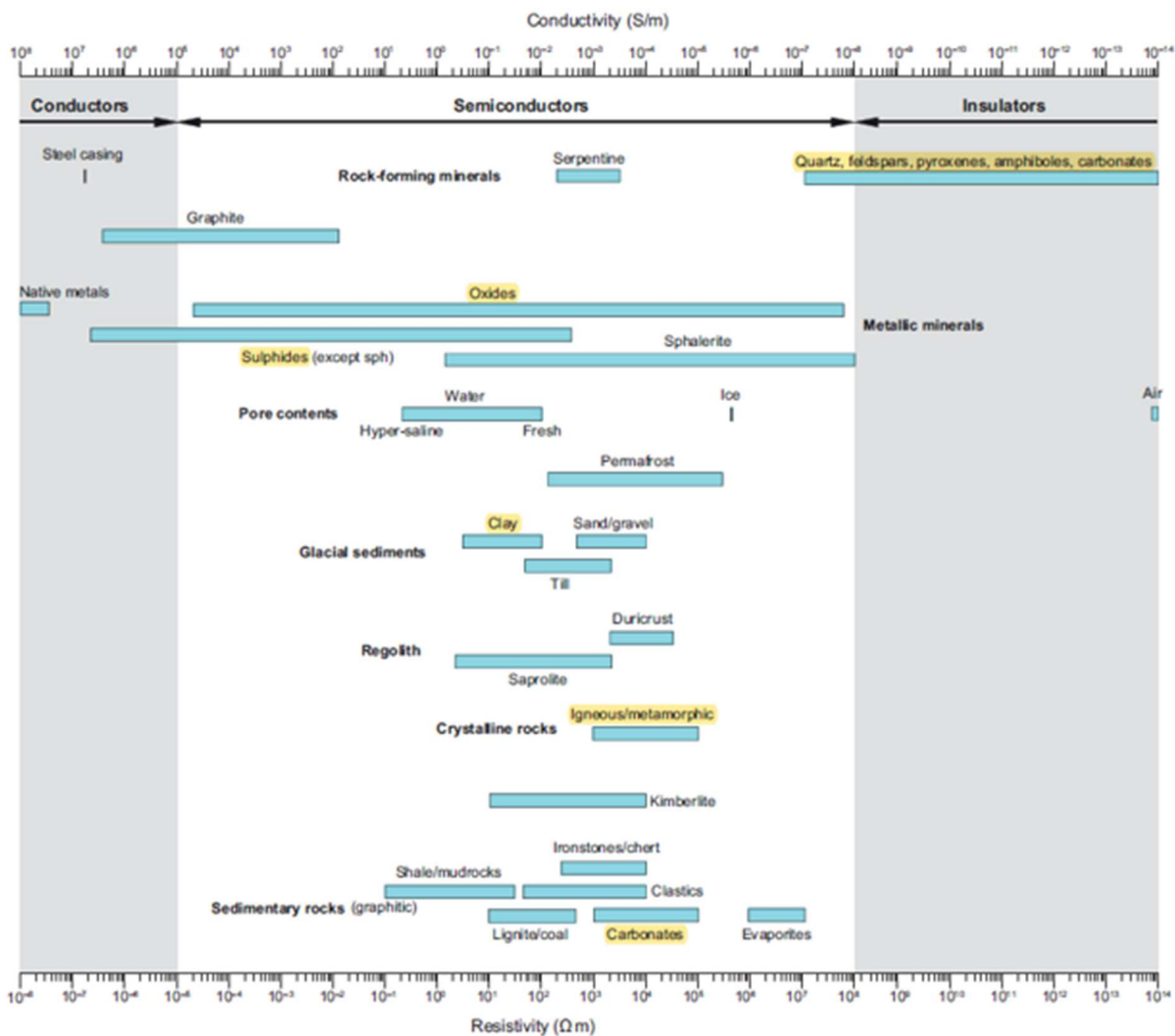


Figure 36. Typical ranges in conductivity/resistivity for some common minerals, rock types and near-surface materials with minerals of area highlighted (Dentith and Mudge 2014).

40V, 40H, 20V, and 20H (Figure 15 and Appendix Figures A2.1.2 – A2.1.4). The conductivity of this high is greater towards the surface changing from 13.8 mS/m at 40V (180 ft depth) to 29 mS/m at 20H (60 ft depth). The 20H map also contains a medium anomaly in the northwest region of the map with a conductivity reaching ~13 mS/m. The area between this anomaly and the map high anomaly is extremely resistive at 0 mS/m. The 20V also contains a northwest medium anomaly that reaches ~9.5 mS/m. Also, the north and southeast contain ~4.5 readings that could be trends beginning to materialize with the higher anomalies found on the map. For the 40H map we begin to see trends forming. The conductivities of this trend range from ~7-4.5 mS/m. The conductivity lows for the map are found along the eastern portion of the map reaching 2.5 mS/m, highly resistive. The 40V map shows a similar trend and conductivity highs but the conductivity low is -8 mS/m indicating that the subsurface material is extremely resistive. Based off these readings, the high conductivity anomalies for the EMD would be in the oxide range but this is not a proper way to interpret this data. Because the area has high anomaly conductivity readings and the remote sensing shows phyllic and advanced argillic minerals on the surface, this could possibly indicate that a variety of mineralization might have been deposited. This possible mineralization in the subsurface would most likely consist of a mixture of oxides and sulfides indicated by the remote sensing data. The SMD electromagnetic readings indicate a clear southeast to northwest trend of high conductivities as seen in Figure 16 of the 40V 180 ft depth profile 'hotmap'. These readings range from -7.6 to 16.4 mS/m. The 40H (120 ft depth), 20V (90 ft), and 20H (60 ft) (Appendix Figures A2.1.5 – A2.1.7) all show a similar trend from the southeast to the northwest with varying conductivities ranging from -2 to 32 mS/m. The highest anomalies are in the southeast corner of the SMD and why the resistivity surveys were targeted for the area (Figure 16 and 17). This trend and the survey results also

implies that the SMD survey zone at depth is tilted dipping slightly towards the southwest which coincides with the faults of the area (Appendix Table A6.2.1).

Electrical Resistivity

Electric resistivity surveying along the earth's surface is a well-known geophysical exploration technique (Bery and Saad, 2012a). Due to its conceptual simplicity, low equipment cost and ease of use, the method is routinely used in mineral exploration (Bery et. al, 2012). The 2 electrical resistivity survey lines performed in the SMD can be seen in Figure 18. The south to north electrical resistivity survey line can be seen in Figure 32 as an inverted conductivity model. The model indicates the presence of high conductivities that could mean possible mineralization

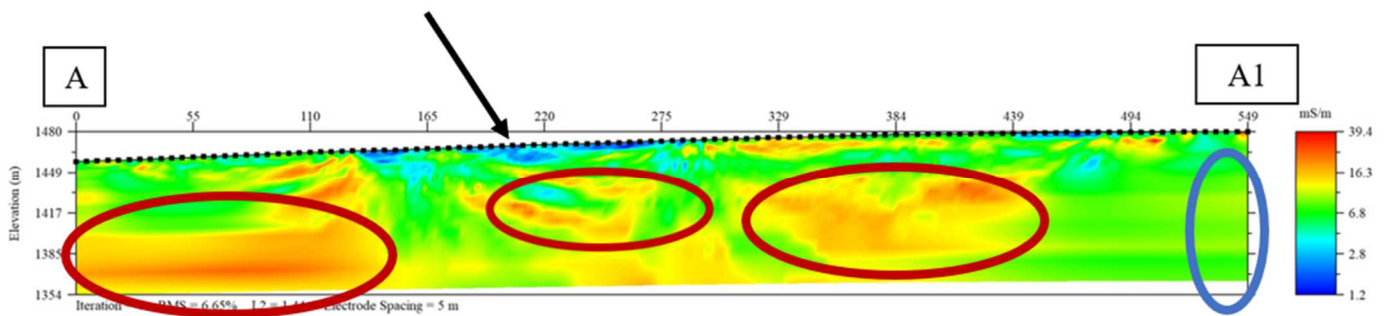


Figure 37. Electrical resistivity inverted conductivity model of the south (A) to north (A1) line with mineralized zones in red circles. Blue circle denotes conductivity lowering towards the north. Black arrow indicates highly resistive area.

as interpreted by the electromagnetics 40V to 20H maps of the area (Figure 17 and Figure 32's red circles; Appendix Figure A2.1.5 – A2.1.7). The high anomaly seen in the southeast of the electromagnetics maps can be seen at the 250 m survey line mark and ~60 m to ~20 m depth of the south to north electrical resistivity survey (Figure 32, center red circle). This association of conductivities between the electromagnetics and electrical resistivity surveys confirms both datasets. This includes the evidence of mineralization for both survey types. The electrical resistivity south to north line also indicates that mineralization may continue to the south (Figure 32, left red circle) but appears to become less conductive towards the north (Figure 32, blue

circle). The trend from southeast to northwest that is interpreted as running along the Livermore Springs fault zone in the electromagnetics section is indicated on Figure 32 as conductivities

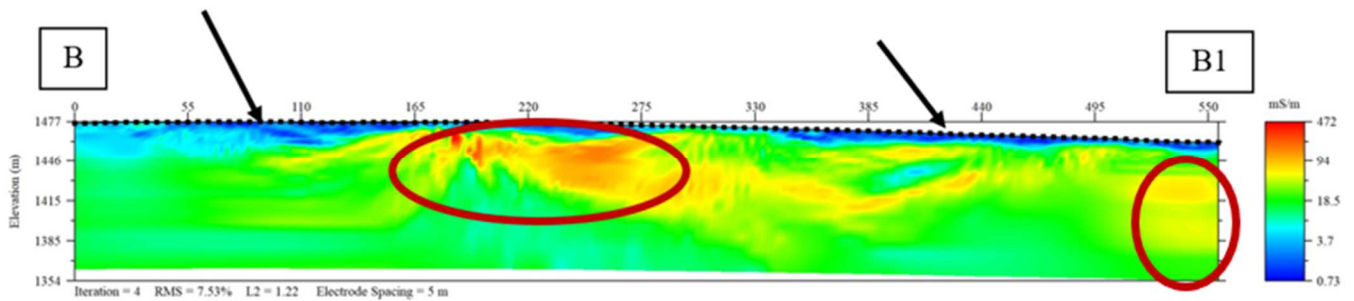


Figure 38. Electrical resistivity inverted conductivity model of the southeast (B) to northwest (B1) with red circle indicating highly conductive mineralized zone. Black arrows denote highly resistive areas at surface.

lessen towards the north but become more prevalent southward. The southeast to northwest model indicates a highly conductive mineralized zone (Figure 33, left red circle) and continual high readings towards the northwest (Figure 33, right red circle) following the trend visualized from the SMD electromagnetics ‘hotmaps’ (Figure 17 and Appendix Figures A2.1.6 - A2.1.8). The black arrows on Figures 32 and 33 indicate highly resistive surface cover. This may be interpreted as high quartz/silicic, feldspars, pyroxenes, and/or carbonates (Figure 31) alluvium that has been washed down to the alluvial fan from higher elevation formations or as a lithocap that is a horizontal to subhorizontal blanket of residual quartz and advanced argillic alteration of hypogene origin, occurring over intrusions (Sillitoe, 1995a; Chang et. al, 2011).

Mineral Spectroscopy

Of the 18 samples tested in the visible and near infrared spectrum and according to the ASCII Reference Library, 17 of the samples had the closest resemblance on the graphs to goethite, with one outlier made up of 64% hematite and 36% goethite. This is not an anomaly

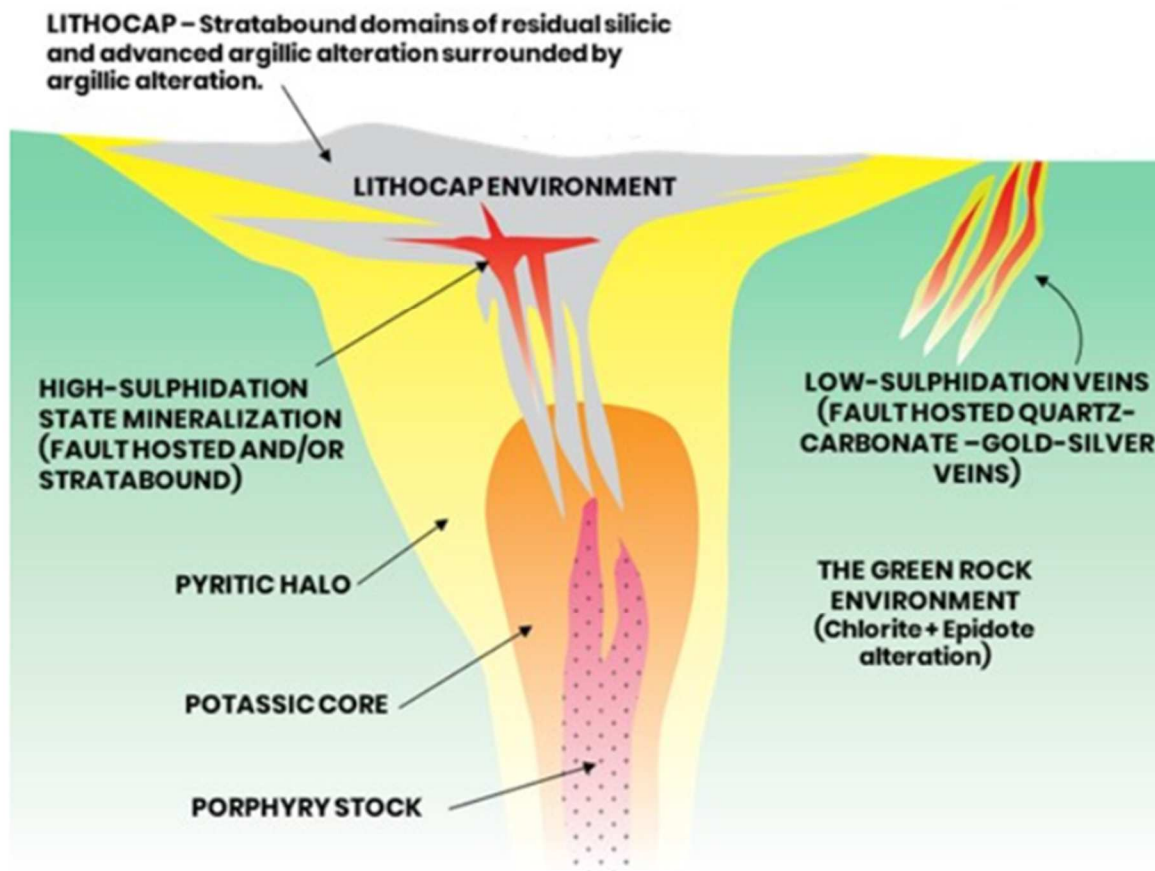


Figure 39. Idealized cross-section of high-sulphidation epithermal and porphyry environments (Modified from Holliday and Cooke 2007).

considering the majority of samples originated in the northern section of the alluvial fan along the hillsides where the prospects tend to be more prevalent. Gypsum was a major or contributing mineral to the assemblage of 8 samples in the short-wave infrared spectrum, which can mean that ‘the presence of sulfate minerals (e.g., gypsum) indicates a low acid production during

weathering and hydrolysis reactions and generation of secondary copper minerals (e.g., malachite and turquoise) may cause the copper depletion of descending aqueous fluids (Mahmoudi, 2018). The presence of malachite can be found in both the SMD and EMD and an old turquoise mining prospect can be found on the aptly named Turquoise Mountain in the EMD. The remaining samples and assemblages contain varied percentages of chlorite-Fe, epidote, dickite, alunite-Na, jarosite, kaolinite, siderite, phengite, and calcite. Since hypogene gangue consists of primary rock-forming and hydrothermal minerals, including plagioclase, potassium feldspar, quartz, micas, chlorite, epidote, amphiboles, pyroxenes, calcite, garnet, aluminum-silicate-sulfate minerals (kaolinite, illite, dickite, alunite, andalusite, and pyrophyllite) (John et. al, 2010), this would mean that the mineral assemblages in the short-wave infrared and the remote sensing hydrothermal alteration map of the SMD's (Figure 14) high concentrations of sericite-muscovite and epidote-chlorite give further credence to this suggestive of a hypogene ore zone. The spectral results do not include any copper minerals but this does not imply that the present exposures do not have the possibility of being part of a porphyry system.

X-ray Diffraction

From the XRD results a ‘best match’ was extrapolated between the mineral spectroscopy results (Table 2). This ‘best match’ was given a low, mid, or high confidence level due to the amount of correlation between the mineral identification the mineral spectroscopy presented versus the XRD top matches. For sample A1, goethite and gypsum matched giving this a high confidence probability. Sample A2 presented matches with gypsum and goethite again giving it a high confidence level. Overall, 1 low, 2 mid, and 4 high confidence levels were applied. Also, sample A2 was found unreliable in the SWIR spectrum yet was a ‘best match’ with the XRD for gypsum and goethite using the mineral spectroscopy identification in the SWIR. For the unreliable results in both the VNIR and SWIR using mineral spectroscopy, 2 confidence levels were high with 1 mid and 1 low. This implies that the reliability parameters set by ‘The Spectral Geologist’ software may not be a dependable guide as to its’ effectiveness as the results still tended toward accurate results. In this study, the XRD being utilized as an accuracy check for the mineral spectroscopy results was successful in that most results contained at least 2 mineral matches.

Table 2. Best Match with Confidence Level Mineral Spectroscopy vs XRD

Sample ID	Mineral Spectroscopy - Visible and Near Infrared	Mineral Spectroscopy - Shortwave Infrared	Mineral Spectroscopy Reliability	X-ray Diffraction (top 5 possible minerals)	Best Match (High, Mid, and Low Confidence Level)
A1	Goethite	61% Chlorite-Fe + 22% Jarosite +16% Gypsum	Unreliable	1) Gypsum 2) Montmorillinite 3) Phengite 4) Goethite 5) Quartz	HIGH: Goethite and Gypsum
A2	Goethite	Gypsum	SWIR - Unreliable	1) Gypsum 2) Jarosite 3) Goethite 4) Quartz 5) Montmorillinite	HIGH: Goethite and Gypsum
B5	Goethite	84% Chlorite-Fe + 16% Gypsum	Reliable	1) Montmorillinite 2) Quartz 3) Jarosite 4) Goethite 5) Gypsum	HIGH: Goethite and Gypsum
C1	Goethite	Dickite	Reliable	1) Montmorillinite 2) Quartz 3) Goethite 4) Orthoclase	MID: Goethite
C8	Goethite - FeOOH	Gypsum	Unreliable	1) Gypsum 2) Goethite 3) Jarosite 4) Quartz	HIGH: Goethite and Gypsum
D2	Goethite	51% Siderite + 49% Phengite	Unreliable	1) Jarosite 2) Quartz Low 3) Orthoclase 4) Illite	LOW
I2	Goethite	Chlorite-FeMg	Unreliable	1) Quartz 2) Jarosite 3) Goethite 4) Montmorillinite	MID: Goethite

Discussion and Speculation

Goethitic leached caps mostly overlie hypogene ore zones where copper leaching and enrichment are restricted, indicating low pyrite to chalcopyrite ratio and reactive host rock alteration assemblages whereas, jarositic leached caps reflect pyrite-rich mineralization and are typically associated with phyllic and advanced argillic alteration zone overprinted by supergene kaolinite alteration, The development of a lithocap is a hypogene phenomenon. The leached cap is the result from the oxidized of supergene processes, usually historical of hypogene. (Gilmour, 1995; Sillitoe, 1995; Sutopo, 2005; Mach, 2008; Mahmoudi, 2018) According to the spectroscopic results, the abundance of goethite identified as the major mineral of the samples in the visible and near infrared would mean that the SMD might be indicative of a goethite leached cap, overlying a hypogene ore zones. Speculatively, the evidence leads to the possibility of a hypogene ore zone as indicated by the combination of remote sensing and ground truth, mineral spectroscopy, and the geophysics surveys' high anomaly conductivities. The data can be viewed to infer that if a PCD is present it is tilted, dipping towards the southwest. The evidence in this project area indicative of a PCD are 1) malachite in collected samples at the SMD's Cottonwood Springs, 2) the intrusive nature of the diorite, monzonite, and quartz monzonite, 3) the arc of minor precious metal deposits/prospects surrounding the SMD and EMD and 4) the evidence of high conductive anomalies at depth using electromagnetics and electrical resistivity surveys.

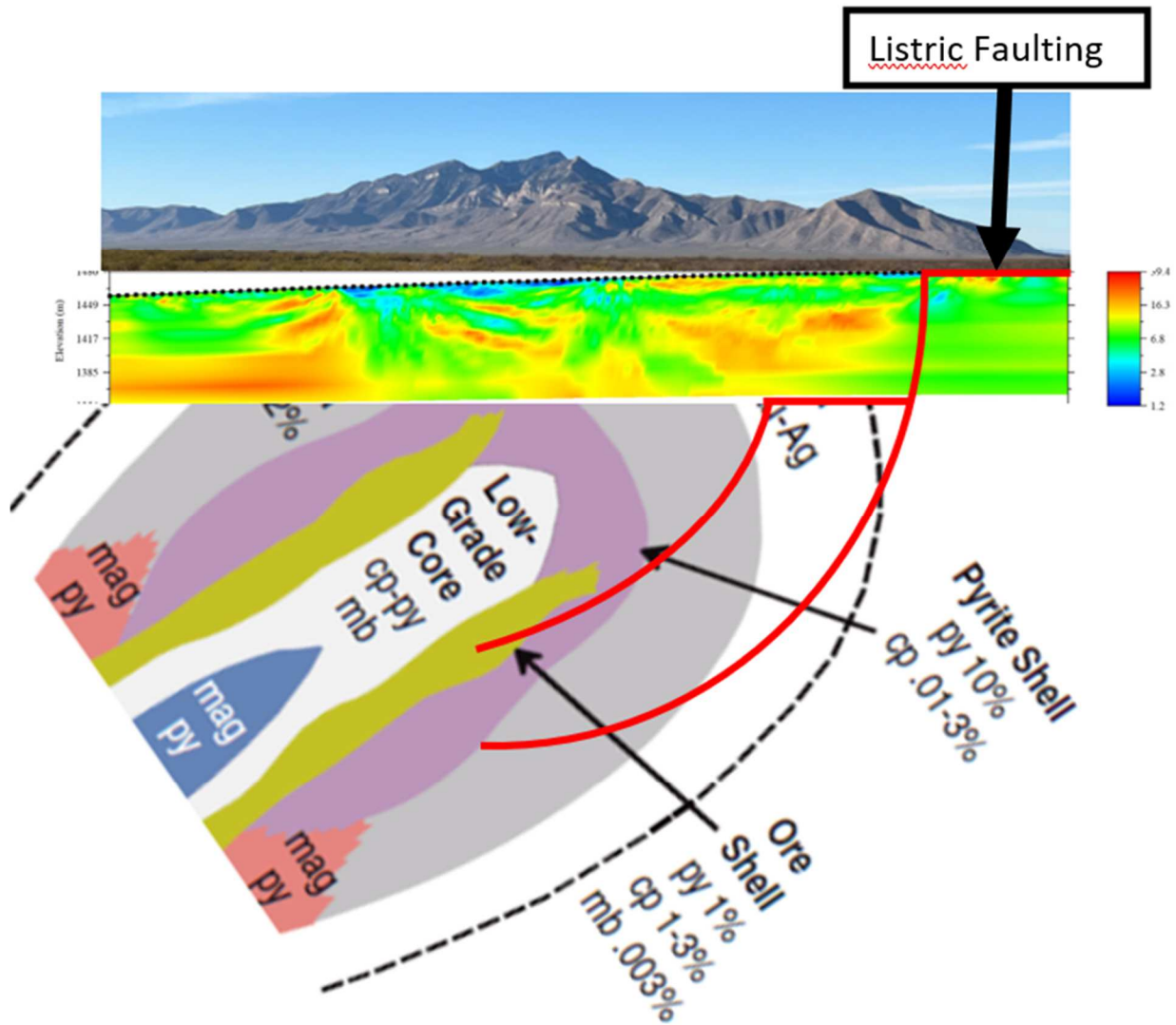


Figure 40. Theoretical model showing possible inferred porphyry with shells tilted in the subsurface due to listric faulting. Modified from Lowell and Guilbert, 1970.

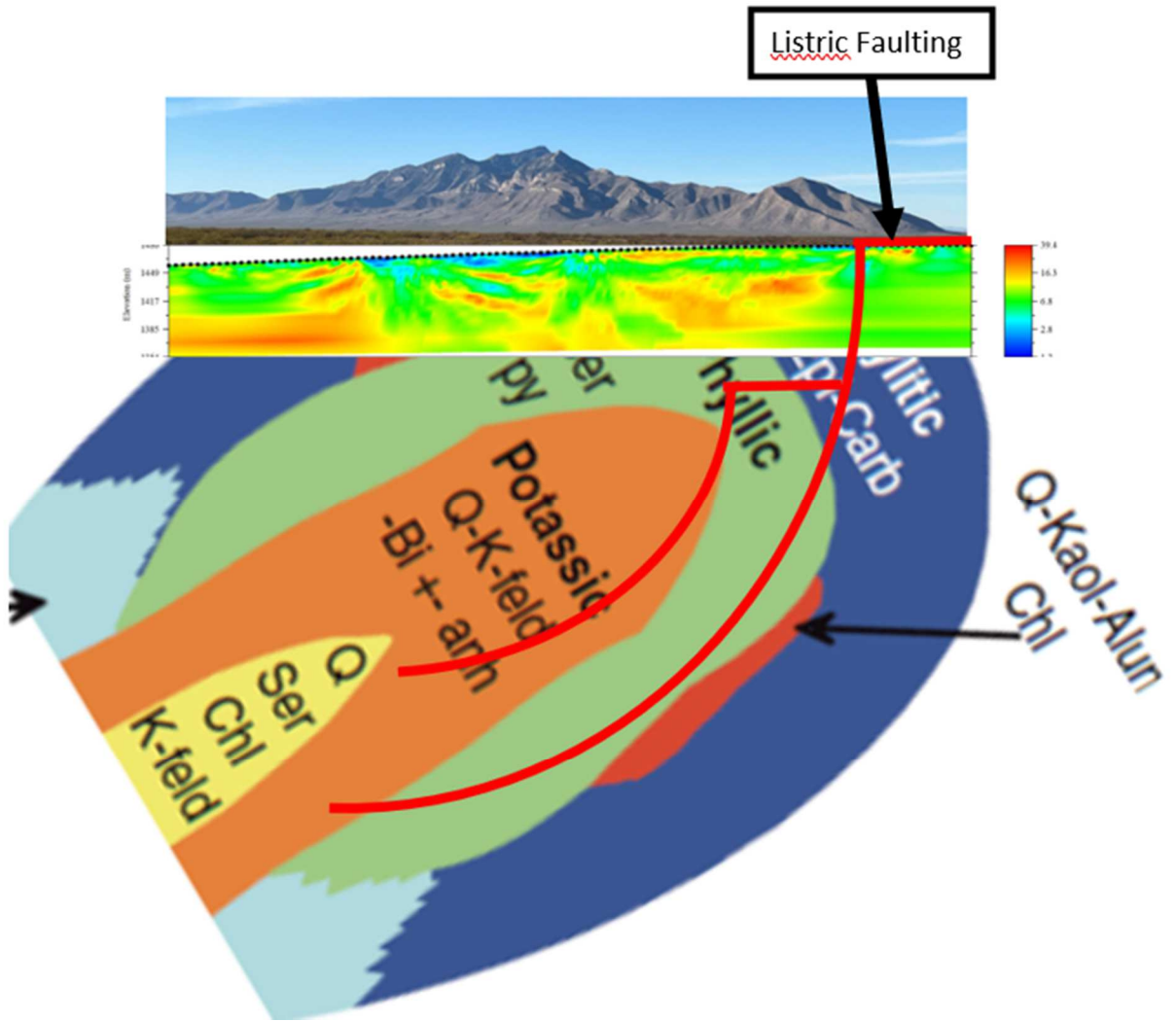


Figure 41. Theoretical model showing possible inferred porphyry with alteration tilted in the subsurface due to listric faulting. Modified from Lowell and Guilbert, 1970.

Chapter 6: Conclusions and Future Work

The exploration evaluation of the EMD and SMD has contributed to the accumulation of physical evidence indicating deposition of mineralization. The EMD remote sensing and electromagnetic surveys indicate near surface hydrothermal alteration and mineralization but the evaluation for this paper is constrained without mineral spectroscopy and electrical resistivity survey testing. Southern Silver Exploration Corp. has evaluated the Eureka area through geochemical and geophysical analysis that produced positive findings resulting in drilling operations currently underway, with a 6-hole 4000 m program. The junior exploration company describes the EMD as a large, well-zoned Laramide-age mineral system consisting of a ring of Carbonate Replacement Deposits (CRDs) around a core of intense clay-sericite-pyrite alteration, which clay mineralogy indicates is the “lithocap” overlying an unexposed porphyry centre (southernsilverexploration.com). Southern Silver also highlights the presence of kaolinite and pyrophyllite according to their investigations confirming the remote sensing performed in this paper is accurate. The SMD remote sensing and mineral spectroscopy confirm the possible occurrence of a goethite leached cap along with the occurrence of many hypogene alteration mineral assemblages. XRD provided additional evidence of gypsum and goethite occurrences confirming the mineral spectroscopy. The possibility of the presence of a lithocap indicates an epithermal level of erosion, and the potential for epithermal and/or porphyry mineralization nearby (Chang et.al, 2011). The electromagnetics and electrical resistivity confirm that conductivities in the ranges of oxide to sulfide mineralization are present at Sylvanite. The location of the near surface high conductivities and trend may be speculatively indicative of a PCD that has been tilted dipping slightly to the southwest.

Future work for the SMD is currently underway in the form of geochemical analysis soon to be performed on ~50 samples acquired in the area. Geophysical analysis of the area in the form of ground gravity and magnetics surveys, along with deeper electrical resistivity and larger area electromagnetics, will contribute to a better definition of the mineralization occurrence and possibly result in a drilling program being initiated by an exploration company. Furthermore, an alluvial fan alteration mapping project in the SMD would help define the extent of intrusion i.e. dikes/Sylvanite Complex and alteration.

References

- Abrams, M.J., Brown, L., Lepley, R., and Sadowski, P., 1983, Remote sensing for porphyry copper deposits in Southern Arizona: *Economic Geology*, v. 78, p. 591–604.
- Amato, J.M., Mack, G.H., Jonell, T.N., Seager, W.R., and Upchurch, G.R., 2017, Onset of the Laramide orogeny and associated magmatism in southern New Mexico based on U-Pb geochronology: *Geological Society of America Bulletin*, v. 129, p. 1209–1226, <https://doi.org/10.1130/B31629.1>.
- Balach, J., Linnemann, J., Jaumann, T., Giebeler, L., 2018, Metal-based nanostructured materials for advanced lithium–sulfur batteries. *J Mater Chem A*. 6:23127–68. doi: 10.1039/C8TA07220E
- Basabilvazo, G., 2000, The Upper Cretaceous Ringbone Formation, Little Hatchet Mountains, southwest New Mexico, in Lawton, T.F., et al., eds., *Southwest Passage—A Trip Through the Phanerozoic: New Mexico Geological Society Fall Field Conference Guidebook 51*, p. 203–210.
- Bery, A. A., Saad, R., Mohamad, E. T., Jinmin, M., Azwin, I. N., Tan, N. A., & Nordiana, M. M. 2012. Electrical resistivity and induced polarization data correlation with conductivity for iron ore exploration. *The Electronic Journal of Geotechnical Engineering*, 17, 3223-3233.
- Chang, Z., Hedenquist, J.W., White, N.C., Cooke, D.R., Roach, M., Deyell, C.L., Garcia, J., Gemell, J.B., McKnight, S., Cuisson, A.L., 2011, Exploration Tools for Linked Porphyry and Epithermal Deposits: Example from the Mankayan Intrusion-Centered Cu-Au District, Luzon, Philippines. *Economic Geology*; 106 (8): p. 1365–1398.
doi: <https://doi.org/10.2113/econgeo.106.8.1365>

- Channell, R., McMillan, N.J., Lawton, T.F., Heizler, M., Esser, R.P., and McLemore, V.T., 2000, Magmatic history of the Little Hatchet Mountains, Hidalgo and Grant Counties, southwestern New Mexico, in Lawton, T.F., et al., eds., *Southwest Passage—A Trip Through the Phanerozoic: New Mexico Geological Society Fall Field Conference Guidebook 51*, p. 141–148.
- Cleary, M.S., 2004, *Quantitative Strain Analysis and Timing of North-South Extension in the Little Hatchet Mountains, Southwest New Mexico* [M.S. thesis]: Las Cruces, New Mexico State University, 105 p.
- Clinkscales, C.A., and Lawton, T.F., 2014, Timing of late Cretaceous shortening and basin development, Little Hatchet Mountains, southwestern New Mexico, USA—Implications for regional Laramide tectonics: *Basin Research*, v. 27, p. 453–472, <https://doi.org/10.1111/bre.12083>.
- Clinkscales, C. A., Lawton, T. F., 2017, Mesozoic–Paleogene structural evolution of the southern U.S. Cordillera as revealed in the Little and Big Hatchet Mountains, southwest New Mexico, USA; *Geosphere*, v. 14, no. 1, p. 162-186.
- Coney, P.J., and Reynolds, S.J., 1977, Cordilleran Benioff zones: *Nature*, v. 270, p. 403–406, <https://doi.org/10.1038/270403a0>.
- Cox, D.P., and Singer, D.A., 1992, Distribution of gold in porphyry copper deposits, *in* DeYoung, J.H., and Hammerstrom, J.M., eds., *Contributions to commodity research: U.S. Geological Survey Bulletin 1877*, p. C1–C14.
- Cross, T.A., 1986, Tectonic controls of foreland basin subsidence and Laramide style deformation, western United States, in Allen, P.A., and Homewood, P., eds., *Foreland Basins:*

International Association of Sedimentologists Special Publication 8, p. 13–39, [https:// doi .org /10 .1002 /9781444303810 .ch1](https://doi.org/10.1002/9781444303810.ch1).

Dahlin, T., Zhou, B., 2004, A numerical comparison of 2D resistivity imaging with 10 electrode arrays; *Geophysical Prospecting*, v. 52, no. 5, p. 379-398.

Dentith, M. C., & Mudge, S. 2014. *Geophysics for the Mineral Exploration Geoscientist*. Cambridge University Press.

Dickinson, W.R., and Snyder, W.S., 1978, Plate tectonics of the Laramide orogeny, in Matthews, V., ed., *Laramide Folding Associated with Basement Block Faulting in the Western United States: Geological Society of America Memoir 151*, p. 355–366, [https:// doi .org /10 .1130 /MEM151 -p355](https://doi.org/10.1130/MEM151-p355).

Dickinson, W.R., Klute, M.A., Hayes, M.J., Janecke, S.U., Lundin, E.R., McKittrick, M.A., and Olivares, M.D., 1988, Paleogeographic and paleotectonic setting of Laramide sedimentary basins in the central Rocky Mountain region: *Geological Society of America Bulletin*, v. 100, p. 1023–1039, [https:// doi .org /10 .1130 /0016 -7606 \(1988\)100 <1023: PAPSOL>2 .3 .CO;2](https://doi.org/10.1130/0016-7606(1988)100<1023:PAPSOL>2.CO;2).

Drewes, H., 1988, Development of the foreland zone and adjacent terranes of the Cordilleran orogenic belt near the U.S.-Mexican border, in Schmidt, C.A., and Perry, W.J., Jr., eds., *Interaction of the Rocky Mountain Foreland and the Cordilleran Thrust Front: Geological Society of America Memoir 171*, p. 447–464, [https:// doi .org /10 .1130 /MEM171 -p447](https://doi.org/10.1130/MEM171-p447).

Faulds, J.E., and Varga, R.J., 1998, The role of accommodation zones and transfer zones in the regional segmentation of extended terranes, in Faulds, J.E., and Stewart, J.H., eds., *Accommodation Zones and Transfer Zones: The Regional Segmentation of the Basin and*

Range Province: Geological Society of America Special Paper 323, p. 1–46, <https://doi.org/10.1130/0-8137-2323-X.1>.

Haldar, S.K., 2017, Chapter 10 - Exploration Guide, Editor(s): S.K. Haldar, Platinum-Nickel-Chromium Deposits, Geology, Exploration and Reserve Base, Elsevier, Pages 247-266, ISBN 9780128020418, <https://doi.org/10.1016/B978-0-12-802041-8.00010-9>.

Halley, S., Dilles, J.H. and Tosdal, R.M., 2015. Footprints: hydrothermal alteration and geochemical dispersion around porphyry copper deposits. *SEG Discovery*, (100), pp.1-17.

Hayes, P.T., 1970. Cretaceous paleogeography of southeastern Arizona and adjacent area. United States Geological Survey Professional Paper 658-B, B1–B42

Hedenquist, J.W., Arribas, A., Jr., and Gonzalez-Urien, E., 2000, Exploration for epithermal gold deposits: *Reviews in Economic Geology*, v. 13, p. 245–277.

Hodgson, S.A., 2000, Structural geology and Laramide tectonics of the Little Hatchet Mountains, southwestern New Mexico, in Lawton, T.F., et al., eds., *Southwest Passage—A Trip Through the Phanerozoic: New Mexico Geological Society Fall Field Conference Guidebook 51*, p. 109–116.

Holliday, J.R. and Cooke, D.R., 2007, Advances in geological models and exploration methods for copper±gold porphyry deposits. In *Proceedings of exploration* (Vol. 7, pp. 791-809).

Hunt, G.R., and Ashley, R.P., 1979, Spectra of altered rocks in the visible and near infrared: *Economic Geology*, v. 74, no. 7, p. 1613–1629.

Jennings, G.R., Lawton, T.F., and Clinkscales, C.A., 2013, Late Cretaceous U/Pb tuff ages from the Skunk Ranch Formation and their implications for age of Laramide deformation, Little

Hatchet Mountains, southwestern New Mexico, U.S.A.: *Cretaceous Research*, v. 18, p. 18–25, <https://doi.org/10.1016/j.cretres.2013.02.001>.

John, D.A., Ayuso, R.A., Barton, M.D., Blakely, R.J., Bodnar, R.J., Dilles, J.H., Gray, Floyd, Graybeal, F.T., Mars, J.C., McPhee, D.K., Seal, R.R., Taylor, R.D., and Vikre, P.G., 2010, Porphyry copper deposit model, chap. B of *Mineral deposit models for resource assessment: U.S. Geological Survey Scientific Investigations Report 2010–5070–B*, 169 p., available only at <http://pubs.usgs.gov/sir/2010/5070/b/>.

Kesler, S.E., 1973, Copper, molybdenum, and gold abundances in porphyry copper deposits: *Economic Geology*, v. 68, p. 106–112.

Kottlowski, F. E. 1964. Sedimentary Basins of Central and Southwestern New Mexico. *AAPG Bulletin*, 48(11), 1879-1879.

Lang, J.R., and Titley, S.R., 1998, Isotopic and geochemical characteristics of Laramide magmatic systems in Arizona and implications for the genesis of porphyry copper deposits: *Economic Geology and the Bulletin of the Society of Economic Geologists*, v. 93, p. 138–170, <https://doi.org/10.2113/gsecongeo.93.2.138>.

Lasky, S.G., 1947, Geology and ore deposits of the Little Hatchet Mountains, Hidalgo and Grant counties, New Mexico: U.S. Geological Survey Professional Paper 208, 101 p.

Lawton, T.F., 2008, Laramide sedimentary basins, in Miall, A.D., ed., *The Sedimentary Basins of the United States and Canada: Volume 5, Sedimentary Basins of the World*: Netherlands, Elsevier, p. 429–450, [https://doi.org/10.1016/S1874-5997\(08\)00012-9](https://doi.org/10.1016/S1874-5997(08)00012-9).

- Lawton, T.F., and Harrigan, P.J., 1998, Broken Jug Formation—Redefinition of lower part of Bisbee Group, Little Hatchet Mountains, Hidalgo County, New Mexico: *New Mexico Geology*, v. 20, p. 69–77.
- Lawton, T.F., and Olmstead, G.A., 1995, Stratigraphy and structure of the lower part of the Bisbee Group, northeastern Chiricahua Mountains, Arizona, in Jacques-Ayala, C., et al., eds., *Studies on the Mesozoic of Sonora and Adjacent Areas: Geological Society of America Special Paper 301*, p. 21–39, <https://doi.org/10.1130/0-8137-2301-9.21>.
- Lawton, T.F., Basabilvazo, G.T., Hodgson, S.A., Wilson, D.A., McIntosh, W.C., Lucas, W.C., Lucas, S.G., and Kietzke, K.K., 1993, Laramide stratigraphy in the Little Hatchet Mountains, southwestern New Mexico: *New Mexico Geology*, v. 15, p. 9–15.
- Leveille, R. A., Stegen, R. J., 2012, The Southwestern North America Porphyry Copper Province; Society of Economic Geologists Inc., Special Publication v. 16, p. 361-401.
- Lowell, J.D., 1968, Geology of the Kalamazoo orebody, San Manuel district, Arizona: *Economic Geology*, v. 63, p. 645–654.
- Lowell, J.D., and Guilbert, J.M., 1970, Lateral and vertical alteration-mineralization zoning porphyry ore deposits: *Economic Geology and the Bulletin of the Society of Economic Geologists*, v. 65, no. 4, p. 373–408.
- Lowell, J.D., 1974, Regional Characteristics of Porphyry Copper Deposits of the Southwest. *Economic Geology*, 69 (5), 601–617.
doi: <https://doi.org/10.2113/gsecongeo.69.5.601>
- Lowell, J.D., 1974, Plate Tectonics and Foreland Basement Deformation. *Geology*, 2 (6), 275–278. doi: [https://doi.org/10.1130/0091-7613\(1974\)2<275:PTAFBD>2.0.CO;2](https://doi.org/10.1130/0091-7613(1974)2<275:PTAFBD>2.0.CO;2)

- Lucas, S.G., and Lawton, T.F., 2000, Stratigraphy of the Bisbee Group (Jurassic–Cretaceous), Little Hatchet Mountains, New Mexico, in Lawton, T.F., et al., eds., Southwest Passage—A Trip Through the Phanerozoic: New Mexico Geological Society Fall Field Conference Guidebook 51, p. 175–194.
- Lucas, S.G., and Lawton, T.F., 2005, Upper Cretaceous marine strata in the Little Hatchet Mountains, southwest New Mexico: *New Mexico Geology*, v. 27, p. 63–68.
- Machin, S.E.K., 2013, Solving the Beartooth problem: Using U-Pb zircon geochronology to investigate the significance of mid-Cretaceous sandstones in New Mexico [M.S. Thesis]: Las Cruces, New Mexico State University, 141 p.
- Mack, G.H., 1987, Mid-Cretaceous (late Albian) change from rift to retroarc foreland basin in southwestern New Mexico: *Geological Society of America Bulletin*, v. 98, p. 507–514, [https://doi.org/10.1130/0016-7606\(1987\)98<507:MLACFR>2.0.CO;2](https://doi.org/10.1130/0016-7606(1987)98<507:MLACFR>2.0.CO;2).
- Mack, G.H., and Clemons, R.A., 1988, Structural and stratigraphic evidence for the Laramide (early Tertiary) Burro uplift in southwestern New Mexico, in Mack, G.H., et al., eds., *Cretaceous and Laramide Tectonic Evolution of Southwestern New Mexico*: New Mexico Geological Society Fall Field Conference Guidebook 39, p. 59–66.
- Mahmoudi, E., Moore, F., Asadi, S., 2018, Leached caps mineralogy and geochemistry as supergene enrichment fertility indicators, Meiduk and Parkam porphyry copper deposits, SW Iran, *Journal of Geochemical Exploration*, Volume 194, Pages 198-209
- Mars, J.C., 2014, Hydrothermal Alteration Maps of the Central and Southern Basin and Range Province of the United States Compiled From Advanced Spaceborne Thermal Emission and

Reflection Radiometer (ASTER) Data, Open-File Report 2013-1139,
<https://pubs.usgs.gov/of/2013/1139/of2013-1139/>

McLemore, V.T., Sutphin, D.M., Hack, D.R., Pease, T.C., 1996, Mining History and Mineral Resources of the Mimbres Resource Area, Dona Ana, Luna, Hidalgo, and Grant Counties, New Mexico, New Mexico Bureau of Mines and Mineral Resources; Openfile Report OF-424, 254 p.

McLemore, V.T., 2008, Potential for Laramide porphyry copper deposits in southwestern New Mexico, Geology of the Gila Wilderness-Silver City area, Mack, Greg, Witcher, James, Lueth, Virgil W.; [eds.], New Mexico, Geological Society 59th Annual Fall Field Conference Guidebook, 210 p.

Saleem Aldossari, M., Fares, G. and Ghrefat, H.A., 2019. Estimation of pozzolanic activity of scoria rocks using ASTER remote sensing. *Journal of Materials in Civil Engineering*, 31(7), p.04019100.

Scarlett, N. V. Y. and Bish, D. L., 2019, Mining and mineral processing, *International Tables for Crystallography* . Vol. H, ch. 7.7, pp. 793-803 doi:10.1107/97809553602060000981

Schaepman, M., 1994, Spectral Signature Analysis Using a Field Goniometer Mounted Spectroradiometer. 171-177.

Schmidt, R.G., 1976, Exploration for porphyry copper deposits in Pakistan using digital processing of Landsat-1 image data: *U.S. Geological Survey Journal of Research*, v. 4, no. 1, p. 27–34

Seager, W.R., 1983, Laramide wrench faults, basement-cored uplifts, and complimentary basins in southern New Mexico: *New Mexico Geology*, v. 5, p. 69–76.

- Seager, W.R., 2004, Laramide (Late Cretaceous–Eocene) tectonics of southwestern New Mexico, in Mack, G.M., and Giles, K.A., eds., *The Geology of New Mexico: A Geologic History*: New Mexico Geological Society Special Publication 11, p. 183–202.
- Seager, W.R., and Mack, G.H., 1986, Laramide paleotectonics of southern New Mexico, in Peterson, J.A., ed., *Paleotectonics and Sedimentation*: American Association of Petroleum Geologists Memoir 41, p. 660–685.
- Seager, W.R., Mack, G.H., and Lawton, T.F., 1997, Structural kinematics and depositional history of a Laramide uplift-basin pair in southern New Mexico: Implications for development of intraforeland basins: *Geological Society of America Bulletin*, v. 109, p. 1389–1401, [https://doi.org/10.1130/0016-7606\(1997\)109<1389:SKADHO>2.3.CO;2](https://doi.org/10.1130/0016-7606(1997)109<1389:SKADHO>2.3.CO;2).
- Seedorff, Eric, Dilles, J.H., Proffett, J.M., Jr., Einaudi, M.T., Zurcher, L., Stavast, W.J.A., Johnson, D.A., and Barton, M.D., 2005, Porphyry deposits—Characteristics and origin of hypogene features: *Society of Economic Geologists, Economic Geology 100th Anniversary Volume, 1905–2005*, p. 251–298.
- Sillitoe, R.H., 1995a, Exploration of porphyry copper lithocaps: *Australasian Institute of Mining and Metallurgy, Publication Series*, v. 9, p. 527–532.
- Sillitoe, R.H., 1999, Styles of high-sulphidation gold, silver and copper mineralization in the porphyry and epithermal environments: *Australian Institute of Mining and Metallurgy, PacRim '99, Bali, Indonesia, 10–13 October, Proceedings*, p. 29–44
- Sillitoe, R.H., 2000. Gold-rich porphyry deposits: descriptive and genetic models and their role in exploration and discovery. *Reviews in Economic Geology*, 13, pp.315-345.

- Sillitoe, R. H. 2010. Porphyry copper systems. *Economic Geology*, 105(1), 3-41.
doi: <https://doi.org/10.2113/gsecongeo.105.1.3>
- Sims, P. K., Stein, H. J., Finn, C.A., 2002, New Mexico structural zone- An analogue of the Colorado mineral belt. U.S. Geological Survey: *Ore Geology Reviews* Vol. 21, no, 3-4, p.221
- Soimart, L. and Ketcham, M., 2016, An Efficient Algorithm for Earth Surface Interpretation from Satellite Imagery. *Eng. J.*, vol. 20, no. 5, pp. 215-228.
- Spatz, D.M., and Wilson, R.T., 1995, Remote sensing characteristics of porphyry copper systems, western American Cordillera. in Pierce, F.W., and Bolm, J.G., eds., *Porphyry copper deposits of the American Cordillera: Arizona Geological Society Digest*, v. 20, p. 94–108.
- Sutopo, B., 2005, *Geological and Geochemical Appraisals of Leached Capping above Andean Porphyry Deposits*. Centre of Excellence in Ore Deposits, University of Tasmania, Australia.
- Thompson, S. and Jacka, A.D., 1981, Pennsylvanian stratigraphy, petrography, and petroleum geology of Big Hatchet Peak section, Hidalgo County, New Mexico: New Mexico Bureau of Mines and Mineral Resources Circular 176
- Titley, S.R., and Beane, R.E., 1981, Porphyry copper deposits: Part I. Geologic settings, petrology, and tectogenesis: *Economic Geology* 75th anniversary volume, p. 214—235
- Zeller, R.A., Jr., 1965, *Geology of the Big Hatchet Mountains Area*: New Mexico Bureau of Mines and Mineral Resources Memoir 16, 128 p.
- Zeller, R.A., Jr., 1970, *Geology of the Little Hatchet Mountains, Hidalgo and Grant Counties, New Mexico*: New Mexico Bureau of Mines and Mineral Resources Bulletin 96, 22 p.

ArcGIS Pro. ESRI, esri.com/en-us/arcgis/products/arcgis-pro/overview/. Accessed 9 Jan. 2022

EM34-3 | EM34-3XL. Geonics Limited, geonics.com/html/em34-3.html. Accessed 9 Jan. 2022

Google Earth Pro. Google Earth, google.com/earth/versions/. Accessed 9 Jan. 2022

GPSMAP® 60CSx. GARMIN, garmin.com/en-US/p/310. Accessed 9 Jan. 2022

High-speed 2D/3D Resistivity/IP/SP Imaging System Package - 112 Electrodes. AGIUSA, agiusa.com/high-speed-2d3d-resistivityipsp-imaging-system-package-112-electrodes. Accessed 9 Jan. 2022

Instruction Manual for EarthImager 2D Version 2.4.0 Resistivity and IP Inversion Software
Copyright 2002-2009 by Advanced Geosciences, Inc. pdfcoffee.com/earth-imager-2-d-manual-3-pdf-free.html. Accessed 9 Jan. 2022

K.D. Jones Instruments, kdjonesinstruments.com/files/2020/07/EM34-manual-013113.pdf. Accessed 9 Jan. 2022

K.D. Jones Instruments, kdjonesinstruments.com/files/2020/07/SuperStingManual.pdf. Accessed 9 Jan. 2022

Southern Silver Exploration Corp., southernsilverexploration.com/projects/oro-polymetallic-project-new-mexico/. Accessed 3 May. 2022

Surfer. Golden Software, goldensoftware.com/products/surfer. Accessed 9 Jan. 2022

Table of Electrical Resistivity and Conductivity, sciencenotes.org/table-of-electrical-resistivity-and-conductivity/. Accessed 9 Jan. 2022

Terra: the EOS Flagship. NASA, terra.nasa.gov/. Accessed 9 Jan. 2022

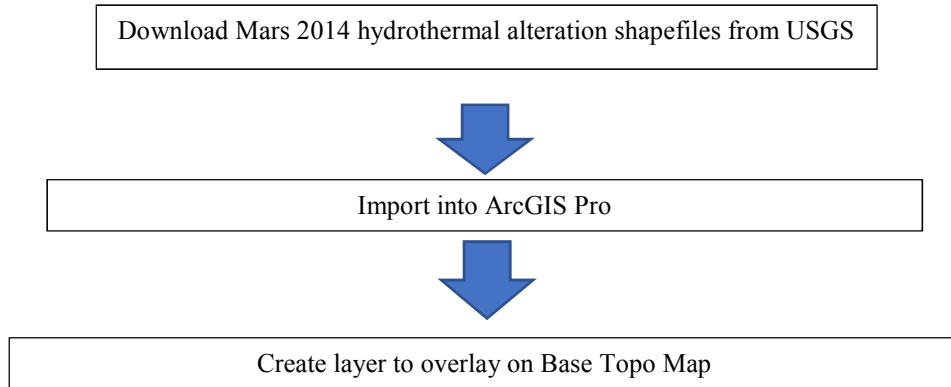
The Spectral Geologist. CSIRO, research.csiro.au/thespectralgeologist/. Accessed 9 Jan. 2022

TNP Terrain Navigator Pro. Trimble, terrainnavigator.com/. Accessed 9 Jan. 2022

Appendix

Remote Sensing

Flow Chart A1.1



Electromagnetics Figures

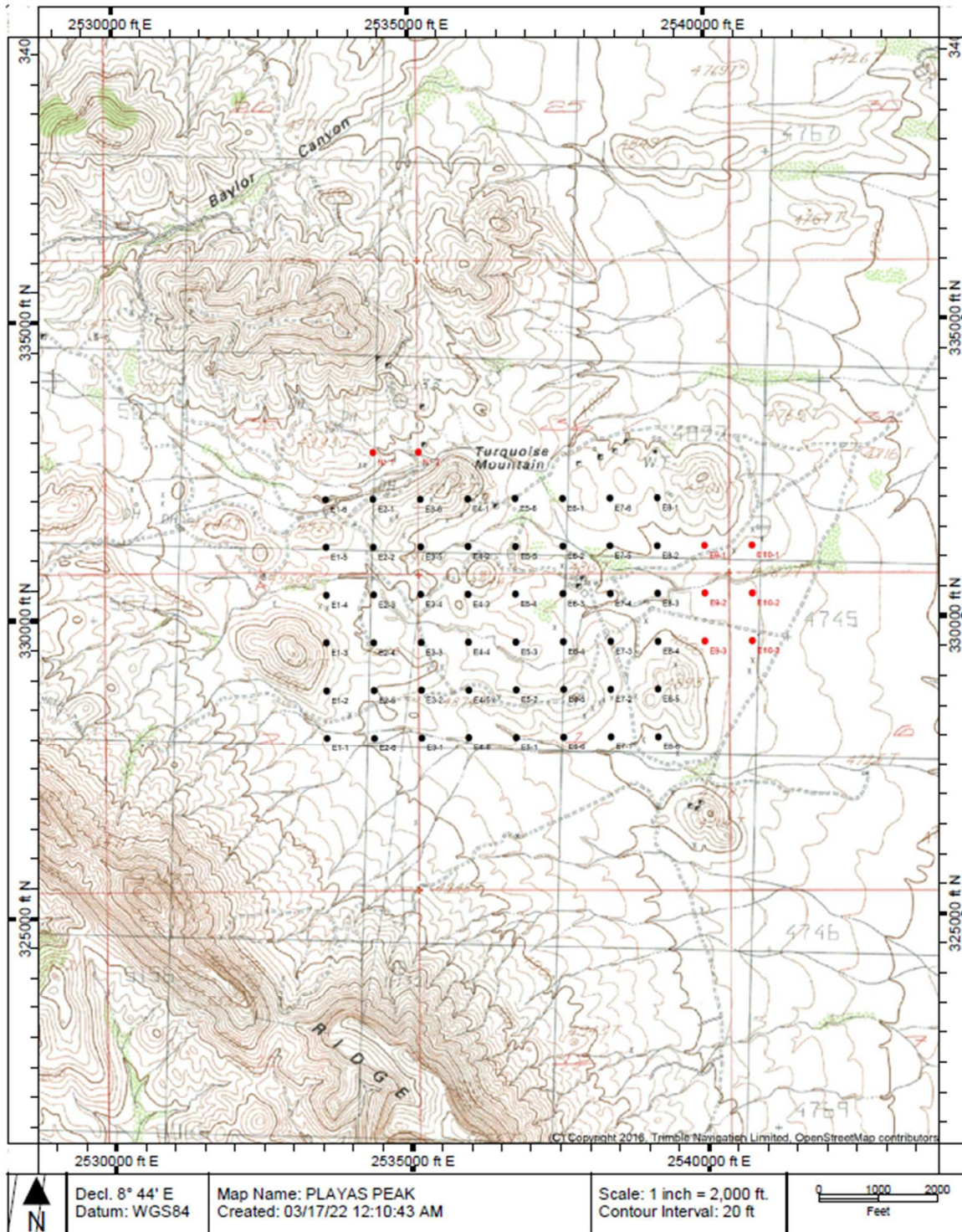


Figure A2.1.1. Eureka GDAP Layout map, for list of GDAPs evaluated see Appendix Table 1,

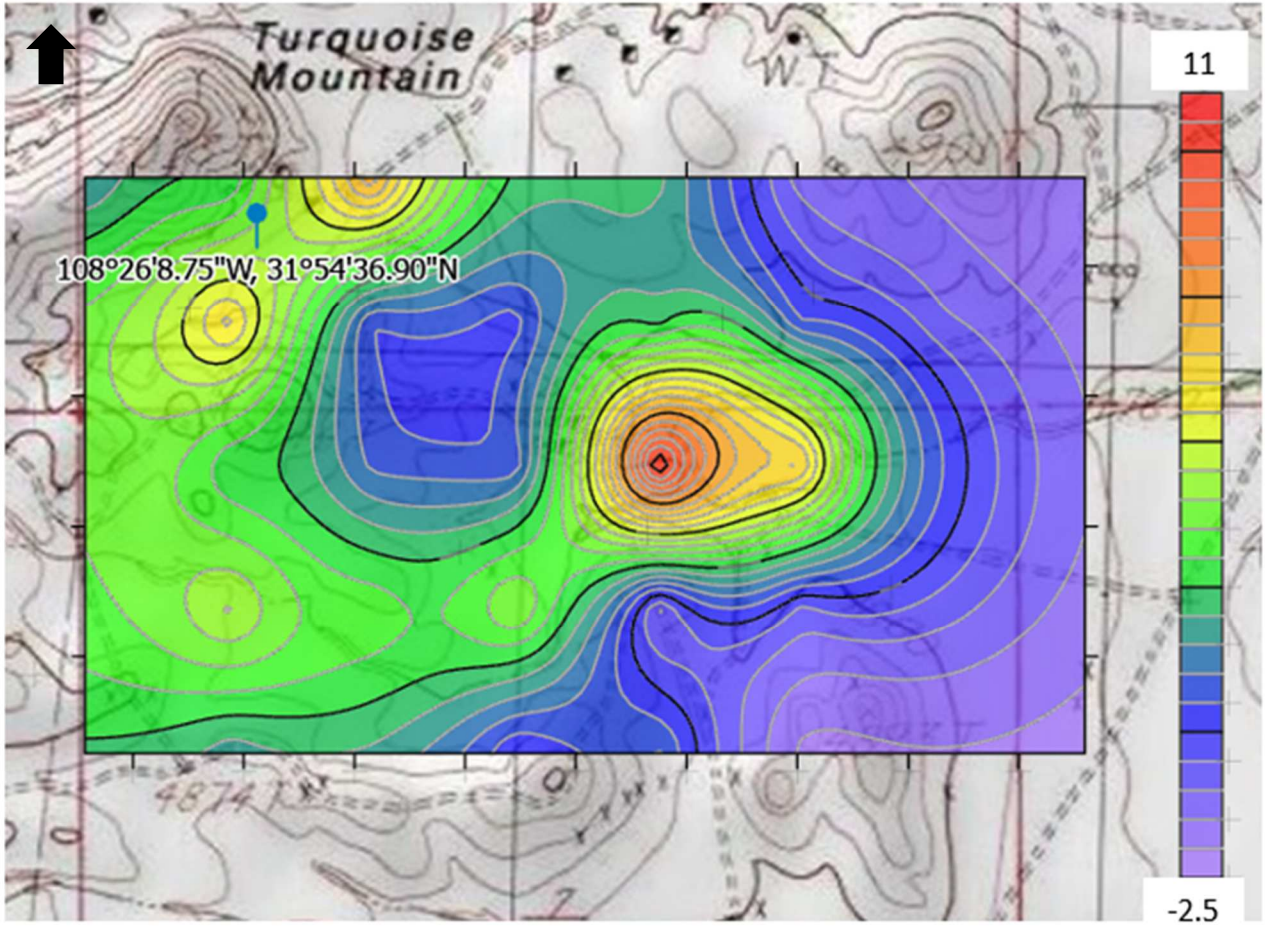


Figure A2.1.2. Eureka 40H showing a basin effect between the map anomaly highs of 10.7 mS/m and a depth profile of 120 ft.

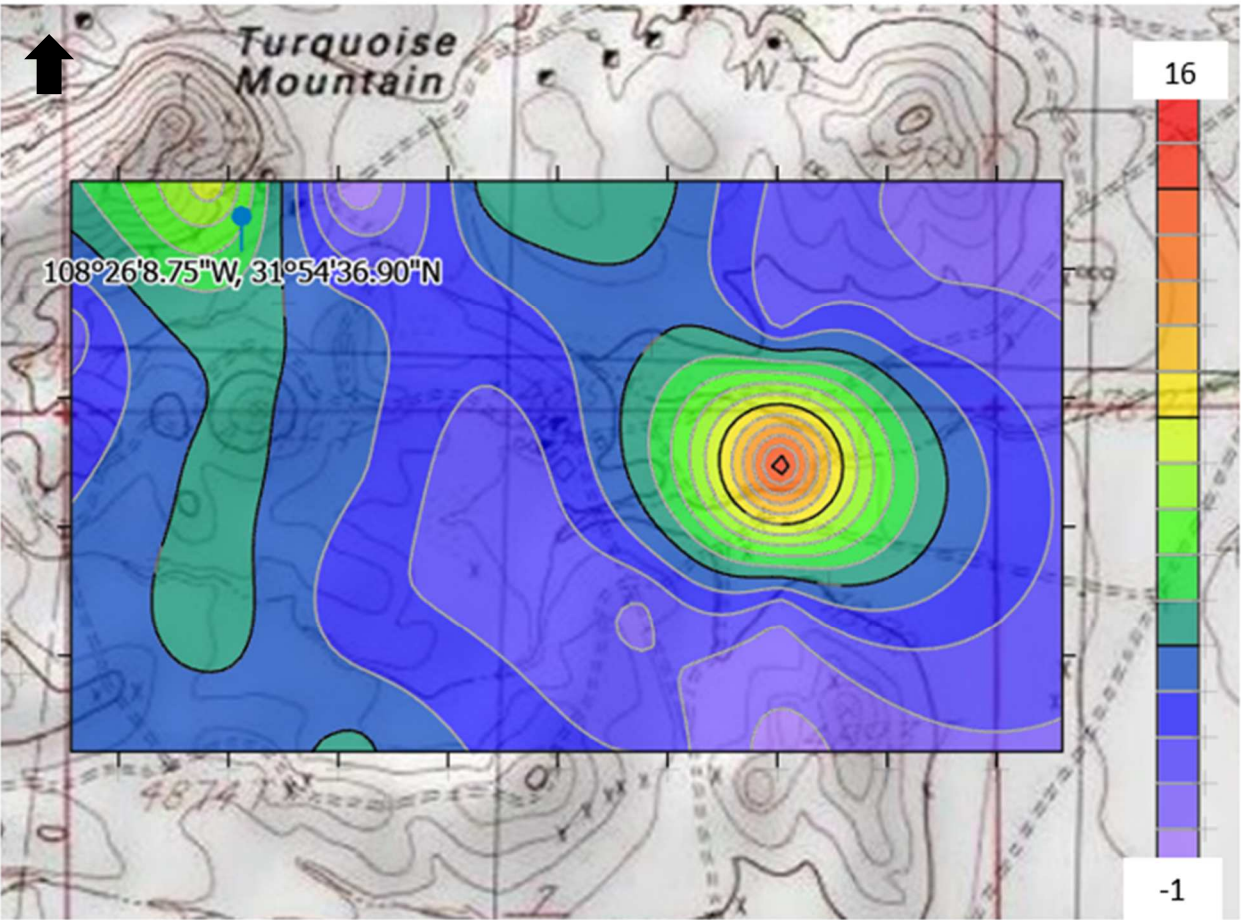


Figure A2.1.3. Eureka 20V showing the basin effect once again between the highs with the highest anomaly at 16 mS/m and a depth profile of 90 ft.

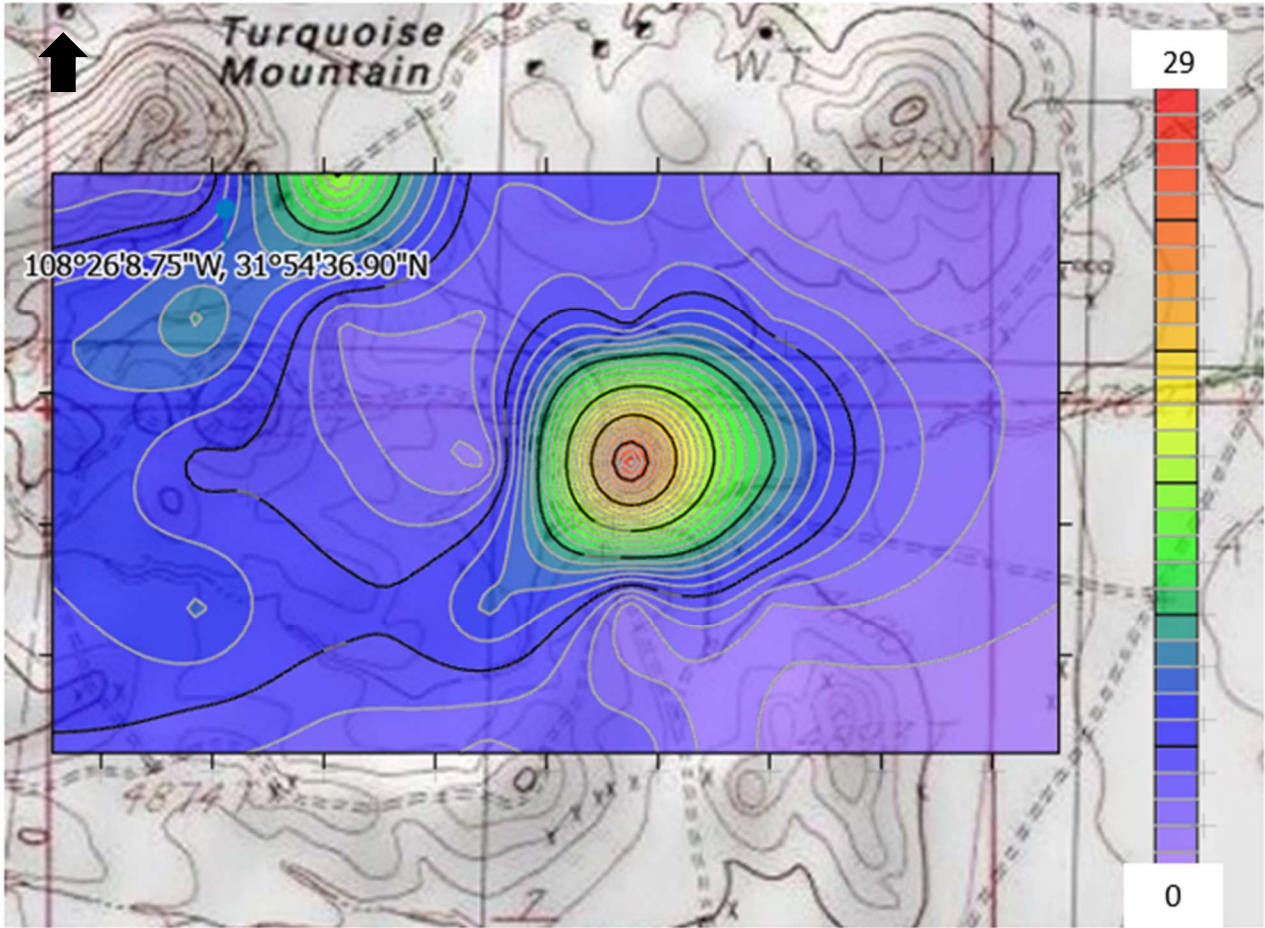


Figure A2.1.4. Eureka 20H has a basin effect like the 40H but clearly more defined considering the extreme high of 29 mS/m at a depth profile of 60 ft.

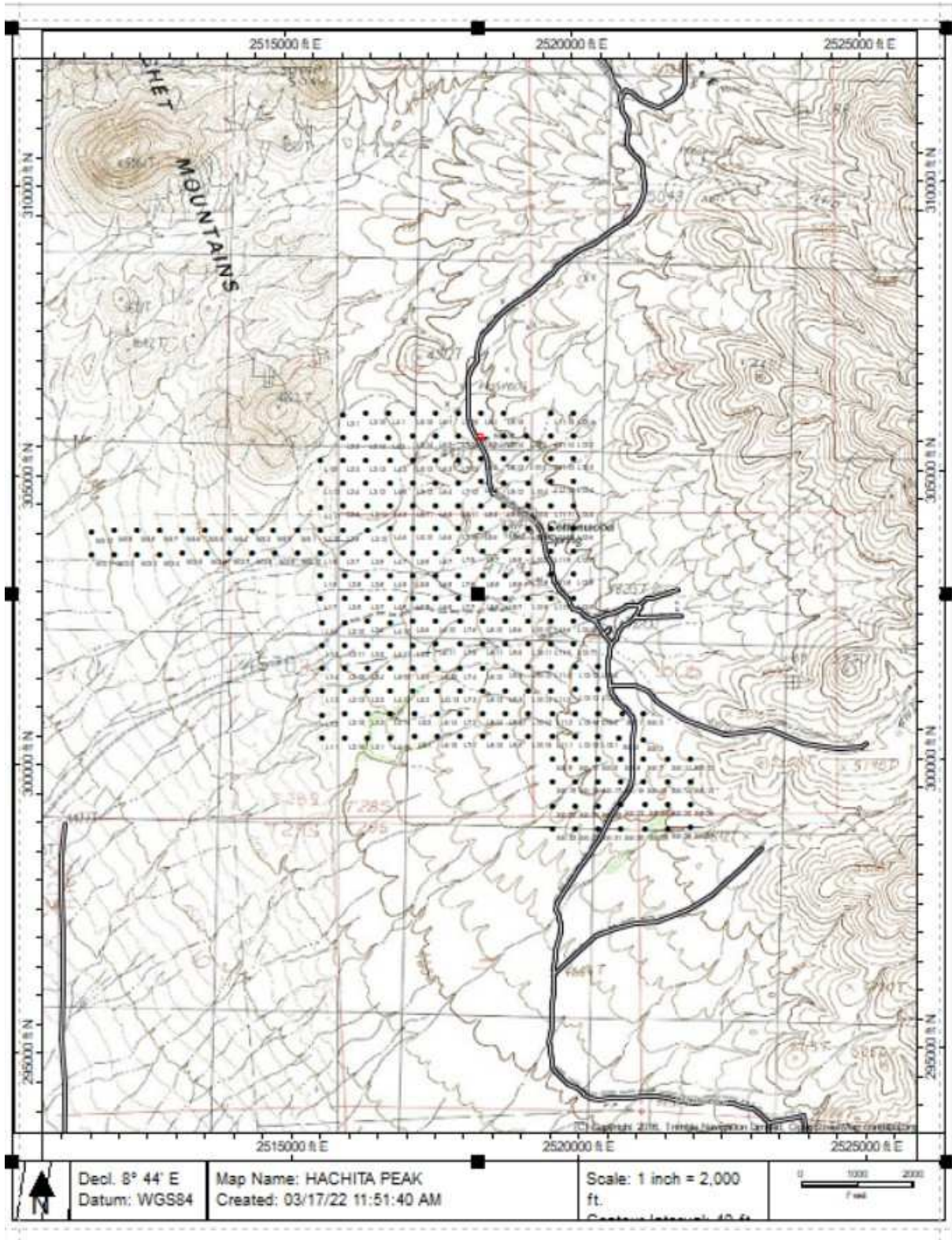


Figure A2.1.5. Sylvanite GDAP Layout map, for list of GDAPs evaluated see Appendix Table 2,

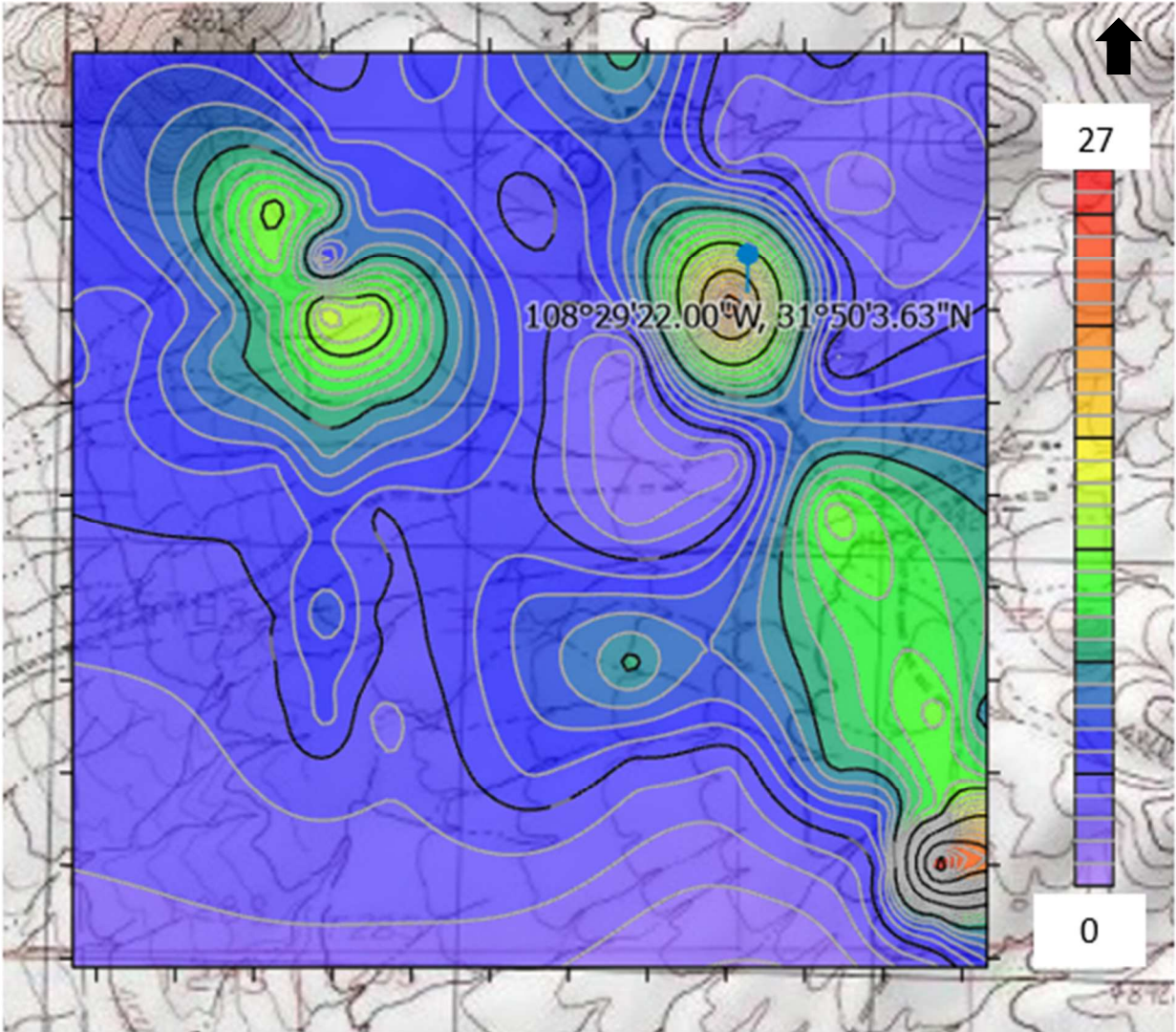


Figure A2.1.6. Sylvania 40H with a southeast to north trend with anomaly highs reaching 26.5 mS/m and a depth profile of 120 ft.

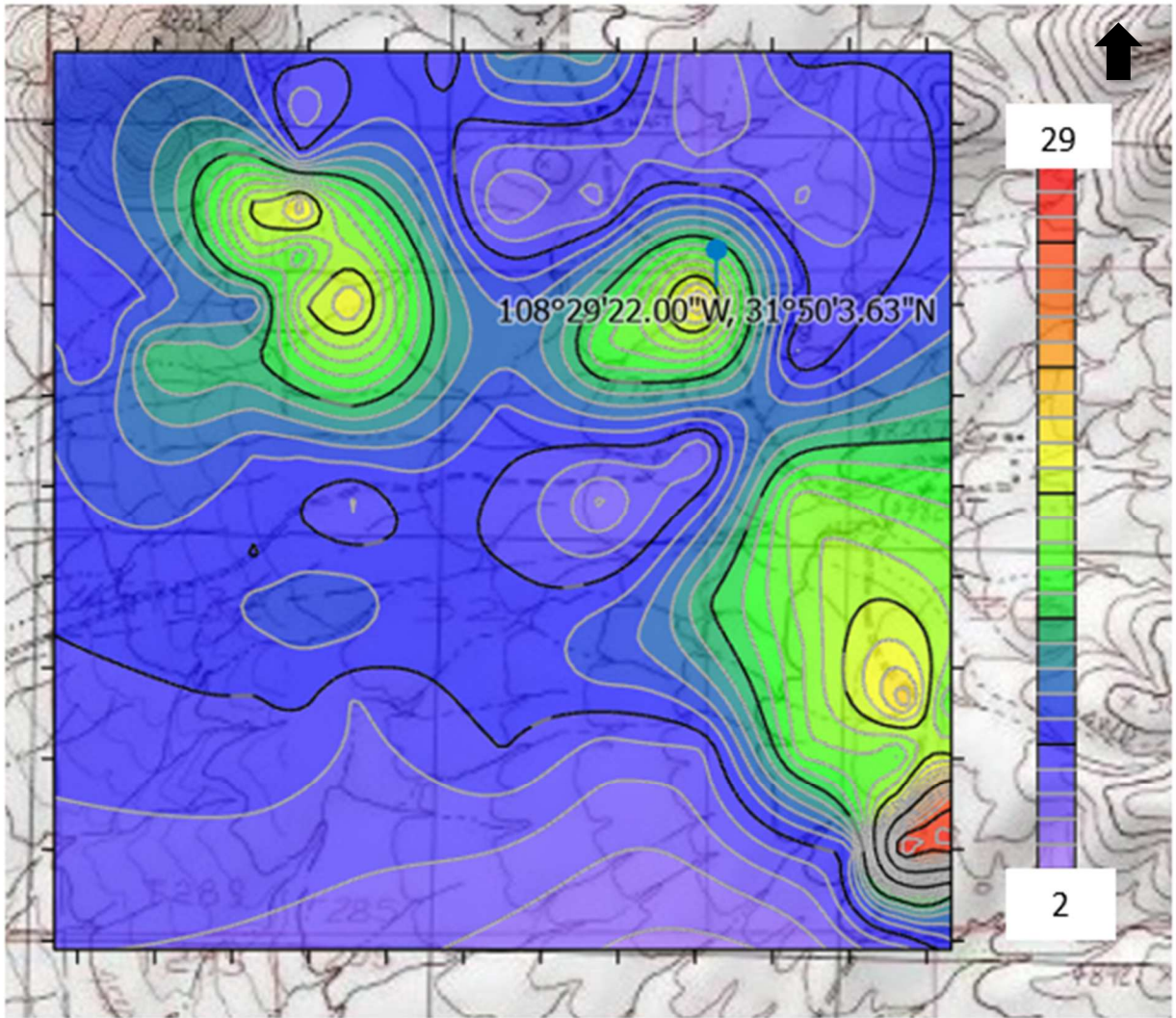


Figure A2.1.7. Sylvania 20V with southeast to north trend with anomaly highs reaching 29 mS/m and a depth profile of 90 ft.

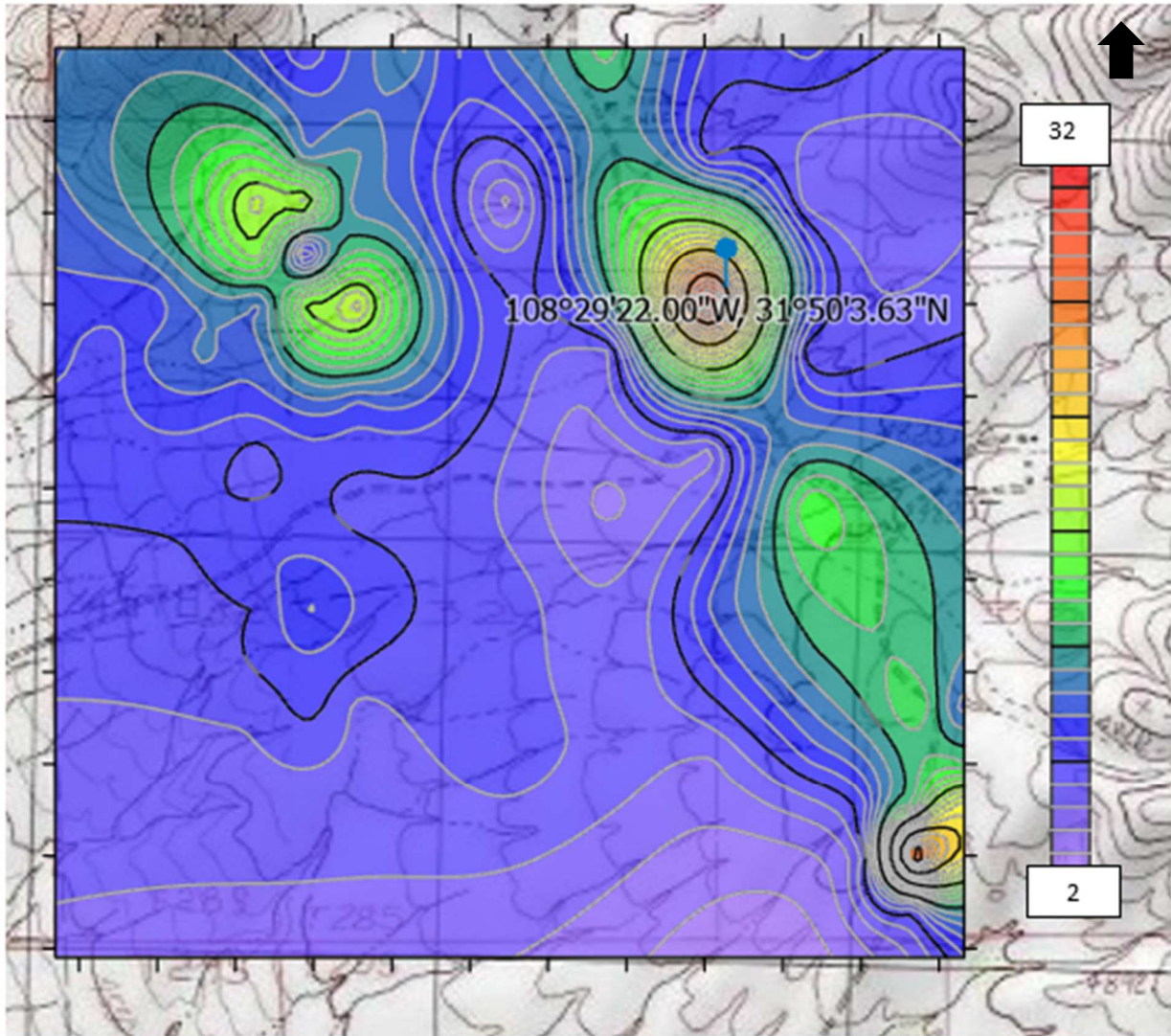


Figure A2.1.8. Sylvania 20H with southeast to north trend with anomaly highs reaching 32 mS/m and a depth profile of 60 ft.

Tables

Table A2.2.1, EMD Conductivity Readings (anomalies highlighted)

Line	40V (1/Ohms)	40H (1/Ohms)	20V (1/Ohms)	20H (1/Ohms)	Latitude	Longitude
E4-1	5.9	2.5	9.8	3.3	31.91131	-108.436
E4-2	3	6.2	5.3	9.3	31.90911	-108.436
E4-3	3.1	2.6	5.3	4.6	31.90691	-108.436
E4-4	5.8	4.6	5.5	7.2	31.90471	-108.436
E4-5	3.2	1.7	4.5	4	31.90251	-108.436
E5-2	1.7	1.9	5.3	3.3	31.90253	-108.434
E5-3	1.3	3.3	3.1	5.3	31.90472	-108.434
E5-4	0.4	0.9	4.2	4	31.90692	-108.434
E5-5	0.2	0.5	4.6	2.9	31.90912	-108.434
E5-6	-2.2	7.4	-0.2	15.5	31.91132	-108.434
E6-1	2	2.4	5.9	4.2	31.91133	-108.431
E6-2	1.5	0.3	3.3	2.9	31.90914	-108.431
E6-3	0.4	0.7	2.2	1.8	31.90694	-108.431
E6-4	-2.1	4.1	2.7	7.3	31.90474	-108.431
E6-5	1.8	0	3.8	2.7	31.90254	-108.431
E7-2	-0.3	1.1	3	3.9	31.90255	-108.428
E7-3	0.4	-1.1	1.8	1.1	31.90475	-108.429
E7-4	-7.6	10.7	5.5	29	31.90695	-108.429
E7-5	2.6	2.3	4.6	4	31.90915	-108.429
E7-6	0.5	2.2	6	4.9	31.91135	-108.429
E8-1	0.3	-1.2	2.8	1.3	31.91136	-108.426
E8-2	-1.4	0.5	2.5	3.9	31.90916	-108.426
E8-3	13.8	6.6	16	10.2	31.90696	-108.426
E8-4	-1.5	-0.6	2.3	1.8	31.90476	-108.426
E8-5	-1.7	-2.1	0.6	0.8	31.90256	-108.426
E3-6	7.4	1.5	5.8	3.1	31.9113	-108.439
E3-5	3	3.7	2.5	6.9	31.9091	-108.439
E10-1	-2.3	-1.7	2	1.9	31.90918	-108.421
E9-1	-0.6	-0.9	2.4	1.9	31.90917	-108.423

Table A2.2.2, SMD Conductivity Readings (anomalies highlighted)

Line	40V (1/Ohms)	40H (1/Ohms)	20V (1/Ohms)	20H (1/Ohms)	Latitude	Longitude
L1-1	3.7	3.4	5.7	4.9	31.82412	-108.501
L1-2	4.3	3.7	5.9	5.2	31.82522	-108.501
L1-3	4.8	4	6.5	6.3	31.82632	-108.501

L1-4	4.4	4	7.3	6	31.82742	-108.501
L1-5	3.3	4.6	5.9	6.9	31.82852	-108.501
L1-6	5	4.2	6.5	6.1	31.82962	-108.501
L1-7	6.8	5	7	5.5	31.83071	-108.501
L1-8	9.2	8.1	9.2	7.4	31.83181	-108.501
L1-9	16.4	10	10.9	8.5	31.83291	-108.501
L1-10	10.9	10.3	8	8.8	31.83401	-108.501
L1-11	7.3	13.5	14.4	15.8	31.83511	-108.501
L1-12	8.1	15	16.3	17.5	31.83621	-108.501
L1-13	5.8	9.4	11	13.7	31.83731	-108.501
L2-1	-0.8	2.8	6.5	6.2	31.83952	-108.5
L2-2	-0.8	4.7	4.2	8.3	31.83842	-108.5
L2-3	1.1	5.4	6	8.9	31.83732	-108.5
L2-4	5.2	12.3	19.1	17.7	31.83622	-108.5
L2-5	5.2	3.6	12.1	5.1	31.83512	-108.5
L2-6	16.1	17	15.9	16.6	31.83402	-108.5
L2-9	6.8	8	7.1	6.6	31.83072	-108.5
L2-12	14.1	7.1	7.8	8.2	31.82742	-108.5
L2-15	5.6	5.4	6.1	6.4	31.82522	-108.5
L4-1	6.7	5.8	6.8	10.2	31.83953	-108.498
L5-15	3.7	4.7	5.3	6.8	31.83954	-108.496
L6-1	2.3	6.5	9.3	9	31.83954	-108.495
L6-4	0	3.1	2.9	2.6	31.83625	-108.495
L6-8	7.5	4.8	7	5.6	31.83185	-108.495
L6-12	7.8	6.4	6.5	5.8	31.82745	-108.495
L6-15	6.5	5.3	6	5.6	31.82415	-108.495
L8-1	2.5	9.8	9.6	12.6	31.83956	-108.492
L8-4	-0.7	6.5	3.8	12.2	31.83628	-108.492
L8-7	4	1.4	13	4.9	31.83298	-108.492
L8-10	1.5	1.2	2.7	2.7	31.82966	-108.492
L8-13	12.2	9.5	8	4	31.82636	-108.492
L8-15	2.5	3.6	4.5	4.8	31.82416	-108.492
L10-1	1.2	3.5	2.9	6.9	31.83957	-108.49
L10-3	0.8	2.1	3.7	5.3	31.83737	-108.49
L10-6	5.5	26.5	19.5	32	31.83407	-108.49
L10-9	1.4	1.1	4	3.5	31.83077	-108.49
L10-12	8.9	7.1	10.8	8.2	31.82748	-108.49
L10-15	6.4	3	4.9	4	31.82418	-108.49
L12-1	2.2	4.5	6.4	7.4	31.83958	-108.487
L12-4	-1.2	1.7	3.9	4.2	31.83629	-108.487
L12-7	2.1	2.8	4.8	5	31.83299	-108.487
L12-10	3.2	13.9	14.9	14.2	31.82963	-108.487
L12-13	8.2	10.2	13.8	10.8	31.82639	-108.487

L12-15	12.9	9.6	13.6	7.5	31.82419	-108.487
SE-5	16.5	6.2	12.5	6.6	31.8231	-108.486
SE-6	17.8	12.2	16.7	11.9	31.8231	-108.485
SE-4	11.5	12.7	12.8	11.6	31.82409	-108.485
SE-1	11.3	13.6	20	13.1	31.82529	-108.485
SE-2	12	8.2	13	8.5	31.82526	-108.483
SE-3	7.7	11.1	16.2	12	31.82402	-108.483
SE-7	12.2	18.6	25.5	19.5	31.82311	-108.483
SE-15	5.1	25.5	27.1	20.4	31.82201	-108.483
SE-16	11.3	32	29	28.8	31.822	-108.485
SE-17	9.5	5.1	6.6	5.1	31.822	-108.486
SE-23	17.5	8.1	11	6.7	31.82091	-108.485
SE-24	7.2	10.3	10	10.9	31.82091	-108.483
SE-30	6.4	2.8	4.6	4.2	31.81981	-108.485
L3-2	4.1	2.6	4.9	4.7	31.82523	-108.499
L3-4	3.3	3.8	7.7	6.9	31.82743	-108.499
L3-6	5.1	3.8	4.8	5.5	31.82963	-108.499
L3-8	12.3	8.5	11.2	7.7	31.83183	-108.499
L3-10	12.2	15.9	18.1	18.8	31.83403	-108.499
L3-12	7.3	5.6	13.3	9.4	31.83623	-108.499
L3-13	3	5.3	8.7	10.2	31.83733	-108.499
W1-1	8.2	7	7.9	9.2	31.83401	-108.503
W1-2	6.2	5.1	7	7.2	31.834	-108.504
W1-3	4.5	4.7	6.5	7.5	31.83401	-108.505
W2-7	6.4	5.3	7.2	7.4	31.83289	-108.507
W2-8	6.7	4.5	6.3	6.3	31.83289	-108.505
W2-9	8.1	6.8	11	8.6	31.8329	-108.504
W2-10	10.6	8.9	10.7	9.3	31.83291	-108.503

Flow Charts

A2.3.1. Equipment Set-up and Null (kdjonesinstruments.com/files/2020/07/EM34-manual-013113.pdf.)

At the beginning of the survey select an area free of "cultural interference" and man-made conductors such as buried pipes, buildings, power lines, steel reinforced concrete, etc.



Having determined the coil separation to be used for the survey, lay the instrument out on the ground accordingly. Connect the reference cable (10, 20 or 40 meters) - one end to the 8-pin connector on the transmitter (Tx) coil and the other end to the "REFERENCE" connector on the receiver console. See attached sketch (page 17) for proper use of thimbles and snaps on the cable.



Connect the transmitter console to the transmitter coil using the appropriate short cable.



Put the "LEVEL" switch on the transmitter console to the "NORMAL" position.



Set the receiver and transmitter coils to the selected coil separation with red circles on the coils both facing in the same direction.



Set transmitter "SEPARATION" switch to selected value and turn on transmitter ("POWER/ON")



Check to see that Battery Monitor Meter indicator on the transmitter console is in the green area of the scale. If not, batteries are low or are not making proper contact to the battery clips. During the transmitter battery check transmitter coil has to be far from metal objects including concrete floor.



To check receiver battery switch the "SEPARATION" switch to "BATT" positions and power switch to "POWER ON" position. The digital meter, on the right side of the front panel, will indicate the condition of the two sets of receiver batteries. If the reading is below the 4.5 (V) check that the battery contacts are clean and rigid. Replace contacts and/or batteries if required. With new batteries, meter reading should be in the range of 6.00 (V).



If after replacement of set of receiver batteries, or check of the battery holder contacts, digital meter still does not register battery level, it is possible that the digital meter or associated components are malfunctioning.



Set receiver "SEPARATION" switch to selected value.



To remove any offsets in the output (DC) circuitry. Leave equipment set up and transmitter on. For the nulling, set coils at the largest separation (10, 20 or 40 m) at which the instrument will be used at the site.



Turn on receiver ("POWER/ON" switch to "ON" **position**).



With receiver coil disconnected and "SENSITIVITY RANGE" switch set to 1000mS/m depress "NULL" push button switch. Both meter readings should go to zero.



If either meter is not at zero reading, release the lock on the appropriate "NULL" control potentiometer, by turning the lock nut on the "NULL" control anti-clockwise for one turn. Keeping the "NULL" switch depressed adjust the "NULL" control to zero the meter.



Lock the "NULL" control. Connect the receiver coil to the receiver console "COIL" connector via the appropriate short cable.

Electrical Resistivity

Figures

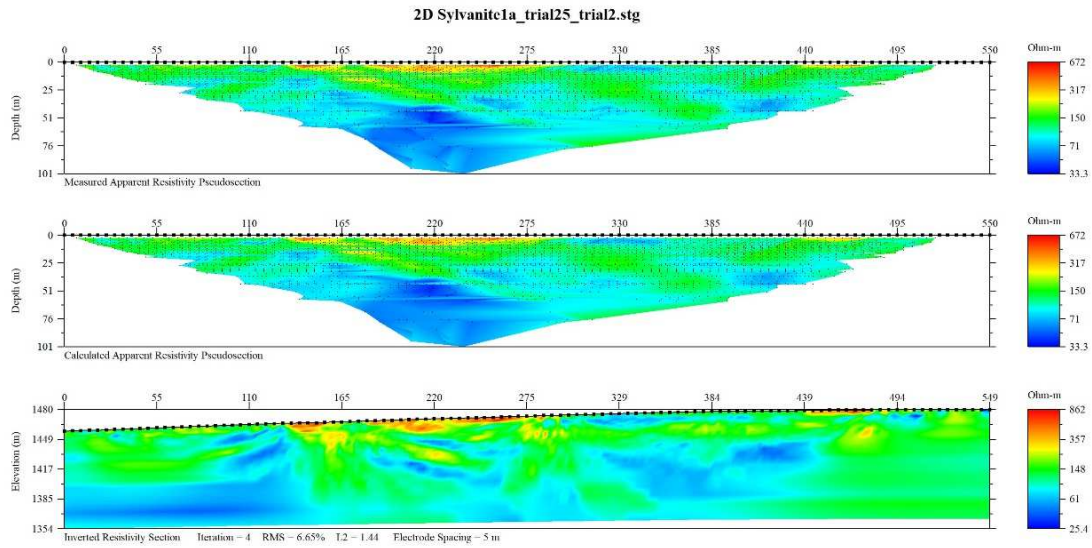


Figure A3.1.1. South to north electrical resistivity survey models, resistivity readings in Ohms/m.

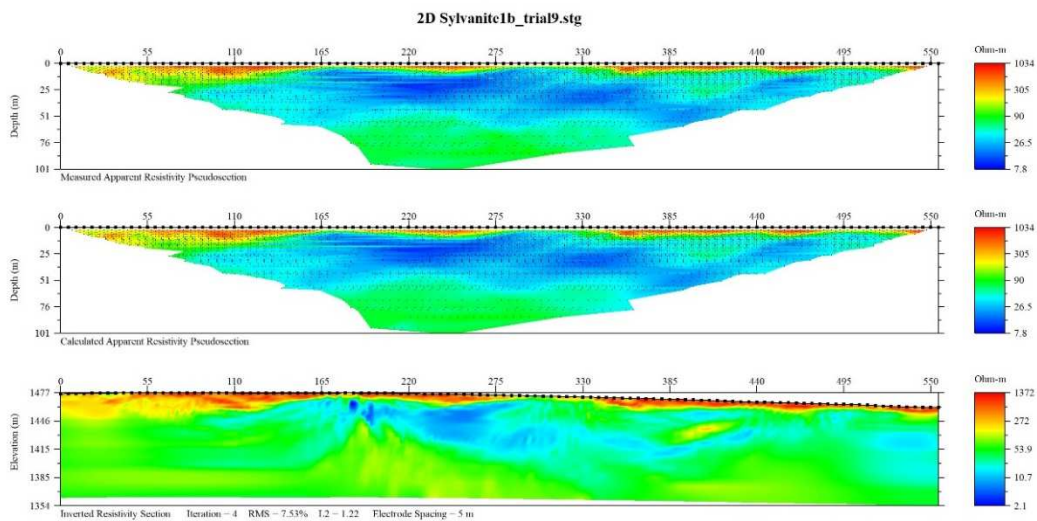
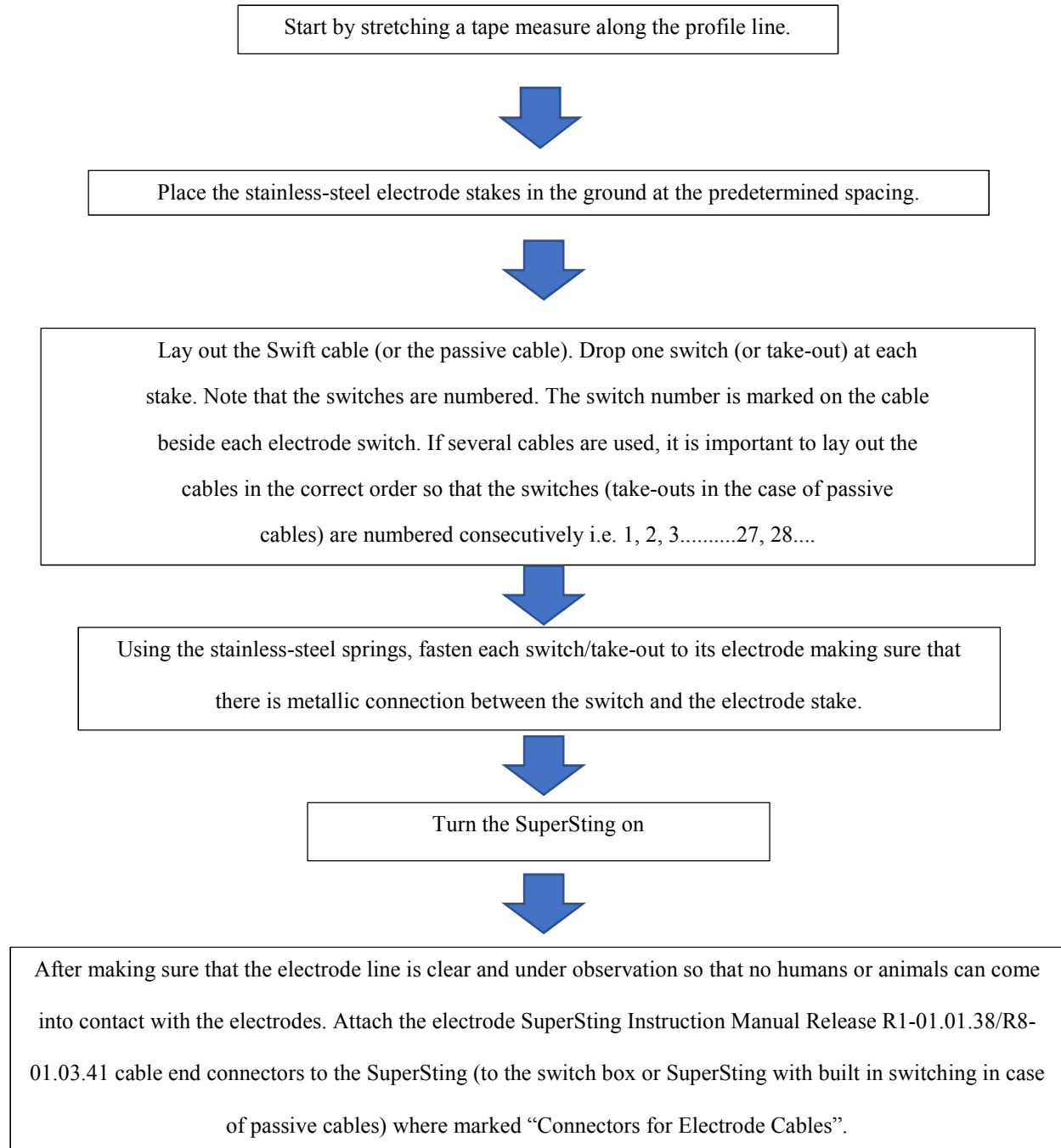


Figure A3.1.2. Southeast to northwest electrical resistivity survey models, resistivity readings in Ohms/m.

Flow Charts

A3.2.1 SuperSting R8 Field Set-up

(kdjonesinstruments.com/files/2020/07/SuperStingManual.pdf)





When using the dual mode Swift system with the SuperSting, the instrument can be connected at either end of the cable lay-out; however it is preferred to connect the instrument in the middle. By connecting in the middle, the effect of voltage drop in the cables is minimized. When using the SuperSting with switch box and passive system it is necessary always to put the instrument with switch box in the middle of the electrode spread where the instrument is connected in either end of the electrode cable.

A3.3.2. Create and run a terrain file (pdfcoffee.com/earth-imager-2-d-manual-3-pdf-free.html)

Use Garmin 60CSx to collect coordinates and elevation at each electrode



Download electrode number, coordinates, and elevation to Excel file



Make a txt file using Notepad including electrode position designation by meters (i.e. 5, 10, 15, 20, etc.) along the survey line as first column and the elevation as the second column



Save as a txt file



Click the Read Data button, e.g., 2D Sylvanite1.stg



Modify inversion settings if you desire. Default surface settings are a safe option for surface data.



Click File/Read Terrain File, e.g., 2D Sylvanite1.stg



Click the green Start Inversion button.

A3.3.3. Removal of poorly-fit data (pdfcoffee.com/earth-imager-2-d-manual-3-pdf-free.html)

At the end of inversion, the user can display a data misfit histogram by choosing View | Convergence and Data Misfit | Data Misfit Histogram.



The horizontal axis shows the absolute value of the relative data misfit that is defined as the ratio the difference between the calculated and measured data to the measured data (apparent resistivity).



In general, any data with a relative data misfit greater than 50% may be considered as a poorly fit data and should be removed. The user should also take the error distribution into consideration. In the figure below, 36% can be used as the removal threshold that is represented with a vertical blue line. The data with a misfit larger than the threshold will be removed after clicking the Remove button.



To set a removal threshold, the user may any of the arrow keys (Left, Right, Up and Down). The Left and Down arrow keys will decrease the threshold. The status bar at the bottom shows the number of data to be removed, and total number of data points.



To remove poorly fit data, set an appropriate misfit threshold, and click the Remove button, and then Start Inversion again. If the user clicks the Cancel button, the threshold selection will have no effect in the following inversion.

Mineral Spectroscopy

Figures (highlights indicate wavelength type and mineral name)

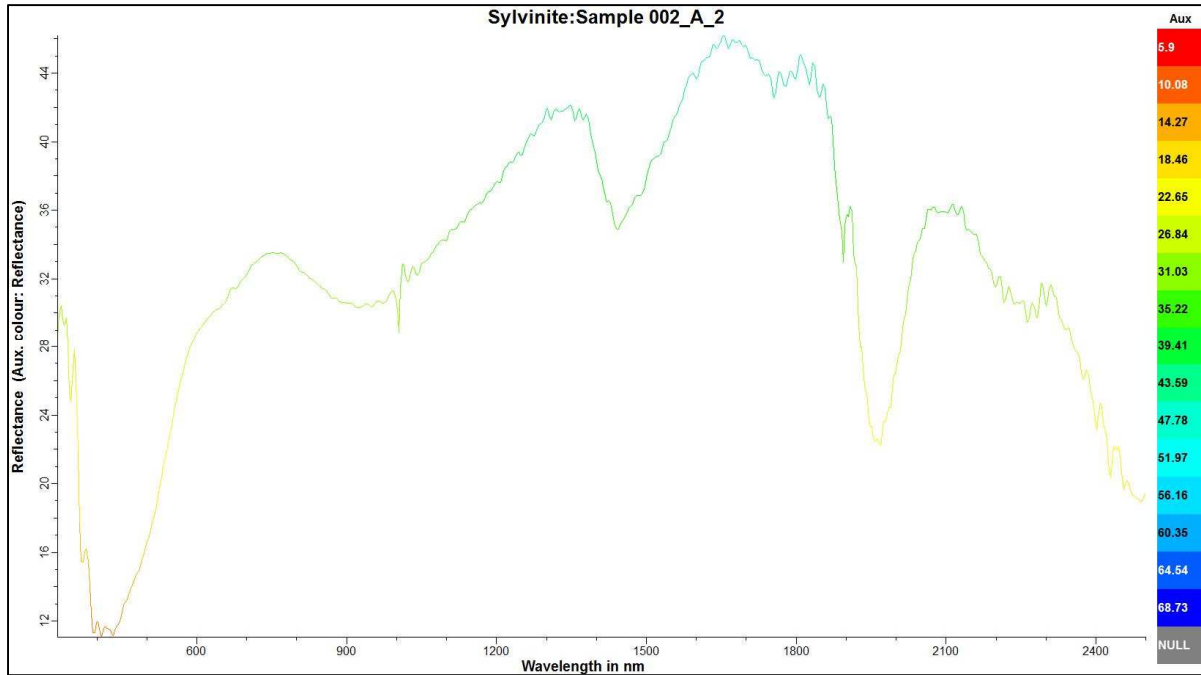


Figure A4.1.1-Sylvanite: Sample 002_A_2; Standard wavelength (CSV import data) with slight modifications.

Graph created using The Spectral Geologist 8.0.7.4. software.

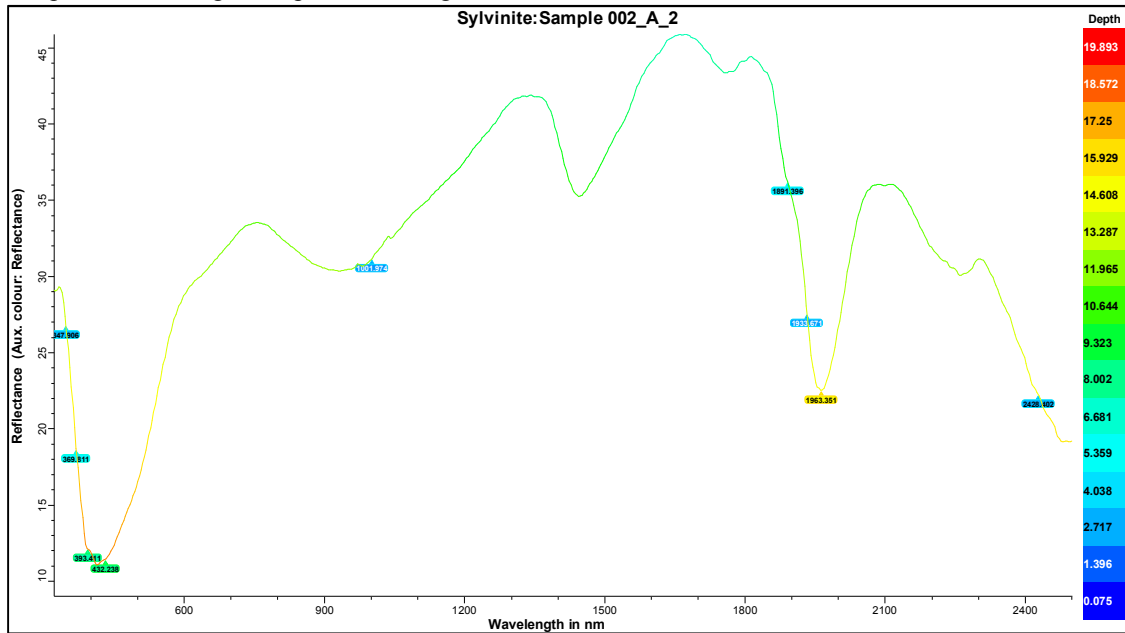


Figure A4.1.2- Sylvanite: Sample 002_A_2; Modified wavelength with feature wavelength (number tags) and smooth (Hi). Graph created using The Spectral Geologist 8.0.7.4. software.

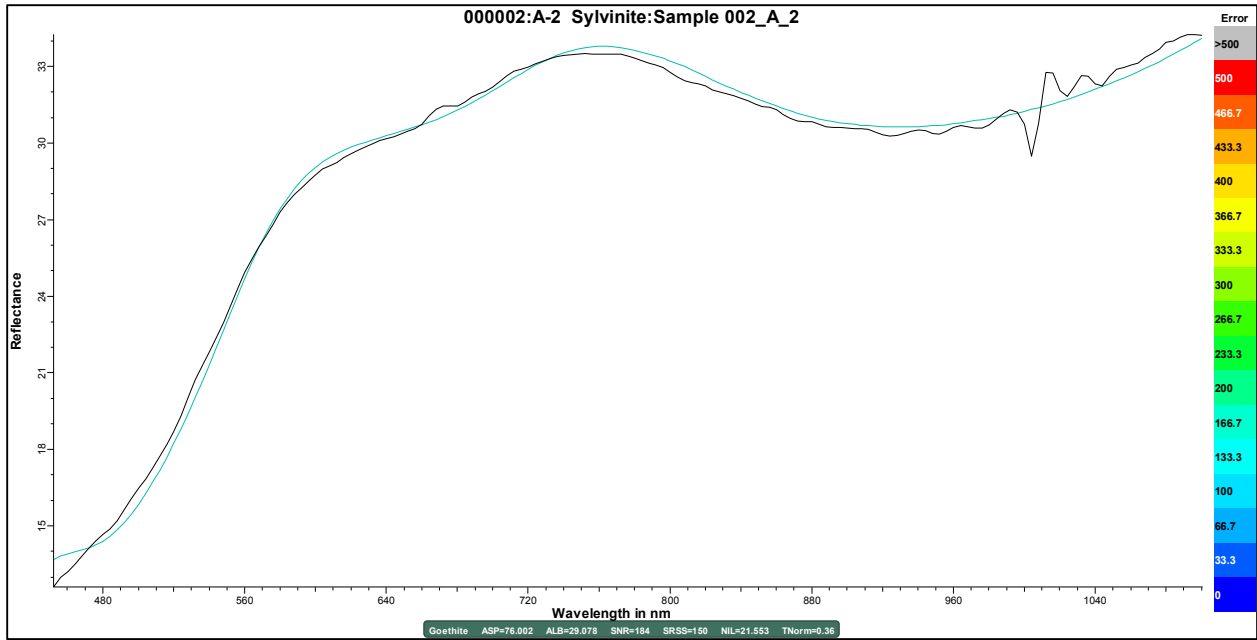
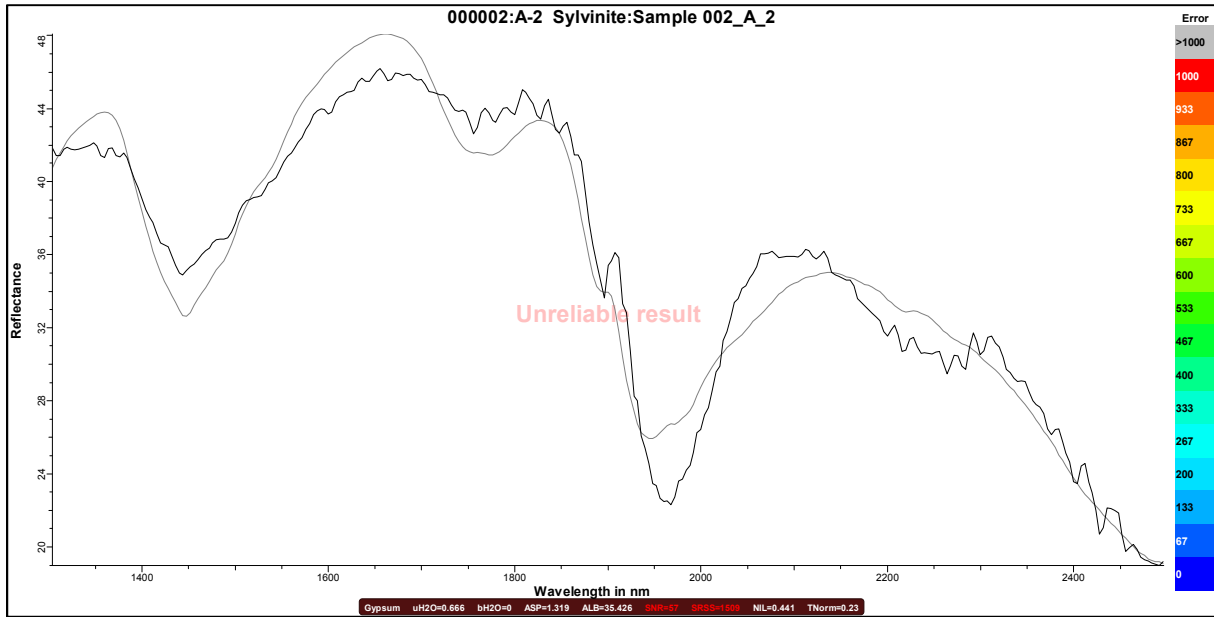


Figure A4.1.3- Sylvanite: Sample 002_A_2; (Goethite) results are in the visible and near-infrared (VNIR). Graph created using The Spectral Geologist 8.0.7.4. software. Blackline represent result spectra using the GER 3700 in direct comparison with the spectral geologist spectral (ASCII) library files (blue) line.

Candidate TSA results	
*Goethite	[150]
Goethite	[860]
Hematite	[1466]
Vegetation-Green	[3934]
86%Goethite + 14%Hematite	[127]
65%Goethite + 35%ODZincalume	[138]
99%Goethite + 1%Vegetation-Green	[150]
100%Goethite + 0%GalvanisedIron	[150]
61%Goethite + 39%Hematite	[445]
94%Goethite + 6%Vegetation-Green	[804]
88%Hematite + 12%Vegetation-Green	[1254]
86%Hematite + 14%GalvanisedIron	[1460]

Figure A4.1.4- Sylvanite: Sample 002_A_2; (Goethite) The Spectral Geologist (ASCII) library list of other possible candidates. Closest candidate is denoted by an Astrid symbol (*Goethite [150]) according to the ASCII library.



FigureA4.1.5- Sylvanite: Sample 002_A2: Gypsum [1509]. Results are in the Short-Wave Infrared (SWIR). Graph created using The Spectral Geologist 8.0.7.4. software. Blackline represent result spectra using the GER 3700 in direct comparison with the spectral geologist spectral (ASCII) library files (blue) line.

Candidate TSA results	
*Gypsum [1509]	71%Gypsum + 29%Pyrophyllite [1464]
Alunite-K [1801]	81%Gypsum + 19%YellowMarker [1468]
Alunite-Na [1907]	73%Gypsum + 27%Alunite-K [1470]
Pyrophyllite [1941]	52%Gypsum + 48%Magnesite [1476]
Kaolinite-WX [1953]	60%Gypsum + 40%Phengite [1476]
Dickite [1955]	82%Gypsum + 18%IsaWhite [1478]
IsaYellow [1957]	59%Gypsum + 41%Kaolinite-WX [1480]
Nacrite [1957]	80%Gypsum + 20%IsaYellow [1480]
YellowMarker [1958]	80%Gypsum + 20%WhiteMarker [1481]
Phengite [1959]	69%Gypsum + 31%Dickite [1487]
IsaWhite [1964]	65%Gypsum + 35%Nacrite [1490]
Magnesite [1966]	88%Gypsum + 12%Topaz [1491]
Siderite [1967]	57%Gypsum + 43%Phengite [1493]
Ankerite [1971]	57%Gypsum + 43%Chlorite-FeMg [1494]
Topaz [1974]	94%Gypsum + 6%PlasticChipTray [1494]
Alunite-NH [1974]	86%Gypsum + 14%Tourmaline [1496]
Phengite [1975]	77%Gypsum + 23%Talc [1497]
Jarosite [1977]	70%Gypsum + 30%Muscovite [1502]
Chlorite-Fe [1980]	54%Gypsum + 46%Chlorite-FeMg [1502]
PlasticChipTray [1981]	83%Gypsum + 17%Kaolinite-PX [1505]
Muscovite [1981]	80%Gypsum + 20%Muscovite [1505]
72%Chlorite-Fe + 28%Gypsum [1447]	
67%Chlorite-Fe + 33%Gypsum [1456]	

Figure A4.1.6- (Gypsum)The Spectral Geologist (ASCII) library list of other possible candidates. Closest candidate is denoted by an Astrid symbol (*Gypsum [1509]) according to the ASCII library.

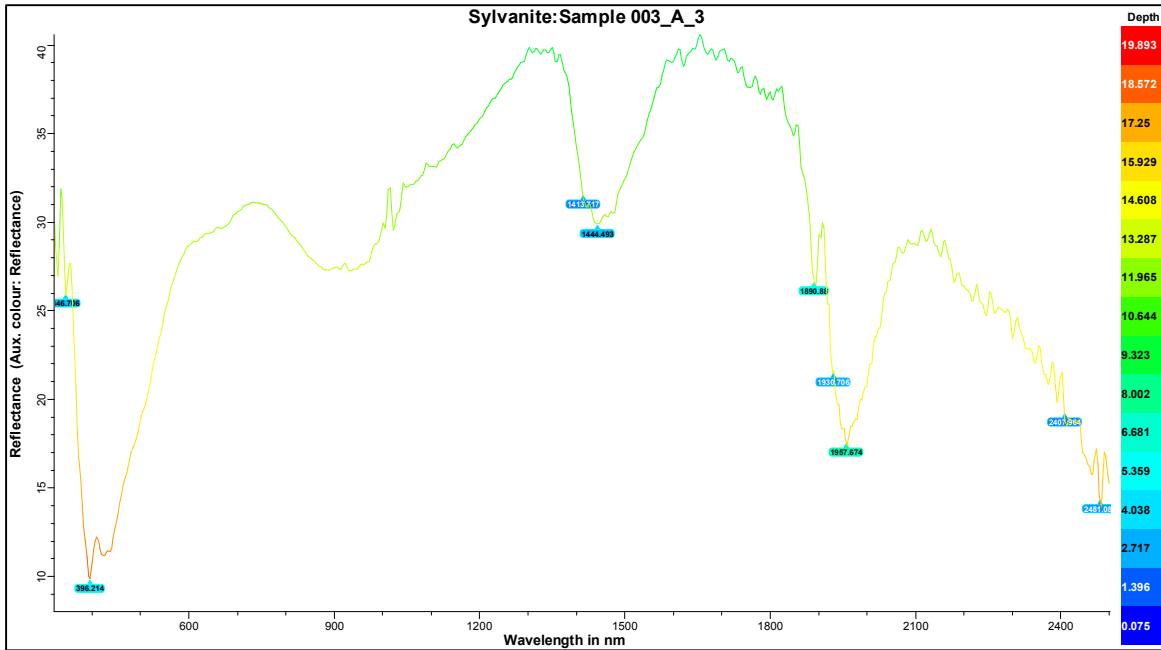


Figure A4.1.7-Sylvanite: Sample 003_A_3; Standard wavelength (CSV import data) with slight modifications. Graph created using The Spectral Geologist 8.0.7.4. software.

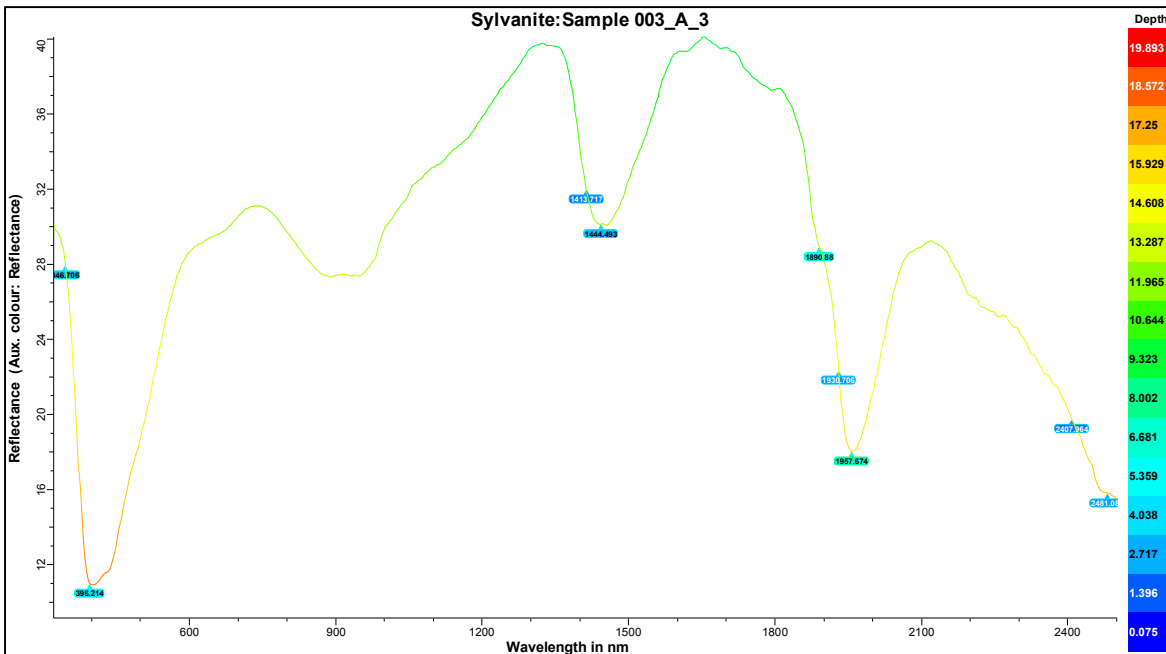


Figure A4.1.8- Sylvanite: Sample 003_A_3; Modified wavelength with feature wavelength (number tags) and smooth (Hi). Graph created using The Spectral Geologist 8.0.7.4. software.

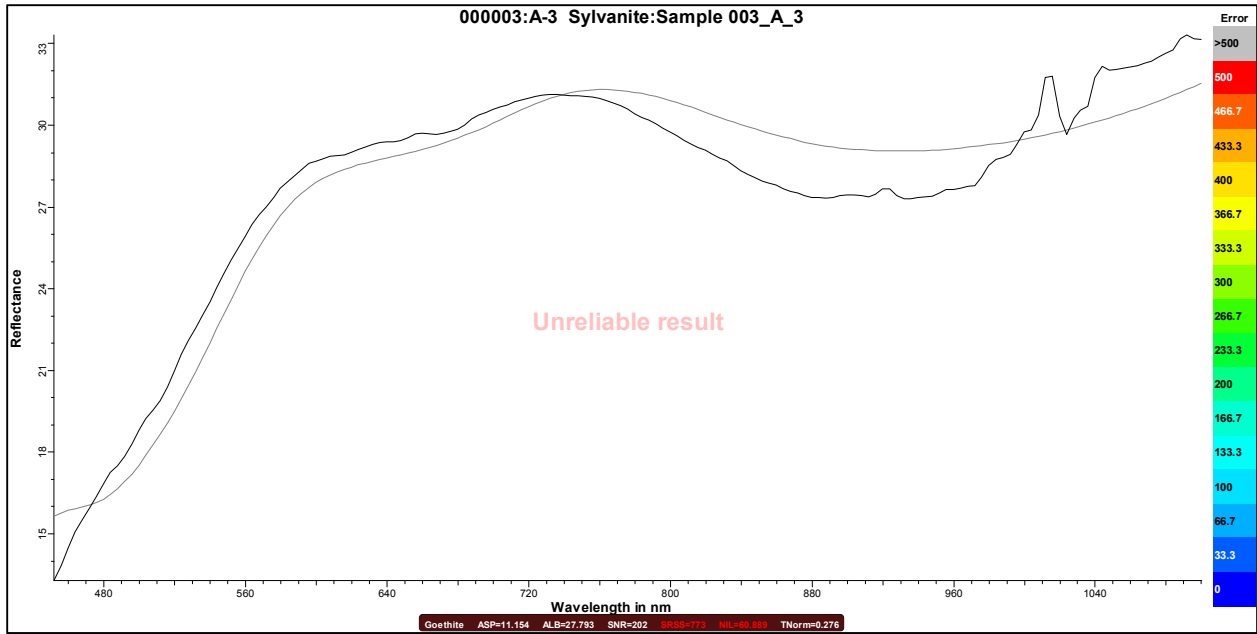


Figure A4.1.9- Sylvanite: Sample 003_A_3; (Goethite) results are in the visible and near-infrared (VNIR). Graph created using The Spectral Geologist 8.0.7.4. software. Blackline represent result spectra using the GER 3700 in direct comparison with the spectral geologist spectral (ASCII) library files (blue) line.

Candidate TSA results	
*Goethite	[773]
Hematite	[1118]
Goethite	[1228]
Vegetation-Green	[3577]
76%ODZincalume + 24%Goethite	[415]
59%Goethite + 41%Hematite	[612]
53%Hematite + 47%Goethite	[675]
64%Goethite + 36%GalvanisedIron	[733]
55%Hematite + 45%GalvanisedIron	[996]
95%Hematite + 5%Vegetation-Green	[1080]
56%ODZincalume + 44%Goethite	[1152]
96%Goethite + 4%Vegetation-Green	[1212]
81%ODZincalume + 19%Vegetation-Green	[3455]

Figure A4.1.10- Sylvanite: Sample 003_A_3; (Goethite) The Spectral Geologist (ASCII) library list of other possible candidates. Closest candidate is denoted by an Astrid symbol (*Goethite [773]) according to the ASCII library.

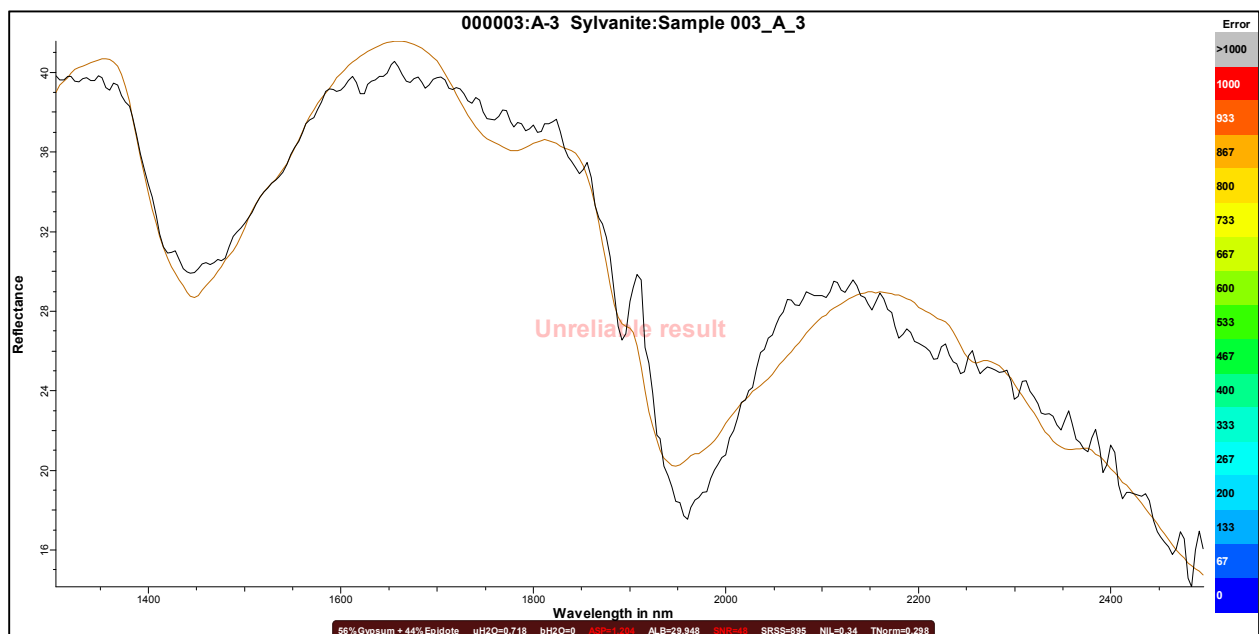


Figure A4.1.11- Sylvanite: Sample 003_A_3: Gypsum 56% and 44% Epidote [895]. Results are in the Short-Wave Infrared (SWIR). Graph created using The Spectral Geologist 8.0.7.4. software.

Candidate TSA results	
Gypsum [932]	79%Gypsum + 21%IsaWhite [915]
65%Ankerite + 35%Gypsum [879]	56%Chlorite-Mg + 44%Gypsum [918]
*56%Gypsum + 44%Epidote [895]	65%Gypsum + 35%Dickite [920]
73%Siderite + 27%Gypsum [895]	79%Gypsum + 21%IsaYellow [921]
69%Gypsum + 31%WhiteMarker [897]	51%Riebeckite + 49%Gypsum [921]
52%Gypsum + 48%Dolomite [901]	69%Gypsum + 31%Jarosite [921]
72%Gypsum + 28%Tourmaline [902]	61%Gypsum + 39%Serpentine [922]
52%Gypsum + 48%Zoisite [905]	56%Chlorite-FeMg + 44%Gypsum [923]
73%Chlorite-FeMg + 27%Gypsum [906]	58%Chlorite-Fe + 42%Gypsum [923]
79%Gypsum + 21%Topaz [906]	65%Gypsum + 35%Nacrite [925]
56%Magnesite + 44%Gypsum [907]	59%Chlorite-Fe + 41%Gypsum [925]
55%Gypsum + 45%Calcite [911]	52%Ankerite + 27%Alunite-NH + 21%Gypsum [838]
57%Gypsum + 43%Alunite-NH [913]	
79%Gypsum + 21%YellowMarker [913]	
57%Chlorite-FeMg + 43%Gypsum [913]	
53%Gypsum + 47%Kaolinite-WX [914]	

Figure A4.1.12- Sylvanite: Sample 003_A3: The Spectral Geologist (ASCII) library list of other possible candidates. Closest candidate is denoted by an Astrid symbol (*Gypsum [895]) according to the ASCII library. Gypsum 56% and 44% Epidote [895]. Results are in the Short-Wave Infrared (SWIR).

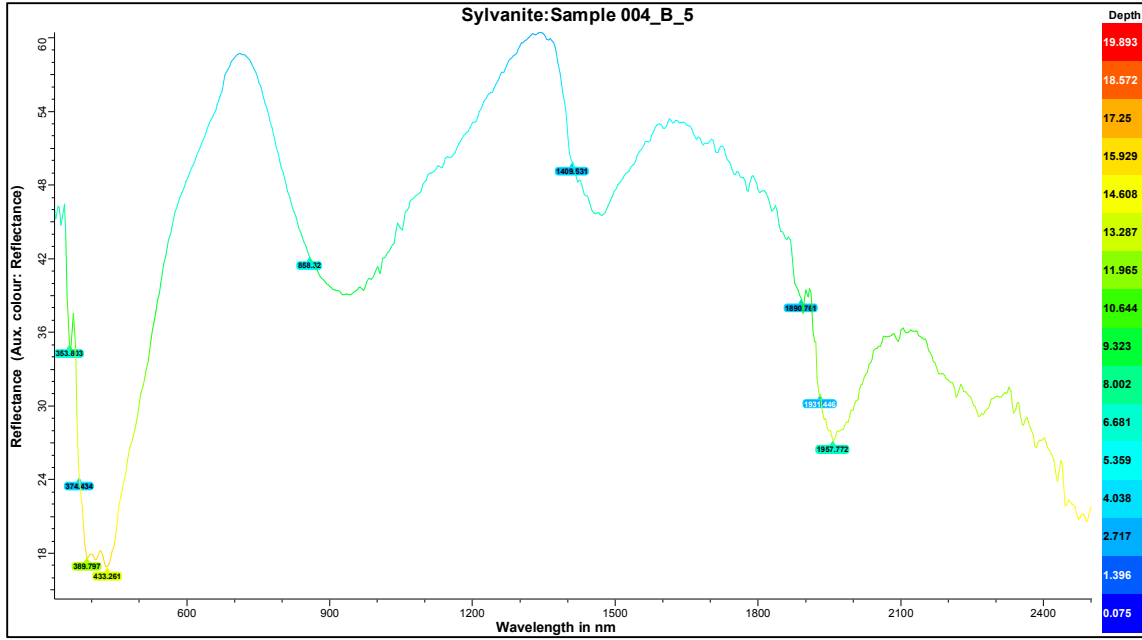


Figure A4.1.13-Sylvanite: Sample 004_B_5; Standard wavelength (CSV import data) with slight modifications.

Graph created using The Spectral Geologist 8.0.7.4. software.

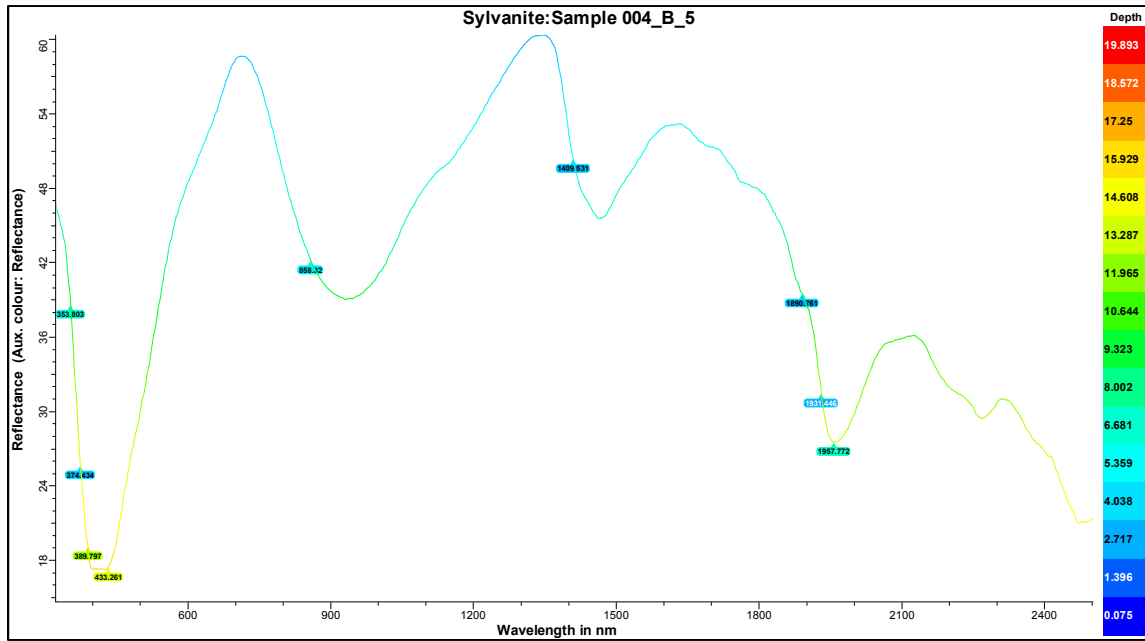


Figure A4.1.14-Sylvanite: Sample 004_B_5; Modified wavelength with feature wavelength (number tags) and smooth (Hi). Graph created using The Spectral Geologist 8.0.7.4. software.

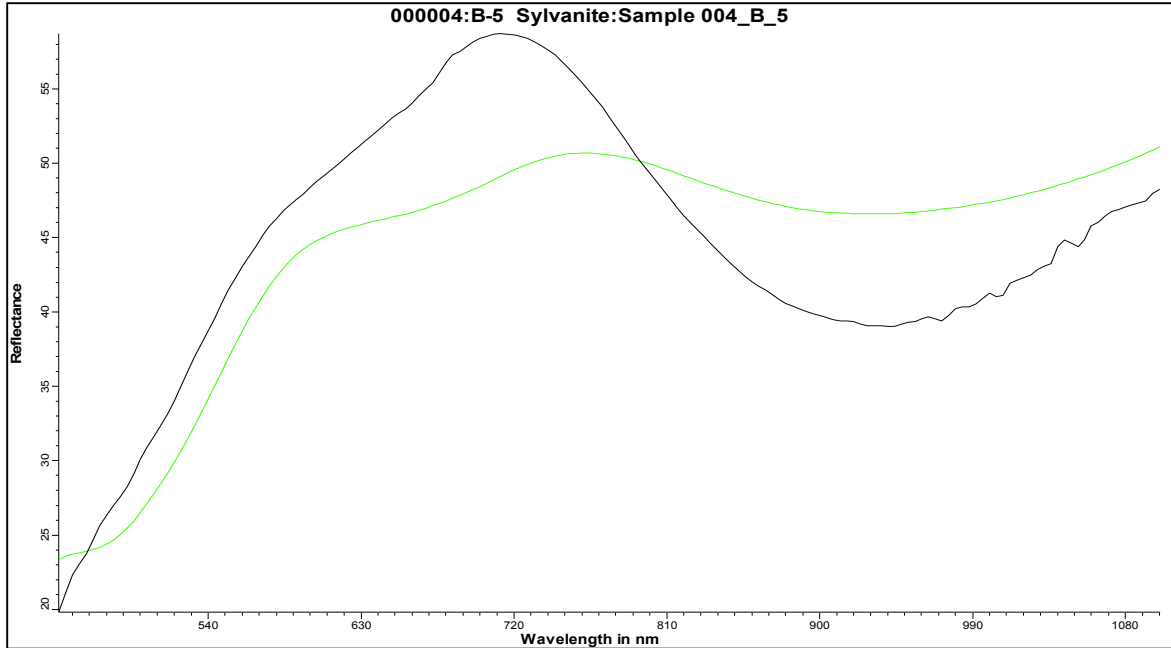


Figure A4.1.15- Sylvanite: Sample 004_B_5; (Goethite {1871}) results are in the visible and near-infrared (VNIR). Graph created using The Spectral Geologist 8.0.7.4. software. Blackline represent result spectra using the GER 3700 in direct comparison with the spectral geologist spectral (ASCII) library files (green) line.

Candidate TSA results	
*Goethite [1871]	
Goethite [2063]	
Hematite [2084]	
Vegetation-Green [5008]	
67%GalvanisedIron + 33%Hematite [1176]	
81%ODZincalume + 19%Goethite [1176]	
67%GalvanisedIron + 33%Goethite [1279]	
50%Goethite + 50%Hematite [1619]	
54%Goethite + 46%Hematite [1688]	
71%ODZincalume + 29%Goethite [1774]	
53%Goethite + 47%GalvanisedIron [1916]	
52%Hematite + 48%ODZincalume [2043]	
86%ODZincalume + 14%Vegetation-Green [4760]	
51%GalvanisedIron + 49%Vegetation-Green [4985]	

Figure A4.1.16- Sylvanite: Sample 004_B_5; (Goethite {1871}) The Spectral Geologist (ASCII) library list of other possible candidates. Closest candidate is denoted by an Astrid symbol (*Goethite [1871]) according to the ASCII library.

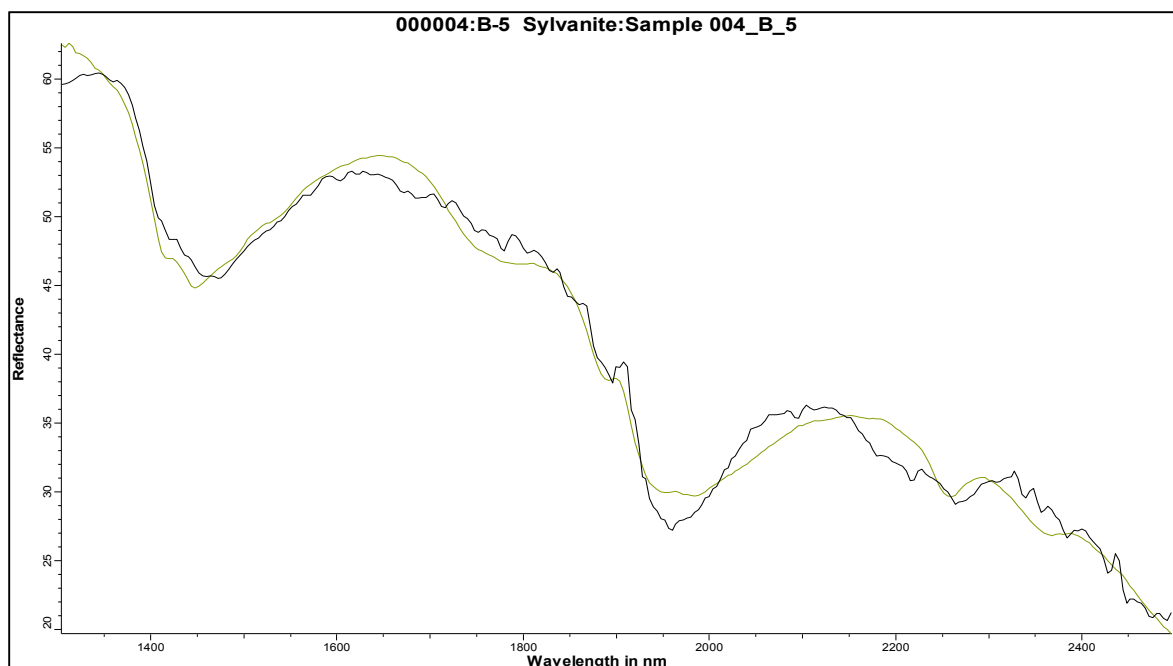


Figure A4.1.17- Sylvanite: Sample 004_B_5: Chlorite-Fe 84% and 16% Gypsum [387]. Results are in the Short-Wave Infrared (SWIR). Graph created using The Spectral Geologist 8.0.7.4. software.

Candidate TSA results	
63%Jarosite + 37%Gypsum [384]	59%Gypsum + 41%Epidote [434]
*84%Chlorite-Fe + 16%Gypsum [387]	69%Jarosite + 31%Epidote [434]
81%Chlorite-Fe + 19%Gypsum [392]	52%Jarosite + 48%Ankerite [434]
71%Chlorite-FeMg + 29%Gypsum [412]	52%Nacrite + 48%Gypsum [434]
81%Chlorite-FeMg + 19%Gypsum [413]	51%Serpentine + 49%Gypsum [435]
73%Chlorite-Mg + 27%Gypsum [414]	64%Chlorite-Fe + 19%Jarosite + 17%Gypsum [351]
67%Magnesite + 33%Gypsum [417]	43%Jarosite + 33%Dickite + 24%Gypsum [355]
58%Jarosite + 42%Dickite [420]	53%Chlorite-Mg + 28%Jarosite + 19%Gypsum [356]
69%Chlorite-Mg + 31%Gypsum [420]	50%Chlorite-FeMg + 29%Jarosite + 20%Gypsum [356]
77%Siderite + 23%Gypsum [420]	49%Chlorite-Mg + 30%Jarosite + 20%Gypsum [356]
53%Dickite + 47%Gypsum [422]	63%Chlorite-FeMg + 22%Jarosite + 16%Gypsum [361]
58%Kaolinite-WX + 42%Gypsum [427]	41%Jarosite + 36%Serpentine + 23%Gypsum [362]
53%Dolomite + 47%Gypsum [427]	46%Jarosite + 27%Talc + 27%Gypsum [363]
72%Chlorite-FeMg + 28%Gypsum [429]	52%Chlorite-FeMg + 30%Jarosite + 19%Gypsum [366]
61%Ankerite + 39%Gypsum [429]	43%Jarosite + 33%Nacrite + 24%Gypsum [366]
55%Gypsum + 45%Talc [430]	41%Jarosite + 34%Kaolinite-WX + 25%Gypsum [367]
76%Jarosite + 24%Alunite-K [430]	49%Jarosite + 28%Gypsum + 23%Epidote [368]
57%Jarosite + 43%Nacrite [431]	45%Jarosite + 29%Calcite + 25%Gypsum [368]
70%Chlorite-FeMg + 30%Gypsum [432]	62%Chlorite-Fe + 22%Magnesite + 16%Gypsum [370]
60%Jarosite + 40%Calcite [432]	47%Jarosite + 27%Gypsum + 26%Actinolite [371]
65%Siderite + 35%Jarosite [432]	49%Siderite + 31%Jarosite + 19%Gypsum [372]
61%Gypsum + 39%Gibbsite [432]	
50%Calcite + 50%Gypsum [433]	

Figure A4.1.18- Sylvanite: Sample 004_B_5: The Spectral Geologist (ASCII) library list of other possible candidates. Closest candidate is denoted by an Astrid symbol *Chlorite-Fe 84% and 16% Gypsum [387]. according to the ASCII library. Results are in the Short-Wave Infrared (SWIR). Graph created using The Spectral Geologist 8.0.7.4. software. (Black) line represent result spectra using the GER 3700 in direct comparison with the spectral geologist spectral (ASCII) library files (green) line.

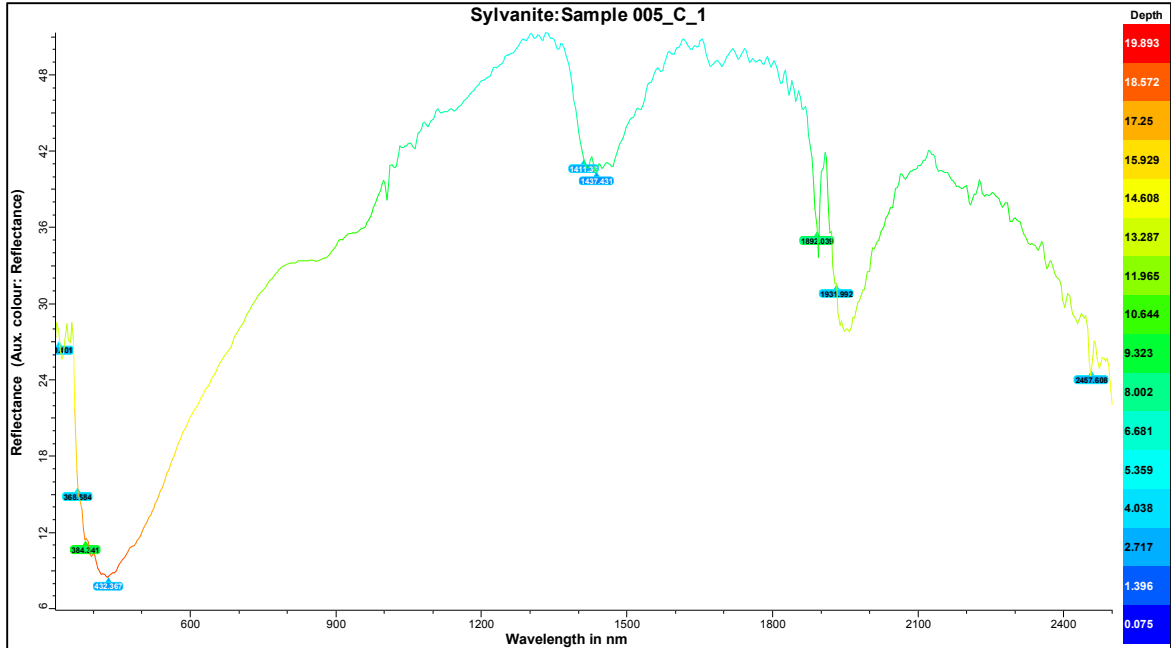


Figure A4.1.19-Sylvanite: Sample 005_C_1; Standard wavelength (CSV import data) with slight modifications.

Graph created using The Spectral Geologist 8.0.7.4. software.

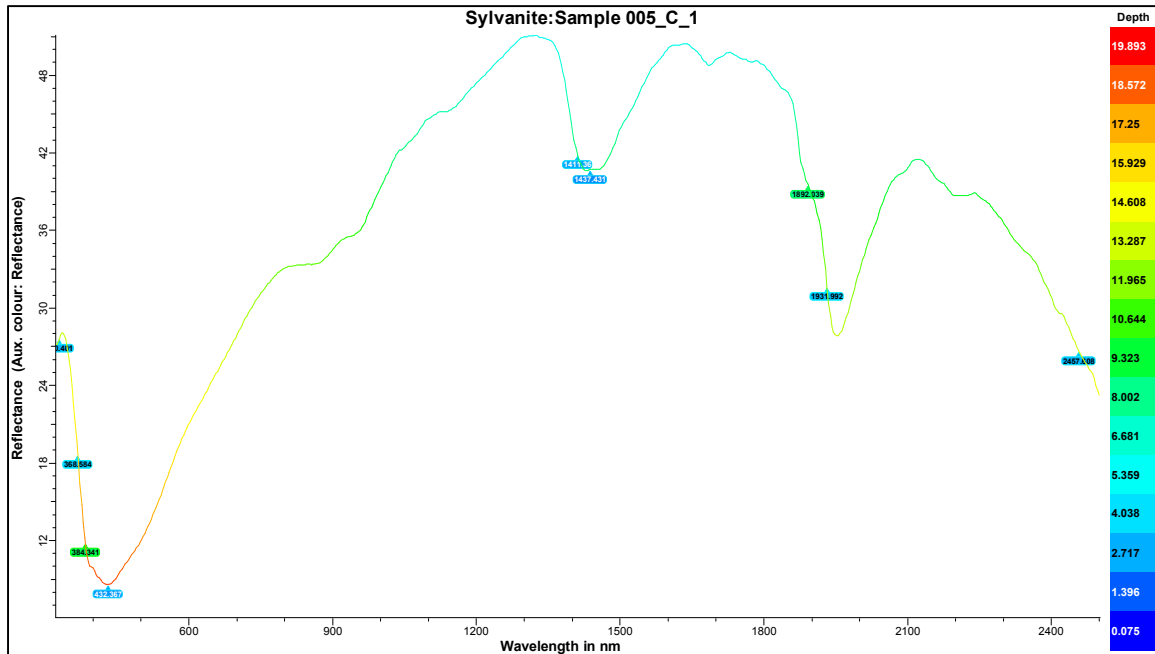


Figure A4.1.20-Sylvanite: Sample 005_C_1; Modified wavelength with feature wavelength (number tags) and smooth (Hi). Graph created using The Spectral Geologist 8.0.7.4. software.

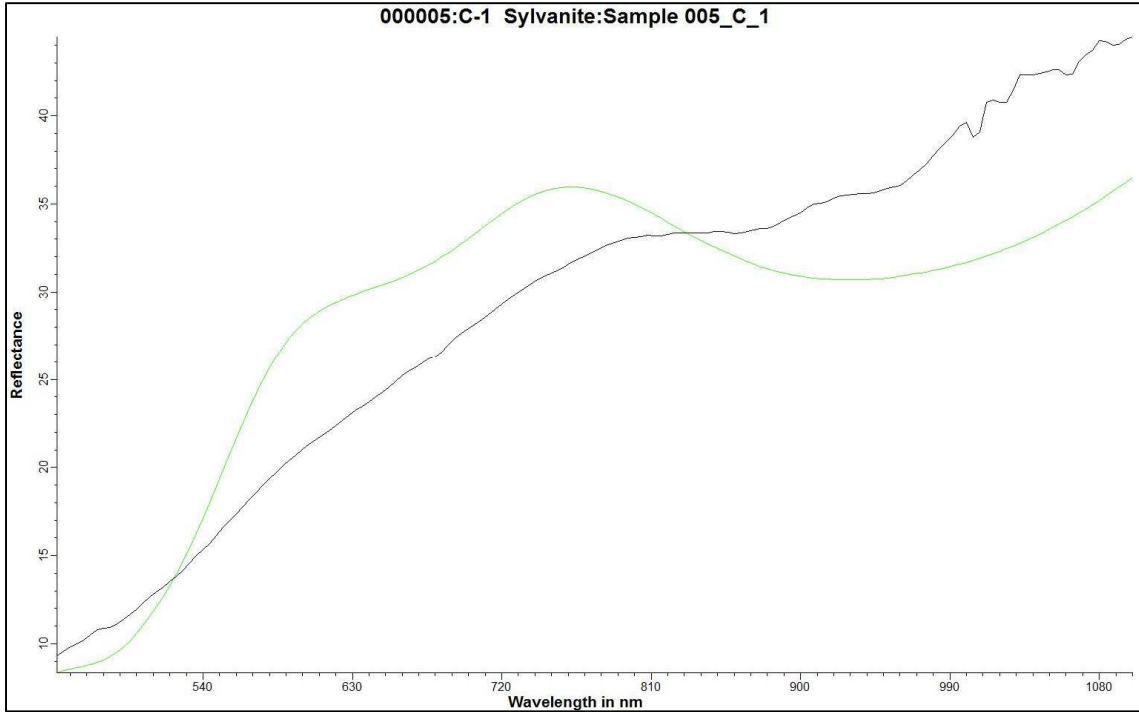


Figure A4.1.21- Sylvanite: Sample 005_C_1; (Goethite {930}) results are in the visible and near-infrared (VNIR). Graph created using The Spectral Geologist 8.0.7.4. software. (Black) line represent result spectra using the GER 3700 in direct comparison with the spectral geologist spectral (ASCII) library files (green) line.

Candidate TSA results	
*Goethite	[930]
Hematite	[1060]
Goethite	[2336]
Vegetation-Green	[3694]
52% Hematite + 48% Goethite	[509]
86% Hematite + 14% Vegetation-Green	[717]
88% Goethite + 12% Vegetation-Green	[778]
72% Hematite + 28% Goethite	[812]
80% Goethite + 20% Vegetation-Green	[1794]

Figure A4.1.22- Sylvanite: Sample 004_C_1; (Goethite {930}) The Spectral Geologist (ASCII) library list of other possible candidates. Closest candidate is denoted by an Astrid symbol (*Goethite [930]) according to the ASCII library.

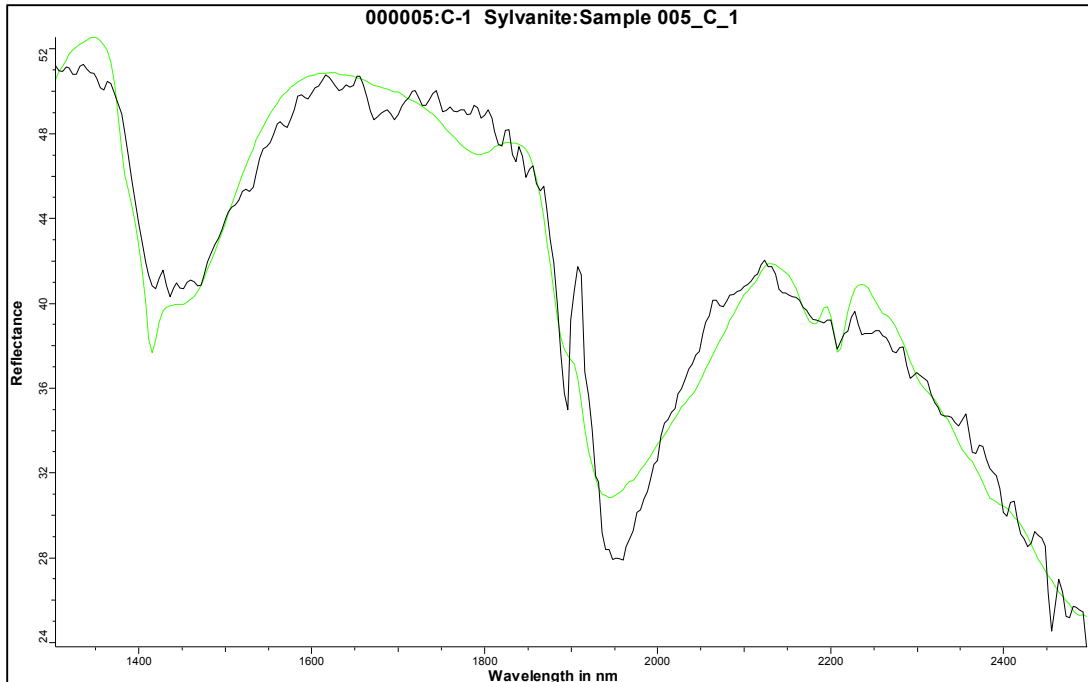


Figure A4.1.23- Sylvanite: Sample 005_C_1: Results are in the Short-Wave Infrared (SWIR). Graph created using The Spectral Geologist 8.0.7.4. software.

Candidate TSA results	
*Dickite	[1266]
Kaolinite-WX	[1277]
Alunite-K	[1304]
Rubellite	[1354]
Jarosite	[1354]
Topaz	[1359]
Nacrite	[1361]
Alunite-Na	[1372]
Gypsum	[1375]
Phengite	[1379]
Chlorite-Fe	[1381]
Phengite	[1385]
Chlorite-Fe	[1387]
Muscovite	[1389]
Muscovite	[1389]
Alunite-NH	[1390]
Paragonite	[1390]
Kaolinite-PX	[1392]
PlasticChipTray	[1394]
Siderite	[1396]
Dolomite	[1398]
YellowMarker	[1400]
Magnesite	[1400]
IsaYellow	[1404]
Pyrophyllite	[1404]

WhiteMarker	[1404]
IsaWhite	[1405]
70%Dickite + 30%Alunite-K	[1188]
64%Dickite + 36%Jarosite	[1198]
76%Kaolinite-WX + 24%Alunite-K	[1218]
72%Kaolinite-WX + 28%Jarosite	[1227]
66%Dickite + 34%Alunite-NH	[1228]
81%Dickite + 19%Gypsum	[1232]
55%Jarosite + 45%Alunite-K	[1234]
80%Chlorite-Fe + 20%Alunite-K	[1237]
93%Dickite + 7%PlasticChipTray	[1238]
76%Dickite + 24%Alunite-Na	[1238]
84%Kaolinite-WX + 16%Gypsum	[1239]
94%Kaolinite-WX + 6%PlasticChipTray	[1239]
82%Chlorite-Fe + 18%Alunite-K	[1240]
56%Chlorite-Fe + 44%Dickite	[1242]
59%Chlorite-Fe + 41%Dickite	[1244]
61%Phengite + 39%Alunite-K	[1245]
48%Dickite + 31%Jarosite + 21%Alunite-K	[1115]
61%Dickite + 31%Alunite-K + 7%PlasticChipTray	[1133]
43%Dickite + 29%Alunite-NH + 28%Jarosite	[1135]

Figure A4.1.24-Sylvanite: Sample 004_C_1: The Spectral Geologist (ASCII) library list of other possible candidates. Closest candidate is denoted by an Astrid symbol *Dickite [1266]. according to the ASCII library. Results are in the Short-Wave Infrared (SWIR). Graph created using The Spectral Geologist 8.0.7.4. software. (Black) line represent result spectra using the GER 3700 in direct comparison with the spectral geologist spectral (ASCII) library files (green) line.

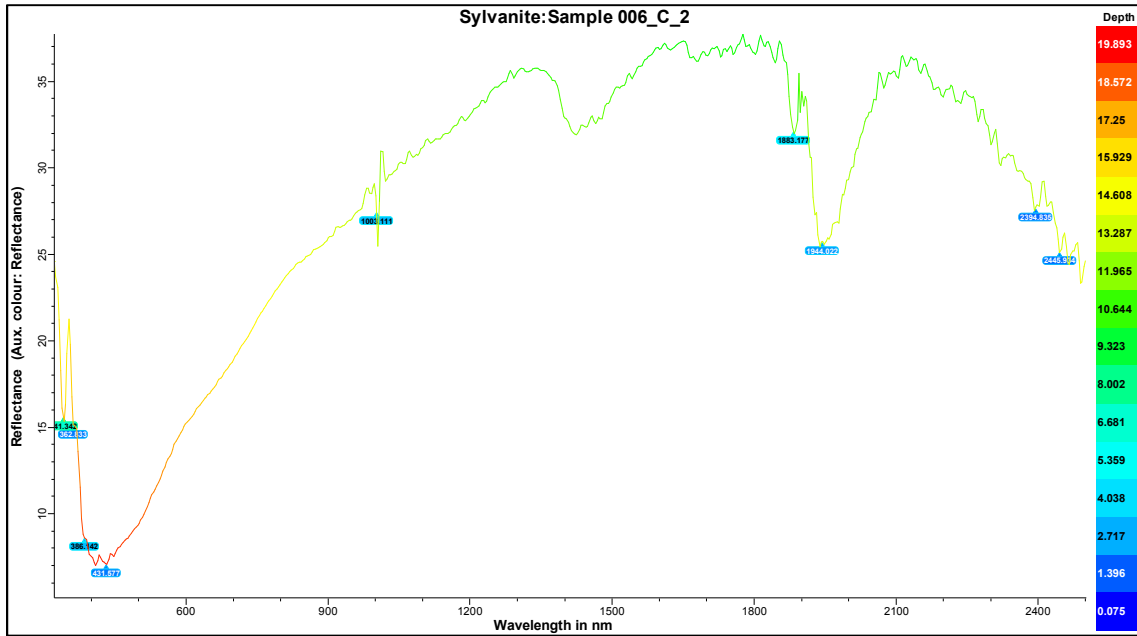


Figure A4.1.25- Sylvanite: Sample 006_C_2; Standard wavelength (CSV import data) with slight modifications.

Graph created using The Spectral Geologist 8.0.7.4. software.

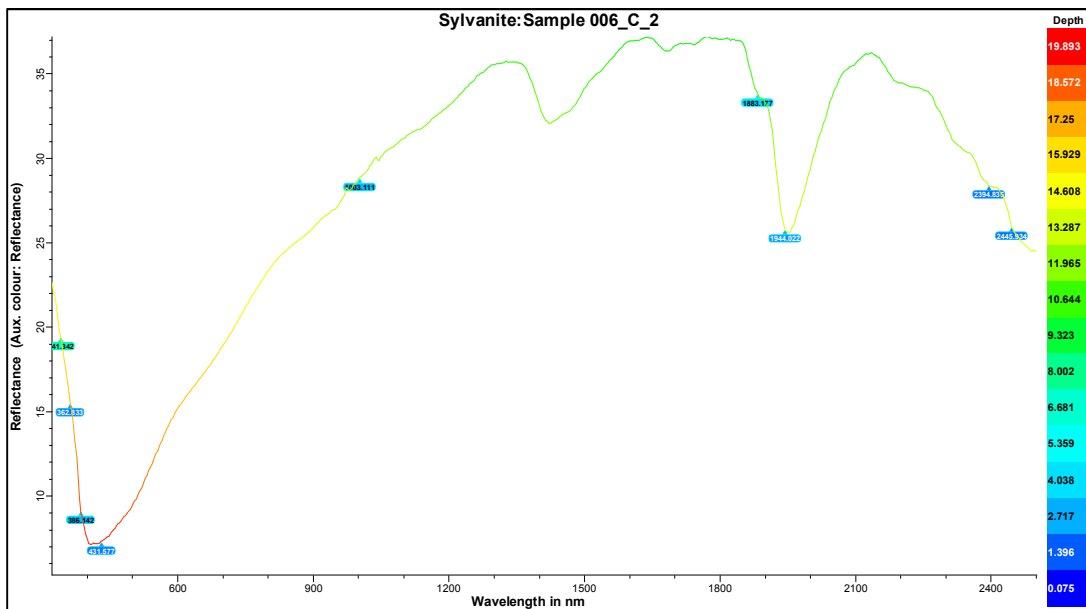


Figure A4.1.26-Sylvanite: Sample 006_C_2; Modified wavelength with feature wavelength (number tags) and smooth (Hi). Graph created using The Spectral Geologist 8.0.7.4. software.

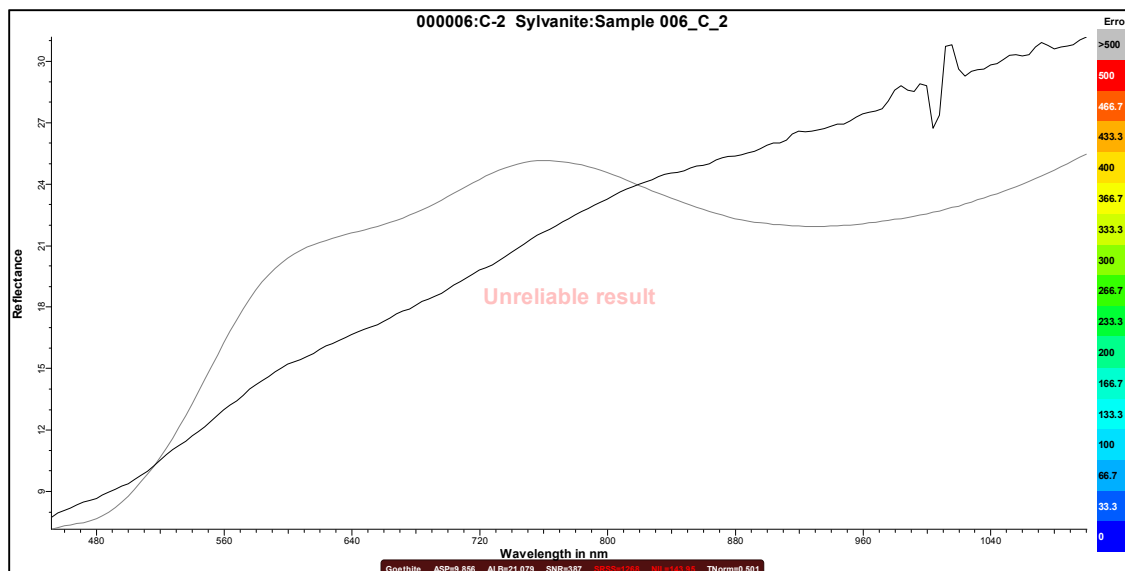


Figure A4.1.27- Sylvanite: Sample 006_C_2; (Goethite {1268}) results are in the visible and near-infrared (VNIR). Graph created using The Spectral Geologist 8.0.7.4. software. (Black) line represent result spectra using the GER 3700 in direct comparison with the spectral geologist spectral (ASCII) library files (Grey) line.

Candidate TSA results	
*Goethite	[1268]
Hematite	[1643]
Goethite	[2763]
Vegetation-Green	[3431]
55%Goethite + 45%Hematite	[990]
84%Goethite + 16%Vegetation-Green	[1022]
82%Hematite + 18%Vegetation-Green	[1120]
71%Hematite + 29%Goethite	[1403]
74%Goethite + 26%Vegetation-Green	[2014]

Figure A4.1.28- Sylvanite: Sample 006_C_2; (Goethite {1268}) The Spectral Geologist (ASCII) library list of other possible candidates. Closest candidate is denoted by an Astrid symbol (*Goethite [1268]) according to the ASCII library.

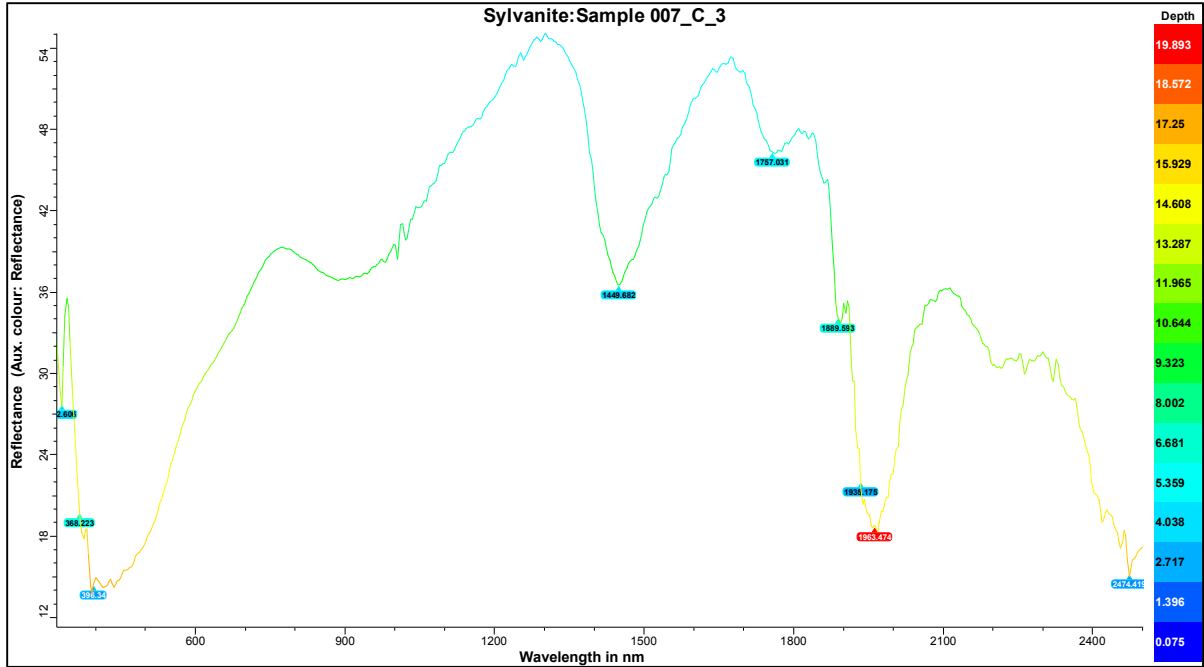


Figure A4.1.31- Sylvanite: Sample 007_C_3; Standard wavelength (CSV import data) with slight modifications.

Graph created using The Spectral Geologist 8.0.7.4. software.

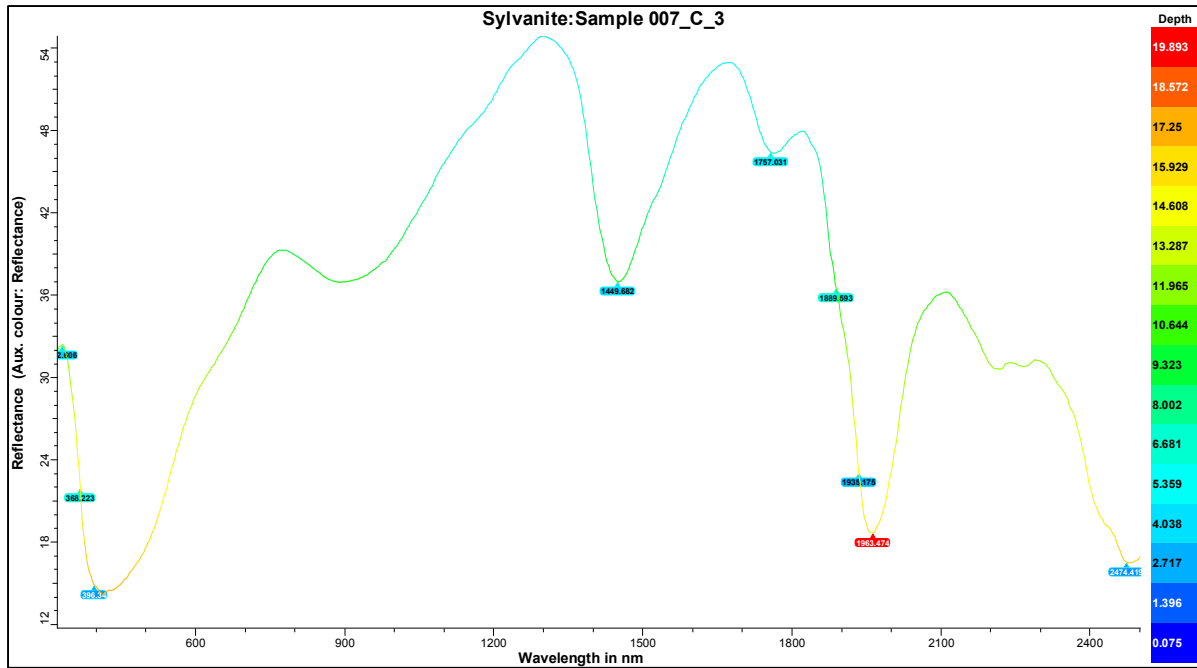


Figure A4.1.32- Sylvanite: Sample 006_C_3; Modified wavelength with feature wavelength (number tags) and smooth (Hi). Graph created using The Spectral Geologist 8.0.7.4. software.

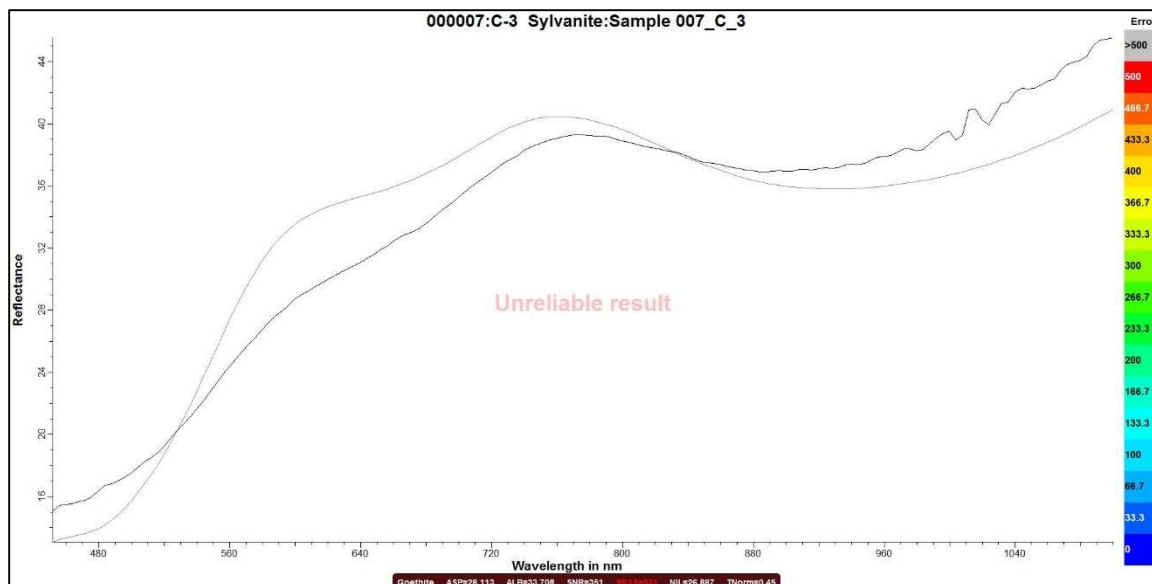


Figure A4.1.33- Sylvanite: Sample 007_C_3; (Goethite {531}) results are in the visible and near-infrared (VNIR). Graph created using The Spectral Geologist 8.0.7.4. software. (Black) line represent result spectra using the GER 3700 in direct comparison with the spectral geologist spectral (ASCII) library files (Grey) line.

Candidate TSA results	
*Goethite [531]	
Hematite [1030]	
Goethite [1647]	
Vegetation-Green [4054]	
55%Goethite + 45%Hematite [182]	
90%Goethite + 10%Vegetation-Green [394]	
59%Hematite + 41%Goethite [406]	
66%Goethite + 34%ODZincalume [517]	
86%Hematite + 14%Vegetation-Green [613]	
84%Goethite + 16%Vegetation-Green [1228]	

Figure A4.1.34- Sylvanite: Sample 007_C_3; (Goethite {531}) The Spectral Geologist (ASCII) library list of other possible candidates. Closest candidate is denoted by an Astrid symbol (*Goethite [531]) according to the ASCII library.

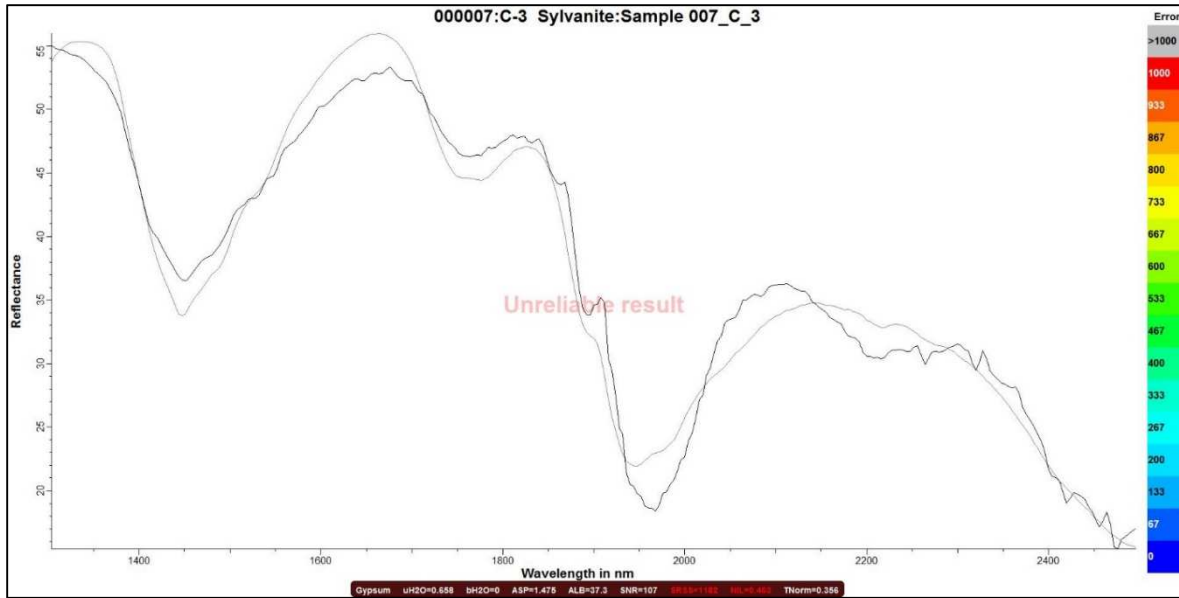


Figure A4.1.35- Sylvanite: Sample 007_C_3: Results are in the Short-Wave Infrared (SWIR). Graph created using The Spectral Geologist 8.0.7.4. software.

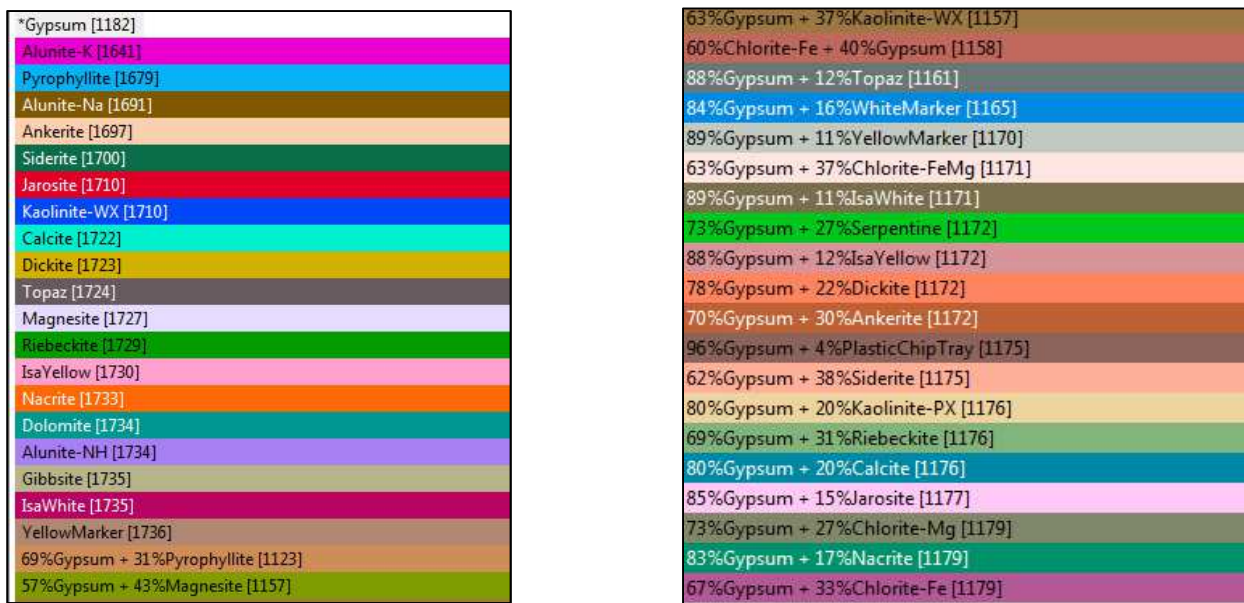


Figure A4.1.36-Sylvanite: Sample 007_C_3: The Spectral Geologist (ASCII) library list of other possible candidates. Closest candidate is denoted by an Astrid symbol *Gypsum [1182]. according to the ASCII library. Results are in the Short-Wave Infrared (SWIR). Graph created using The Spectral Geologist 8.0.7.4. software. (Black) line represent result spectra using the GER 3700 in direct comparison with the spectral geologist spectral (ASCII) library files (grey) line.

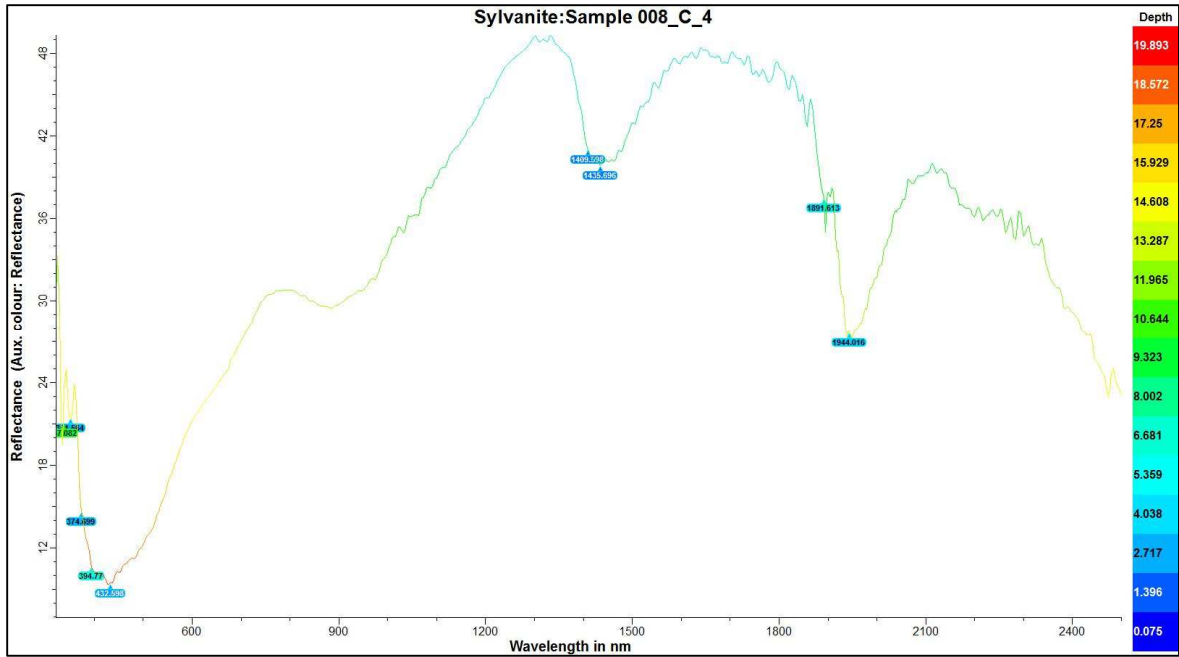


Figure A4.1.37- Sylvaniaite: Sample 008_C_4; Standard wavelength (CSV import data) with slight modifications.

Graph created using The Spectral Geologist 8.0.7.4. software.

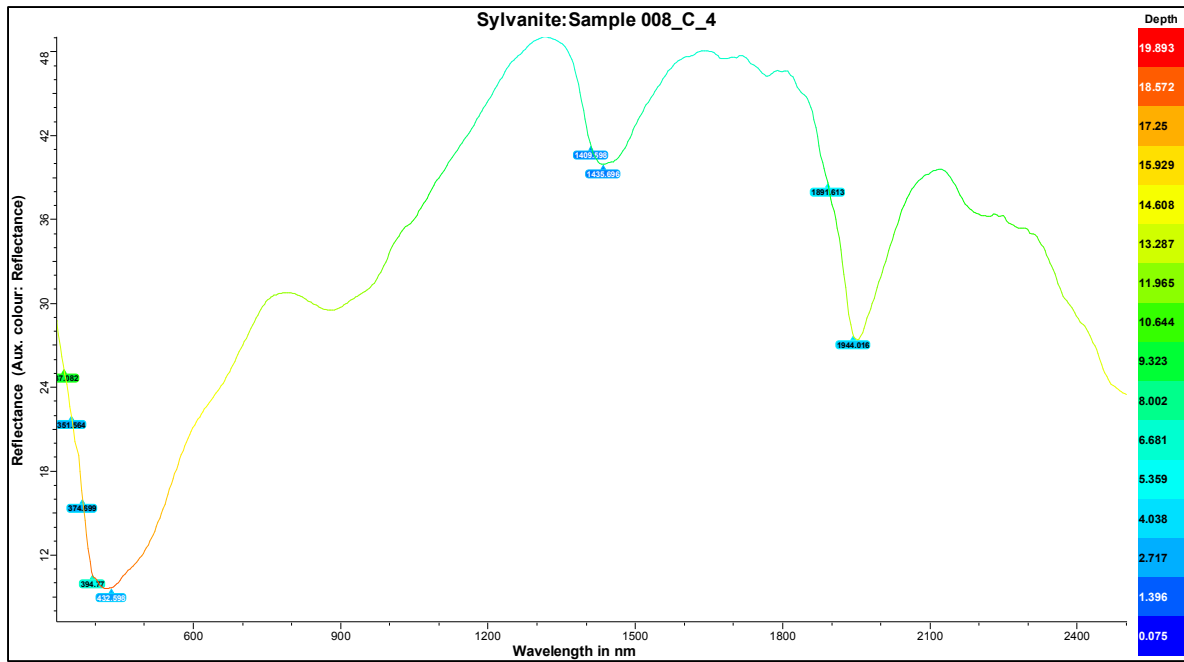


Figure A4.1.38- Sylvaniaite: Sample 008_C_4; Modified wavelength with feature wavelength (number tags) and smooth (Hi). Graph created using The Spectral Geologist 8.0.7.4. software.

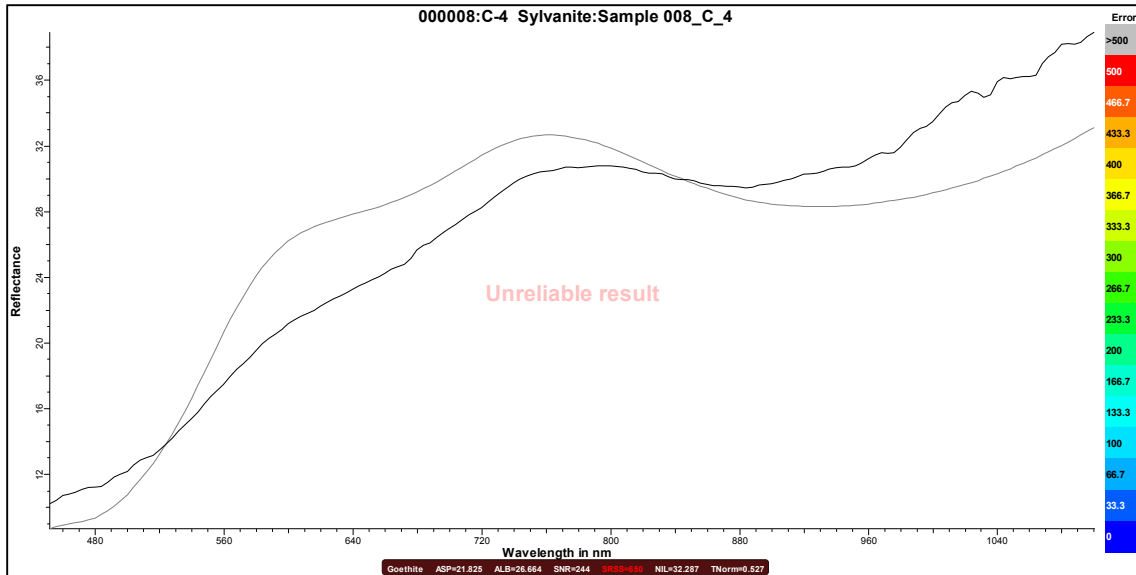


Figure A4.1.39- Sylvanite: Sample 008_C_4; (Goethite {650}) results are in the visible and near-infrared (VNIR). Graph created using The Spectral Geologist 8.0.7.4. software. (Black) line represent result spectra using the GER 3700 in direct comparison with the spectral geologist spectral (ASCII) library files (Brown) line.

Candidate TSA results	
*Goethite [650]	
Hematite [894]	
Goethite [1819]	
Vegetation-Green [3892]	
50%Goethite + 50%Hematite [224]	
64%Hematite + 36%Goethite [439]	
89%Goethite + 11%Vegetation-Green [508]	
87%Hematite + 13%Vegetation-Green [529]	
66%Goethite + 34%ODZincalume [636]	
83%Goethite + 17%Vegetation-Green [1374]	

Figure A4.1.40- Sylvanite: Sample 008_C_4; (Goethite {650}) The Spectral Geologist (ASCII) library list of other possible candidates. Closest candidate is denoted by an Astrid symbol (*Goethite [650]) according to the ASCII library.

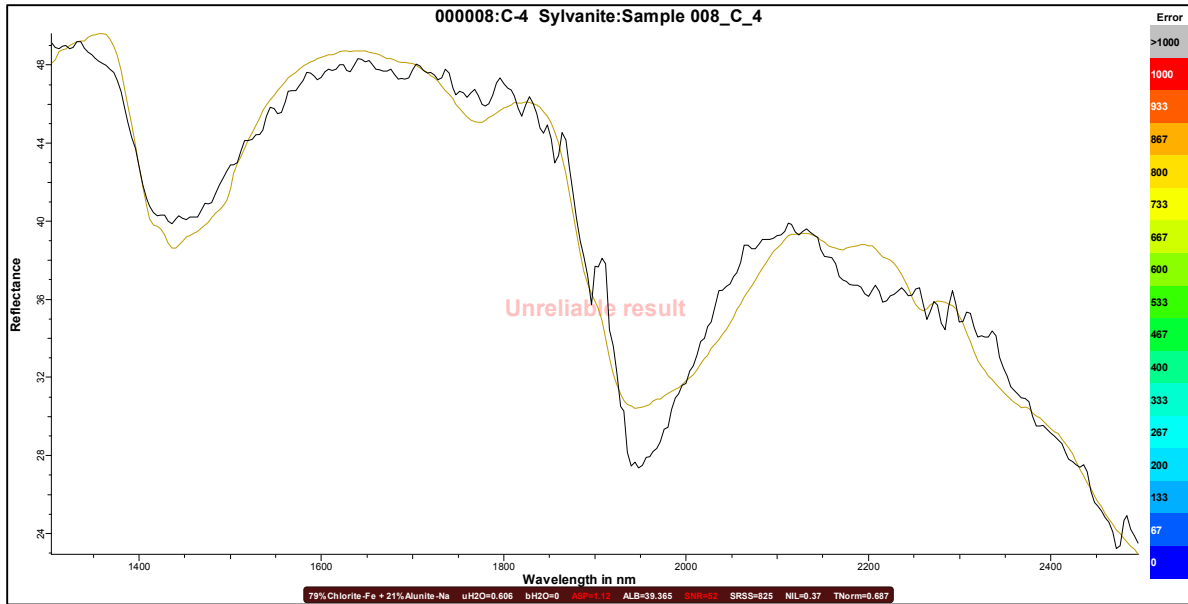


Figure A4.1.41- Sylvanite: Sample 008_C_4: Results are in the Short-Wave Infrared (SWIR). Graph created using The Spectral Geologist 8.0.7.4. software.

Candidate TSA results	
Gypsum [866]	
Alunite-K [867]	
Kaolinite-WX [881]	
Alunite-Na [887]	
Jarosite [907]	
Siderite [932]	
Alunite-NH [936]	
Topaz [937]	
Kaolinite-PX [939]	
Zoisite [942]	
Chlorite-Fe [942]	
Talc [943]	
Actinolite [943]	
Nacrite [946]	
Ankerite [947]	
Tremolite [949]	
Muscovite [949]	
Dickite [950]	
Phengite [951]	
Chlorite-Fe [952]	
Rubellite [953]	
Pyrophyllite [953]	
Chlorite-Mg [953]	
Epidote [954]	
Phengite [954]	
Hornblende [957]	
Muscovite [957]	
Chlorite-Mg [959]	
Chlorite-FeMg [959]	
72%Kaolinite-WX + 28%Gypsum [783]	
56%Jarosite + 44%Alunite-K [797]	

81%Chlorite-Fe + 19%Gypsum [806]
82%Chlorite-Fe + 18%Alunite-K [808]
83%Chlorite-Fe + 17%Gypsum [810]
*77%Siderite + 23%Alunite-K [816]
52%Alunite-K + 48%Gypsum [818]
69%Kaolinite-WX + 31%Alunite-K [819]
56%Jarosite + 44%Gypsum [823]
58%Zoisite + 42%Alunite-K [824]
*79%Chlorite-Fe + 21%Alunite-Na [825]
71%Chlorite-Mg + 29%Alunite-K [826]
52%Jarosite + 48%Alunite-Na [826]
59%Zoisite + 41%Gypsum [827]
77%Chlorite-Fe + 23%Alunite-K [827]
68%Chlorite-Mg + 32%Alunite-K [827]
66%Kaolinite-WX + 34%Jarosite [828]
68%Kaolinite-WX + 32%Alunite-Na [831]
58%Kaolinite-PX + 42%Gypsum [831]
53%Actinolite + 47%Alunite-K [831]

Figure A4.1.42-Sylvanite: Sample 008_C_4: The Spectral Geologist (ASCII) library list of other possible candidates. Closest candidate is denoted by an Astrid symbol *79 % Chlorite-Fe+ 21 % Alunite-Na [825] according to the ASCII library. Results are in the Short-Wave Infrared (SWIR). Graph created using The Spectral Geologist 8.0.7.4. software. (Black) line represent result spectra using the GER 3700 in direct comparison with the spectral geologist spectral (ASCII) library files (Brown) line.

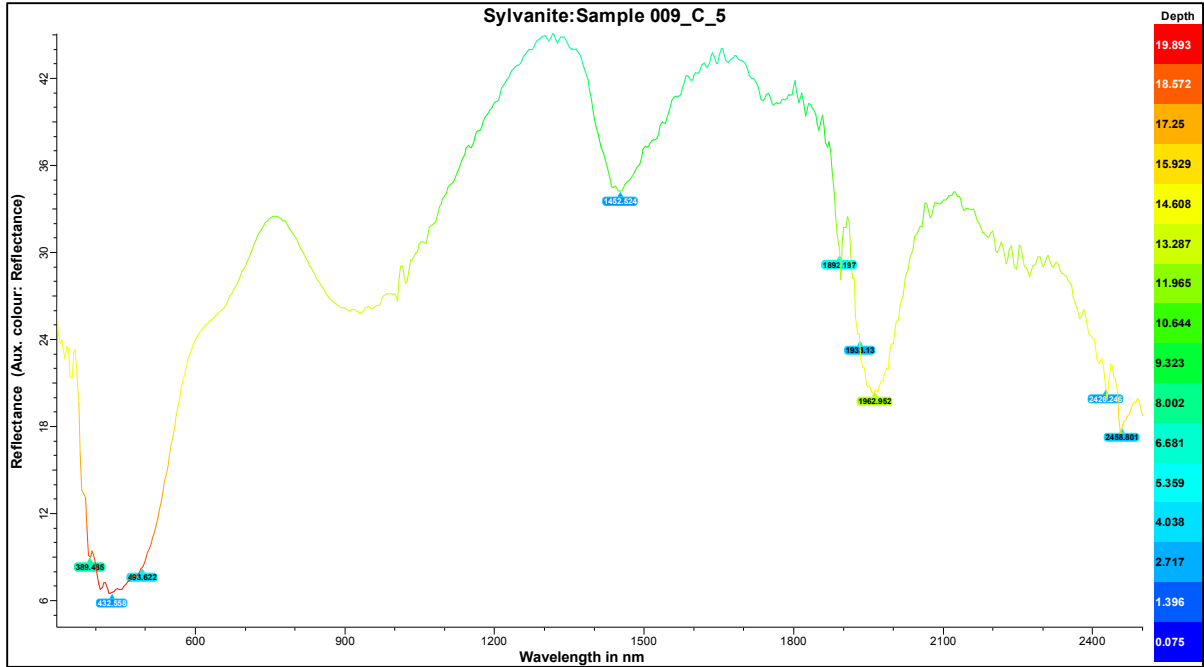


Figure A4.1.43 Sylvanite: Sample 009_C_5; Standard wavelength (CSV import data) with slight modifications.

Graph created using The Spectral Geologist 8.0.7.4. software.

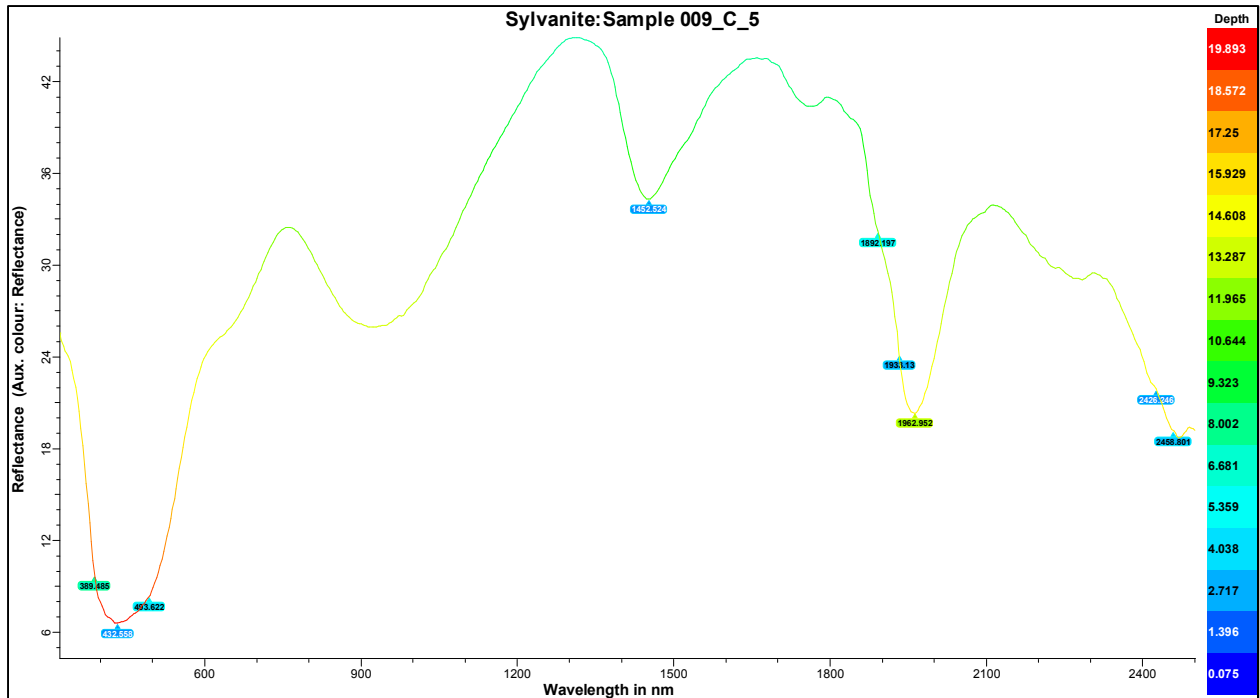


Figure A4.1.44- Sylvanite: Sample 009_C_5; Modified wavelength with feature wavelength (number tags) and smooth (Hi). Graph created using The Spectral Geologist 8.0.7.4. software.

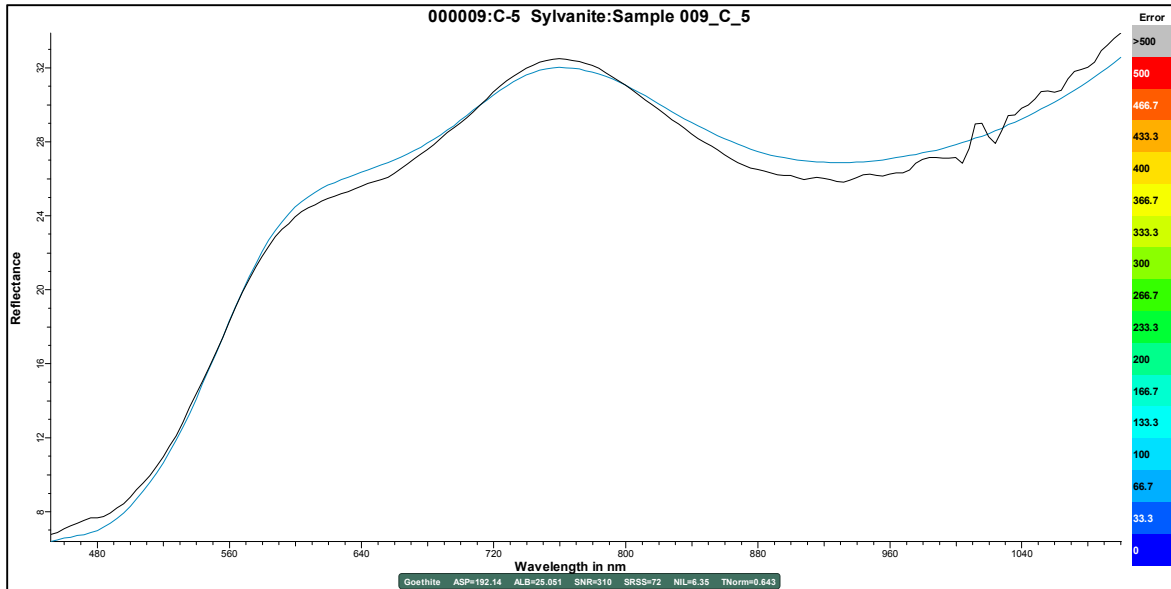


Figure A4.1.45- Sylvanite: Sample 009_C_5; (Goethite {72}) results are in the visible and near-infrared (VNIR). Graph created using The Spectral Geologist 8.0.7.4. software. (Black) line represent result spectra using the GER 3700 in direct comparison with the spectral geologist spectral (ASCII) library files (Blue) line.

Candidate TSA results	
*Goethite [72]	
Goethite [506]	
Hematite [1715]	
Vegetation-Green [4508]	
56%Goethite + 44%ODZincalume [39]	
87%Goethite + 13%Hematite [48]	
81%Goethite + 19%GalvanisedIron [61]	
98%Goethite + 2%Vegetation-Green [67]	
67%Goethite + 33%Hematite [151]	
95%Goethite + 5%Vegetation-Green [449]	
87%Hematite + 13%Vegetation-Green [1393]	
73%Hematite + 27%GalvanisedIron [1680]	

Figure A4.1.46- Sylvanite: Sample 008_C_5; (Goethite {72}) results are in the visible and near-infrared (VNIR). Graph created using The Spectral Geologist 8.0.7.4. software. (Black) line represent result spectra using the GER 3700 in direct comparison with the spectral geologist spectral (ASCII) library files (blue) line.

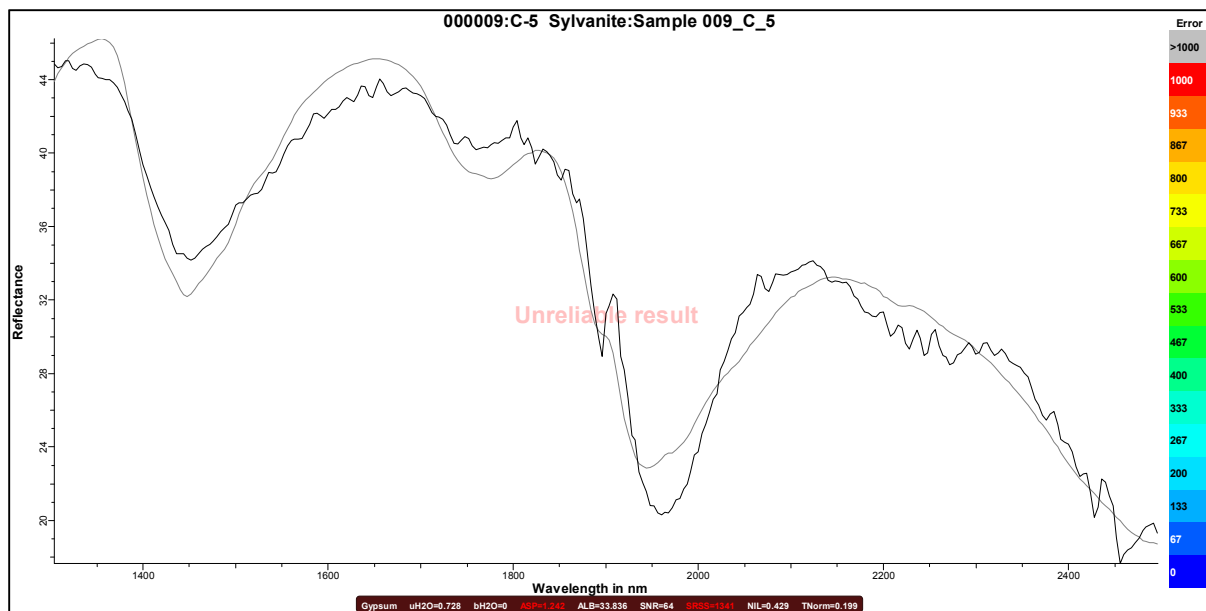


Figure A4.1.47- Sylvanite: Sample 009_C_5: Results are in the Short-Wave Infrared (SWIR). Graph created using The Spectral Geologist 8.0.7.4. software.

Candidate TSA results	
*Gypsum [1341]	70%Chlorite-Fe + 30%Gypsum [1306]
Alunite-K [1480]	53%Magnesite + 47%Gypsum [1308]
Alunite-Na [1573]	79%Gypsum + 21%YellowMarker [1309]
Jarosite [1613]	57%Gypsum + 43%Zoisite [1309]
Phengite [1617]	76%Gypsum + 24%IsaYellow [1312]
Kaolinite-WX [1622]	55%Chlorite-FeMg + 45%Gypsum [1313]
Ankerite [1623]	80%Gypsum + 20%IsaWhite [1313]
IsaYellow [1632]	78%Gypsum + 22%WhiteMarker [1319]
Siderite [1634]	67%Gypsum + 33%Jarosite [1320]
Dickite [1634]	65%Gypsum + 35%Dickite [1320]
YellowMarker [1639]	51%Phengite + 49%Gypsum [1321]
Magnesite [1640]	81%Gypsum + 19%Tourmaline [1322]
Alunite-NH [1640]	70%Gypsum + 30%Talc [1323]
IsaWhite [1640]	93%Gypsum + 7%PlasticChipTray [1325]
Dolomite [1641]	58%Chlorite-Fe + 42%Gypsum [1326]
Phengite [1645]	50%Gypsum + 50%Chlorite-Mg [1327]
Zoisite [1650]	60%Gypsum + 40%Ankerite [1328]
Talc [1653]	88%Gypsum + 12%Topaz [1328]
Topaz [1653]	58%Chlorite-FeMg + 42%Gypsum [1330]
Tourmaline [1654]	74%Gypsum + 26%Alunite-NH [1333]
PlasticChipTray [1655]	
63%Gypsum + 37%Alunite-K [1283]	
50%Phengite + 50%Gypsum [1291]	
51%Gypsum + 49%Kaolinite-WX [1306]	

Figure A4.1.48-Sylvanite: Sample 009_C_5: The Spectral Geologist (ASCII) library list of other possible candidates. Closest candidate is denoted by an Astrid symbol *Gypsum [1341] according to the ASCII library. Results are in the Short-Wave Infrared (SWIR). Graph created using The Spectral Geologist 8.0.7.4. software. (Black) line represent result spectra using the GER 3700 in direct comparison with the spectral geologist spectral (ASCII) library files (Grey) line.

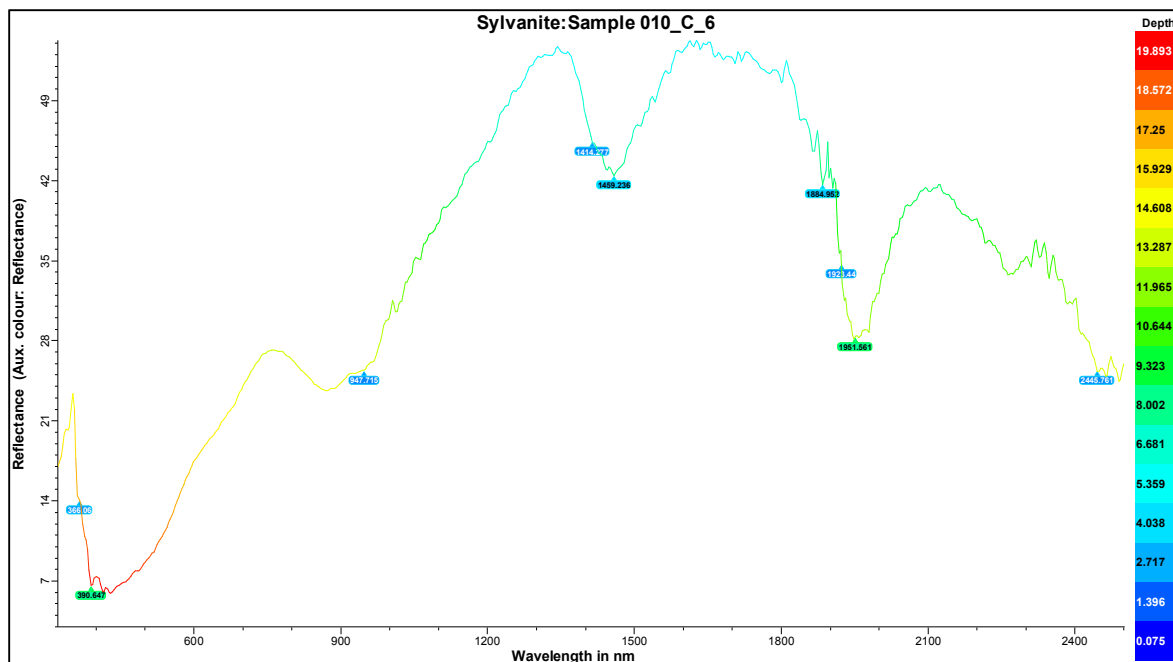


Figure A4.1.49- Sylvanite: Sample 010_C_6; Standard wavelength (CSV import data) with slight modifications.

Graph created using The Spectral Geologist 8.0.7.4. software.

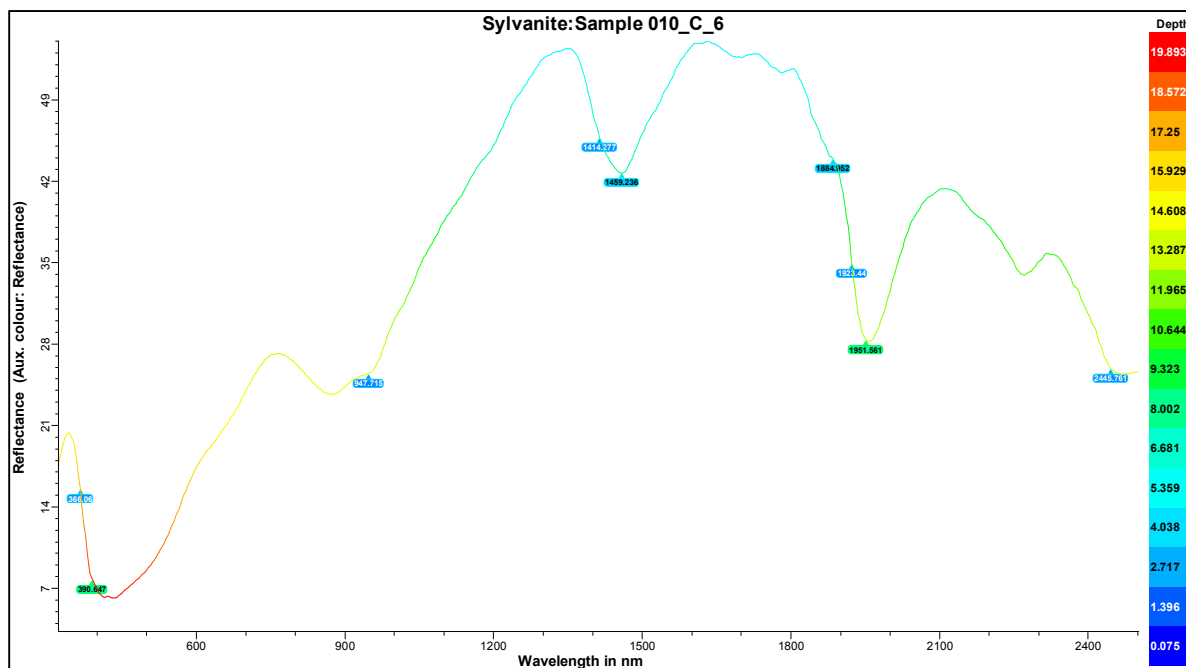


Figure A4.1.50- Sylvanite: Sample 010_C_6; Modified wavelength with feature wavelength (number tags) and smooth (Hi). Graph created using The Spectral Geologist 8.0.7.4. software.

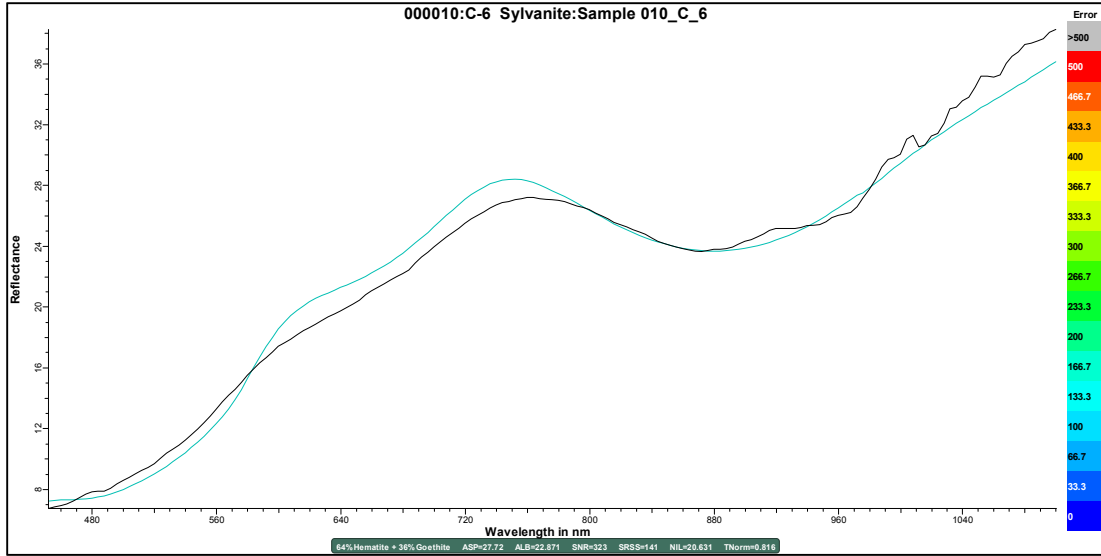


Figure A4.1.51- Sylvanite: Sample 010_C_6; (*64 % Hematite +36 % Goethite {141}) results are in the visible and near-infrared (VNIR). Graph created using The Spectral Geologist 8.0.7.4. software. (Black) line represent result spectra using the GER 3700 in direct comparison with the spectral geologist spectral (ASCII) library files (Blue) line.

Candidate TSA results	
Hematite	[512]
Goethite	[891]
Goethite	[1949]
Vegetation-Green	[4513]
*64% Hematite + 36% Goethite	[141]
71% Hematite + 29% Goethite	[218]
92% Hematite + 8% Vegetation-Green	[363]
65% ODZincalume + 35% Goethite	[695]
93% Goethite + 7% Vegetation-Green	[826]
87% Goethite + 13% Vegetation-Green	[1669]
93% Goethite + 7% ODZincalume	[1949]
68% ODZincalume + 32% Vegetation-Green	[4455]

Figure A4.1.52- Sylvanite: Sample 010_C_6; *64 % Hematite +36 % Goethite {141} results are in the visible and near-infrared (VNIR). Graph created using The Spectral Geologist 8.0.7.4. software. (Black) line represent result spectra using the GER 3700 in direct comparison with the spectral geologist spectral (ASCII) library files (blue) line.

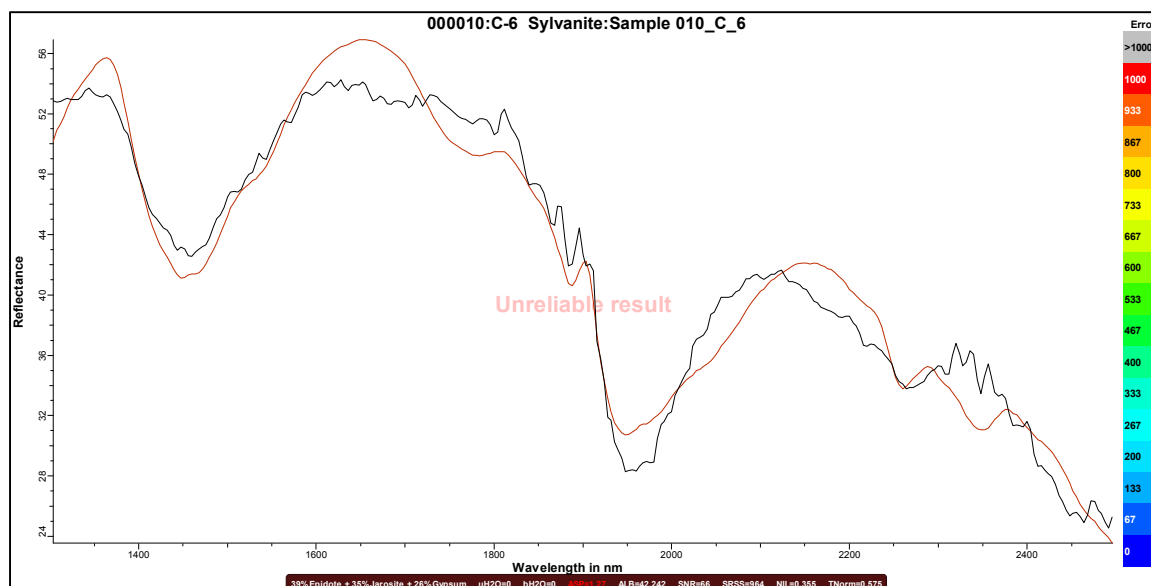


Figure A4.1.53- Sylvaniaite: Sample 010_C_6: Results are in the Short-Wave Infrared (SWIR). Graph created using The Spectral Geologist 8.0.7.4. software.

Candidate TSA results
59%Ankerite + 22%Jarosite + 19%Gypsum [944]
*39%Epidote + 35%Jarosite + 26%Gypsum [964]

Figure A4.1.54-Sylvaniaite: Sample 010_C_6: The Spectral Geologist (ASCII) library list of other possible candidates. Closest candidate is denoted by an Astrid symbol *39% Epidote + 35 % Jarosite +26 % Gypsum [964] according to the ASCII library. Results are in the Short-Wave Infrared (SWIR). Graph created using The Spectral Geologist 8.0.7.4. software. (Black) line represent result spectra using the GER 3700 in direct comparison with the spectral geologist spectral (ASCII) library files (Red) line.

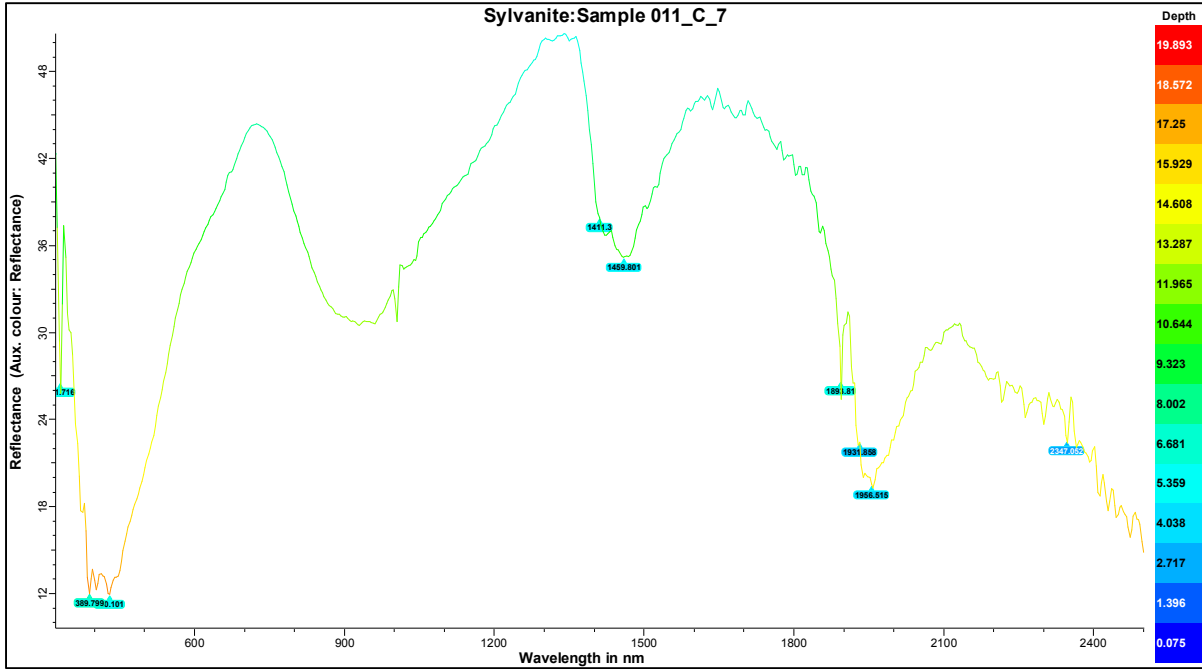


Figure A4.1.55- Sylvanite: Sample 011_C_7; Standard wavelength (CSV import data) with slight modifications.

Graph created using The Spectral Geologist 8.0.7.4. software.

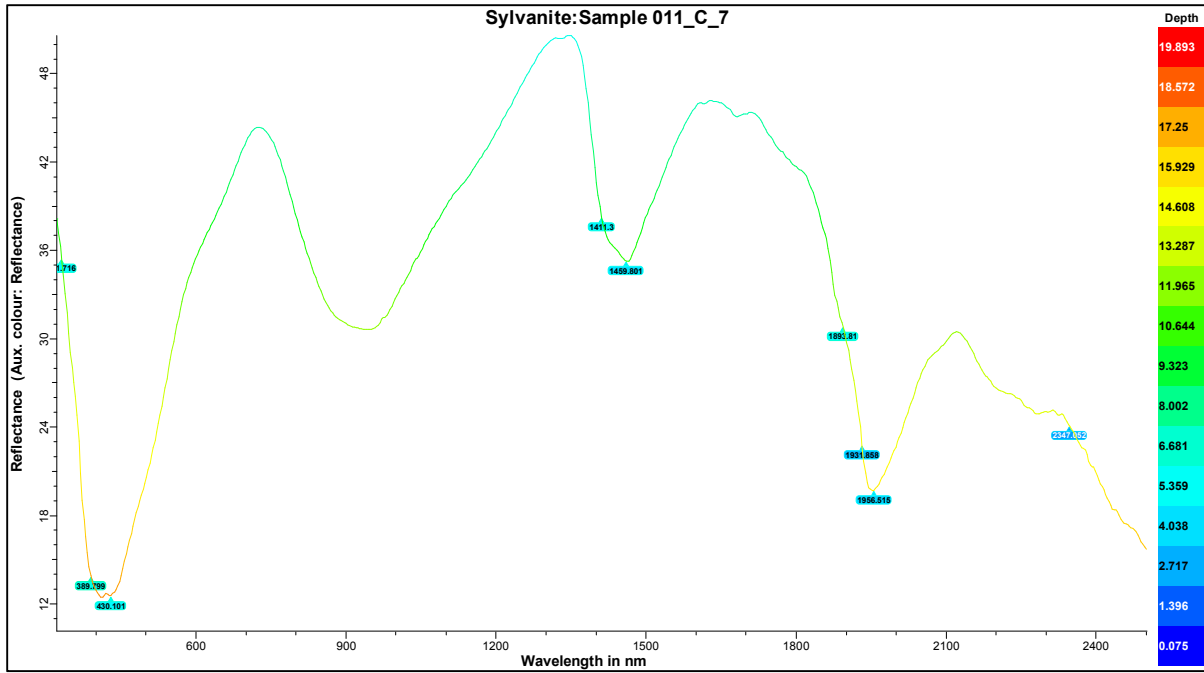


Figure A4.1.56- Sylvanite: Sample 011_C_7; Modified wavelength with feature wavelength (number tags) and smooth (Hi). Graph created using The Spectral Geologist 8.0.7.4. software.

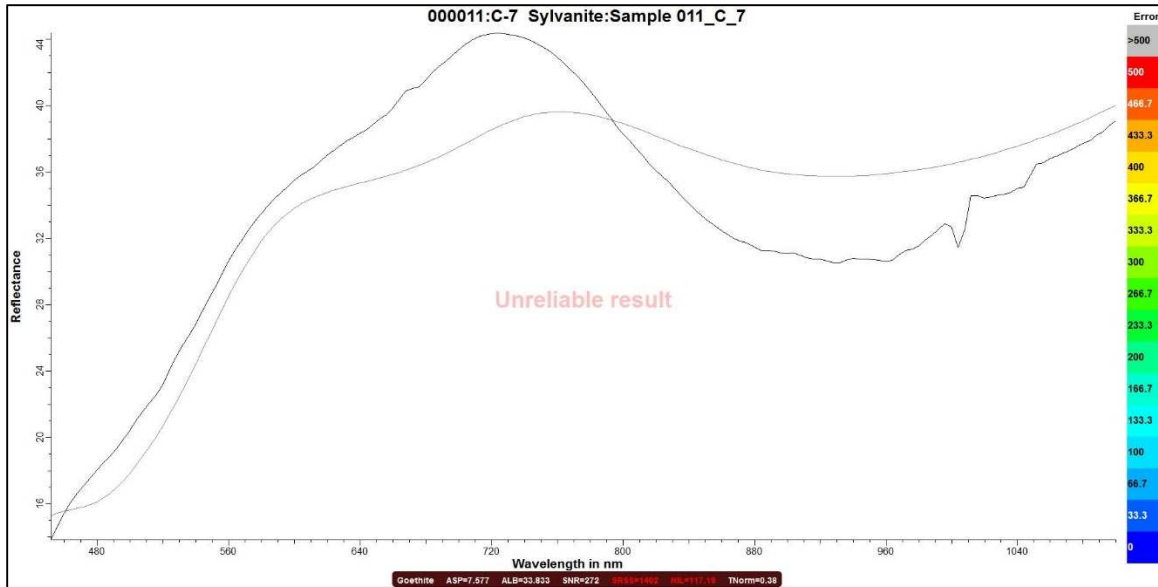


Figure A4.1.57- Sylvanite: Sample 011_C_7; *Goethite {1402}) results are in the visible and near-infrared (VNIR). Graph created using The Spectral Geologist 8.0.7.4. software. (Black) line represent result spectra using the GER 3700 in direct comparison with the spectral geologist spectral (ASCII) library files (Blue) line.

Candidate TSA results	
*Goethite	[1402]
Hematite	[1666]
Goethite	[1687]
Vegetation-Green	[5034]
79%ODZincalume + 21%Goethite	[811]
62%GalvanisedIron + 38%Hematite	[987]
61%GalvanisedIron + 39%Goethite	[1014]
51%Hematite + 49%Goethite	[1080]
53%Goethite + 47%Hematite	[1155]
64%ODZincalume + 36%Goethite	[1497]
71%Goethite + 29%GalvanisedIron	[1649]
98%Hematite + 2%Vegetation-Green	[1661]
80%Hematite + 20%ODZincalume	[1662]
83%ODZincalume + 17%Vegetation-Green	[4828]

Figure A4.1.58- Sylvanite: Sample 011_C_7; *Goethite {1402} results are in the visible and near-infrared (VNIR). Graph created using The Spectral Geologist 8.0.7.4. software. (Black) line represent result spectra using the GER 3700 in direct comparison with the spectral geologist spectral (ASCII) library files (Light Grey) line.

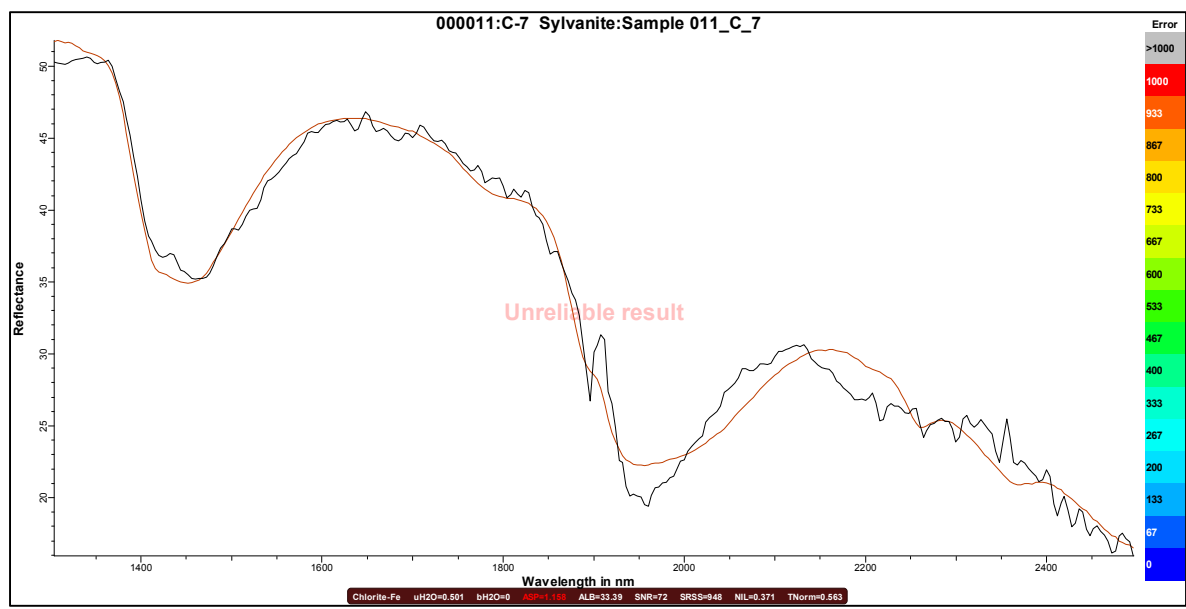


Figure A4.1.59- Sylvanite: Sample 011_C_7: Results are in the Short-Wave Infrared (SWIR). Graph created using The Spectral Geologist 8.0.7.4. software.



Figure A4.1.60-Sylvanite: Sample 011_C_7: The Spectral Geologist (ASCII) library list of other possible candidates. Closest candidate is denoted by an Astrid symbol *Chlorite-Fe [948] according to the ASCII library. Results are in the Short-Wave Infrared (SWIR). Graph created using The Spectral Geologist 8.0.7.4. software. (Black) line represent result spectra using the GER 3700 in direct comparison with the spectral geologist spectral (ASCII) library files (Brown) line.

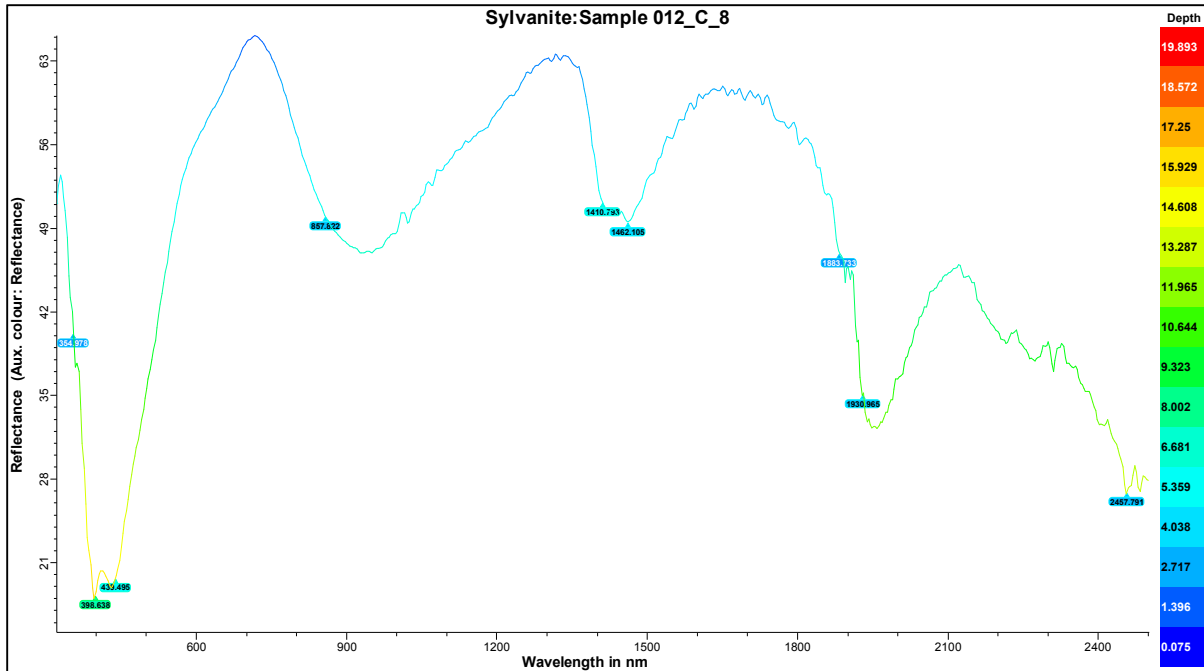


Figure A4.1.61- Sylvanite: Sample 012_C_8; Standard wavelength (CSV import data) with slight modifications.

Graph created using The Spectral Geologist 8.0.7.4. software

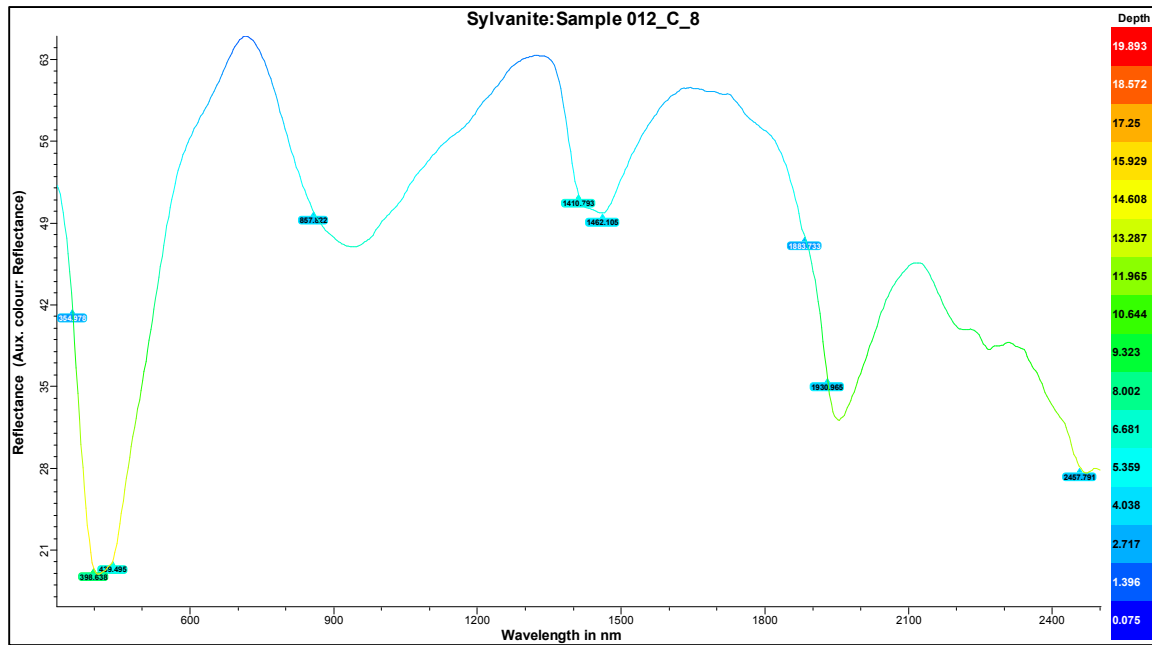


Figure A4.1.62- Sylvanite: Sample 012_C_8; Modified wavelength with feature wavelength (number tags) and smooth (Hi). Graph created using The Spectral Geologist 8.0.7.4. software.

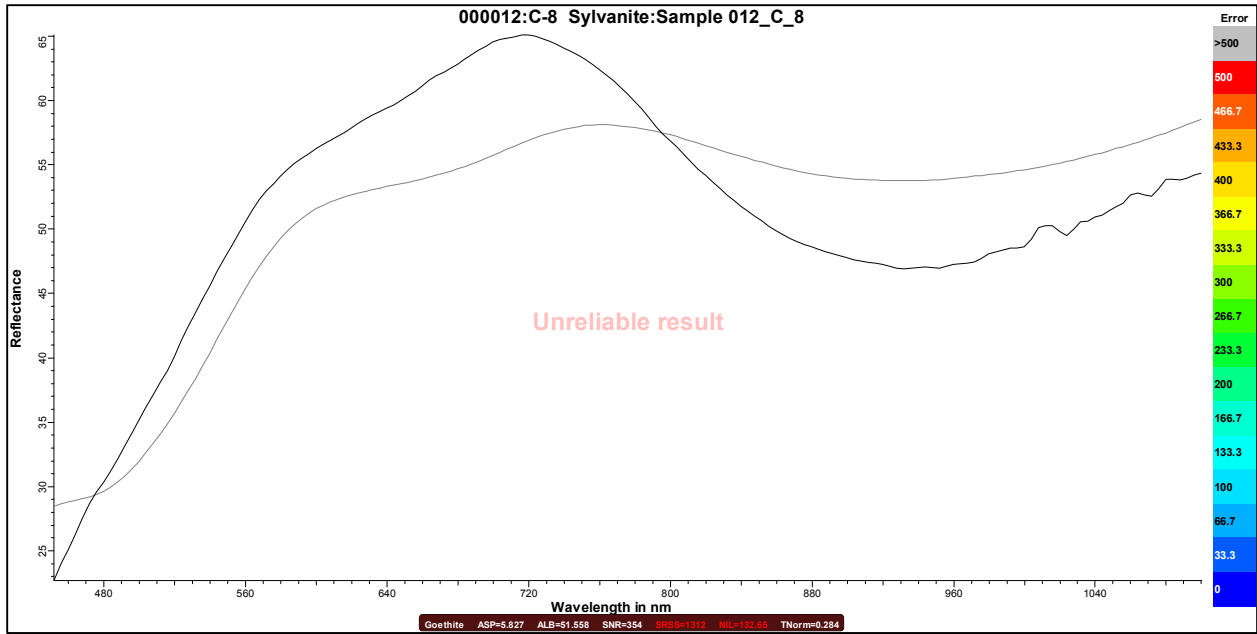


Figure A4.1.63- Sylvanite: Sample 012_C_8; *Goethite {1312} results are in the visible and near-infrared (VNIR). Graph created using The Spectral Geologist 8.0.7.4. software. (Black) line represent result spectra using the GER 3700 in direct comparison with the spectral geologist spectral (ASCII) library files (Grey) line.

Candidate TSA results	
*Goethite	[1312]
Goethite	[1588]
Hematite	[1804]
Vegetation-Green	[4040]
64%GalvanisedIron + 36%Goethite	[926]
78%ODZincalume + 22%Goethite	[947]
64%GalvanisedIron + 36%Hematite	[1250]
71%Goethite + 29%Hematite	[1251]
56%Goethite + 44%Hematite	[1292]
61%ODZincalume + 39%Goethite	[1484]
61%Goethite + 39%GalvanisedIron	[1525]
99%Hematite + 1%Vegetation-Green	[1802]
100%Hematite + 0%ODZincalume	[1804]
81%ODZincalume + 19%Vegetation-Green	[3950]
71%Vegetation-Green + 29%GalvanisedIron	[4037]

Figure A4.1.64- Sylvanite: Sample 012_C_8; *Goethite {1312} results are in the visible and near-infrared (VNIR). Graph created using The Spectral Geologist 8.0.7.4. software. (Black) line represent result spectra using the GER 3700 in direct comparison with the spectral geologist spectral (ASCII) library files (Grey) line.

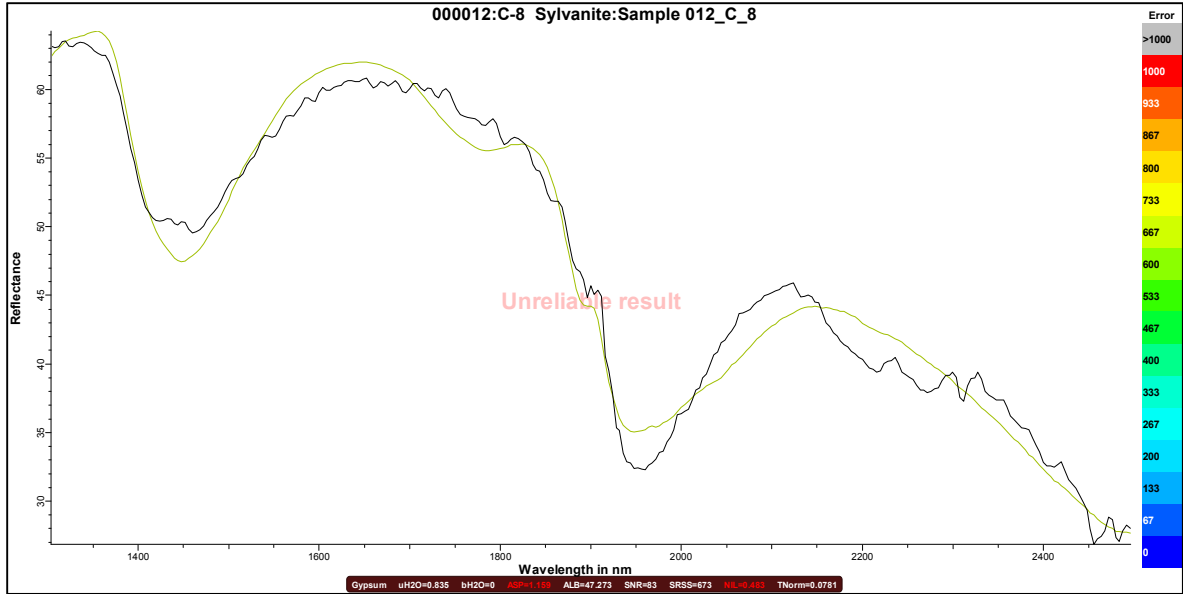


Figure A4.1.65- Sylvanite: Sample 012_C_8: Results are in the Short-Wave Infrared (SWIR). Graph created using The Spectral Geologist 8.0.7.4. software.



Figure A4.1.66-Sylvanite: Sample 012_C_8: The Spectral Geologist (ASCII) library list of other possible candidates. Closest candidate is denoted by an Astrid symbol *Gypsum [673] according to the ASCII library. Results are in the Short-Wave Infrared (SWIR). Graph created using The Spectral Geologist 8.0.7.4. software. (Black) line represent result spectra using the GER 3700 in direct comparison with the spectral geologist spectral (ASCII) library files (Green) line.

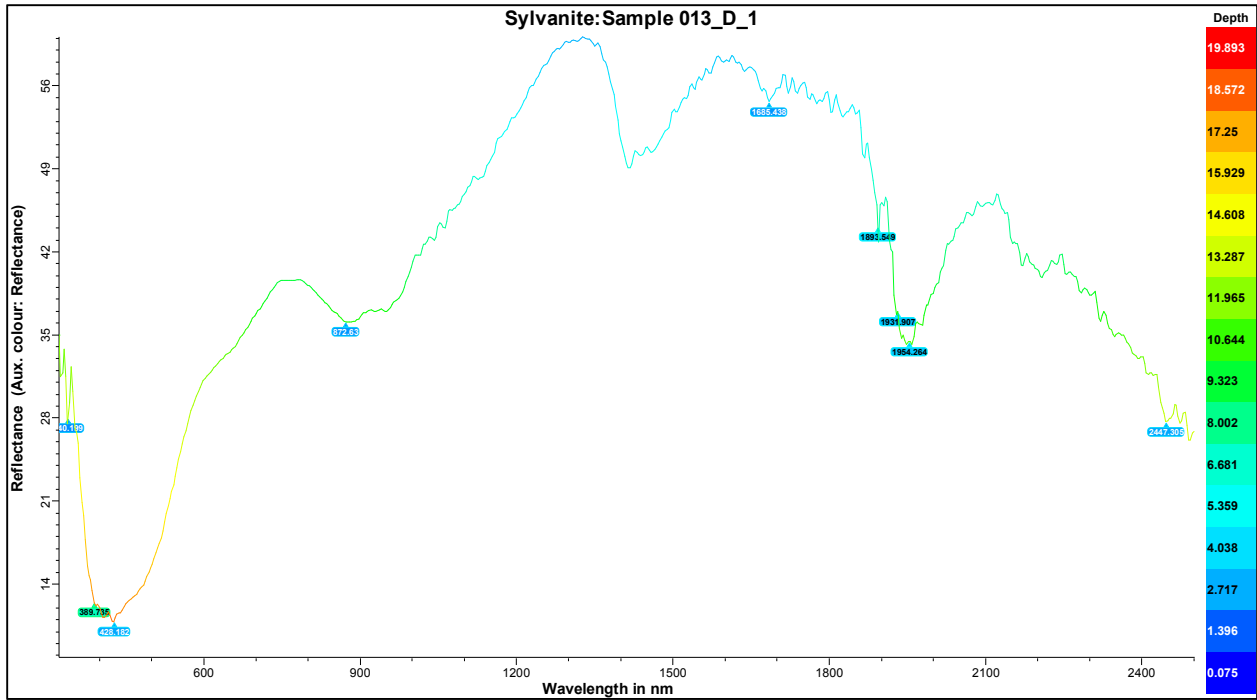


Figure A4.1.67- Sylvanite: Sample 013_D_1; Standard wavelength (CSV import data) with slight modifications.

Graph created using The Spectral Geologist 8.0.7.4. software

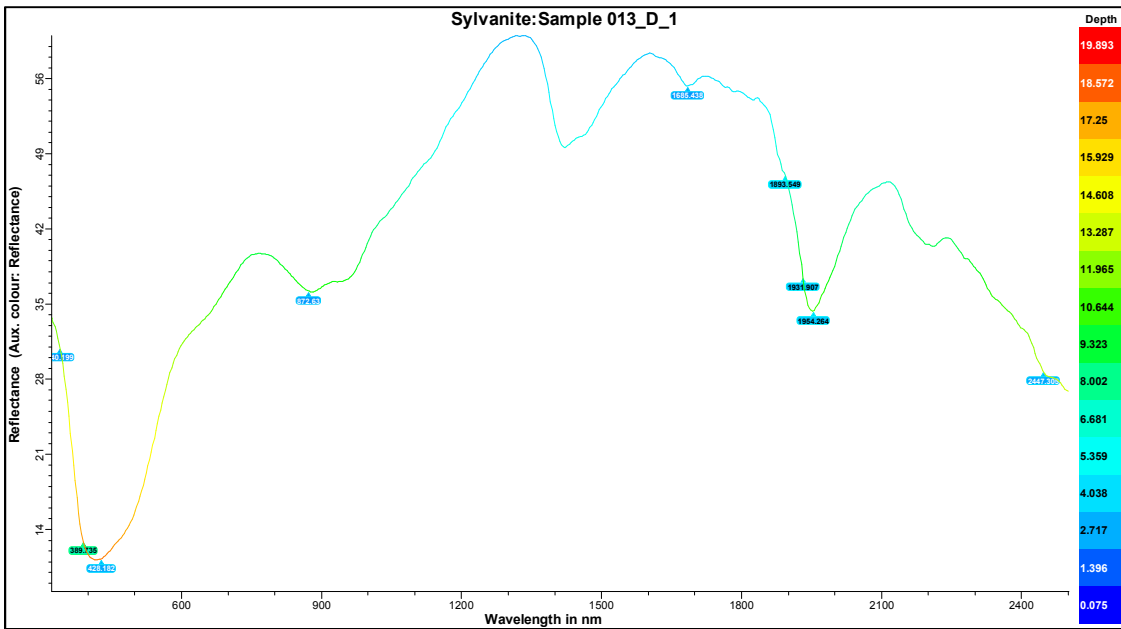


Figure A4.1.68- Sylvanite: Sample 013_D_1; Modified wavelength with feature wavelength (number tags) and smooth (Hi). Graph created using The Spectral Geologist 8.0.7.4. software.

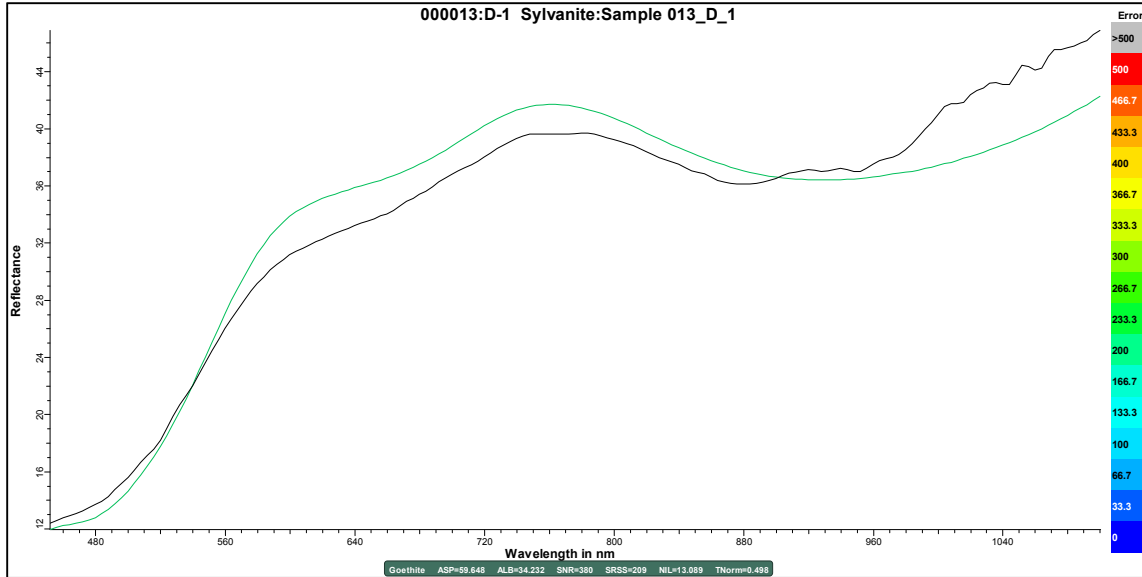


Figure A4.1.69- Sylvanite: Sample 013_D_1; *Goethite {209}) results are in the visible and near-infrared (VNIR). Graph created using The Spectral Geologist 8.0.7.4. software. (Black) line represent result spectra using the GER 3700 in direct comparison with the spectral geologist spectral (ASCII) library files (Green) line.

Candidate TSA results
*Goethite [209]
Goethite [919]
Hematite [1153]
Vegetation-Green [4011]
70%Goethite + 30%Hematite [89]
51%ODZincalume + 49%Goethite [158]
97%Goethite + 3%Vegetation-Green [197]
53%Goethite + 47%Hematite [271]
92%Goethite + 8%Vegetation-Green [814]
89%Hematite + 11%Vegetation-Green [930]

Figure A4.1.70- Sylvanite: Sample 013_D_1; *Goethite {209}) results are in the visible and near-infrared (VNIR). Graph created using The Spectral Geologist 8.0.7.4. software. (Black) line represent result spectra using the GER 3700 in direct comparison with the spectral geologist spectral (ASCII) library files (Green) line.

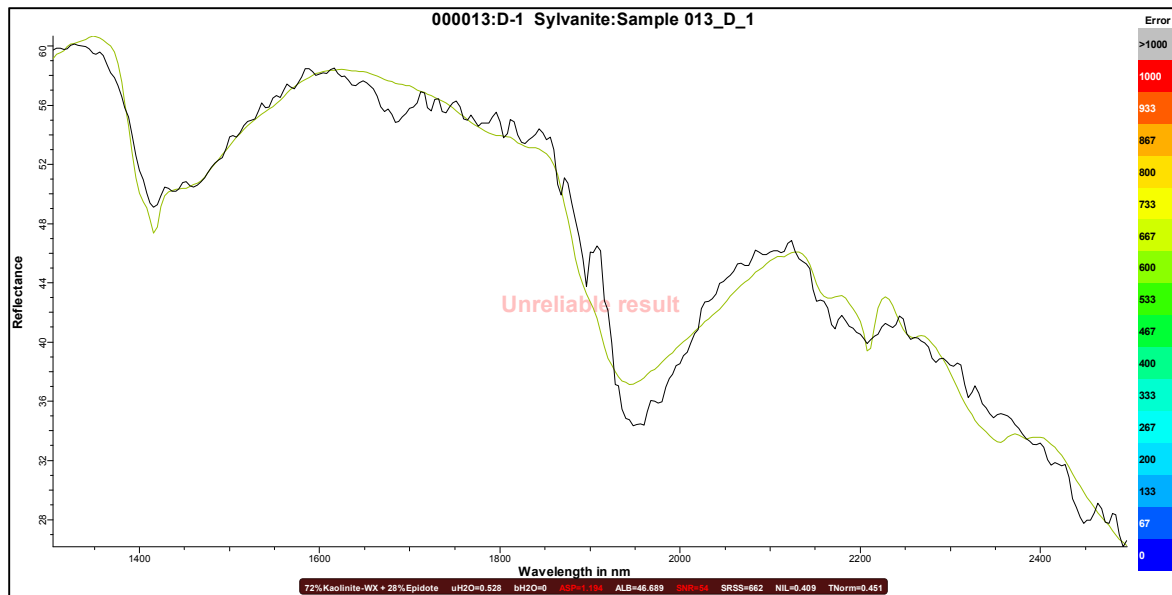


Figure A4.1.71- Sylvanite: Sample 013_D_1: Results are in the Short-Wave Infrared (SWIR). Graph created using The Spectral Geologist 8.0.7.4. software.

Candidate TSA results	
Kaolinite-WX [717]	74%Ankerite + 26%Alunite-K [704]
65%Kaolinite-WX + 35%Dolomite [653]	57%Dickite + 43%Alunite-Na [707]
57%Kaolinite-WX + 43%Ankerite [661]	73%Kaolinite-WX + 27%Chlorite-Mg [709]
*72%Kaolinite-WX + 28%Epidote [662]	75%Dolomite + 25%Topaz [709]
56%Siderite + 44%Kaolinite-WX [667]	80%Kaolinite-WX + 20%Magnesite [711]
74%Kaolinite-WX + 26%Alunite-Na [670]	65%Kaolinite-WX + 35%Chlorite-FeMg [711]
58%Dolomite + 42%Alunite-Na [675]	78%Kaolinite-WX + 22%Chlorite-FeMg [712]
67%Dolomite + 33%Alunite-K [688]	47%Kaolinite-WX + 33%Dolomite + 20%Alunite-Na [594]
83%Kaolinite-WX + 17%Alunite-K [688]	42%Kaolinite-WX + 40%Ankerite + 17%Alunite-Na [606]
66%Ankerite + 34%Alunite-Na [689]	53%Kaolinite-WX + 26%Epidote + 21%Alunite-Na [607]
77%Siderite + 23%Alunite-Na [692]	48%Kaolinite-WX + 31%Dolomite + 21%Alunite-NH [617]
51%Alunite-Na + 49%Epidote [698]	57%Dolomite + 28%Alunite-K + 16%Topaz [623]
79%Kaolinite-WX + 21%Alunite-NH [701]	43%Kaolinite-WX + 39%Ankerite + 18%Alunite-NH [628]
78%Kaolinite-WX + 22%Calcite [701]	41%Dolomite + 31%Dickite + 28%Alunite-Na [629]
83%Siderite + 17%Alunite-K [702]	
69%Alunite-Na + 31%Topaz [702]	

Figure A4.1.72-Sylvanite: Sample 013_D_1: The Spectral Geologist (ASCII) library list of other possible candidates. Closest candidate is denoted by an Astrid symbol *72 % Kaolinite-WX + 28% Epidote [662] according to the ASCII library. Results are in the Short-Wave Infrared (SWIR). Graph created using The Spectral Geologist 8.0.7.4. software. (Black) line represent result spectra using the GER 3700 in direct comparison with the spectral geologist spectral (ASCII) library files (Green) line.

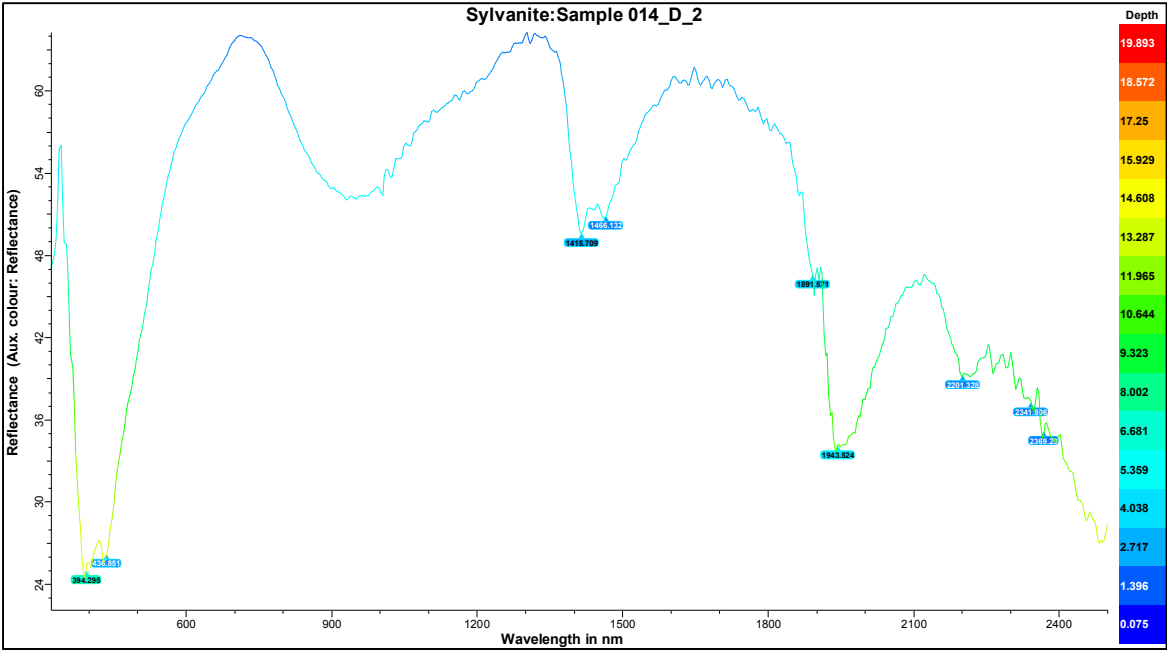


Figure A4.1.73- Sylvanite: Sample 014_D_2; Standard wavelength (CSV import data) with slight modifications.

Graph created using The Spectral Geologist 8.0.7.4. software

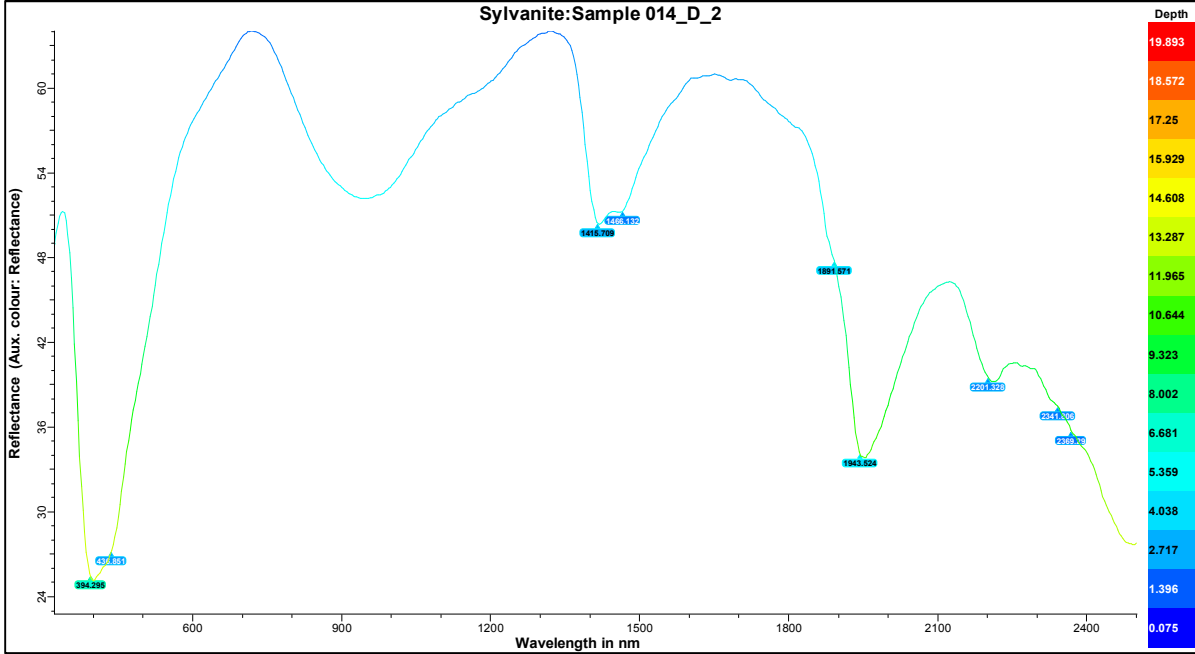


Figure A4.1.74- Sylvanite: Sample 014_D_2; Modified wavelength with feature wavelength (number tags) and smooth (Hi). Graph created using The Spectral Geologist 8.0.7.4. software.

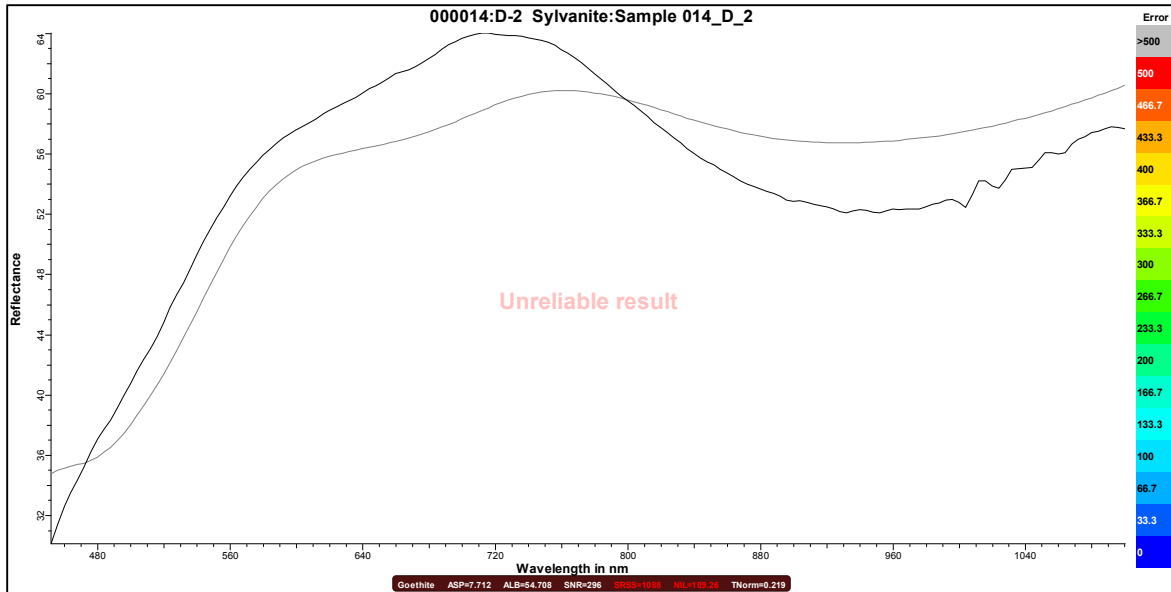


Figure A4.1.75- Sylvanite: Sample 014_D_2; *Goethite {1088} results are in the visible and near-infrared (VNIR). Graph created using The Spectral Geologist 8.0.7.4. software. (Black) line represent result spectra using the GER 3700 in direct comparison with the spectral geologist spectral (ASCII) library files (Grey) line.

Candidate TSA results	
*Goethite [1088]	
Goethite [1438]	
Hematite [1709]	
Vegetation-Green [3956]	
61%GalvanisedIron + 39%Goethite [759]	
74%ODZincalume + 26%Goethite [819]	
73%Goethite + 27%Hematite [1031]	
57%Goethite + 43%Hematite [1109]	
61%GalvanisedIron + 39%Hematite [1230]	
51%ODZincalume + 49%Goethite [1390]	
70%Goethite + 30%GalvanisedIron [1406]	
100%Goethite + 0%Vegetation-Green [1438]	
95%Hematite + 5%Vegetation-Green [1683]	
75%ODZincalume + 25%Vegetation-Green [3901]	
95%Vegetation-Green + 5%GalvanisedIron [3956]	

Figure A4.1.76- Sylvanite: Sample 014_D_2; *Goethite {1088} results are in the visible and near-infrared (VNIR). Graph created using The Spectral Geologist 8.0.7.4. software. (Black) line represent result spectra using the GER 3700 in direct comparison with the spectral geologist spectral (ASCII) library files (Light Grey) line.

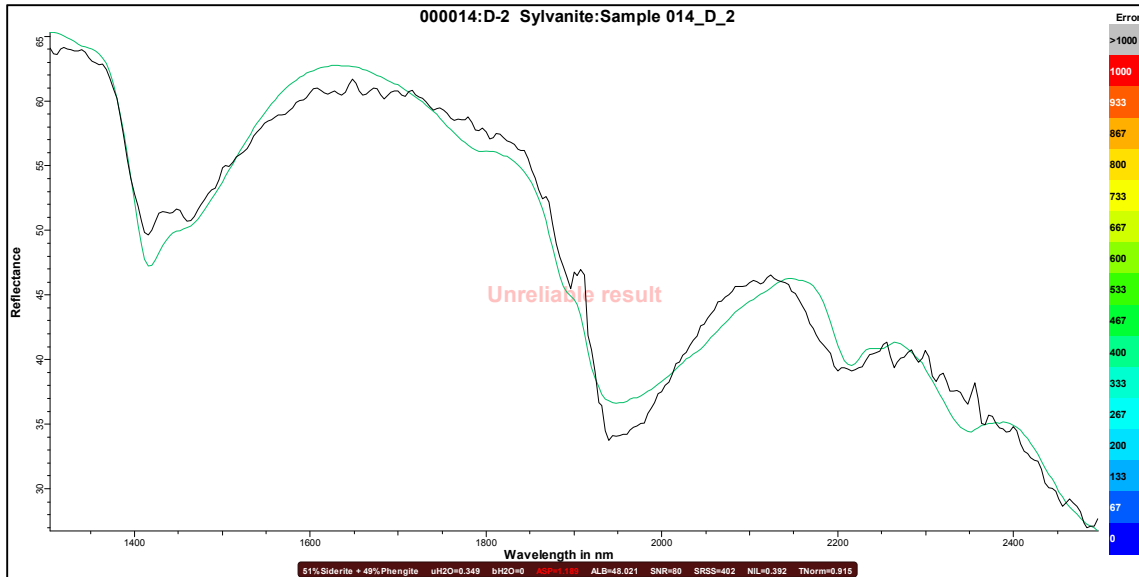


Figure A4.1.77- Sylvanite: Sample 014_D_2: Results are in the Short-Wave Infrared (SWIR). Graph created using The Spectral Geologist 8.0.7.4. software.

Candidate TSA results	
Muscovite [462]	56% Muscovite + 44% Chlorite-Mg [437]
Muscovite [465]	59% Phengite + 41% Dolomite [437]
Phengite [467]	51% Ankerite + 49% Phengite [437]
*51% Siderite + 49% Phengite [402]	61% Phengite + 39% Chlorite-Mg [439]
80% Muscovite + 20% Gypsum [405]	76% Phengite + 24% Calcite [439]
83% Phengite + 17% Gypsum [409]	75% Muscovite + 25% Calcite [440]
81% Muscovite + 19% Gypsum [409]	74% Muscovite + 26% Calcite [440]
53% Siderite + 47% Muscovite [410]	59% Muscovite + 41% Chlorite-Mg [441]
55% Siderite + 45% Muscovite [412]	56% Chlorite-Fe + 44% Muscovite [441]
63% Phengite + 37% Ankerite [413]	80% Muscovite + 20% Jarosite [444]
61% Muscovite + 39% Ankerite [414]	54% Chlorite-Fe + 46% Muscovite [445]
72% Phengite + 28% Dolomite [415]	55% Siderite + 28% Phengite + 17% Alunite-NH [371]
58% Muscovite + 42% Ankerite [416]	50% Phengite + 33% Ankerite + 17% Alunite-NH [374]
70% Muscovite + 30% Dolomite [417]	56% Phengite + 25% Dolomite + 19% Alunite-NH [375]
68% Muscovite + 32% Dolomite [420]	
64% Siderite + 36% Phengite [425]	
73% Phengite + 27% Gypsum [429]	
84% Chlorite-Fe + 16% Gypsum [431]	

Figure A4.1.78-Sylvanite: Sample 014_D_2: The Spectral Geologist (ASCII) library list of other possible candidates. Closest candidate is denoted by an Astrid symbol *51 % Siderite + 49% Phengite [402] according to the ASCII library. Results are in the Short-Wave Infrared (SWIR). Graph created using The Spectral Geologist 8.0.7.4. software. (Black) line represent result spectra using the GER 3700 in direct comparison with the spectral geologist spectral (ASCII) library files (Green) line.

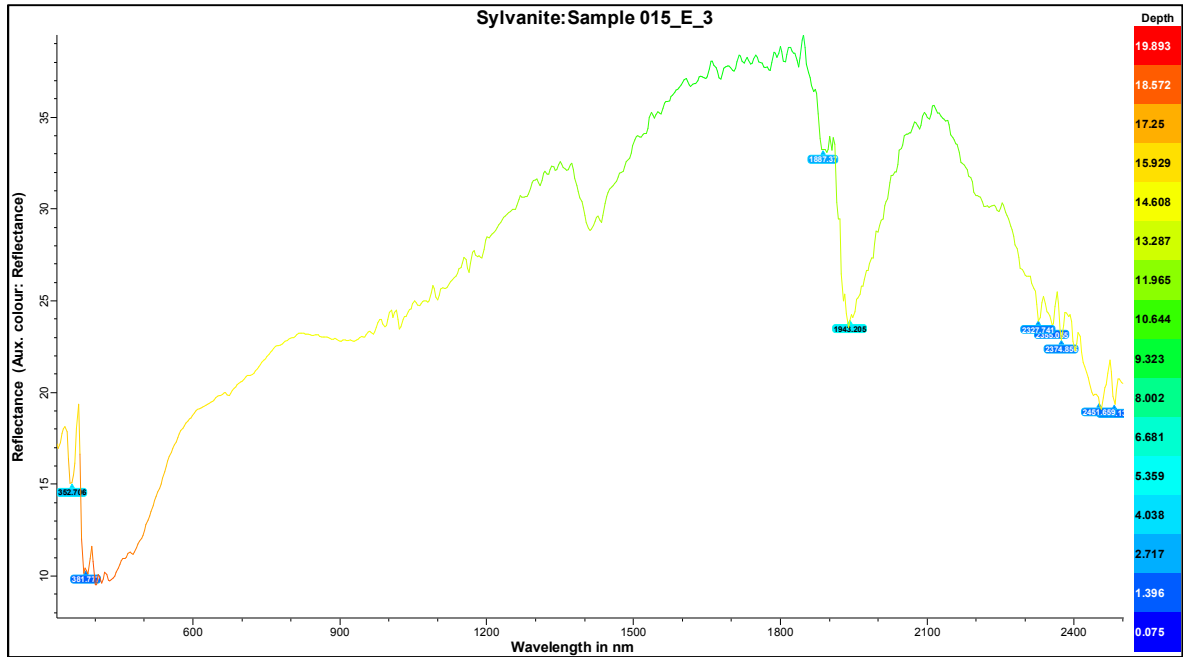


Figure A4.1.79- Sylvanite: Sample 015_E_3; Standard wavelength (CSV import data) with slight modifications.

Graph created using The Spectral Geologist 8.0.7.4. software

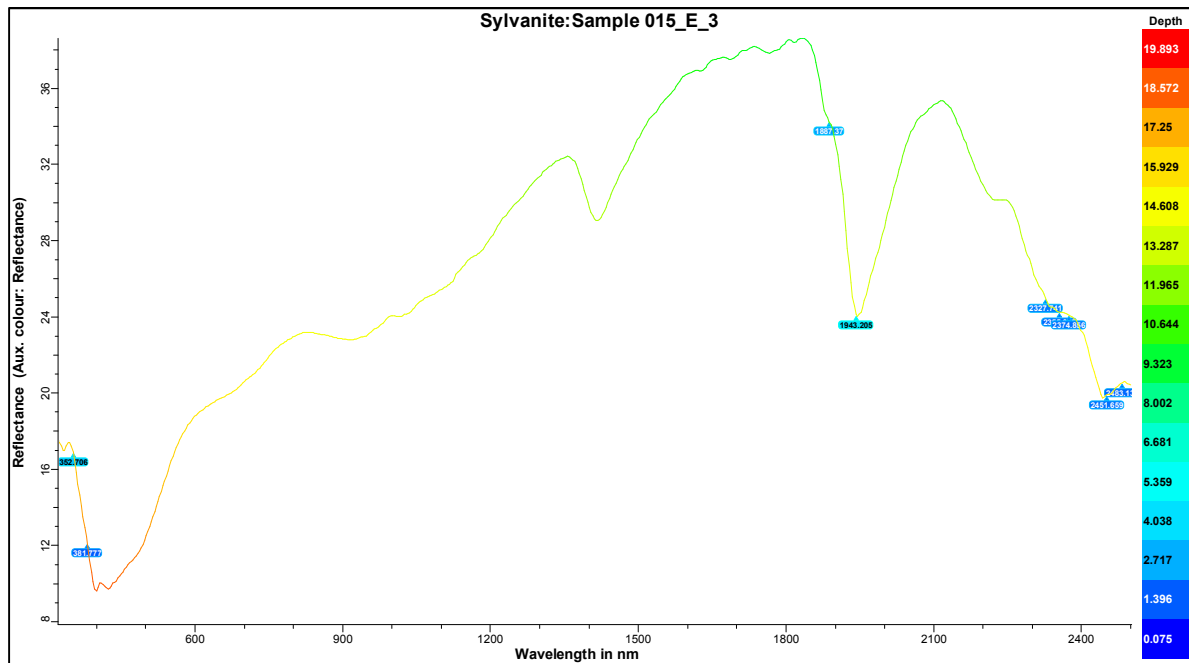


Figure A4.1.80- Sylvanite: Sample 015_E_3; Modified wavelength with feature wavelength (number tags) and smooth (Hi). Graph created using The Spectral Geologist 8.0.7.4. software.

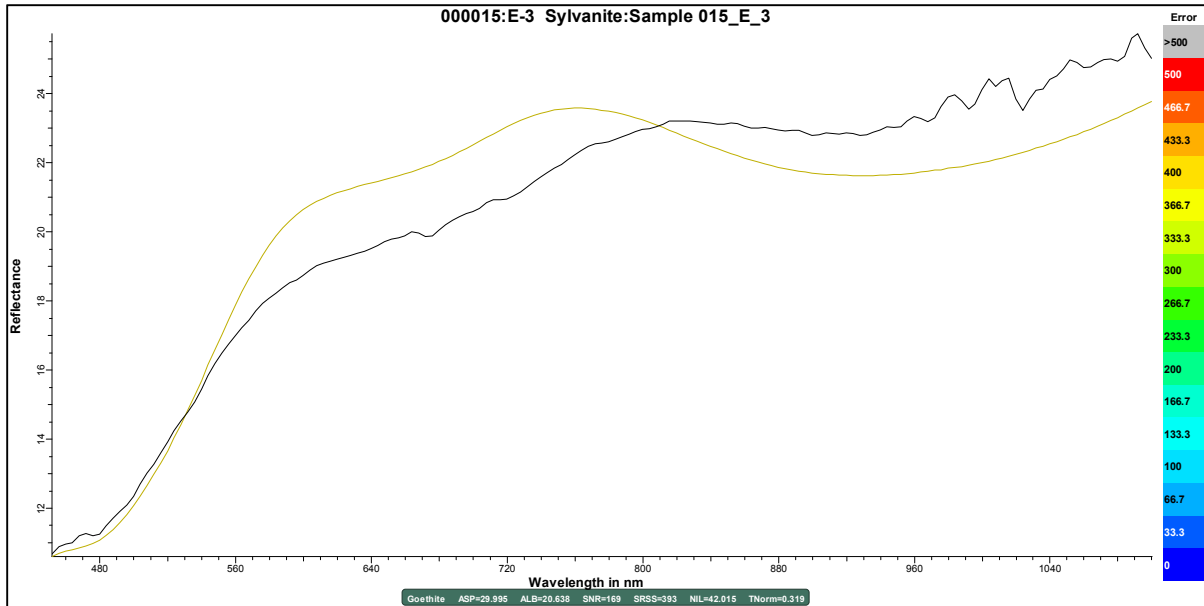


Figure A4.1.81- Sylvanite: Sample 015_E_3; *Goethite {393}) results are in the visible and near-infrared (VNIR). Graph created using The Spectral Geologist 8.0.7.4. software. (Black) line represent result spectra using the GER 3700 in direct comparison with the spectral geologist spectral (ASCII) library files (Brown) line.

Candidate TSA results	
*Goethite [393]	
Goethite [1340]	
Hematite [1706]	
Vegetation-Green [3190]	
90%Goethite + 10%Vegetation-Green [286]	
85%Goethite + 15%Hematite [368]	
56%Goethite + 44%Hematite [826]	
84%Goethite + 16%Vegetation-Green [996]	
80%Hematite + 20%Vegetation-Green [1150]	

Figure A4.1.82- Sylvanite: Sample 015_E_3; *Goethite {393}) results are in the visible and near-infrared (VNIR). Graph created using The Spectral Geologist 8.0.7.4. software. (Black) line represent result spectra using the GER 3700 in direct comparison with the spectral geologist spectral (ASCII) library files (Brown) line.

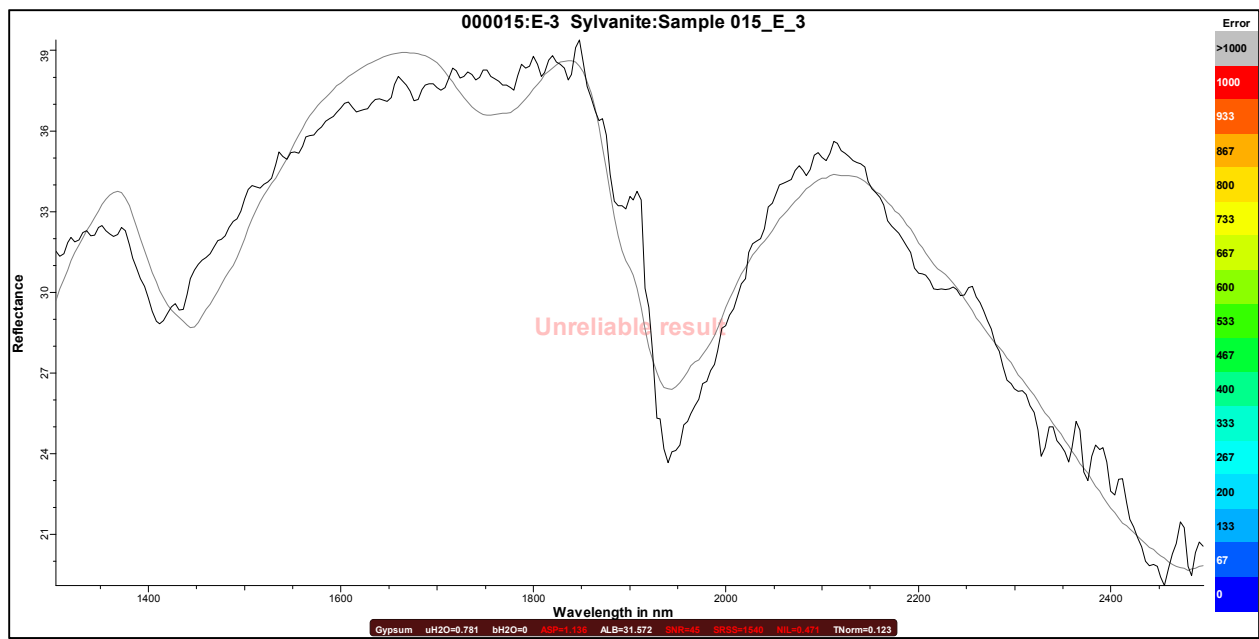


Figure A4.1.83- Sylvaniaite: Sample 015_E_3: Results are in the Short-Wave Infrared (SWIR). Graph created using The Spectral Geologist 8.0.7.4. software.

Candidate TSA results	
*Gypsum	[1540]
Ankerite	[1615]
Alunite-Na	[1618]
Dickite	[1621]
Nacrite	[1623]
Dolomite	[1623]
Tourmaline	[1625]
Alunite-K	[1637]
Siderite	[1649]
Muscovite	[1671]
Muscovite	[1675]
Phengite	[1677]
Phengite	[1683]
Alunite-NH	[1691]
Paragonite	[1694]
Epidote	[1698]
Calcite	[1698]
Topaz	[1708]
Kaolinite-WX	[1710]
Pyrophyllite	[1712]
Talc	[1714]
IsaYellow	[1714]
YellowMarker	[1717]
Rubellite	[1717]
IsaWhite	[1718]
Kaolinite-PX	[1719]
PlasticChipTray	[1724]
Magnesite	[1724]

Magnesite	[1724]
WhiteMarker	[1725]
56%Gypsum + 44%Tourmaline	[1397]
61%Dickite + 39%Gypsum	[1430]
67%Nacrite + 33%Gypsum	[1433]
61%Dolomite + 39%Gypsum	[1450]
70%Ankerite + 30%Gypsum	[1451]
66%Muscovite + 34%Gypsum	[1465]
71%Phengite + 29%Gypsum	[1467]
60%Dolomite + 40%Alunite-Na	[1470]
64%Phlogopite + 36%Gypsum	[1470]
68%Muscovite + 32%Gypsum	[1470]
69%Ankerite + 31%Alunite-Na	[1471]
59%Phengite + 41%Gypsum	[1473]
67%Dolomite + 33%Alunite-K	[1474]
76%Ankerite + 24%Alunite-K	[1478]
55%Ankerite + 45%Nacrite	[1480]
76%Siderite + 24%Gypsum	[1481]
68%Chlorite-Mg + 32%Gypsum	[1483]
66%Gypsum + 34%WhiteMarker	[1488]
55%Nacrite + 45%Dolomite	[1492]
54%Paragonite + 46%Gypsum	[1494]
76%Gypsum + 24%Topaz	[1498]

Figure A4.1.84-Sylvaniaite: Sample 015_E_3: The Spectral Geologist (ASCII) library list of other possible candidates. Closest candidate is denoted by an Astrid symbol *Gypsum [1540] according to the ASCII library. Results are in the Short-Wave Infrared (SWIR). Graph created using The Spectral Geologist 8.0.7.4. software. (Black) line represent result spectra using the GER 3700 in direct comparison with the spectral geologist spectral (ASCII) library files (Light Grey) line.

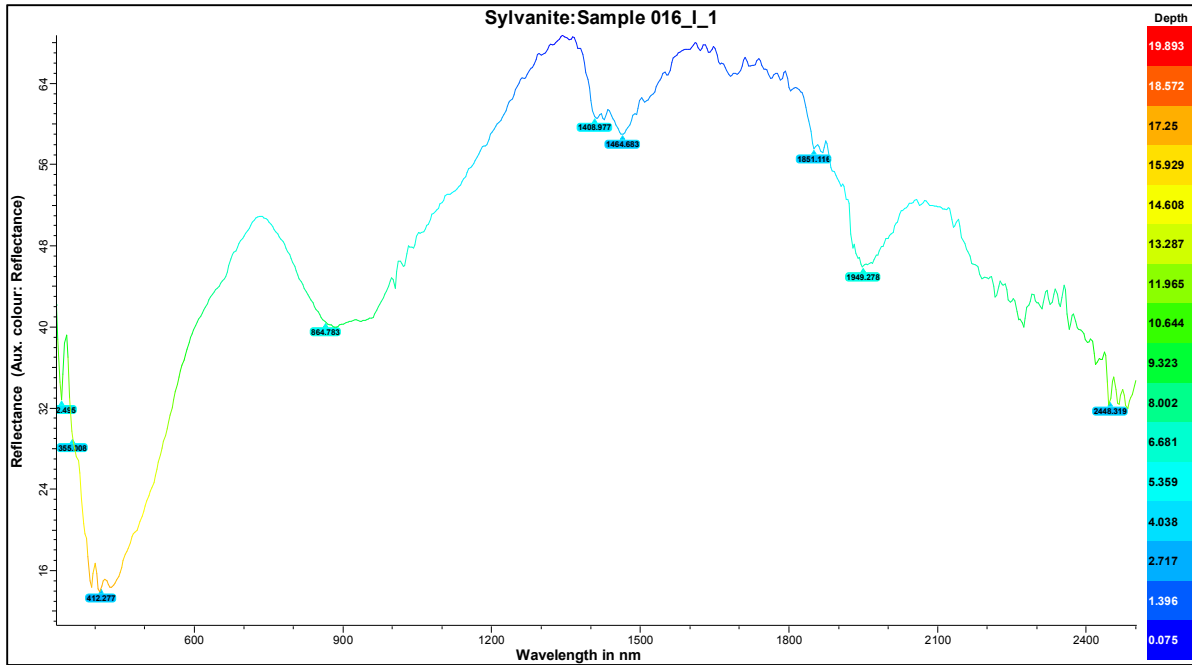


Figure A4.1.85- Sylvanite: Sample 016_I_1; Standard wavelength (CSV import data) with slight modifications.

Graph created using The Spectral Geologist 8.0.7.4. software

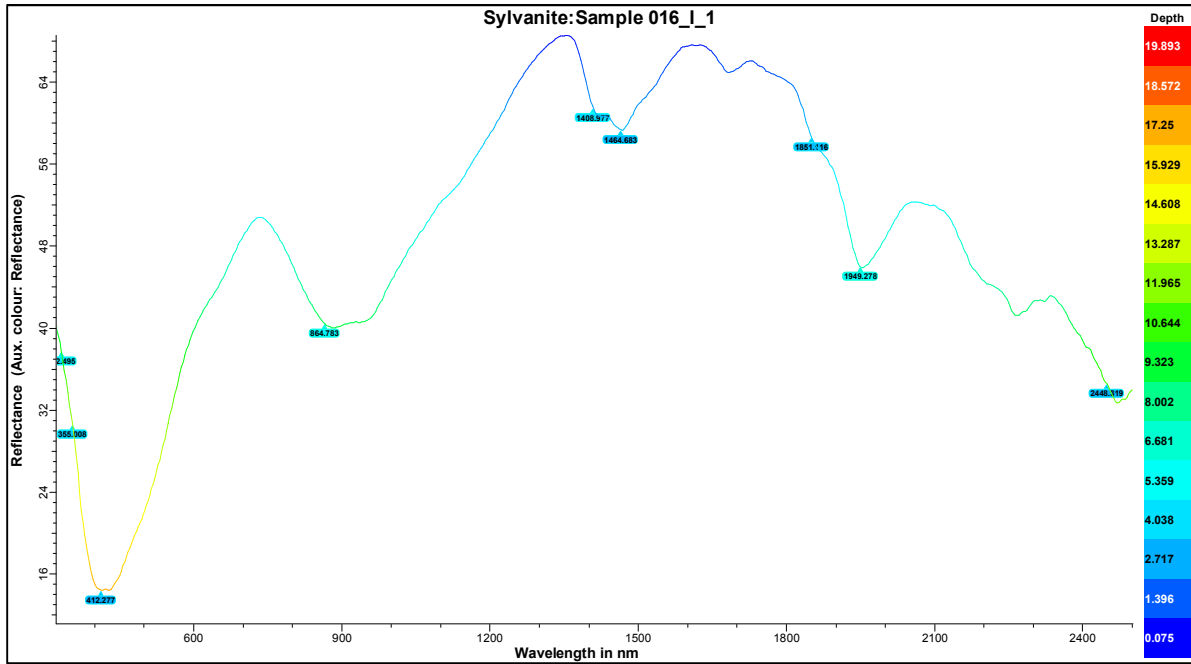


Figure A4.1.86- Sylvanite: Sample 016_I_1; Modified wavelength with feature wavelength (number tags) and smooth (Hi). Graph created using The Spectral Geologist 8.0.7.4. software.

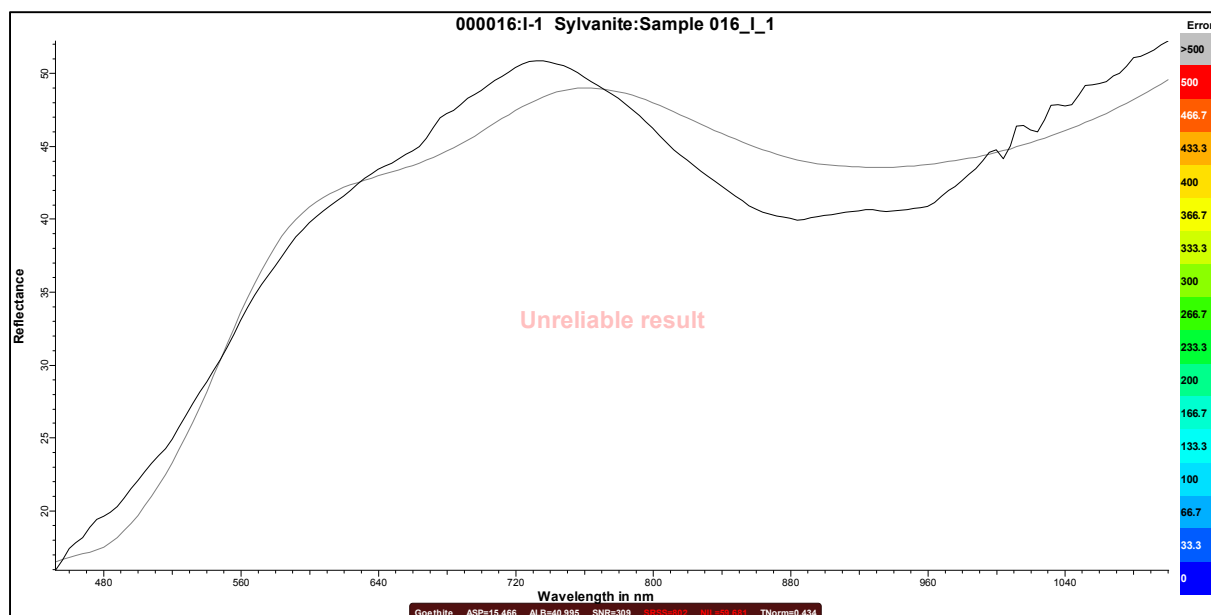


Figure A4.1.87- Sylvanite: Sample 016_I_1; *Goethite {802}) results are in the visible and near-infrared (VNIR).

Graph created using The Spectral Geologist 8.0.7.4. software. (Black) line represent result spectra using the GER 3700 in direct comparison with the spectral geologist spectral (ASCII) library files (Brown) line.

Candidate TSA results
*Goethite [802]
Hematite [960]
Goethite [1478]
Vegetation-Green [5008]
51%Hematite + 49%Goethite [413]
73%ODZincalume + 27%Goethite [437]
59%Hematite + 41%Goethite [451]
71%Goethite + 29%GalvanisedIron [773]
57%Hematite + 43%GalvanisedIron [808]
97%Hematite + 3%Vegetation-Green [936]
54%Goethite + 46%ODZincalume [1430]
97%Goethite + 3%Vegetation-Green [1459]
75%ODZincalume + 25%Vegetation-Green [4923]

Figure A4.1.88- Sylvanite: Sample 016_I_1; *Goethite {802}) results are in the visible and near-infrared (VNIR).

Graph created using The Spectral Geologist 8.0.7.4. software. (Black) line represent result spectra using the GER 3700 in direct comparison with the spectral geologist spectral (ASCII) library files (Dark Grey) line.

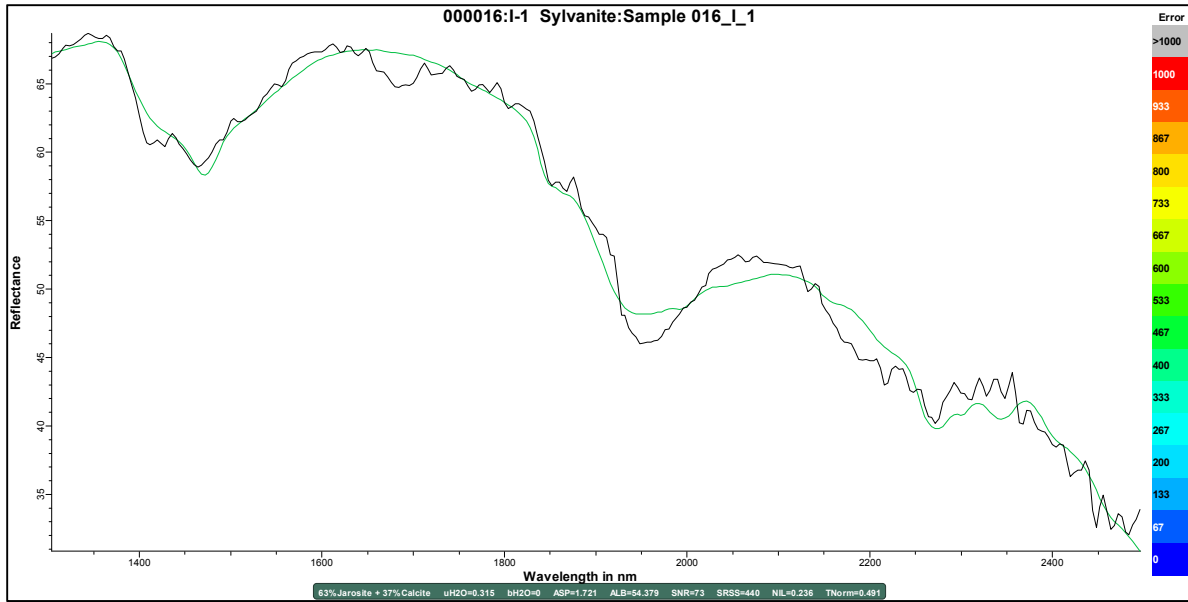


Figure A4.1.89- Sylvania: Sample 016_I_1: Results are in the Short-Wave Infrared (SWIR). Graph created using The Spectral Geologist 8.0.7.4. software.

Candidate TSA results	
56%Jarosite + 44%Phlogopite [439]	83%Jarosite + 17%Talc [500]
*63%Jarosite + 37%Calcite [440]	57%Jarosite + 43%Chlorite-Fe [502]
53%Chlorite-Mg + 47%Jarosite [448]	79%Jarosite + 21%Zoisite [503]
59%Siderite + 41%Jarosite [451]	85%Jarosite + 15%Tremolite [503]
65%Jarosite + 35%Phlogopite [461]	48%Jarosite + 31%Phlogopite + 20%Calcite [396]
64%Jarosite + 36%Serpentine [465]	53%Jarosite + 24%Calcite + 23%Phlogopite [406]
59%Jarosite + 41%Ankerite [465]	47%Jarosite + 33%Phlogopite + 20%Ankerite [416]
75%Jarosite + 25%Epidote [468]	40%Jarosite + 33%Siderite + 26%Phlogopite [417]
52%Chlorite-FeMg + 48%Jarosite [472]	55%Jarosite + 25%Calcite + 20%Serpentine [422]
69%Jarosite + 31%Dolomite [472]	49%Jarosite + 26%Ankerite + 25%Phlogopite [424]
55%Jarosite + 45%Chlorite-FeMg [473]	49%Jarosite + 31%Chlorite-Mg + 20%Calcite [426]
58%Jarosite + 42%Chlorite-Mg [480]	41%Jarosite + 41%Siderite + 18%Phlogopite [426]
82%Jarosite + 18%Pyrophyllite [482]	47%Jarosite + 27%Phlogopite + 26%Chlorite-Mg [428]
55%Chlorite-FeMg + 45%Jarosite [485]	48%Jarosite + 36%Phlogopite + 16%Riebeckite [429]
54%Jarosite + 46%Chlorite-FeMg [487]	52%Jarosite + 28%Calcite + 20%Riebeckite [429]
67%Jarosite + 33%Riebeckite [497]	49%Jarosite + 33%Phlogopite + 18%Chlorite-FeMg [430]
79%Jarosite + 21%Actinolite [497]	
83%Jarosite + 17%Gibbsite [498]	
72%Jarosite + 28%Hornblende [499]	

Figure A4.1.90-Sylvania: Sample 016_I_1: The Spectral Geologist (ASCII) library list of other possible candidates. Closest candidate is denoted by an Astrid symbol *63 % Jarosite + 37 % Calcite [440] according to the ASCII library. Results are in the Short-Wave Infrared (SWIR). Graph created using The Spectral Geologist 8.0.7.4. software. (Black) line represent result spectra using the GER 3700 in direct comparison with the spectral geologist spectral (ASCII) library files (Green) line.

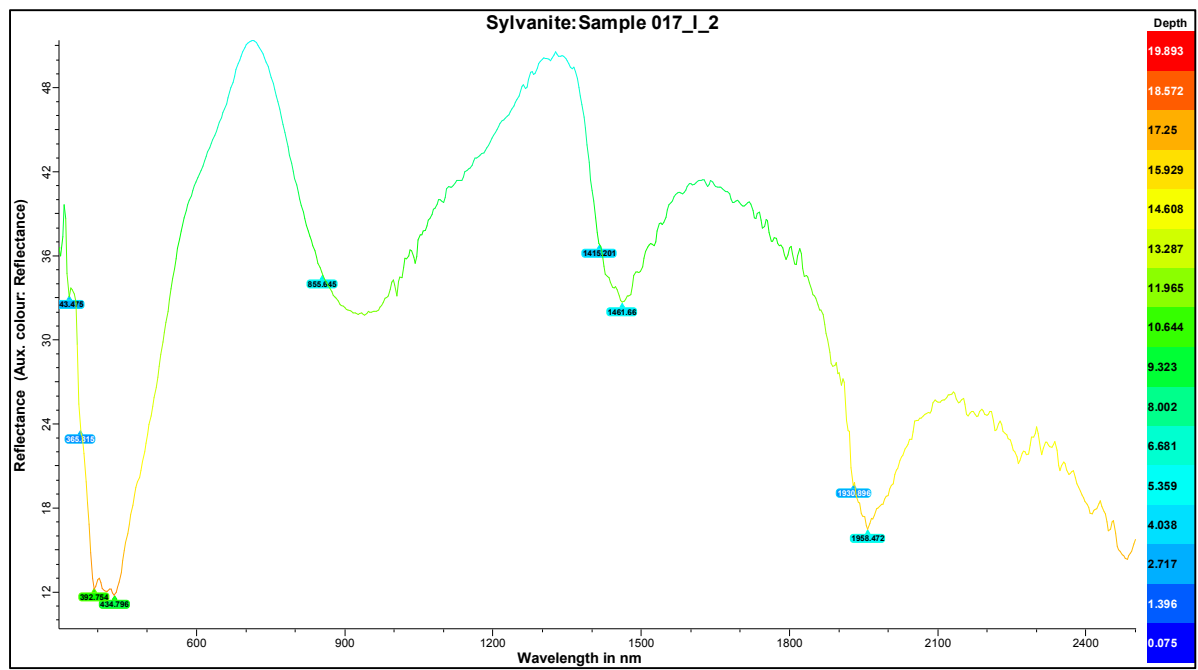


Figure A4.1.91- Sylvanite: Sample 017_I_2; Standard wavelength (CSV import data) with slight modifications.

Graph created using The Spectral Geologist 8.0.7.4. software

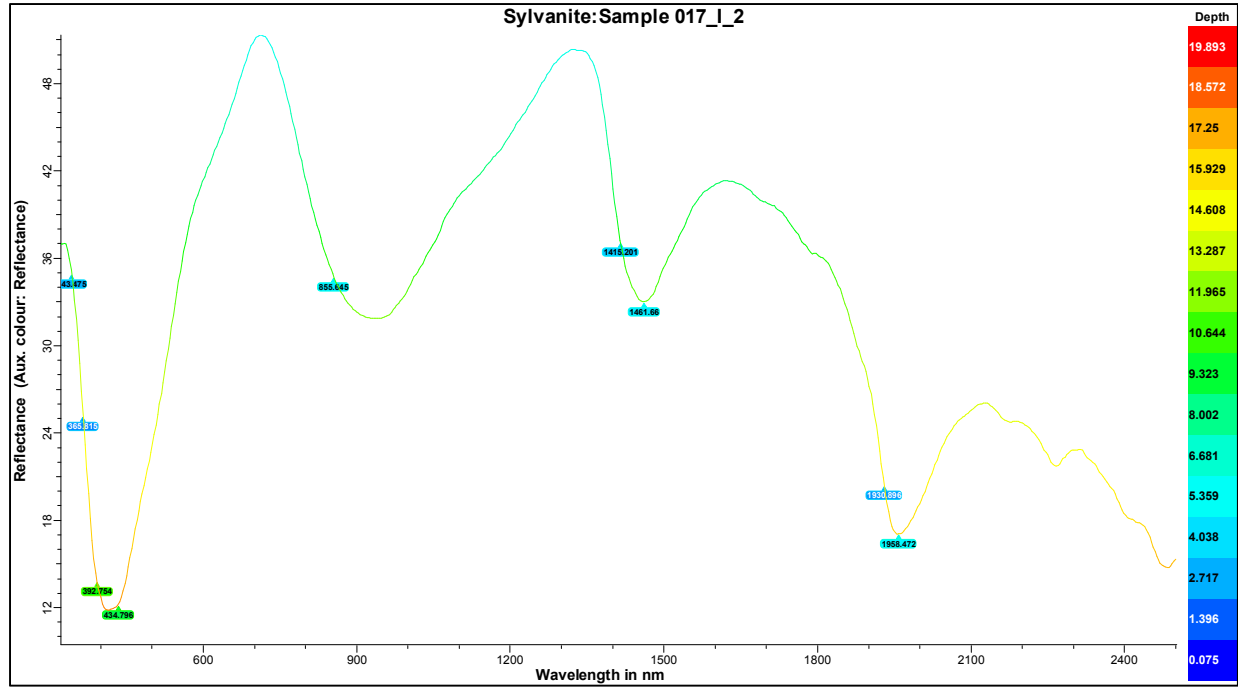


Figure A4.1.92- Sylvanite: Sample 017_I_2; Modified wavelength with feature wavelength (number tags) and smooth (Hi). Graph created using The Spectral Geologist 8.0.7.4. software.

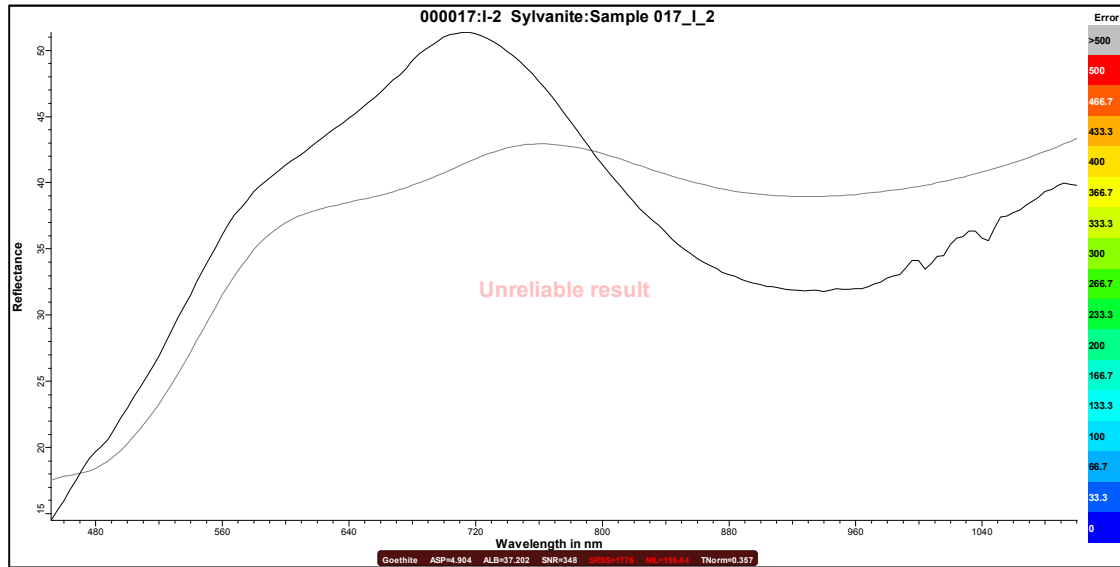


Figure A4.1.93- Sylvanite: Sample 017_I_2; *Goethite {1776}) results are in the visible and near-infrared (VNIR). Graph created using The Spectral Geologist 8.0.7.4. software. (Black) line represent result spectra using the GER 3700 in direct comparison with the spectral geologist spectral (ASCII) library files (Brown) line.

Candidate TSA results	
*Goethite	[1776]
Goethite	[1929]
Hematite	[2079]
Vegetation-Green	[4998]
81%ODZincalume + 19%Goethite	[1093]
67%GalvanisedIron + 33%Goethite	[1209]
67%GalvanisedIron + 33%Hematite	[1230]
54%Goethite + 46%Hematite	[1554]
59%Goethite + 41%Hematite	[1633]
71%ODZincalume + 29%Goethite	[1642]
54%Goethite + 46%GalvanisedIron	[1790]
53%Hematite + 47%ODZincalume	[2043]
86%ODZincalume + 14%Vegetation-Green	[4776]
54%Vegetation-Green + 46%GalvanisedIron	[4983]

Figure A4.1.94- Sylvanite: Sample 017_I_2; *Goethite {1776}) results are in the visible and near-infrared (VNIR). Graph created using The Spectral Geologist 8.0.7.4. software. (Black) line represent result spectra using the GER 3700 in direct comparison with the spectral geologist spectral (ASCII) library files (Dark Grey) line.

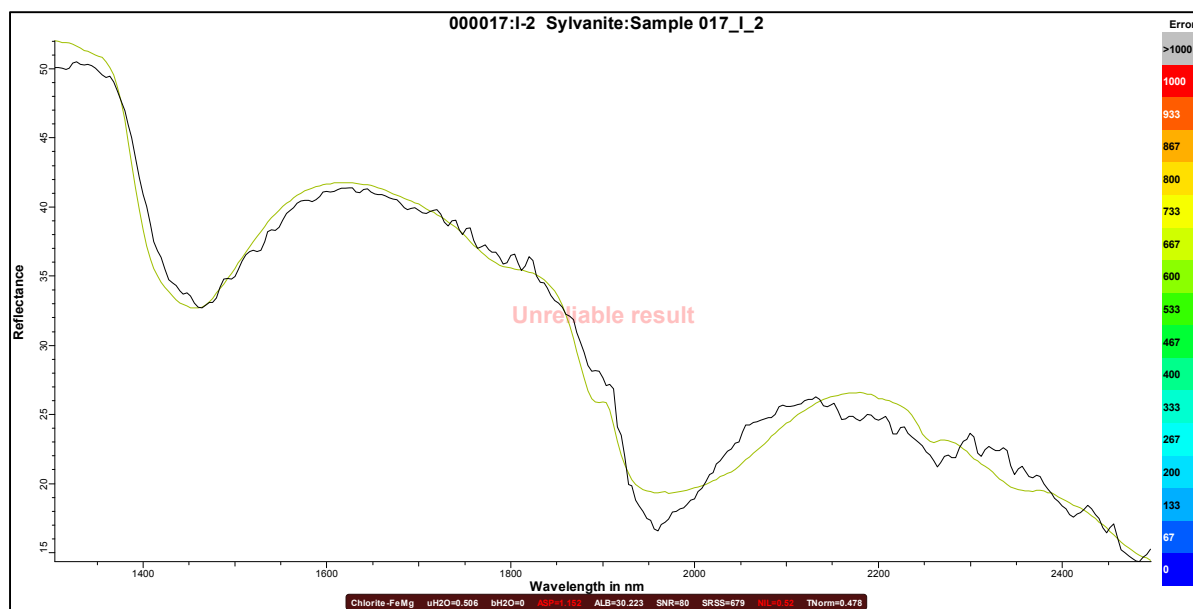


Figure A4.1.95- Sylvanite: Sample 017_I_2: Results are in the Short-Wave Infrared (SWIR). Graph created using The Spectral Geologist 8.0.7.4. software.

Candidate TSA results	
Jarosite [604]	
Siderite [630]	
Gypsum [643]	
Gibbsite [669]	
Ankerite [670]	
Calcite [671]	
Riebeckite [677]	
IsaYellow [678]	
*Chlorite-FeMg [679]	
Chlorite-Fe [681]	
IsaWhite [681]	
YellowMarker [682]	
Chlorite-FeMg [683]	
Chlorite-Mg [684]	
Tremolite [685]	
Actinolite [686]	
PlasticChipTray [686]	
Hornblende [687]	
WhiteMarker [687]	
Pyrophyllite [688]	
Chlorite-FeMg [689]	
Talc [690]	
Epidote [691]	

Figure A4.1.96-Sylvanite: Sample 017_I_2: The Spectral Geologist (ASCII) library list of other possible candidates. Closest candidate is denoted by an Astrid symbol *Chlorite-FeMg [679] according to the ASCII library.

Results are in the Short-Wave Infrared (SWIR). Graph created using The Spectral Geologist 8.0.7.4. software.

(Black) line represent result spectra using the GER 3700 in direct comparison with the spectral geologist spectral (ASCII) library files (Green) line.

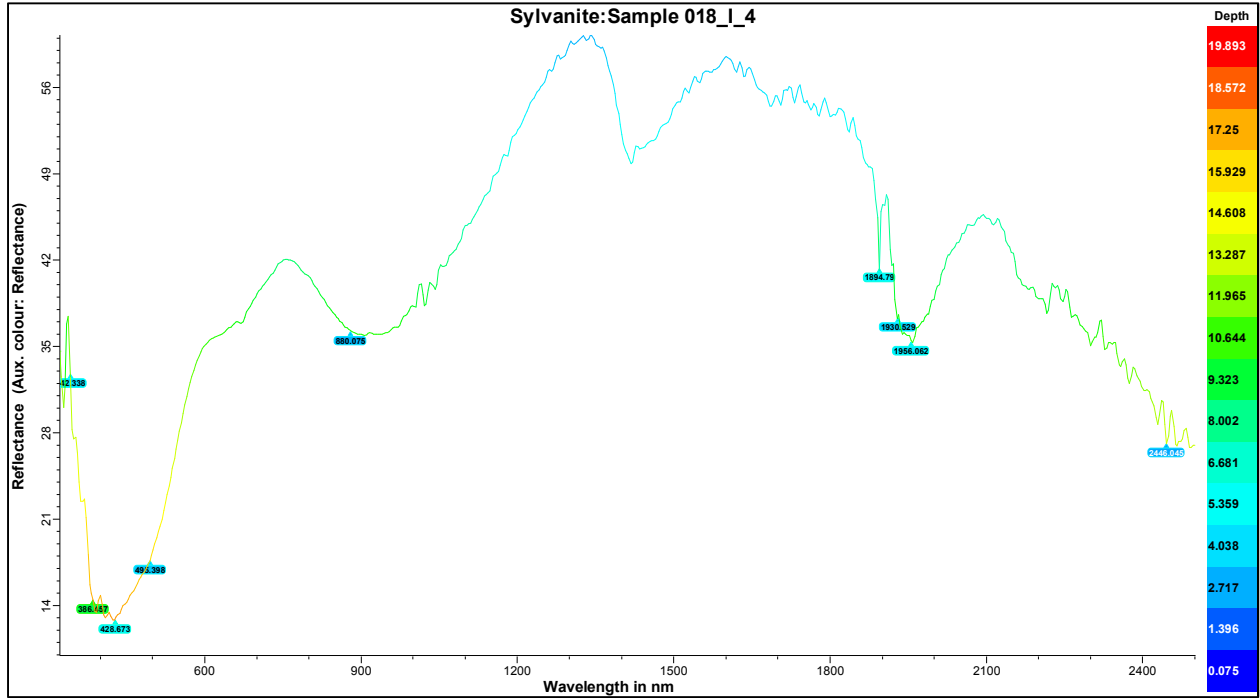


Figure A4.1.97- Sylvanite: Sample 018_I_4; Standard wavelength (CSV import data) with slight modifications.

Graph created using The Spectral Geologist 8.0.7.4. software

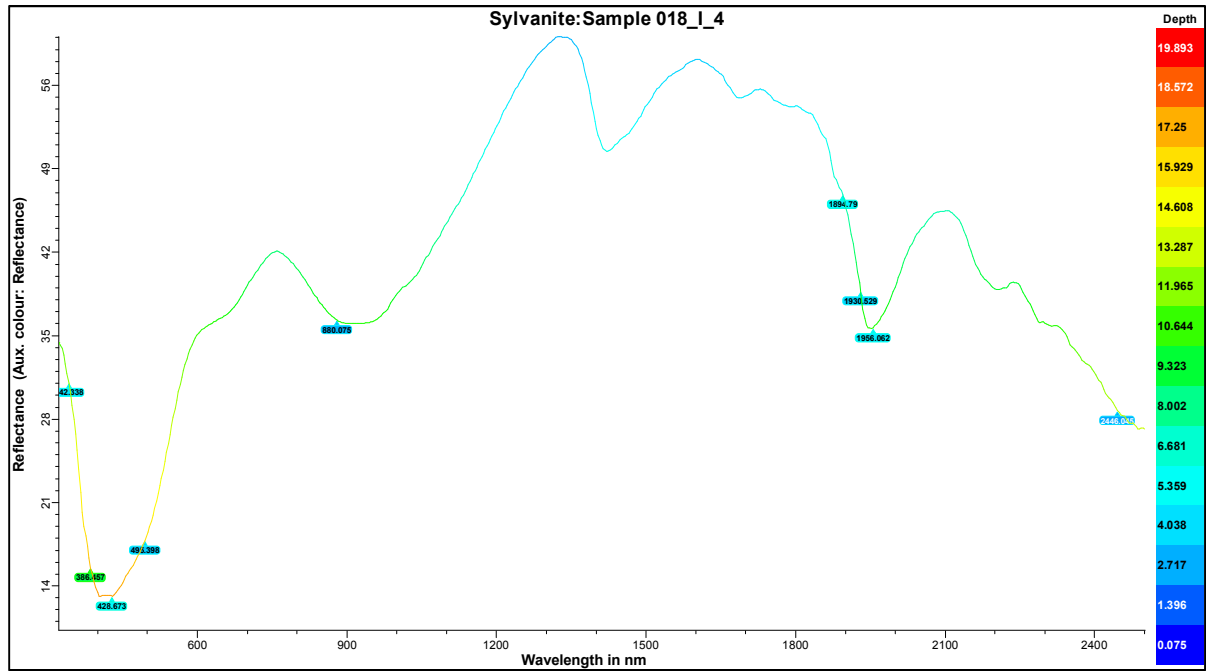


Figure A4.1.98- Sylvanite: Sample 018_I_4; Modified wavelength with feature wavelength (number tags) and smooth (Hi). Graph created using The Spectral Geologist 8.0.7.4. software.

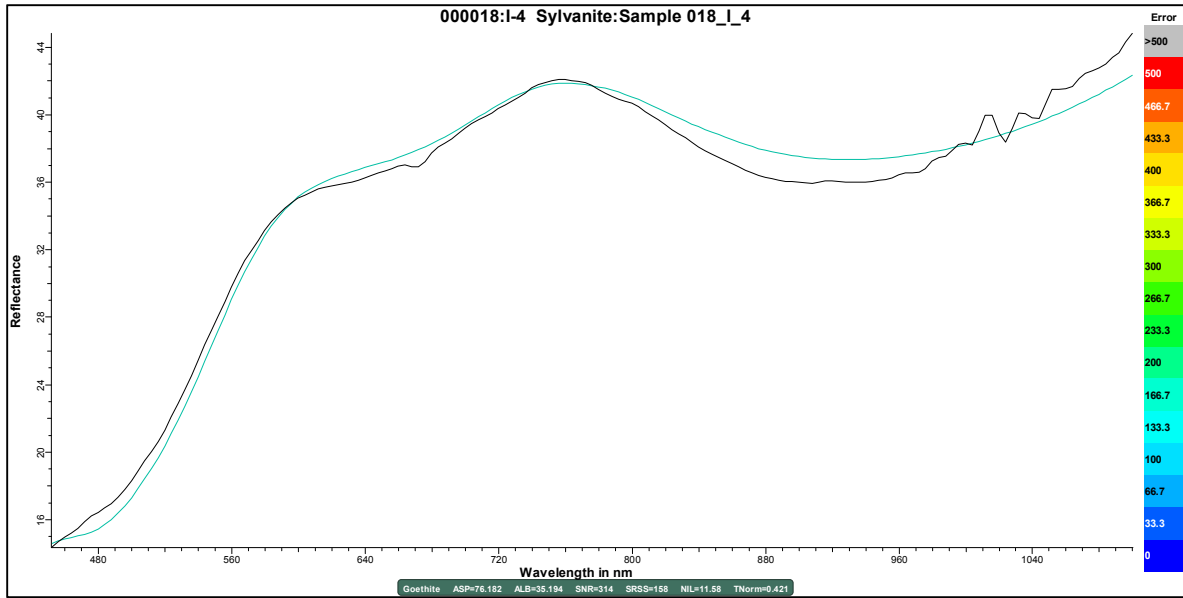


Figure A4.1.99- Sylvanite: Sample 018_I_4; *Goethite {158}) results are in the visible and near-infrared (VNIR). Graph created using The Spectral Geologist 8.0.7.4. software. (Black) line represent result spectra using the GER 3700 in direct comparison with the spectral geologist spectral (ASCII) library files (Brown) line.

Candidate TSA results	
*Goethite	[158]
Goethite	[550]
Hematite	[1433]
Vegetation-Green	[3904]
58%ODZincalume + 42%Goethite	[72]
82%Goethite + 18%Hematite	[118]
75%Goethite + 25%GalvanisedIron	[138]
97%Goethite + 3%Vegetation-Green	[150]
65%Goethite + 35%Hematite	[191]
94%Goethite + 6%Vegetation-Green	[492]
87%Hematite + 13%Vegetation-Green	[1168]
68%Hematite + 32%GalvanisedIron	[1380]
73%Vegetation-Green + 27%ODZincalume	[3903]

Figure A4.1.100- Sylvanite: Sample 018_I_4; *Goethite {158}) results are in the visible and near-infrared (VNIR). Graph created using The Spectral Geologist 8.0.7.4. software. (Black) line represent result spectra using the GER 3700 in direct comparison with the spectral geologist spectral (ASCII) library files (Blue) line.

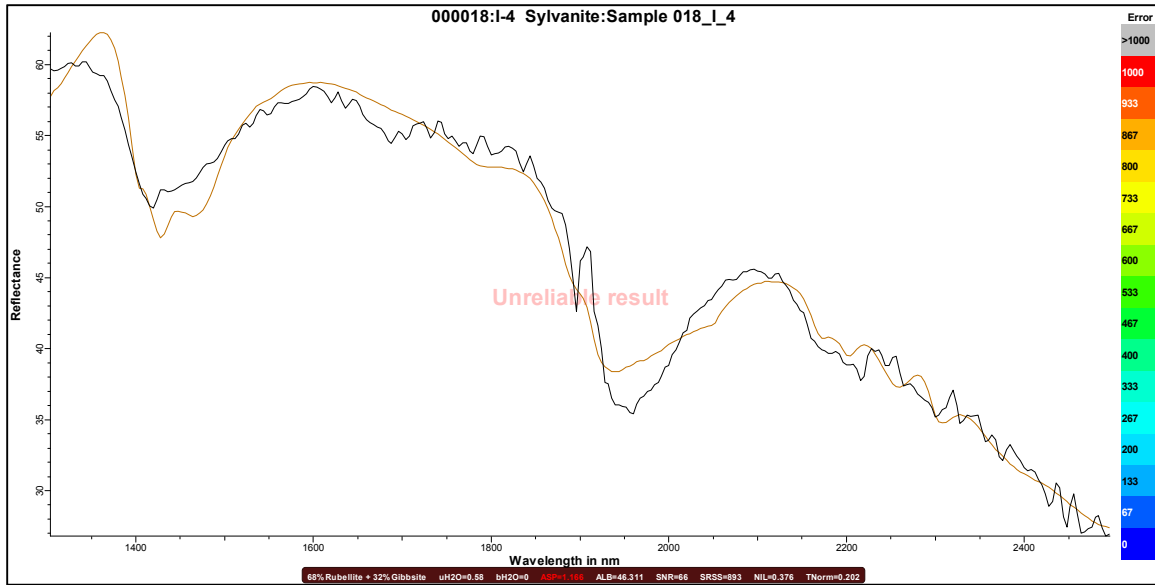


Figure A4.1.101- Sylvanite: Sample 018_I_4: Results are in the Short-Wave Infrared (SWIR). Graph created using The Spectral Geologist 8.0.7.4. software.

Candidate TSA results	
Rubellite [913]	
Dickite [948]	
Kaolinite-WX [977]	
Dolomite [978]	
Siderite [984]	
Paragonite [996]	
Ankerite [996]	
59%Dolomite + 41%Rubellite [830]	
78%Siderite + 22%Rubellite [838]	
66%Ankerite + 34%Rubellite [841]	
55%Calcite + 45%Rubellite [860]	
59%Dickite + 41%Rubellite [866]	
68%Rubellite + 32%Gypsum [871]	
53%Dickite + 47%Dolomite [876]	
55%Rubellite + 45%Jarosite [879]	
62%Chlorite-Mg + 38%Rubellite [886]	
58%Kaolinite-WX + 42%Rubellite [887]	
62%Dickite + 38%Jarosite [889]	
63%Chlorite-Mg + 37%Rubellite [890]	
68%Siderite + 32%Dickite [890]	
51%Rubellite + 49%Zoisite [891]	
53%Ankerite + 47%Dickite [891]	
63%Rubellite + 37%Epidote [891]	
*68%Rubellite + 32%Gibbsite [893]	
57%Chlorite-FeMg + 43%Rubellite [895]	
53%Rubellite + 47%Nacrite [897]	

65%Rubellite + 35%Talc [897]
51%Muscovite + 49%Rubellite [898]
59%Rubellite + 41%Vegetation-Dry [898]
63%Rubellite + 37%Alunite-NH [899]
84%Rubellite + 16%Topaz [900]
57%Kaolinite-WX + 43%Dolomite [900]
66%Chlorite-Fe + 34%Rubellite [901]
76%Rubellite + 24%Alunite-K [901]
72%Rubellite + 28%Alunite-Na [902]
60%Chlorite-Fe + 40%Rubellite [902]
43%Dolomite + 32%Dickite + 25%Rubellite [792]
45%Dolomite + 27%Rubellite + 27%Alunite-NH [794]
50%Ankerite + 28%Dickite + 22%Rubellite [803]
67%Siderite + 17%Rubellite + 16%Alunite-NH [803]
65%Siderite + 19%Dickite + 16%Rubellite [805]
53%Ankerite + 24%Rubellite + 22%Alunite-NH [809]
43%Dolomite + 31%Kaolinite-WX + 26%Rubellite [810]
46%Dolomite + 27%Rubellite + 27%Nacrite [813]
53%Dolomite + 32%Rubellite + 16%Alunite-Na [813]
47%Dolomite + 34%Rubellite + 19%Jarosite [815]
44%Dolomite + 29%Muscovite + 27%Rubellite [815]
44%Dolomite + 29%Muscovite + 27%Rubellite [818]

Figure A4.1.102-Sylvanite: Sample 018_I_4: The Spectral Geologist (ASCII) library list of other possible candidates. Closest candidate is denoted by an Astrid symbol * 68 % Rubellite + 32 % Gibbsite [893] according to the ASCII library. Results are in the Short-Wave Infrared (SWIR).



Figure A4.1.103. Sample 002_A_2



Figure A4.1.104. Sample 010_C_6



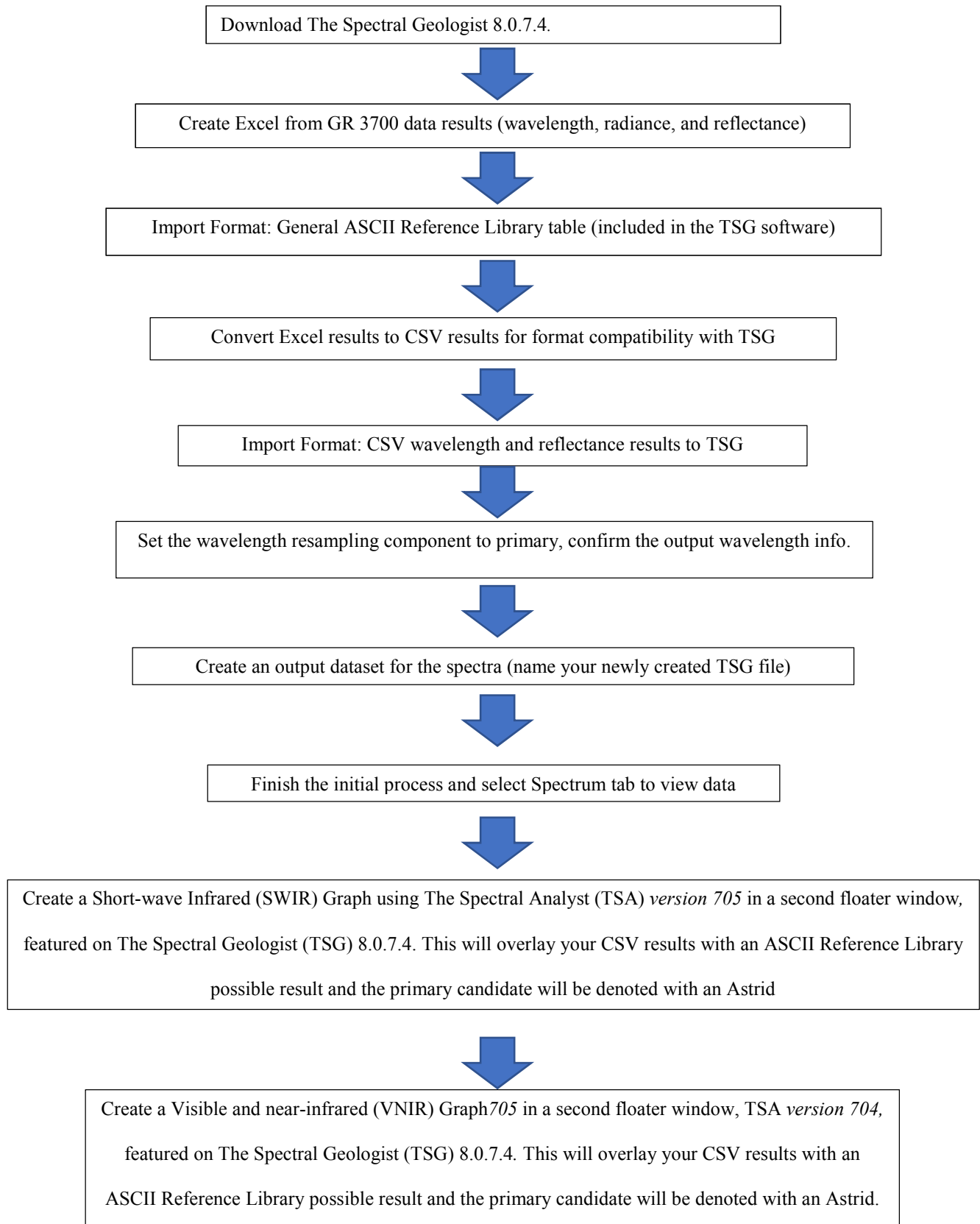
Figure A4.1.105. Sample 011_C_7



Figure A4.1.10. Sample 017_I_2

Flow Charts

A4.2.1. Spectroscopy ‘The Spectral Geologist’ Data Interpolation



X-ray Diffraction

Figures

Commander Sample ID (Coupled TwoTheta/Theta)

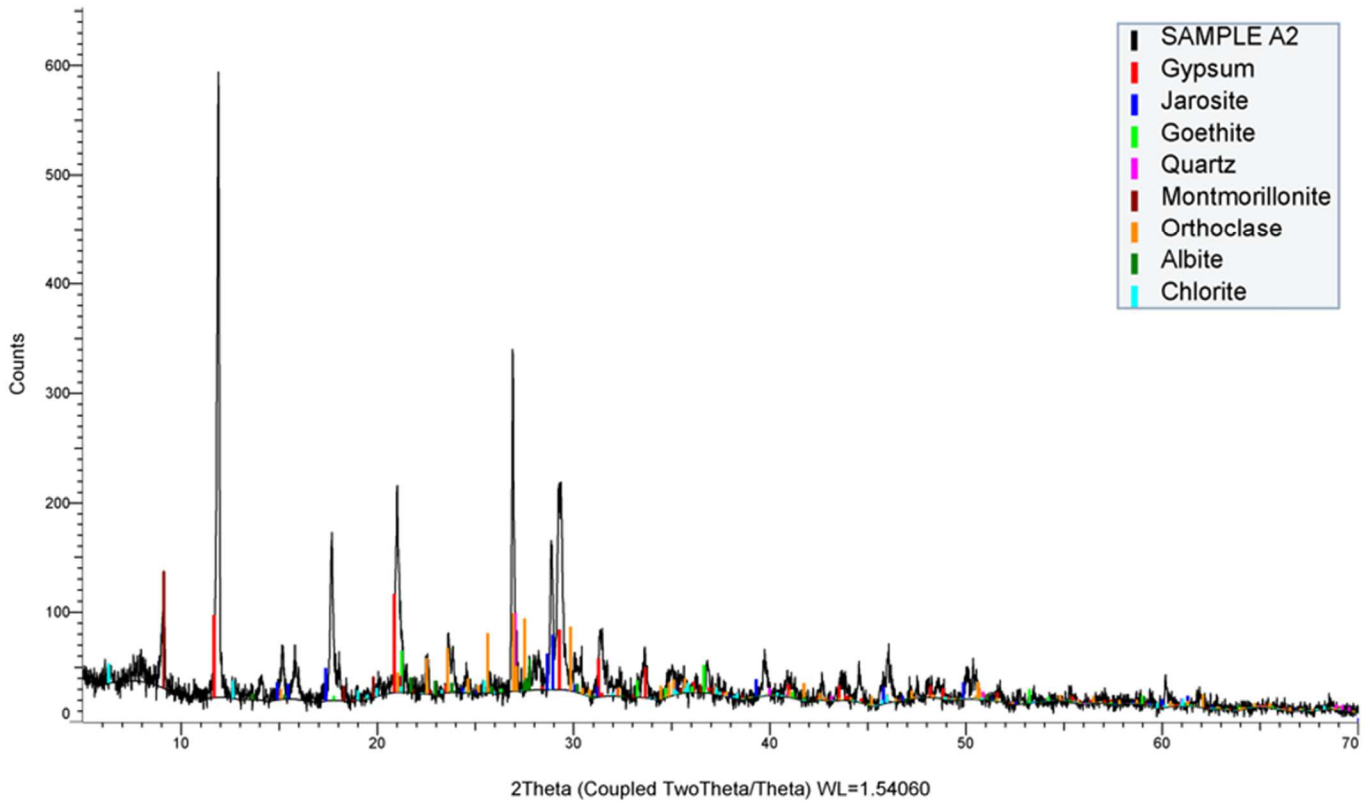


Figure A5.1.1. XRD sample A2 with top 8 matches.

Commander Sample ID (Coupled TwoTheta/Theta)

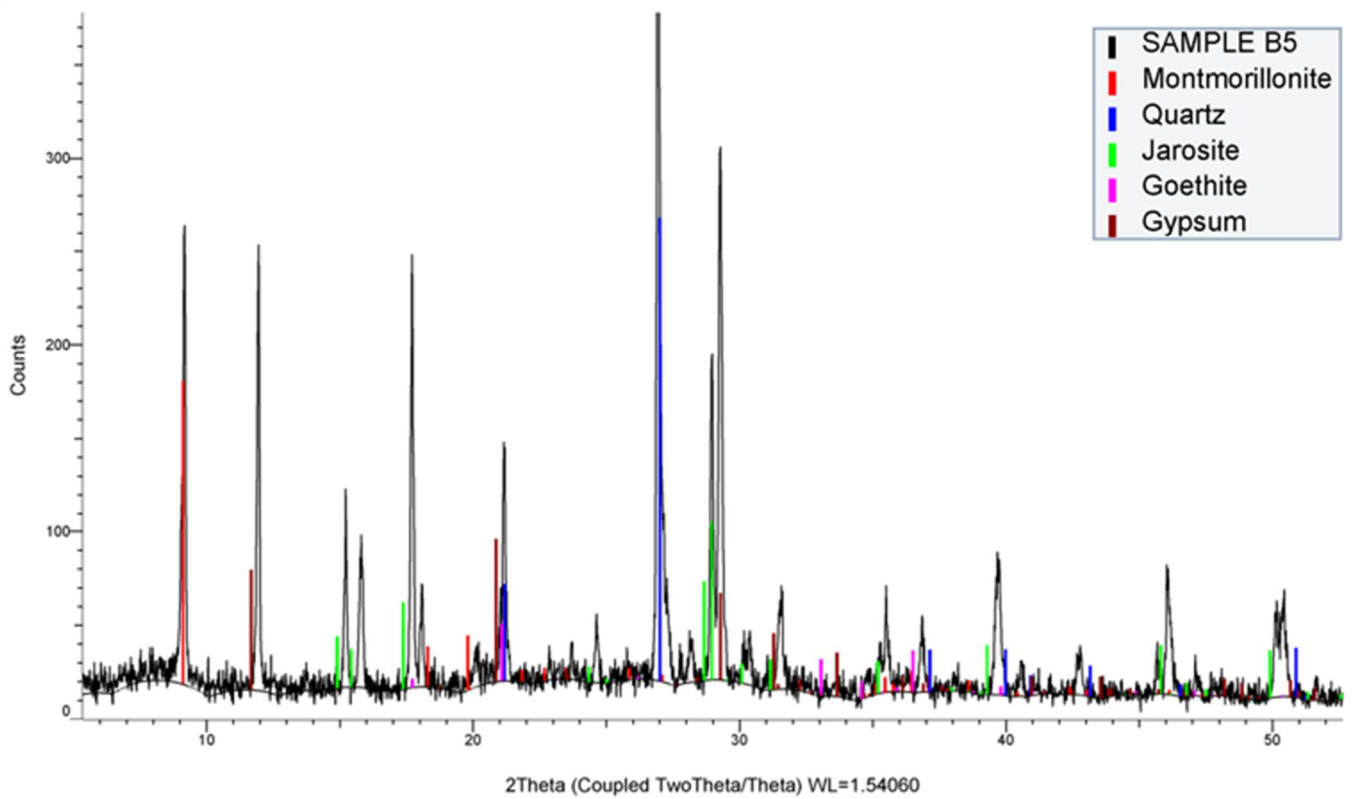


Figure A5.1.2. XRD sample B5 with top 5 matches.

Commander Sample ID (Coupled TwoTheta/Theta)

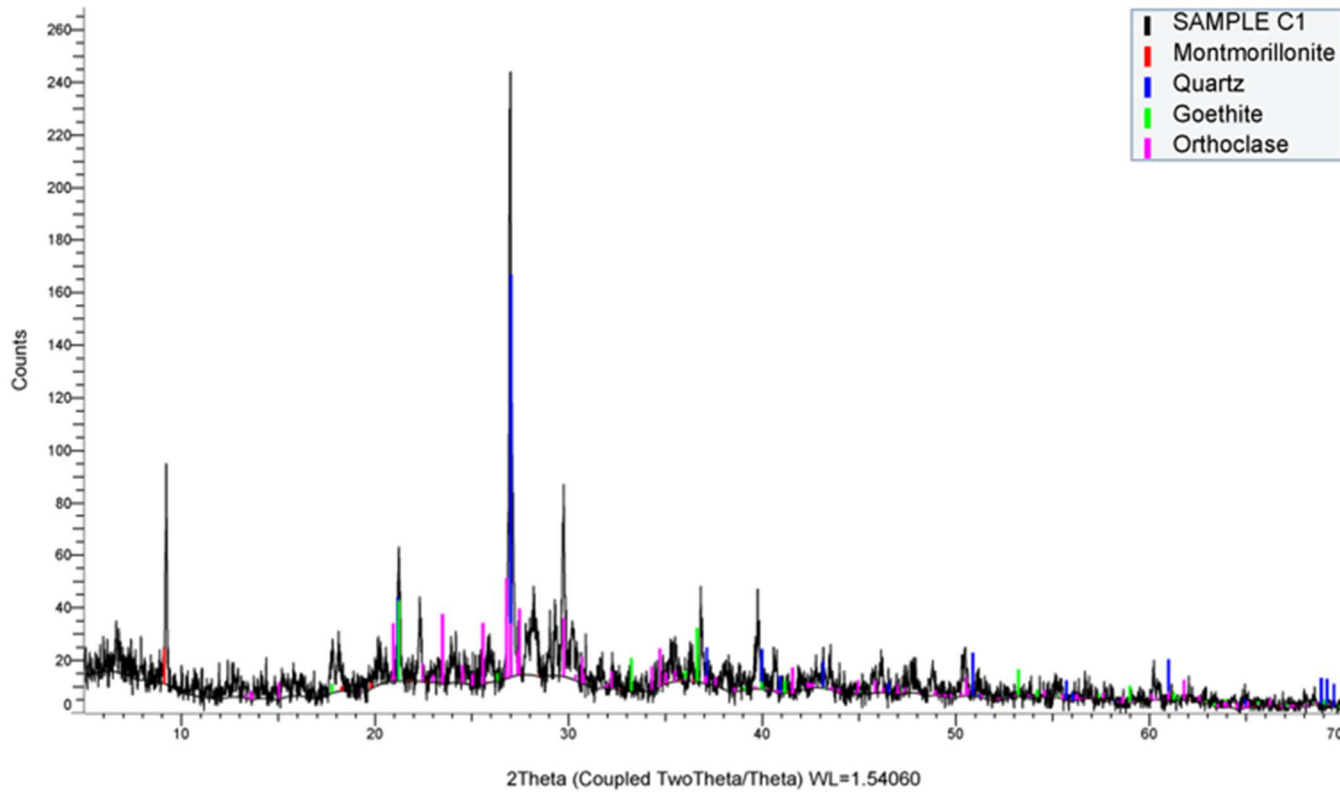


Figure A5.1.3. XRD sample C1 with top 4 matches.

Commander Sample ID (Coupled TwoTheta/Theta)

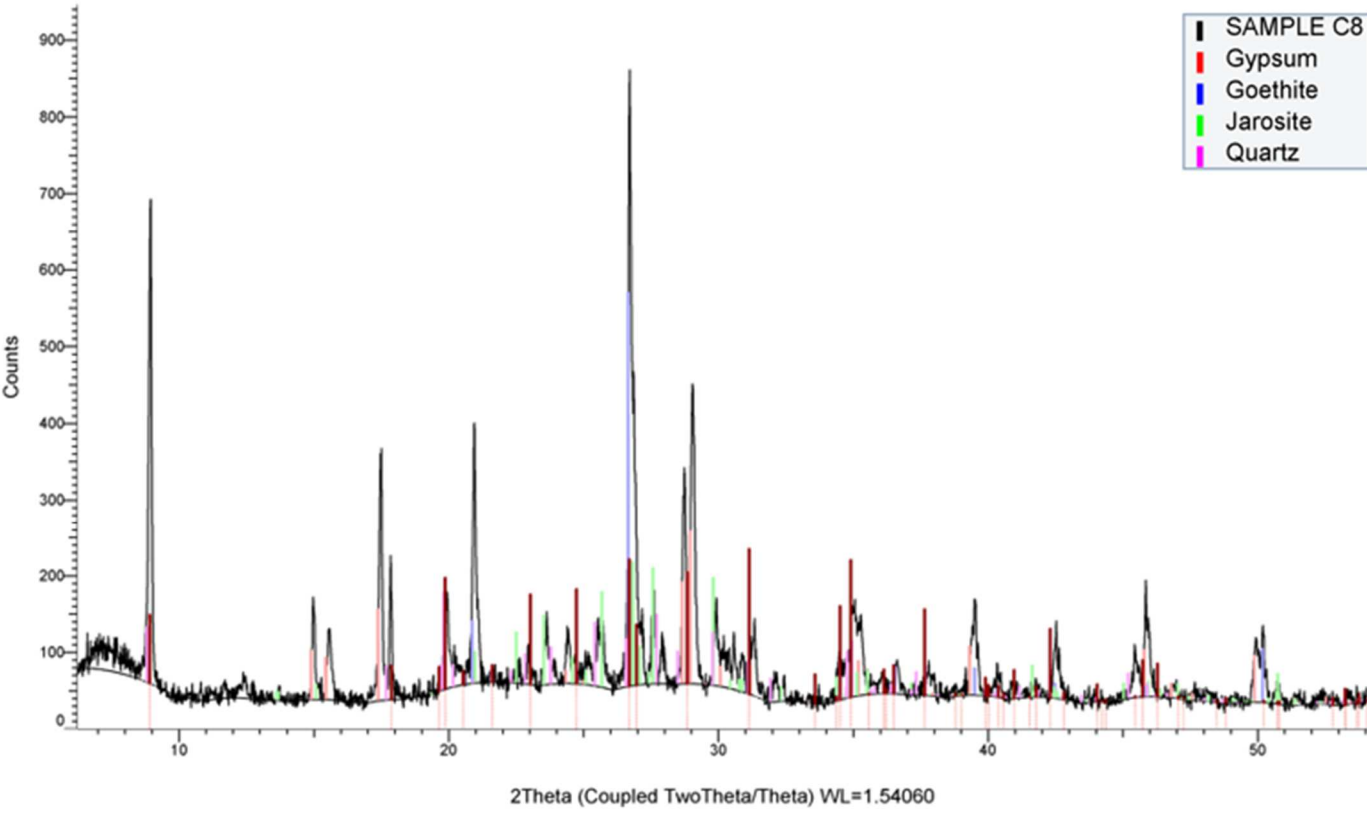


Figure A5.1.4. XRD sample C8 with top 4 matches.

Commander Sample ID (Coupled TwoTheta/Theta)

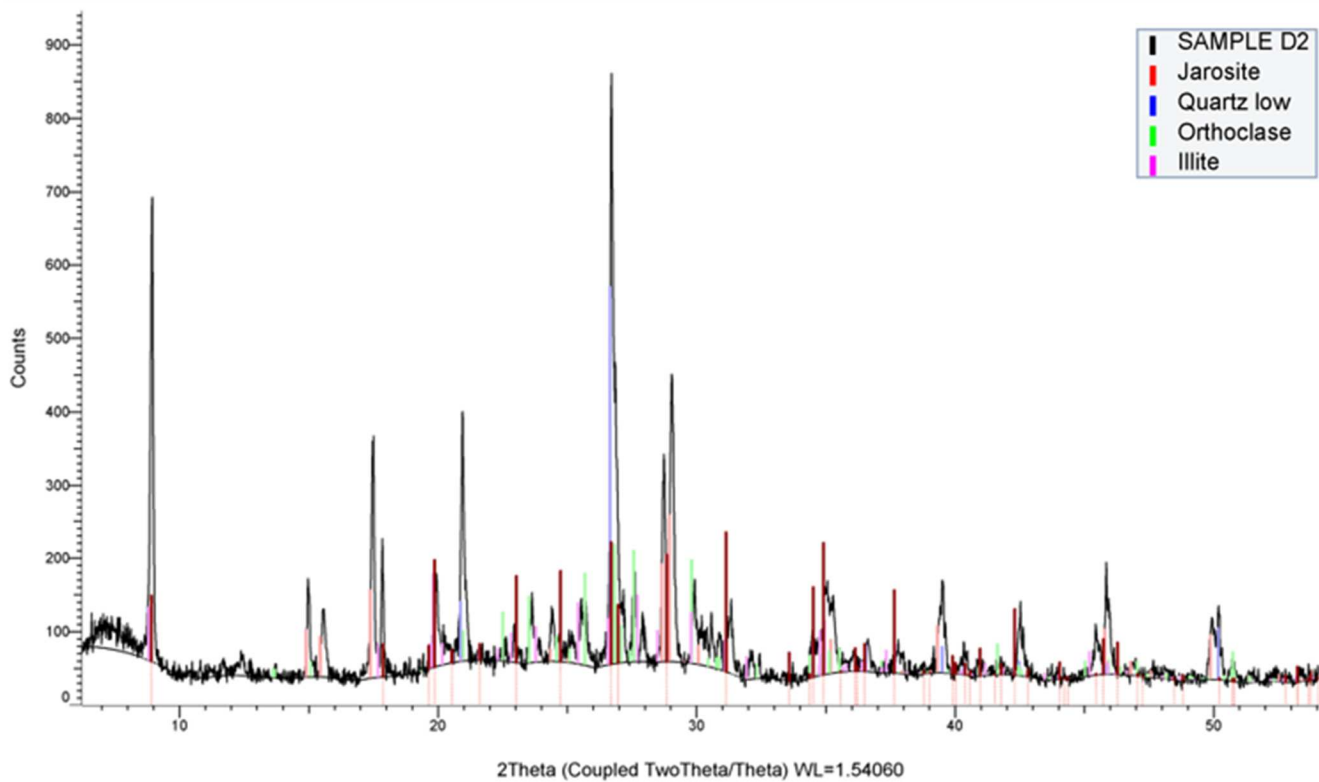


Figure A5.1.5. XRD sample D2 with top 4 matches.

Commander Sample ID (Coupled TwoTheta/Theta)

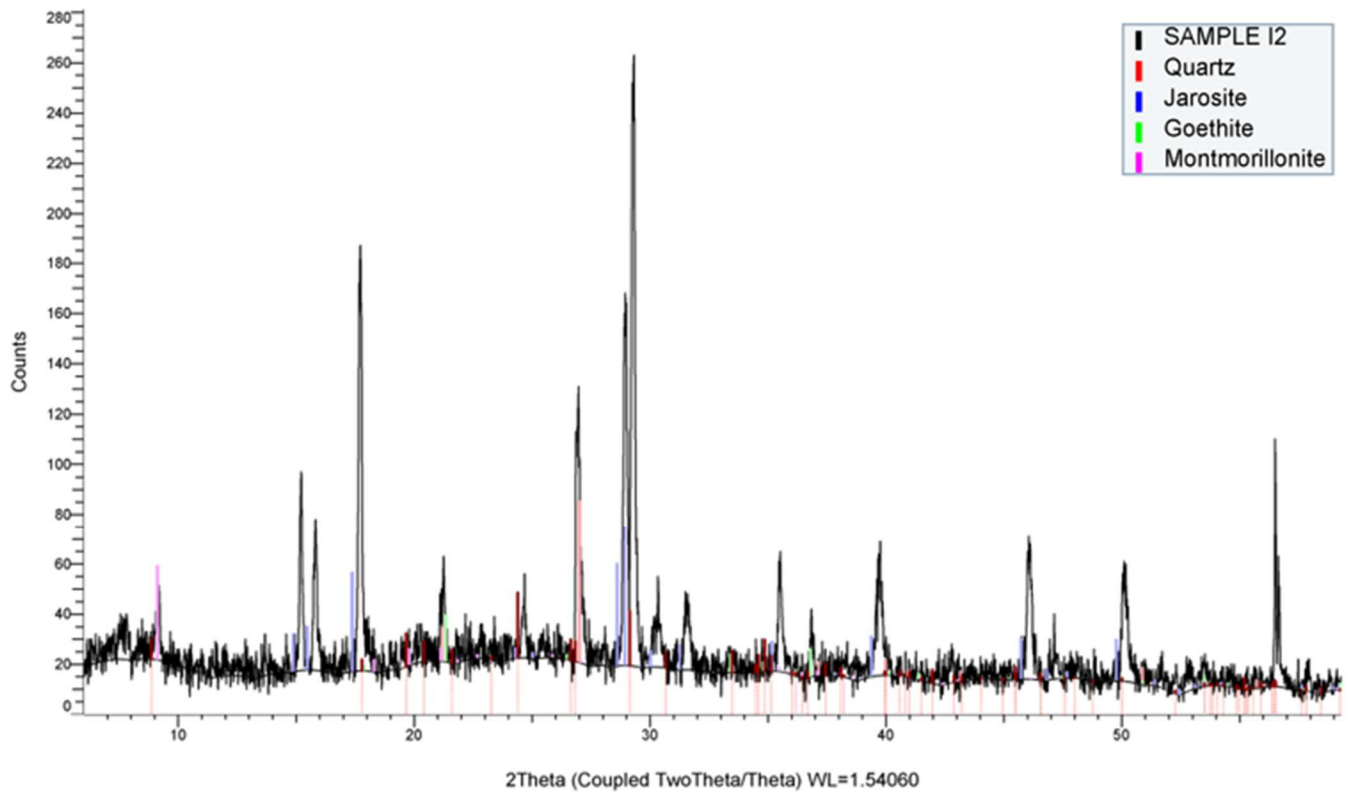
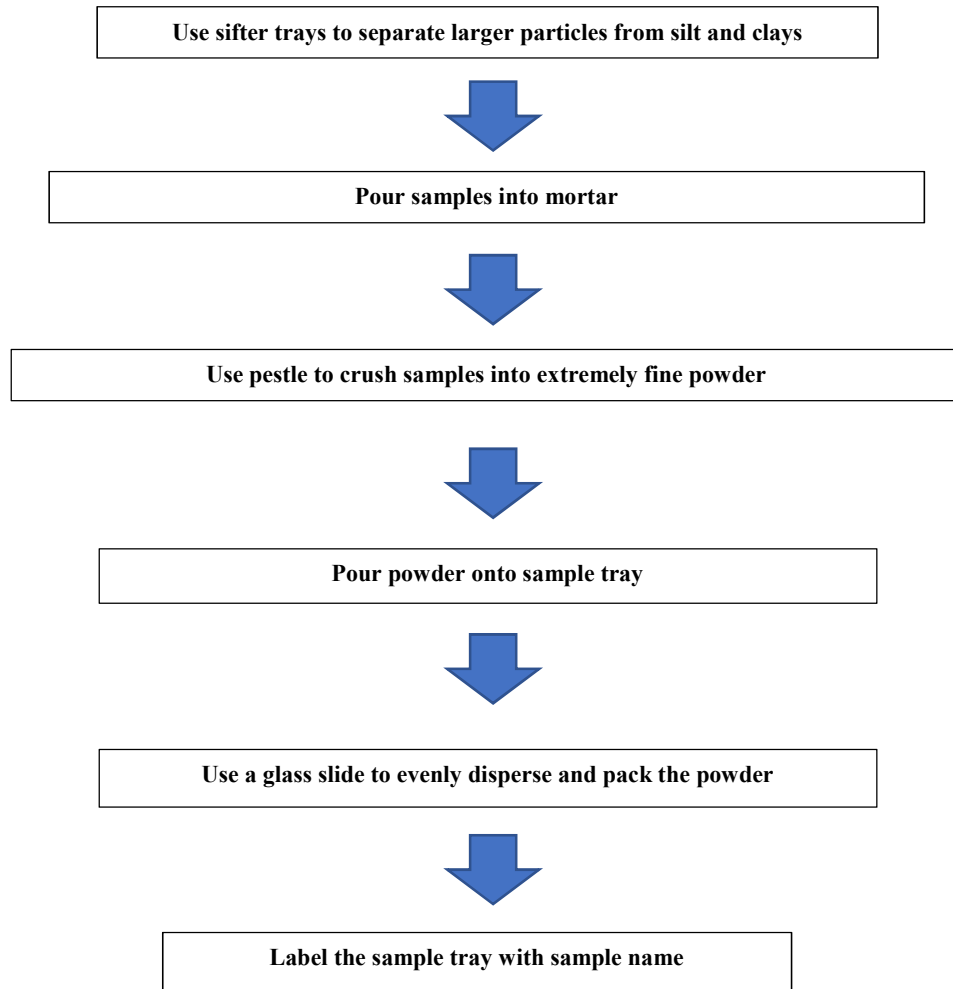


Figure A5.1.6. XRD sample I2 with top 4 matches.

Flow Charts

A5.2.1. X-ray Diffraction Sample Preparation



Additional Figures and Tables

Table A6.2.1. Faults of the Little Hatchet Mountains

Faults Name	Fault Type	Strike	Dip
Ringbone Reverse Fault	Reverse	SE	~25 SW
Beacon Hill Fault	Normal	SE	~40 SW
Hidalgo Reverse Fault	Reverse	SE	~45 SW
Howells Ridge Thrust Fault	Thrust	SE	~30 SW
Mojado Thrust Fault	Thrust	E, SE	~20 S, SW
Bull Canyon Fault	Normal	E, SE	~45 S, SW
Copper Dick Fault	Normal	W	~50 N
Livermore Spring Fault	Oblique strike/slip	S	~60 W
Windmill Reverse Fault	Reverse	SE	~45 SW
Granite Pass Reverse Fault	Reverse	E, SE	~57 S, SW

Table A6.2.2. EMD Mine/Prospect Data (McLemore et. al, 1996)

Mine/Prospect Name	Latitude	Longitude	Commodities	Years of Production	Development	Host	Type of Deposit
American (Alaska, Oregon, Maine, Florida, Monarch)	31 54' 27"	108 25' 47"	Pb, Ag, Cu, Au, Zn	1881-1960	300 ft shaft, 2000 ft drifts	Sylvanite quartz monzonite stock, Cret Hell-To-Finish Formation	Laramide vein
Copper King	31 54' 30"	108 25' 35"	Pb, Ag, Cu, Au, Zn, turquoise	unknown	pits	Cret U Bar Formation	Laramide skarn
Cricket	31 54' 30"	108 26' 15"	Pb, Ag, Cu, Au, Zn	unknown	pits	Sylvanite quartz monzonite stock	Laramide vein
Dugout	31 54' 00"	108 25' 47"	Pb, Ag, Cu, Au, Zn	unknown	pits	Tertiary volcanics	Laramide vein
Gold King Group (Fraction, Gold Howard, Lanny, Cpt. Henry,	31 54' 55"	108 26' 15"	Cu, Au, Ag, Zn, Pb, turquoise	unknown	shafts, adits, pits	Sylvanite quartz monzonite stock	Laramide vein
Hornet (Bonanza, Moab, Silver Crown, Nabob)	31 53' 48"	108 25' 40"	Zn, Pb, Ag, Cu, Au	1882-1958	150 ft shaft, 1200 ft drifts	Cret U Bar Formation	Laramide skarn
King 400	31 54' 52"	108 26' 20"	Cu, Au, Ag, Zn, Pb	1878-1930's	shaft	Sylvanite quartz monzonite stock	Laramide vein
Last Chance	31 53' 58"	108 25' 40"	Cu, Au, Ag, Zn, Pb	unknown	pits	Cret U Bar Formation	Laramide skarn
Miss Pickel	31 54' 40"	108 27' 30"	Pb, Zn, As	1924-1937	shaft	Cret Hell-To-Finish Formation	Laramide skarn
National group (Copper King, Silver King, Esmeraldo, Silver	31 54' 38"	108 25' 15"	Ag, Cu, Pb, Au, Zn, turquoise	1904-1929	50-217 ft shafts (5), 700 ft drifts	Cret U Bar Formation	Laramide skarn
Silver Bell	31 52' 35"	108 25' 35"	Pb, Ag, Cu, Au, Zn	unknown	pit	Cret Hell-To-Finish Formation	Laramide skarn
Silver Tree	31 56' 35"	108 29' 00"	Pb, Ag, Cu, Au, Zn	unknown	shafts	Tertiary volcanics	Laramide vein
Sites Tunnel	31 55' 10"	108 26' 45"	Pb, Ag, Cu, Au, Zn	unknown	adit	Sylvanite quartz monzonite stock	Laramide vein
Turquoise Mountain (Gold King, Cameo, Azure, Calmea)	31 54' 55"	108 26' 15"	Cu, turquoise	1885-1905	pits, shafts	Sylvanite quartz monzonite stock	Laramide vein
unknown	31 55' 00"	108 27' 25"	Cu, Au, Ag, Zn, Pb	unknown	pits	Sylvanite quartz monzonite stock	Laramide vein
unknown (Beacon Hill)	31 55' 00"	108 27' 30"	Cu, Au, Ag, Zn, Pb	unknown	shaft	Sylvanite quartz monzonite stock	Laramide vein
unknown	31 56' 30"	108 27' 30"	Cu, Au, Ag, Zn, Pb	unknown	pits, shafts	Cret Mojado Formation	Laramide vein
unknown (Hill 5758)	31 53' 00"	108 27' 40"	Fe	none	pits?	Sylvanite quartz monzonite stock	disseminated
unknown turquoise pit	31 54' 00"	108 26' 15"	Cu, turquoise	unknown	pit	Tertiary ash-flow tuff	Laramide vein, disseminated
Wasp	31 53' 45"	108 25' 35"	Pb, Zn, Ag, V, Cu	unknown	shaft	Cret U Bar Formation	Laramide skarn

Table A6.2.3. SMD Mine/Prospect Data (McLemore et. al, 1996)

Mine/Prospect Name	Latitude	Longitude	Commodities	Years of Production	Development	Host	Type of Deposit
Albert Bader Placer Deposits	31 51' 15"	108 29' 10"	Au	1908	pits, planning	Cenozoic alluvial gravels	placer gold
Broken Jug	31 49' 58"	108 27' 25"	Au, Cu	unknown	adit, pits	Sylvanite quartz monzonite stock	Laramide vein
Buckhorn (Wood, Russell, Barney)	31 50' 39"	108 27' 46"	Au, Ag, Cu, Pb, Zn, Bi, Te	1880's - 1940	A shaft and an adit	Cret Hell-To-Finish Formation	Laramide vein
Cactus (Crump, Three Snakes)	31 48' 06"	108 27' 08"	W, Mo, As, Cu, Bi	1943	pits, planning	Cret Mojado Formation	Laramide skarn
Clemmie	31 49' 30"	108 25' 56"	Au, Bi, Te, Cu	1908-1910	50 ft shafts, 20 ft of drifts	Cret Hell-To-Finish Formation	Laramide skarn
Copper Dick	31 51' 2"	108 27' 38"	Cu, Ag, Au, Pb	1905-1954	100 ft shaft, pit, trench	Cret Hell-To-Finish Formation	Laramide skarn
Cottonwood Springs Placers (Livermore)	31 50' 00"	108 29' 26"	Au	Abandoned in 1908	pits	Cenozoic alluvial gravels	placer gold
Creep (Bonner claims)	31 49' 43"	108 28' 00"	As, Au, Te, Bi, Cu	none	adits (265, 165 ft), 60 ft shaft	Cret U Bar Formation	Laramide vein
Eagle Point	31 45' 48"	108 27' 24"	W, Mo, Pb, Cu, Ag, Zn	1943	opencut, trenches, adit	Penn. Horquilla Limestone	Laramide skarn
Gold Acres	31 51' 26"	108 27' 00"	Au, Ag, Cu, Zn, Pb	unknown	pits, shafts	Cret Hell-To-Finish Formation	Laramide skarn, placer gold
Gold Hill (Hardscrabble, Silver Lake)	31 49' 16"	108 27' 07"	Au, Ag, Cu, Bi, Te	1908-1941	3 adits, pits	Cret Hell-To-Finish Formation	Laramide vein
Golden Eagle	31 49' 50"	108 27' 27"	Au, Ag, Cu	Pre 1910	30 ft shaft	Sylvanite quartz monzonite stock	Laramide vein
Green (Little Mildred, Martin)	31 49' 30"	108 27' 30"	Au, Ag, Cu	1920, 1935	adit	Cret Hell-To-Finish Formation	Laramide vein
Hachita (Omega, Omega 1 and 2)	31 50' 25"	108 28' 10"	Ba	N/A	2 shallow shafts, pits	Sylvanite quartz monzonite stock	Laramide vein
Hand Car	31 50' 15"	108 28' 00"	Au, Cu	N/A	opencuts, 20 ft shaft	Sylvanite quartz monzonite stock	Laramide vein
Jowell (Jarrell, Bar Z)	31 50' 28"	108 29' 15"	Cu, Ag, Au, Zn	1900's	65 and 90 ft deep shafts	Cret Hell-To-Finish Formation	Laramide skarn
King Solomon Mine	31 49' 36"	108 27' 13"	Cu, Au	unknown	pits	Sylvanite quartz monzonite stock	Laramide vein
Knickerbocker (Quartzite)	31 47' 25"	108 27' 10"	Ag	early 1880's	pits	Cret Mojado Formation	Laramide vein
Little Hatchet (Albert Bader Property, Santa Maria, Faria)	31 51' 18"	108 28' 45"	Pb, Cu, Ag, Au, Zn, Mo, V, Ba	N/A	3 shafts, 90-100 ft, 1200 ft of drifts	Cret Hell-To-Finish Formation	Laramide skarn
Pearl (Monte Cristo)	31 48' 28"	108 27' 25"	Au, Ag	1909	3 adits (60, 80, and 90 ft long)	Cret U Bar Formation	Laramide vein
Ridgewood (Adelina, Monrانيا)	31 49' 16"	108 27' 00"	Au, Cu, Ag	1909	Surface cuts, shaft, 40 ft adit	Cret Hell-To-Finish Formation	Laramide skarn
Silver Lake	31 49' 48"	108 27' 32"	Au, Ag, Cu	unknown	pits	Cret Hell-To-Finish Formation	Laramide skarn
Silver Trail	31 51' 15"	108 28' 45"	V, Pb, Zn, Cu, Ag	1909	pits, shafts	Cret Hell-To-Finish Formation	Laramide vein
Wake-Up-Charlie	31 49' 44"	108 28' 07"	Au, Cu, Bi, Te	1908	2 shafts (60, 100 ft deep)	Sylvanite quartz monzonite stock	Laramide vein, placer gold
Yellow Jacket	31 49' 30"	108 28' 10"	Au, Cu, Pb, Ag	1908	shaft	Cret Hell-To-Finish Formation	Laramide skarn
unknown	31 47' 25"	108 26' 15"	Ag	none	pits	Cret Mojado Formation	Laramide vein
unknown	31 49' 10"	108 27' 45"	Cu, Au, Ag, Zn	unknown	adit	Tertiary Diorite	Laramide vein
unknown	31 50' 00"	108 27' 40"	Au?, Ag?	none	pits	Sylvanite quartz monzonite stock	disseminated
unknown (Grant County)	31 52' 25"	108 26' 5"	Au	unknown	pits	Cenozoic alluvial gravels	placer gold

Vita

Kenneth C. Singh currently lives in Bagdad, Arizona. While attending University of Texas at El Paso he graduated Dec. 2019 with a Bachelor of Science in Geology maintaining a GPA of 3.39, and a Major GPA of 3.85 and will graduate with a Masters of Science in Geological Sciences. He has attended many conventions and conferences taking shortcourses that include 'Geophysics for the Mineral Exploration Geoscientist' at the Prospectors and Developers Association of Canada 2018 Toronto, Canada; 'Faults, Veins, Breccias, and their Alterations' at the International Association on the Genesis of Ore Deposits 2018 Salta, Argentina; and 'Porphyry deposits: Characteristics, origins and exploration strategies' at the Society of Economic Geologists 2019 Santiago, Chile. His work experience includes starting a job at Freeport McMoRan Bagdad Mine, Arizona as a Geologist I beginning in May 2022. He has worked as a Graduate Teaching Assistant at the University of Texas at El Paso from Jan. 2020-May 2022, a Geology Summer Intern at Freeport McMoRan Morenci Mine from May 2021-Aug.2021, and served in the United States Marine Corps as an Infantry Sergeant/Squad Leader from Apr. 2006-Apr.2014. His involvement in organizations includes President of the Society of Economic Geologists: UTEP Student Chapter from 2020-2022, President of the Center for Entrepreneurial Geosciences from 2019-2020, Vice President of the Center for Entrepreneurial Geosciences from 2018-2019, and Secretary of the Society of Economic Geologists: UTEP Student Chapter from 2018-2019.

Email: kcsingh@miners.utep.edu

Typist: Kenneth C. Singh